On the modeling and numerical simulation of fretting wear

Quentin Caradec

INSTITUT POLYTECHNIQUE DE PARIS

NNT : 2023IPPAE012

Thèse de doctorat

ENSTA IP PARIS

On the modeling and numerical simulation of fretting wear

Thèse de doctorat de l'Institut Polytechnique de Paris
préparée à l'École nationale supérieure de techniques avancées

École doctorale n°626 École doctorale de l'Institut Polytechnique de Paris (EDIPP)
Spécialité de doctorat: Mécanique des fluides et des solides, acoustique

Thèse présentée et soutenue à Saclay, le 6 novembre 2023, par

QUENTIN CARADEC

Composition du Jury :

Philippe Dufrénoy Professeur, Université de Lille (LaMcube)	Président
Siegfried Fouvry Directeur de recherche CNRS, École Centrale de Lyon (LTDS)	Rapporteur
Vladislav Yastrebov Chargé de recherche (HDR) CNRS, École des Mines de Paris (CdM)	Rapporteur
Daniel Nélias Professeur, INSA Lyon (LaMCoS)	Examinateur
Thomas Pasutto Ingénieur-Chercheur, EDF R&D	Examinateur
Habibou Maitournam Professeur, ENSTA Paris (IMSIA)	Directeur de thèse
Matthieu Breuzé Ingénieur-Chercheur, CEA (SEMT)	Co-encadrant
Claude Stolz Directeur de recherche CNRS, ENSTA Paris (IMSIA)	Invité
Jean-Luc Fayard Ingénieur-Chercheur, CEA (SEMT)	Invité

Acknowledgments

Ces quelques mots introductifs en français, rédigés quelques jours après la soutenance de ma thèse, sont l'occasion pour moi d'exprimer ma profonde reconnaissance envers toutes les personnes ayant contribué à ce travail.

Je souhaite en premier lieu remercier Matthieu Breuzé, qui m'a encadré durant ces trois années au CEA, pour sa grande implication, sa disponibilité sans faille et sa sympathie constante. Travailler à ses côtés a été un véritable plaisir, et son engagement a été un moteur essentiel dans la réalisation de ce projet.

Je souhaite également exprimer toute ma gratitude à Habibou Maitournam, mon directeur de thèse, pour son accompagnement attentif, ses très nombreux conseils et la bienveillance qu'il a toujours manifestée à mon égard. Nos discussions ont toujours été pour moi source de motivation, qu'il a sû générer par son enthousiasme et son optimisme inaltérables.

Un grand merci également à Jean-Luc Fayard, Benoît Prabel et Claude Stolz pour leurs contributions précieuses à travers les nombreuses et toujours très enrichissantes discussions que nous avons pu avoir. Leur expertise a été un atout majeur dans la réalisation de ce travail.

J'aimerais ensuite remercier mes rapporteurs Vladislav Yastrebov et Siegfried Fouvry. Merci à eux deux d'avoir accepté cette mission, pour leur lecture approfondie de mon manuscrit et les commentaires très constructifs qui en ont résulté. Merci également à Philippe Dufrénoy, Daniel Nélias et Thomas Pasutto d'avoir accepté de faire partie de mon jury et pour leur implication dans l'évaluation de ce travail.

La réussite de ce projet a grandement bénéficié d'un environnement de travail propice. À ce titre, je veux remercier l'ensemble des collègues du LM2S du CEA Saclay et, plus généralement, les collègues du CEA dont j'ai croisé la route pendant ces trois ans. Merci de m'avoir accueilli au labo durant ces trois années, ça a toujours été un réel plaisir de vous côtoyer au quotidien. L'ambiance bienveillante et le cadre de travail serein ont permis la réalisation de cette thèse dans les meilleures conditions.

Pour finir, je souhaite remercier l'ensemble de mon entourage pour m'avoir toujours permis de bénéficier d'un cadre de vie le plus favorable possible. Merci donc à mes parents, ma famille, mes amis ainsi qu'à mes colocataires successifs, qui à eux tous m'ont toujours garanti un environnement équilibré. Je suis très reconnaissant de savoir pouvoir toujours compter sur eux.

Enfin, je tiens à particulièrement remercier Sahra, à qui les mots exprimés au paragraphe précédent s'appliquent bien entendu également. Merci en particulier pour ton soutien indéfectible et tes encouragements constants. Ta présence m'a toujours été d'une grande aide et a eu, je crois, un impact significatif sur la réussite de ce travail.

Nomenclature

General notations

$\forall$, $\exists$, $\in$	For all, there exists, in
$[a,b]$, $]a,b[$, $[a,b[$	Closed, open, half-open (left-closed) intervals
$\Leftrightarrow$	If and only if
$\underline{a}$, $\underline{\underline{A}}$, $\underline{\underline{\underline{A}}}$	1st order tensor (vector), 2nd order tensor, 4th order tensor of $\mathbb{R}^3$
$\lvert a\rvert$, $\lVert\underline{a}\rVert$	Absolute value of a, euclidean norm of $\underline{a}$
$\underline{\nabla a}$, $\mathrm{div}(\underline{a})$	Gradient of a, divergence of $\underline{a}$
$\mathrm{Tr}(\underline{\underline{A}})$	Trace of $\underline{\underline{A}}$
$\underline{a}\cdot\underline{b}$, $\underline{\underline{A}}:\underline{\underline{B}}$	Dot product of $\underline{a}$ and $\underline{b}$, tensor contraction of $\underline{\underline{A}}$ and $\underline{\underline{B}}$
$\boldsymbol{M}$, $\boldsymbol{M}^T$, $\boldsymbol{M}^{-1}$	Matrix, transpose of a matrix, inverse of a matrix
$[\![a]\!]_\Gamma$	Discontinuity of a across surface Γ
$\langle a\rangle_+$	Macaulay brackets: $\langle a\rangle_+ = \frac{1}{2}(a+\lvert a\rvert)$
δ_{ij}	Kronecker's symbol
$\dot{a}$, $\partial_n a$	Physical time derivative of a, pseudo-time derivative of a (respectively derivatives with respect to time t or fretting cycle number n)
f', $\frac{\partial f}{\partial x}$	Derivative of a function f of a single variable, partial derivative with respect to x of a function f of several variables

Main symbols

t, n	Physical time, fretting cycle number
V, h	Wear volume, wear depth
K, α	Archard's wear coefficient, friction energy wear coefficient
μ	Coulomb's coefficient of friction
E, ν	Young's modulus, Poisson's ratio
F_n, F_t, δ	Normal force, tangential force, tangential displacement

E_{d}, e_{d}	Energy dissipated by friction, surface density of energy dissipated by friction
$\underline{u}$, $\underline{\underline{\varepsilon}}$	Displacement vector, linearized strain tensor
$\underline{\underline{\sigma}}$, $\underline{T}$, σ_n, $\underline{\tau}$	Cauchy stress tensor, stress vector, normal stress, tangential stress vector
$\underline{\underline{\underline{\underline{C}}}}$	Fourth-order elasticity tensor
ψ	Specific free energy
$\mathcal{D}$	Dissipation power
$\mathcal{G}$	Thermodynamic generalized force associated with wear
d, Y	Damage scalar variable, thermodynamic generalized force associated with damage
Γ_0, ϕ, v_n	Level set, signed distance to the level set, level set propagation velocity
λ	Lagrange multiplier
Δn	Acceleration factor for cycle jump
$\underline{\underline{\varepsilon^{\mathrm{p}}}}$, $\varepsilon_{\mathrm{c}}^{\mathrm{p}}$, $\varepsilon_{\mathrm{eq}}^{\mathrm{p}}$	Plastic strain tensor, cumulative plastic strain, equivalent plastic strain
$\underline{\underline{\sigma^{\mathrm{d}}}}$, σ_{VM}, σ_0	Deviatoric stress tensor, von Mises equivalent stress, initial von Mises yield stress

Abbreviations

i.e.	*id est*
s.t.	such that
DCM	Direct cyclic method
FE, FEM	Finite element, finite element method
TLS	Thick level set
TTS	Tribologically transformed structure

Contents

Introduction

As time goes by, structures are headed towards an inexorable deterioration. Materials interact with their surroundings, leading to an alteration of their properties and initial structure in the long run. The surfaces of solid bodies are especially exposed to the interactions with the outer environment and are particularly prone to degradation. When they come into contact and experience relative motion against counterparts, they may endure significant transformations. The study of such interactions belongs to the field of tribology. Within this discipline, wear is defined as the progressive loss of material from the surface of a solid body due to repeated contacts accompanied by relative motion.

In French, the verb "*user*"[1] refers either to the usage of an object or to its deterioration, the polysemy of the term stressing the relentless and irreversible nature of wear phenomena: as an object is used, its degradation becomes unavoidable. Excessive wear needs to be controlled, as it often leads to reduced performance, increased maintenance or, in the most extreme cases, failure of engineering systems. Wear can impact the lifespan of a wide range of components and structures from the simplest everyday items to the most complex industrial systems.

Wear issues in industrial contexts

Wear issues exist in a large diversity of industrial sectors. For instance, in the automotive industry, the contact of the vehicle on the road generates a progressive wear on the tires which need to be regularly replaced. In the railway sector, rails endure a progressive surface degradation due to the repeated train passes. Similar problems occur at the blade-disk interface in aircraft engines. In biomedical applications, wear reportedly occurs on hip joint prostheses. The issues are not only related to the deterioration of structural parts, but also to the emission of particles that comes as a result. Wear related to road-tire contacts and friction brake is known to generate high amounts of particulate matter, resulting in a pollution that causes important public health issues.

Regarding nuclear power plants, wear-related problems are closely monitored. In particular, in pressurized water reactors, wear may occur as a result of the repeated contacts between control rods and their guides. The role of the rod cluster control assembly is to control the power level in the reactor, and it also serves as a safety mechanism when an emergency shut down is required. Control rods are made of nitrided stainless steel tubes containing neutron absorbers, and pass through stainless steel guide cards (Figure 1). Control rods experience flow-induced vibrations due to the water flow in the reactor core, leading to repeated contacts with the guide cards. The contact kinetics is likely a combination of impact, sliding and fretting – namely a cyclic motion of relative sliding with a very small displacement amplitude. The process, which operates in a complex aqueous environment at about 300°C and 150 bars, may cause wear on the guide cards.

[1] To wear, or to use.

This generates additional maintenance costs related to the replacement of the worn parts, which could be reduced by improving the predictive capabilities for wear phenomena.

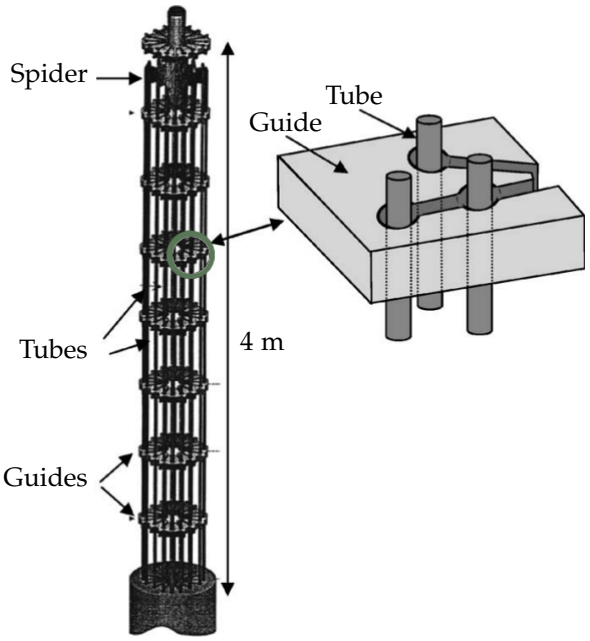

Figure 1: Rod cluster control assembly in a pressurized water nuclear reactor, with a zoom on a control rod tube passing through a guide card [Kaczorowski and Vernot 2006].

A complex phenomenon

The understanding of wear mechanisms remains limited to this day, and needs to be improved in order to enhance predictive capabilities. Wear of materials is a highly intricate problem which combines a variety of different processes. It is a multidisciplinary problem that involves physics, chemistry, materials science and mechanical engineering. It is also a multiscale phenomenon: short-term, microscopic mechanisms give rise to the long-term, macroscopic occurrence of surface material removal. For these reasons, no widely adopted unified wear model exists and studies on the subject are mainly conducted through experimental approaches. Regarding the application context of guide cards wear following contacts with control rods in pressurized water nuclear reactors, a previous study was carried out by Marc (2018). Fretting tests were conducted on a stainless steel cylinder-plane contact, meant to represent the tube-guide system. The experimental tests were made at room temperature and atmospheric pressure, either in a dry air environment or in a lithium-boron aqueous solution reflecting the actual chemistry in a pressurized water reactor.

Positioning of the study

The work reported in this dissertation relies on the experimental results obtained by Marc (2018), and proposes an attempt to tackle the problem of fretting wear through the angle of modeling and numerical simulation. The most widespread models are empirical, and while they enable a fair correlation with experimentally measured wear kinetics in many cases, they sometimes suffer from poor predictive capacities. An alternative approach based on a more theoretical ground is proposed in this work. Although research on the topic is often carried out from the perspective of

materials science, the modeling approach followed here is based on the framework of continuum mechanics and thermodynamics. The purpose of the study conducted here is to define a modeling methodology that could enable a better capture of the progressive mechanical degradation leading to surface material removal.

Furthermore, the numerical simulation of wear presents its own share of difficulties. This is mainly related to the multiscale nature of the phenomenon, which requires to perform long and costly computations to simulate the progressive evolution of wear. In addition, wear problems involve several non-linearities such as frictional contact, surface geometry evolution due to material removal, or non-linear material behavior. The work presented here aims at addressing some of these issues by providing numerical methods enabling the simulation of high-cycle fretting wear at reasonable computational costs.

Presentation of the document

A literature review on the different mechanisms at stake in the fretting wear of ductile metals is provided in Chapter 1. It outlines the great diversity of underlying processes behind wear and stresses the difficulties faced in modeling approaches.

Thereafter, a modeling framework is presented in Chapter 2. It is based on continuum thermodynamics to ensure the definition of a physically consistent model. In this chapter, it is proposed to account for wear by means of a damage-like variable whose role is to quantify the progressive accumulation of degradation ultimately leading to material detachment.

A wear simulation process is defined in Chapter 3 to compute wear evolution, using the finite element method. It integrates the use of a damage-based wear model as defined in the previous chapter. The use of a more classical friction energy-based wear law is also considered.

Simulation of fretting wear is very time-consuming due to the need to compute high numbers of cycles. To deal with this issue, a cycle jump method is frequently used, but may lead to unstable wear computations when the size of the cycle jump is too large. In Chapter 4, an implicit cycle jump method is presented as opposed to classical explicit methods. The implicit method, along with the use of an adaptive cycle jump, proves its efficiency to accurately simulate the high-cycle evolution of fretting wear. The simulations performed in this chapter assume that wear evolution is governed by a friction energy-based wear law.

Up to this point, all the developments are conducted assuming a linear elastic material behavior. In Chapter 5, a simulation process is presented to integrate the use of an elastoplastic material behavior model within wear computation frameworks. It relies on the direct determination of stabilized states for cyclic plasticity and provides a means to capture the interaction between surface geometry evolution due to wear and evolution of plastic strain.

Chapter 1

Phenomenology of fretting wear mechanisms

A short literature review on the various mechanisms encountered in fretting wear

1.1 Introduction

Wear is defined as a progressive material removal from the surface of a solid generated by repeated tribological loadings. It may take different forms and operate at various rates, but in all cases leads to an alteration of the surface geometry. It is generally measured on a global scale as a wear volume V – namely the volume of material lost by the solid on its surface – or on a local scale as a wear depth h at each point of the surface.

This chapter proposes an overview of the different wear mechanisms as described in the literature, with a focus on fretting wear of ductile metallic materials. It relies on the analysis of various experimental and analytical results. The large diversity of phenomena encountered and of parameters of influence is highlighted, which stresses the difficulties faced when dealing with modeling aspects. The bibliographical work proposed here is intended to offer an insight into the most predominant features of fretting wear that need to be taken into account for modeling purposes.

The most commonly described wear modes are presented at first. This provides an overview of the surface interaction mechanisms at the asperity scale that can produce wear particles. Then, fretting motion is defined with the associated degradation mechanisms and the peculiarities of wear phenomena occurring under fretting motion for metals are outlined. Finally, several of the most widely used wear models are presented.

1.2 General considerations on wear

When dealing with wear issues, one of the first difficulty encountered is that behind the same name, hides in fact a variety of distinct phenomena. Indeed, whereas wear refers to the macroscopic manifestation of material removal from a solid's surface, different microscopic mechanisms can be its source. Consequently, investigating wear problems on a system often starts by understanding the mechanisms in action.

For that purpose, researchers came up with different ways of classifying wear phenomena, be it by type of loading, by severity, or by the mechanisms at the asperity level that lead to material removal.

1.2.1 Classification of wear processes

Wear processes can first be categorized by type of loading. The main motion types likely to generate wear are unidirectional or bidirectional sliding, fretting, impact or erosion [Ko et al. 1997]. Provided that the displacement amplitude is large enough, bidirectional sliding causes wear damage that is rather similar to unidirectional sliding [Waterhouse 1984]. For smaller tangential displacement amplitudes, the motion is identified as fretting and the resulting damage has its own particularities, as described in Section 1.3. This is mostly due to the fact that the contact interface has a poor access to the environment, which promotes debris retention. In this work, focus is on wear occurring under fretting conditions. Two other loading types may induce wear damage, namely impact and erosion. Impact refers to the dynamic strike of a surface onto another, while erosion designates the degradation process on a surface subjected to a fluid flow. In the latter situation, wear occurs under the action of small particles carried by the fluid. These two load types are out of scope in the present study.

In addition to the load type, some authors categorize wear processes as being either mild or severe wear [Ko et al. 1997]. Although the difference between these two categories is not well defined and quite arbitrary, the transition between both is related to an important variation of the wear kinetics, which is sometimes accompanied by the occurrence of plastic strain in the near-surface layer. In addition, whereas mild wear is a phenomenon essentially localized in the asperities and leads to smooth worn surfaces, severe wear originates in deeper surface layers and generates rougher surfaces [Waterhouse 2000].

However, these types of classification give little to no indication about the underlying microscopic particles detachment mechanisms. Thus, wear is most often described by the particle detachment mode, namely abrasion, adhesion, fatigue or corrosion.

1.2.2 Wear particles detachment modes

Different mechanisms have been described at the surface asperities scale for wear debris generation. They consider the interaction between two opposing asperities with different possible outcomes. As they rely on asperities interactions, the following descriptions assume contacts between rough surfaces. Considering contact between asperities rather than smooth surfaces implies that the local contact pressure exerted on the asperities is much greater than the global macroscopic contact pressure. This is due to the fact that the real contact surface between asperities is smaller than the apparent contact surface [Vakis et al. 2018].

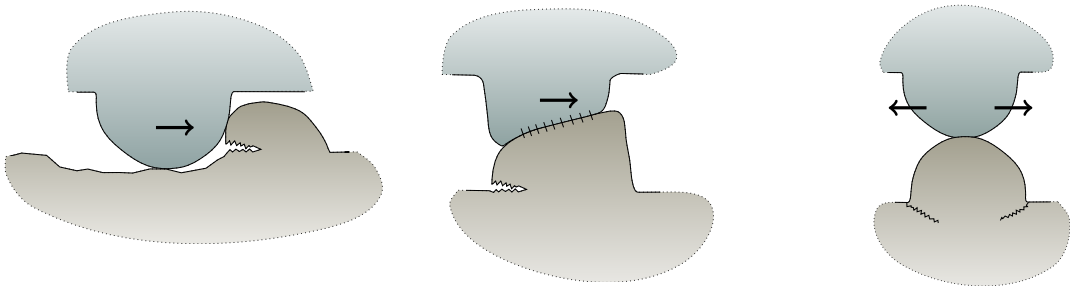

(a) Abrasive wear **(b)** Adhesive wear **(c)** Fatigue wear

Figure 1.1: Schematic representation of particles detachment modes at the asperities scale.

Abrasion refers to a situation in which an asperity of a harder surface tears an asperity of a softer surface away (Figure 1.1a). The particle is detached by brittle or ductile fracture. Abrasive wear is thus related to a difference of hardness between the abrading and the abraded bodies [Khruschov 1974]. However, this wear mode can operate between two solids of equivalent hardness when the contact is subjected to the presence of a third body made of debris harder than the primary bodies.

Adhesive wear is often a feature of wear occurring between two metallic materials. When a metallic surface meets another, bonds can form at the asperities tip under the high pressures experienced locally by the asperities. As sliding occurs, wear debris may form as a result of the strong shear stress in the asperities (Figure 1.1b). This particle detachment mechanism is often related to the presence of important plastic strain and to metal transfers from one surface to the other [Burwell and Strang 1952].

Fatigue wear occurs when repeated tangential loading of an asperity causes the nucleation and propagation of fatigue cracks (Figure 1.1c). Growth of fatigue cracks and their coalescence may lead to the formation of wear debris.

Corrosive wear describes the phenomenon in which wear is activated by corrosion effects. When the tribological system operates in a corrosive environment, oxidation of the contacting surfaces creates a passive film. The repeated destruction process of this film followed by further oxidation of the uncovered material is referred to as corrosive wear or tribocorrosion [Mischler and Munoz 2018].

To these four classically described mechanisms, one may add **delamination wear** as described by Suh [Suh 1973, 1977]. The delamination theory of wear states that flake-like debris may be formed as a result of the following sequence. First, a near-surface material layer experiences strong plastic strains, which leads to the formation of voids and cracks. The cracks subsequently propagate parallel to the surface and end up producing flake-like debris which are later crushed into smaller particles. In this description of wear, the difference between mild and severe wear is related to the difference between high-cycle and low-cycle fatigue.

In practice, a combination of several mechanisms is frequently encountered [Ko et al. 1997]. Regarding metals for instance, adhesive wear may be prevented in presence of a passive oxidized film on the surface. In this situation, a typical mixed wear mode consists in the initial abrasion of the passive film followed by further wear by adhesion and fatigue when the protective film is worn out and the metal becomes uncovered [Waterhouse 1977].

The different wear categories presented here were used by Lim and Ashby to empirically build wear maps for steels subjected to sliding [Lim and Ashby 1987]. They gave the predominant particle detachment mode as a function of normal load and sliding speed, as well as wear kinetics isolines and mild versus severe wear zones.

1.2.3 Three-body wear

The *third body approach* in wear problems was mainly fathered by Godet in the 1970s and 1980s [Godet 1984]. The third body, as opposed to the two primary bodies, refers to the solid or liquid medium which may be trapped in the interface between contacting bodies as shown in Figure 1.2. It is mainly composed of the wear debris detached from the primary bodies, which may remain stuck within the interface for a while before being ejected. The presence of third body greatly alters the stress distribution in the contact and the interactions between the surfaces. Third body has therefore a great influence on wear processes. The three-body approach leads to consider the wear problem not only as a particle detachment problem, but as a more complex process that involves the formation of wear debris, their interactions within the contact interface and their ejection from the contact. As a consequence, the wear kinetics may be considered not to be governed by the rate of debris formation but rather by the rate of debris ejection.

Berthier designates this whole process as the *tribological circuit* and proposes a simple description of it based on the mass conservation of debris in the interface [Berthier 2001]. The problem is regarded as a flow problem with a source flow (debris formation), internal flows (debris transport within the interface), recirculation flows (debris going out of the contact before coming back in due to contact motion) and a sink flow (debris definitive ejection). In this approach, the wear rate is not defined as the rate of debris formation (in other words particles detachment), but as the rate of debris ejection. The conservation problem is then written denoting the mass source flow J^{in} and the mass sink flow J^{out}. If we denote M^{TB} the total third body mass, the conservation problem reads

$$\frac{dM^{\text{TB}}}{dt} = J^{\text{in}} - J^{\text{out}}. \tag{1.1}$$

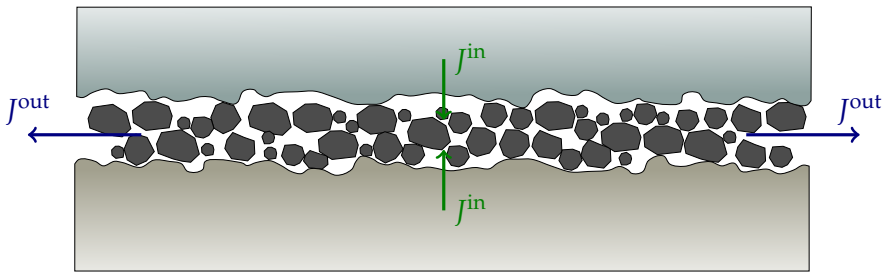

Figure 1.2: Schematic representation of two contacting bodies with third body particles trapped in the interface.

Fillot et al. bring this description further by relating the source and sink terms to the mass of debris in the interface [Fillot et al. 2007]. They make the following argumentation. As increasing the source flow of detached particles leads to an increase in the third body mass, they assume that in return an increase in the third body mass facilitates the accommodation of the relative displacement between the two surfaces. This introduces a negative feedback loop in the process: increasing the source flow increases the total mass which decreases the source flow. Similarly, they assume that increasing the third body quantity facilitates the debris ejection, which increases the sink term and thus decreases the third body mass. Under these assumptions, the third body quantity evolves towards a stable equilibrium point and the debris formation and ejection flows reach a steady state as depicted in Figure 1.3.

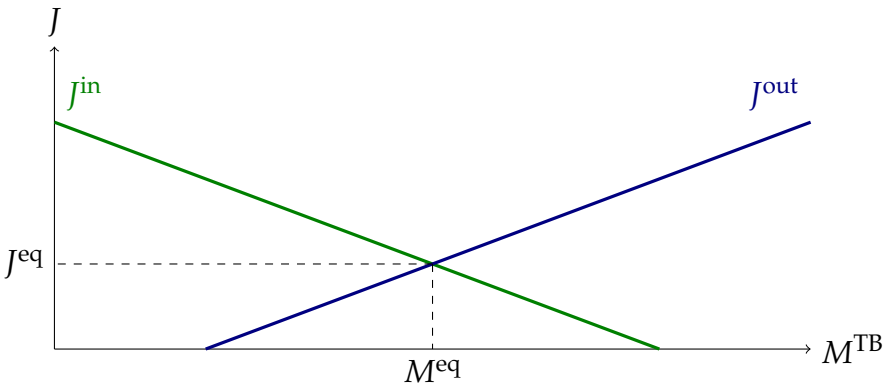

Figure 1.3: Evolution of the debris formation and ejection flows with respect to the mass of third body in the interface [Fillot et al. 2007].

Nevertheless, three-body tribology remains an extremely complex problem. The third body is made of a mixture of diverse interfacial elements and its behavior is very difficult to model. The study of the third body rheology constitutes a research field in itself [Iordanoff et al. 2002]. The importance of third body in fretting wear problems needs however to be outlined, as the small displacement amplitude in fretting enables wear debris to remain trapped in the interface even more easily.

1.3 Fretting motion

1.3.1 Definition of fretting

Among the various loadings likely to generate wear, *fretting* refers to a cyclic tangential sliding motion between two contacting bodies, with small[1] displacement amplitudes. Fretting motion is usually characterized by the normal force applied to the contacting solids, the tangential load, the tangential displacement amplitude, and the motion frequency.

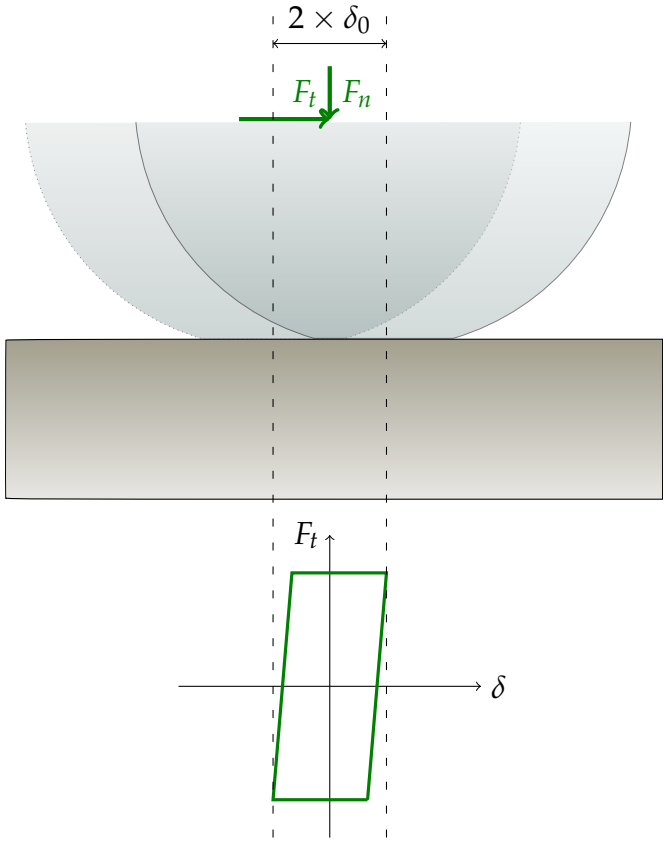

Figure 1.4: Schematic representation of a cylinder-plane contact in fretting motion, with the associated fretting loop.

Each fretting cycle is described by a fretting loop, which represents the hysteretic path of the tangential load F_t as a function of displacement δ along the cycle as depicted in Figure 1.4. During a cycle, the displacement δ evolves in the range $[-\delta_0, \delta_0]$. The slope during the change of displacement direction is related to the elastic compliance of the system. The integral of the fretting loop is equal to the energy dissipated during the cycle E_d:

$$E_d = \int_{\text{cycle}} F_t \, d\delta. \tag{1.2}$$

Assuming that the dissipated energy equals the friction energy and that friction follows Coulomb's

[1]Small displacement amplitude is usually understood as "smaller than half the contact width", such that there exists a zone in the contact interface that is never exposed to the outer environment. In practice, fretting displacement amplitudes are often comprised in the range from a few tens to a few hundreds micrometers [Waterhouse 1984].

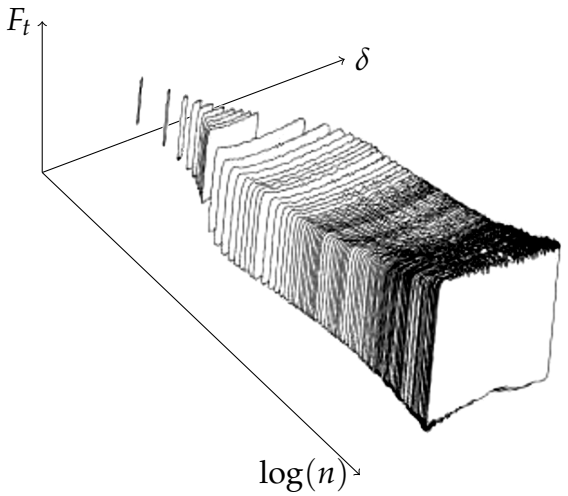

Figure 1.5: Example of fretting log [Marc 2018].

law, and neglecting the impact of the aforementioned slope on the integral computation, we get the following approximation for the energy dissipated by friction:

$$E_d \approx 4\mu F_n \delta_0 \tag{1.3}$$

where μ is Coulomb's coefficient of friction and F_n is the normal load.

Compiling the fretting loop of each successive cycle, a fretting log is obtained. It allows to see the evolution of the fretting regime throughout the experiment.

1.3.2 Fretting regimes and degradation modes

Different fretting regimes exist and generate different types of damage. The **stick regime** refers to a situation in which the tangential load is too low to generate sliding. The tangential relative displacement between the two solids is very small, and is totally accommodated by the elastic strain of the solids such that there is no sliding at the contact. In this case, the fretting loop has no hysteresis: there is no frictional energy dissipation (Figure 1.6a). For higher tangential loads, sliding occurs at the interface between the solid bodies. There exists a **partial slip** regime in which the tangential load is sufficient for sliding to partially occur on the contact area, but not to bring the whole area into slip. In that partial slip regime, the outer area of the contact surface undergoes higher local tangential stresses combined with lower normal stresses than the central part of the contact. Hence, there is an outer zone of the contact surface that slides as a result, and an inner zone that remains stuck. The typical aspect of a fretting loop in partial slip is depicted in Figure 1.6b. Finally, for even higher tangential loads, the whole contact area experiences sufficiently high tangential stress to slide: this is the **gross slip** regime (Figure 1.6c).

Vingsbo and Söderberg represent the different fretting regimes in fretting maps, that show the fretting regime depending on the normal force, tangential force amplitude, displacement amplitude or frequency [Vingsbo and Söderberg 1988], as depicted for example in Figure 1.7. Later, Vincent et al. extend fretting maps by relating the fretting regime to the dominant surface degradation mechanism [Vincent et al. 1992]:

- In the stick regime, there is a limited surface degradation. On the contact surface, there is no

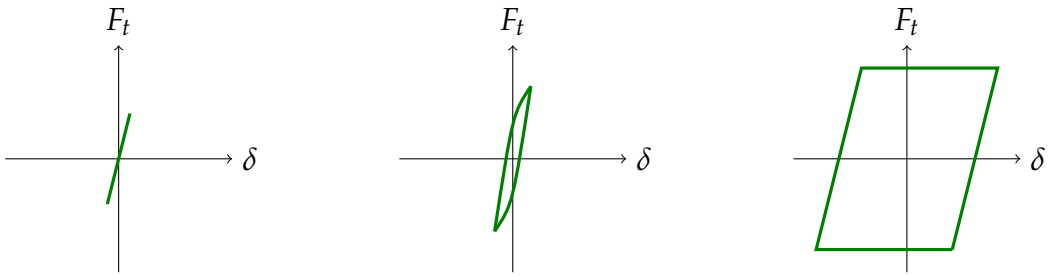

(a) Stick regime **(b)** Partial slip regime **(c)** Gross slip regime

Figure 1.6: Fretting loops for (a) stick regime (b) partial slip regime and (c) gross slip regime.

significant corrosion and wear, nor fatigue cracks.

- In the partial slip regime, the wear and corrosive effects are poor. However, fatigue cracks may nucleate and propagate. The major degradation mechanism is referred to as fretting fatigue.
- In the gross slip regime, surface degradation occurs due to wear, possibly with corrosion. Fatigue cracks nucleation is prevented, and the degradation mechanism is called fretting wear.

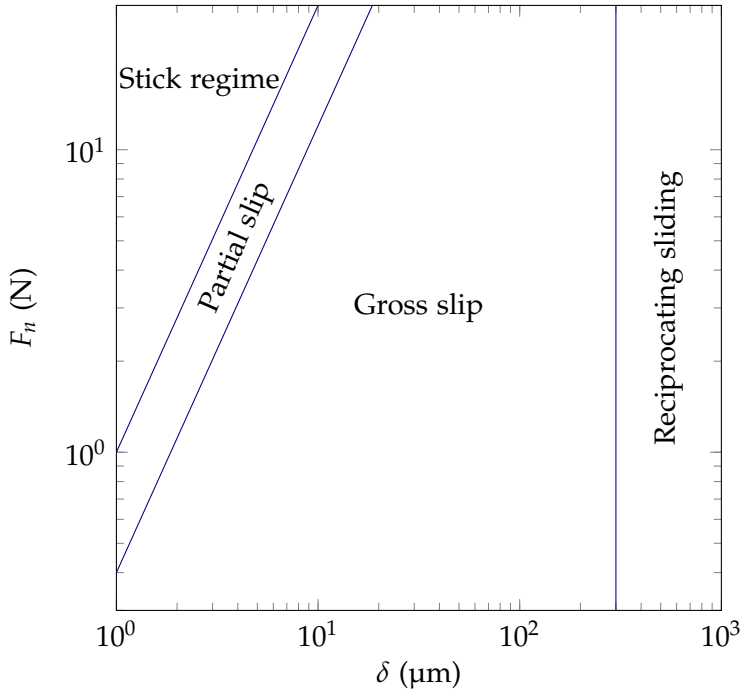

Figure 1.7: Example of fretting map as a function of normal load and displacement amplitude [Vingsbo and Söderberg 1988].

The association between partial slip regime and fatigue damage on the one hand, and gross slip regime and wear damage on the other hand, has been widely studied and documented. Several authors investigated the competition between fatigue crack nucleation and wear evolution in both fretting regimes [Waterhouse 1984, Fouvry et al. 1996]. They argue that in partial slip regime, the wear kinetics is low enough to allow time for fatigue cracks to nucleate. As the displacement amplitude increases, wear kinetics increases as well and in gross slip regime wear occurs sufficiently fast to eliminate the nucleation zones from the surface. It was also mentioned that the formation of wear particles offers a protection against crack nucleation due to the third body layer accommodating the velocity difference between the surfaces [Berthier et al. 1988]. The knowledge of the

competition phenomenon was enhanced later using numerical computations [Ding et al. 2004]. It was established that in case of gross slip, the evolution of wear favors subsurface compressive stress near the contact edges, which extends fatigue life. Moreover, the maximal stress location, which means the location of the most probable crack nucleation, constantly moves outwards due to the enlargement of the contact area which does not leave enough time for cracks to nucleate. On the opposite, in partial slip the stress concentration is always located in the vicinity of the contact edge or of the stick-slip boundary, which does not move during the transformation [Madge et al. 2007]. The high shear stress is suitable for rapid crack nucleation. This observation was later confirmed using finite elements computations [Garcin et al. 2015].

1.3.3 Mechanical response under fretting motion

Hertzian contacts

In order to assess the degradation generated by fretting processes, the computation of contact stresses is of prime importance. An early analytical theory of contact was given by Hertz in the 19$^{\text{th}}$ century for elastic bodies [Hertz 1882]. A simple analytical solution is given for the contact pressure distribution between two elastic cylinders in contact subjected to a normal force per unit (out-of-plane) length F_n (Figure 1.8). Let us denote respectively E_1 and E_2 the Young's moduli of bodies 1 and 2, ν_1 and ν_2 their Poisson's ratios and R_1 and R_2 their radii. Hertz's model gives the maximal pressure exerted at the center of the contact surface:

$$p_{\max} = \sqrt{\frac{F_n E^*}{\pi R^*}} \tag{1.4}$$

and the contact surface half width is:

$$a = \sqrt{\frac{4F_n R^*}{\pi E^*}} \tag{1.5}$$

where E^* is the contact equivalent Young's modulus:

$$E^* = \left(\frac{1-\nu_1^2}{E_1} + \frac{1-\nu_2^2}{E_2} \right)^{-1} \tag{1.6}$$

and R^* is the equivalent radius:

$$R^* = \left(\frac{1}{R_1} + \frac{1}{R_2} \right)^{-1}. \tag{1.7}$$

The contact pressure distribution on the contact surface reads:

$$p(x) = p_{\max} \sqrt{1 - \frac{x^2}{a^2}} \text{ if } |x| \leq a. \tag{1.8}$$

When the contact is subjected to frictional sliding, the tangential friction stress q can be computed using analytical equations formulated by Cattaneo and Mindlin [Cattaneo 1938, Mindlin 1949]. These solutions enable to capture the evolution of tangential stress during the stick-to-slip transition and are therefore suitable in partial or gross slip fretting conditions. For instance in the gross slip case, the tangential stress profiles are shown in Figure 1.9 at different stages of the

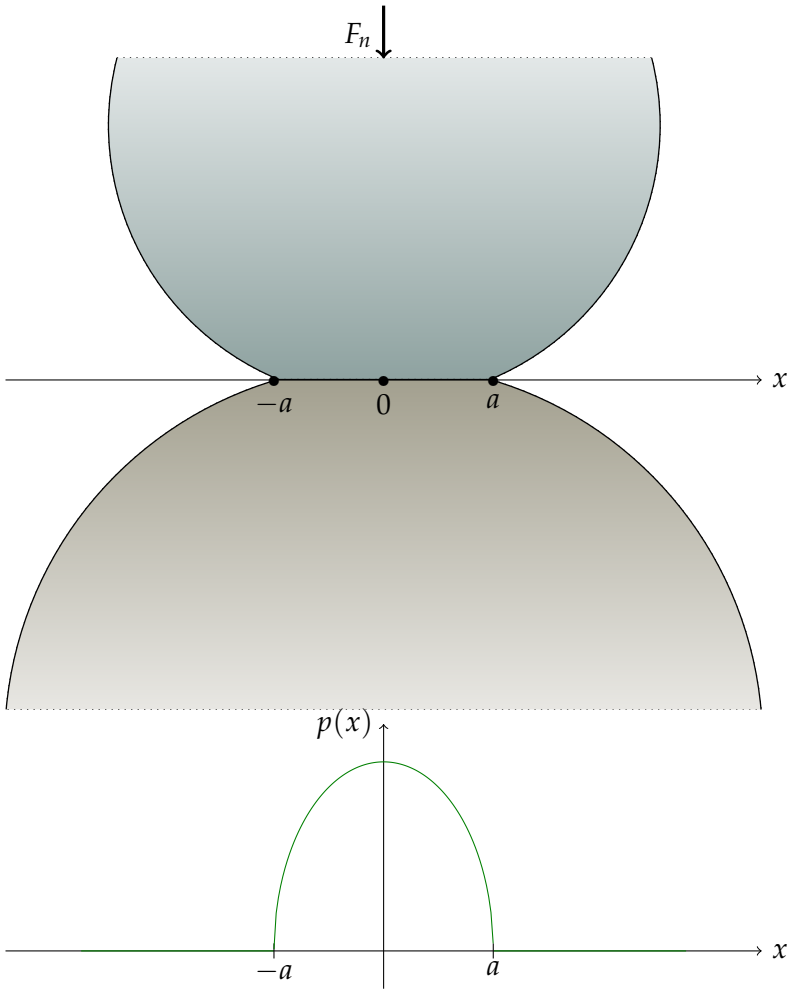

Figure 1.8: Schematic representation of two cylindrical bodies in contact and contact pressure given by Hertz's elastic model.

fretting cycle. Given such evolution during a change of displacement direction, tangential contact stress clearly proves to be path-dependent.

Stress state under elastic contacts

The material degradations caused by fretting loading stem from the history of the mechanical state endured by the solid. Considering an elastic half-space subjected to a normal and tangential stress distribution on its free surface, a solution for the stress field in the two-dimensional plane strain case may be provided [Johnson 1985]. This solution derives from the solution to Flamant's problem of a two-dimensional elastic half-space subjected to a point loading. Let us consider the two-dimensional plane (x, y) and a semi-infinite elastic body occupying the half-space $(y \leq 0)$. The solid is subjected to a normal pressure distribution $p(x)$ and tangential stress $q(x)$ on the free

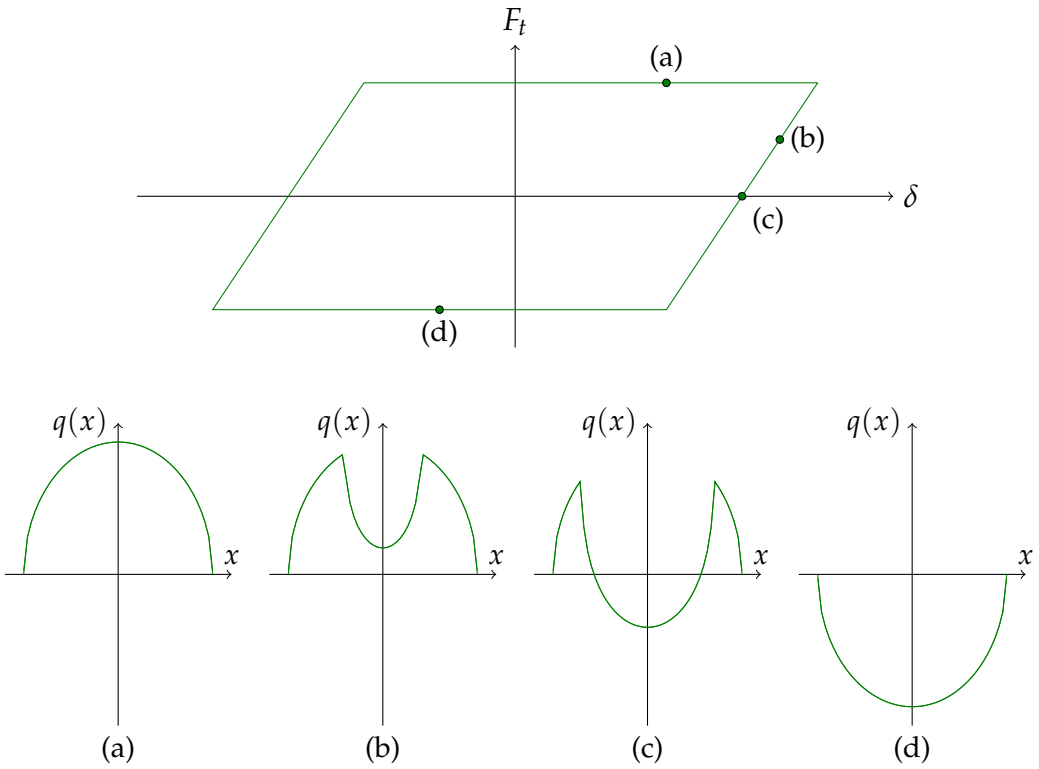

Figure 1.9: Mindlin's solution for tangential contact stress in gross slip at different stages of a fretting cycle.

surface $y = 0$ for $x \in [-a, b]$. The components of the stress field read:

$$\sigma_{xx}(x,y) = -\frac{2y}{\pi}\int_{-a}^{b}\frac{p(s)(x-s)^2}{((x-s)^2+y^2)^2}ds - \frac{2}{\pi}\int_{-a}^{b}\frac{q(s)(x-s)^3}{((x-s)^2+y^2)^2}ds \tag{1.9}$$

$$\sigma_{yy}(x,y) = -\frac{2y^3}{\pi}\int_{-a}^{b}\frac{p(s)}{((x-s)^2+y^2)^2}ds - \frac{2y^2}{\pi}\int_{-a}^{b}\frac{q(s)(x-s)}{((x-s)^2+y^2)^2}ds \tag{1.10}$$

$$\sigma_{xy}(x,y) = -\frac{2y^2}{\pi}\int_{-a}^{b}\frac{p(s)(x-s)}{((x-s)^2+y^2)^2}ds - \frac{2y}{\pi}\int_{-a}^{b}\frac{q(s)(x-s)^2}{((x-s)^2+y^2)^2}ds \tag{1.11}$$

$$\sigma_{zz}(x,y) = \nu(\sigma_{xx}(x,y) + \sigma_{yy}(x,y)). \tag{1.12}$$

Based on this solution, one can easily compute the stress field generated by a fretting loading, assuming for example a Hertzian contact in gross slip with friction following Coulomb's law. For example, Figure 1.10 depicts the stress components fields computed using a coefficient of friction $\mu = 0.9$.

Contact between inelastic bodies

These results are only valid in the elastic domain. Johnson also provides insights on the behavior of elastoplastic bodies under frictional contact [Johnson 1985]. First, assuming a von Mises yield criterion, Johnson gives the location of plastic yield onset for pure normal contact under a plane strain assumption. It occurs in the bulk material under the contact center at depth $0.7a$ where a is the contact half width. Plastic yield onsets as soon as the maximum contact pressure reaches $p_{\max} = 1.79\sigma_y$ where σ_y is von Mises yield stress. Considering now a frictional sliding contact

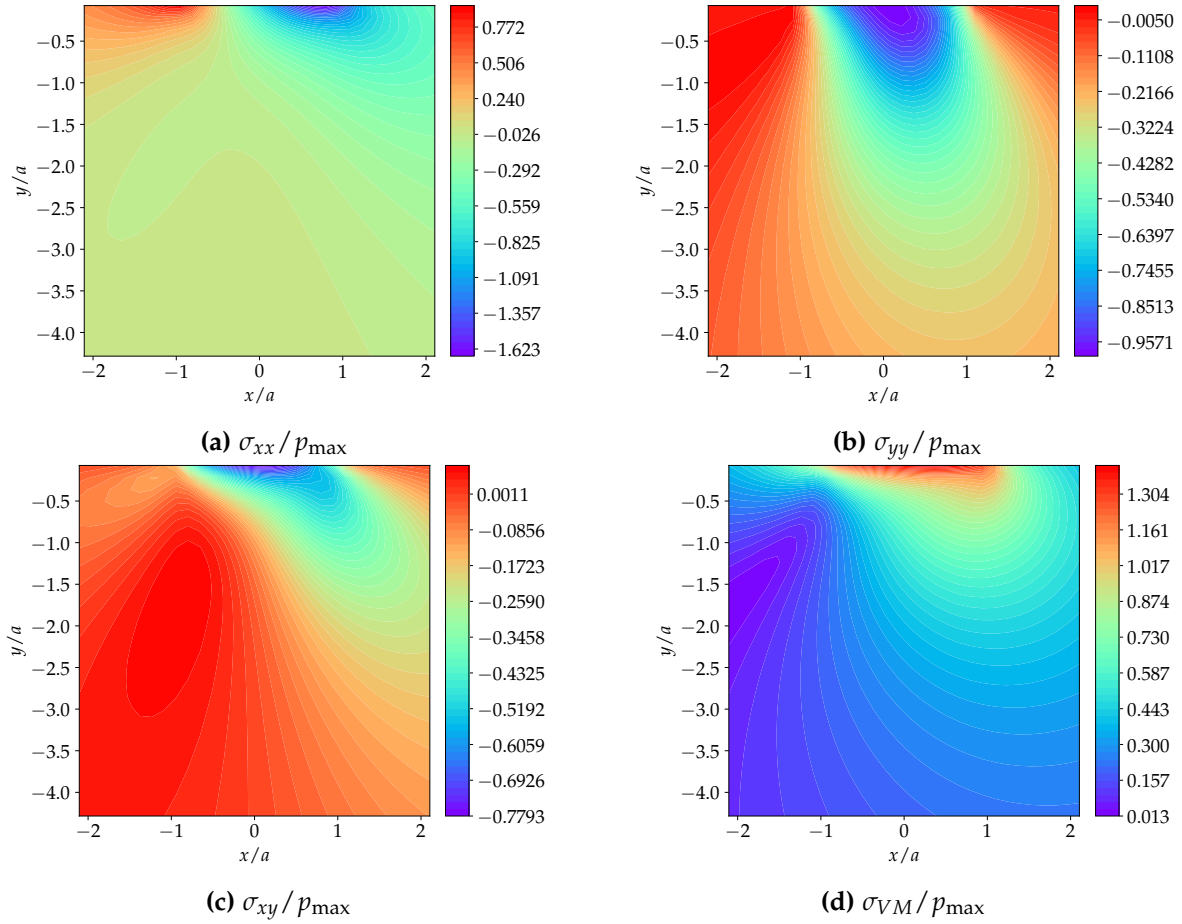

(a) $\sigma_{xx}/p_{\max}$ **(b)** $\sigma_{yy}/p_{\max}$

(c) $\sigma_{xy}/p_{\max}$ **(d)** $\sigma_{VM}/p_{\max}$

Figure 1.10: Stress fields computed analytically for a semi-infinite elastic body subjected on its upper surface to a Hertzian contact with frictional sliding following Coulomb's law with a coefficient of friction $\mu = 0.9$. (a) xx stress, (b) yy stress, (c) xy stress, (d) von Mises equivalent stress. The dimensions are nondimensionalized by the contact half-width a.

that follows Coulomb's law, plastic yield onset is altered depending on the value of the coefficient of friction μ. Indeed, the presence of additional shear stress makes plastic yield occur for lower normal pressures: $p_{\max}$ value at first yield is a decreasing function of μ. Moreover, the location of plastic yield onset remains unchanged for $\mu < 0.3$ (onset at depth $0.7a$), but plastic yield onsets on the contact surface for coefficients of friction $\mu > 0.3$.

When subjected to a reciprocating motion as in the case of fretting, elastoplastic bodies may display different response types depending on the cyclic hardening behavior of the material (Figure 1.11):

- The first regime corresponds to the situation in which the initial yield limit is never reached. In that case, the solid remains elastic.
- The **elastic shakedown** regime corresponds to a situation in which plastic yield initially occurs, but eventually ceases. After a certain time, the solid behaves elastically and no further plastic yield occurs.
- The **plastic shakedown** regime refers to a situation in which plastic yield occurs cycle after cycle, but the plastic strain remains bounded. A periodic stabilized state is asymptotically reached where plastic strain evolves within each cycle but at the end of the cycle, the plastic

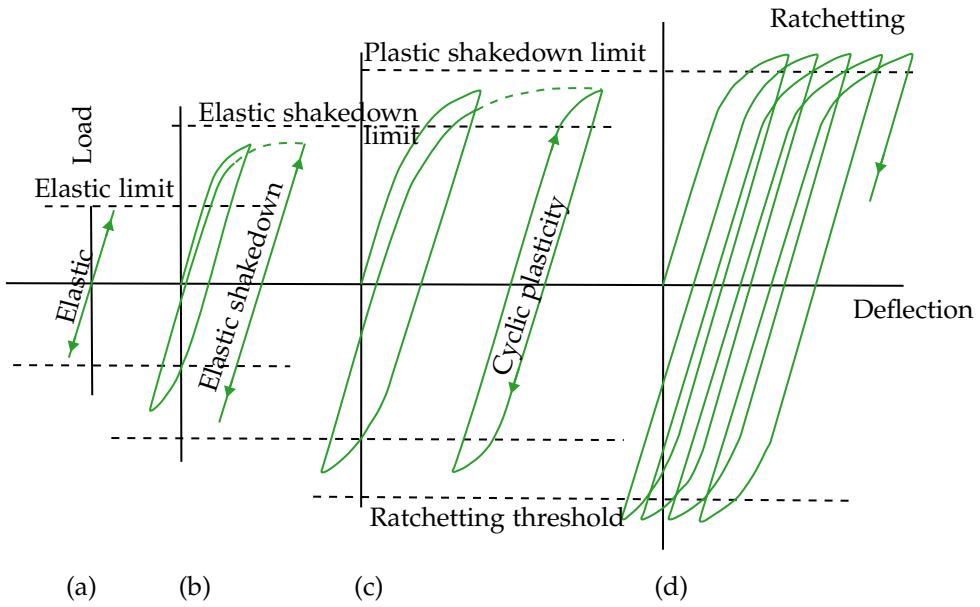

Figure 1.11: Shakedown regimes: (a) elastic, (b) elastic shakedown, (c) plastic shakedown, (d) ratchetting [Johnson 1985].

strain of the start of the cycle is retrieved.

- Finally, the **ratchetting** regime corresponds to the situation of unbounded plastic strain evolution. Plastic strain grows cycle after cycle.

Johnson proposes shakedown maps showing the shakedown limits in terms of normal pressure and coefficient of friction (Figure 1.12) [Johnson 1985]. The normal maximal pressure p_{max} is nondimensionalized into a loading parameter p_{max}/k where k is the shear elastic limit. The limits between the different shakedown regimes are decreasing functions of the coefficient of friction, in other words friction tends to promote plasticity due to the additional shear stress it implies.

1.4 Fretting wear mechanisms of ductile materials

The particular situation of ductile metals wearing under fretting conditions has been widely investigated. Because of the low displacement amplitudes, fretting motion generates specific mechanisms for particles detachment, with strong third body interactions. High plastic strains are often observed in the near surface material layer, and oxidation seems to play a major role as well. Furthermore, the reciprocating nature of the motion has an impact as well because of the Bauschinger effect. The alternated displacement may indeed affect the density of dislocations in the vicinity of the surface and thus impact the wear behavior [Tang et al. 2023].

In this section, the specific debris formation processes encountered under fretting conditions are first reviewed. Then, the effect of third body interactions is dealt with. Finally, an insight into corrosion effects in fretting is given.

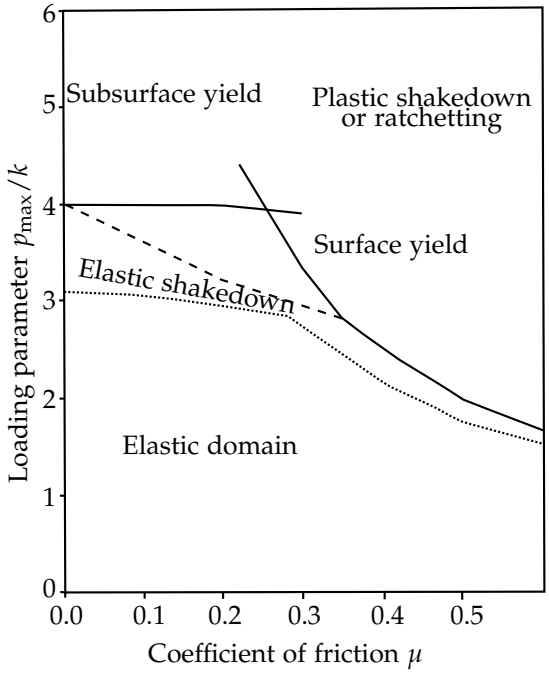

Figure 1.12: Example of shakedown map in the case of a line contact [Johnson 1985].

1.4.1 Underlying mechanisms of wear debris formation in fretting

Hurricks describes the mechanism of wear debris formation for ductile steels under fretting as follows [Hurricks 1972]: first, a material layer in surface undergoes severe plastic strains and hardens. Then, a material detachment process occurs in the hardened layer. This process is the result of crack propagations initiated by adhesion phenomena.

Predominance of adhesion and fatigue

The predominance of adhesion and fatigue over abrasion for debris formation in fretting is supported by other authors [Stowers and Rabinowicz 1973]. In general, metallic bodies are initially covered by a very thin passive oxide film [Waterhouse 1977]. This film is worn as a first step during fretting, leading to contacts between the uncovered metals which generates adhesion. These adhesion phenomena subsequently lead to mechanisms like fatigue or delamination [Suh 1973, 1977]. For instance, Waterhouse and Taylor observe delamination on fretting tests on different ductile materials [Waterhouse and Taylor 1974]. The same kind of observations was also related by Ko et al. (1997) and Kapoor and Franklin (2000). As in the delamination theory of wear, plastic strain is often described as a major feature of fretting [Waterhouse 2000, Ko et al. 1997].

The sequence of events leading to surface degradation and wear in fretting which was described by Colombié also involves strong adhesion-induced plastic deformation [Colombié 1986]. After the initial oxide layer is removed, the adhesion caused by metallic contacts generates high plastic strains which is enhanced by the presence of third body particles. The plastic strain is generally higher near the edges of the wear scar which may create beadings there. This effect is known as *plowing* and is characterized by the presence of edge bumps generated by plastic material displacement as depicted in Figure 1.13a [Elleuch and Fouvry 2002, Fouvry et al. 2004, Marc et al. 2016]. It is accompanied by an increase of the tangential force along the displacement which is visible on the

fretting loop (Figure 1.13b).

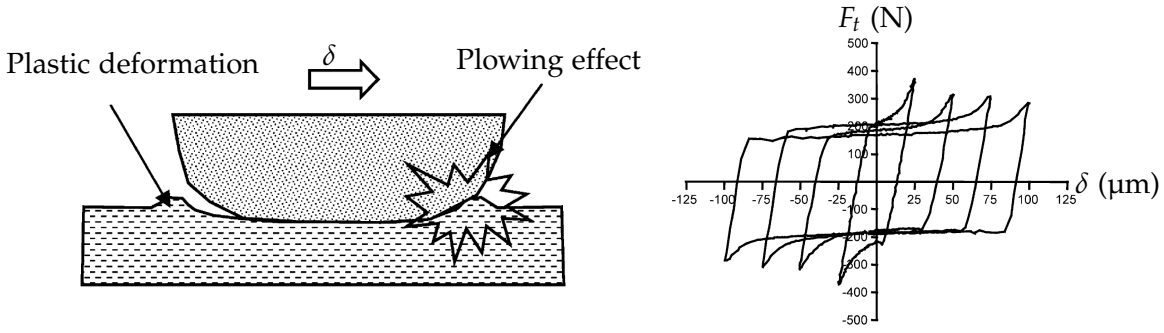

(a) Wear scar with plastic bumps on the edges

(b) Fretting loop

Figure 1.13: Illustration of the plowing effect [Fouvry et al. 2004].

Correlation between wear rate and accumulation of near-surface plastic strains

Fouvry et al. established a correlation between the occurrence of surface plastic strain and the severity of wear [Fouvry et al. 2001]. They made different gross slip fretting tests on sintered steel alloys, in which variations in the sintering process leads to various coefficients of friction μ. According to Johnson (1985), for line contacts, $\mu < 0.3$ leads to in-depth plastic strain onset while $\mu > 0.3$ leads to surface plastic strain onset. Based on their experimental results, Fouvry et al. observe a correlation between wear kinetics and shakedown behavior. Figure 1.14 shows the wear coefficient[2] obtained from their different test results plotted on Johnson's shakedown map[3]. Two wear regimes are identified by an important shift in the wear coefficient and are referred to as mild or severe wear. Severe wear is correlated to plastic strain accumulation near the surface (corresponding to a plastic shakedown or ratchetting regime), while mild wear corresponds to an asymptotic return to an elastic regime. This suggests that plastic strain accumulation in the vicinity of the surface is of utmost importance regarding fretting wear kinetics.

The idea of quantifying wear by the accumulation of plastic strain was developed by Kapoor and Johnson, who described a wear mechanism resulting from ratchetting in the asperities [Kapoor and Johnson 1994, Kapoor et al. 1996, Kapoor 1997]. The process is the consequence of very high local stresses and considers wear damage as a phenomenon localized in the asperities. It seems however that this model applies mainly to low friction situations. Fouvry shows on additional experimental tests that with high friction coefficients, using Johnson's shakedown map allows to predict the mild-to-severe wear transition better than Kapoor's model [Fouvry 2001]. While low friction fretting wear is likely related to a very local high amount of cumulated plastic strain in the asperities, high friction fretting wear seems to be linked to an accumulation of more macroscopic plastic strain in a surface material layer. For example, Kapoor and Franklin observe for high friction fretting wear of ductile metals a mechanism close to delamination [Kapoor and Franklin 2000]. They describe the presence of a surface layer, commonly known as a *tribologically transformed structure* (TTS), with altered mechanical properties compared with sound material. The thickness of the TTS layer is one or two orders of magnitude greater than the asperities typical height.

[2]The wear coefficient is defined here as the Archard's wear law coefficient, which measures the worn volume per unit sliding distance and per unit normal force. See Section 1.5.1.

[3]See Section 1.3.3.

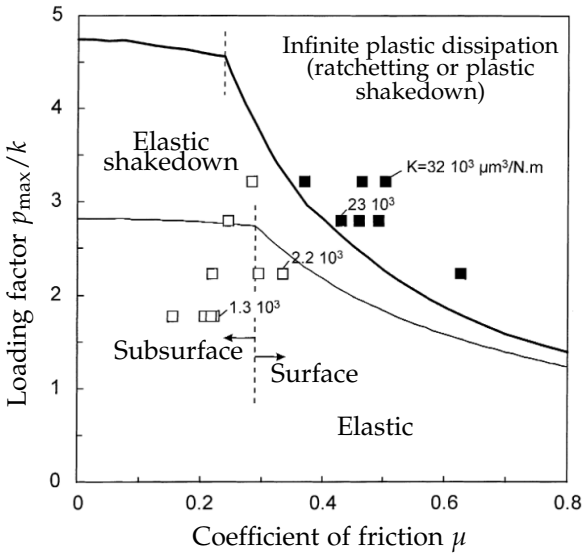

Figure 1.14: Different fretting wear tests with the associated wear coefficients represented in a shakedown map for line contact [Fouvry et al. 2001].

Formation of a tribologically transformed structure

The formation of a TTS layer caused by fretting loading has been thoroughly described. It is characterized by a higher hardness and it is made of much finer grains than the bulk material [Zhou et al. 1997]. The chemical composition of the TTS layer is not altered, but it can have endured crystallographic phase transformations, as mentioned for example by van Herpen et al. who observed a partial austenite to martensite transition [van Herpen et al. 2001]. The formation mechanisms described for the TTS layer mainly originate from strong plastic strains [Rigney et al. 1984]. Blanchard describes the TTS formation mechanism as a recrystallization mechanism induced by the large plastic strains [Blanchard et al. 1991]. This description considers that there exists a critical plastic strain level above which recrystallization is enabled and thus TTS is formed, yielding a distinct transition between the TTS zone and the untransformed material. This approach was transcribed into an energy approach by Sauger et al. (2000). They consider that TTS is formed when the cumulated friction energy reaches a threshold which is related to the aforementioned plastic strain threshold. The following sequence is proposed for formation and subsequent destruction of the TTS: first, plastic strains accumulate in a surface layer. Then, as the cumulated plastic strain (or cumulated friction energy) reaches a certain threshold, there is a rapid formation of TTS. Then, due to further supply of external work, the TTS layer is progressively deteriorated which eventually leads to the formation of wear debris with flake-like shapes. A steady-state regime is reached in which the TTS layer thickness is constant, meaning that the formation rate equals the destruction rate. In this situation, friction energy is dissipated on the one hand by TTS formation, on the other hand by TTS destruction. This sequence is depicted in Figure 1.15 as the evolution of TTS formation and wear debris production rates as functions of the cumulated friction energy.

When the TTS layer is fully formed, the typical stack of layers in surface is as follows (see Figure 1.16) [Zhou et al. 1997, Sauger et al. 2000, Kirk et al. 2019]: in surface lies a very thin oxide debris bed. Right below the TTS layer usually has a thickness of a few tens of micrometers. This layer is very distinctly delimited from an underneath zone that has endured plastic deformation – not sufficiently however to create TTS. The presence of a TTS layer was largely documented by other

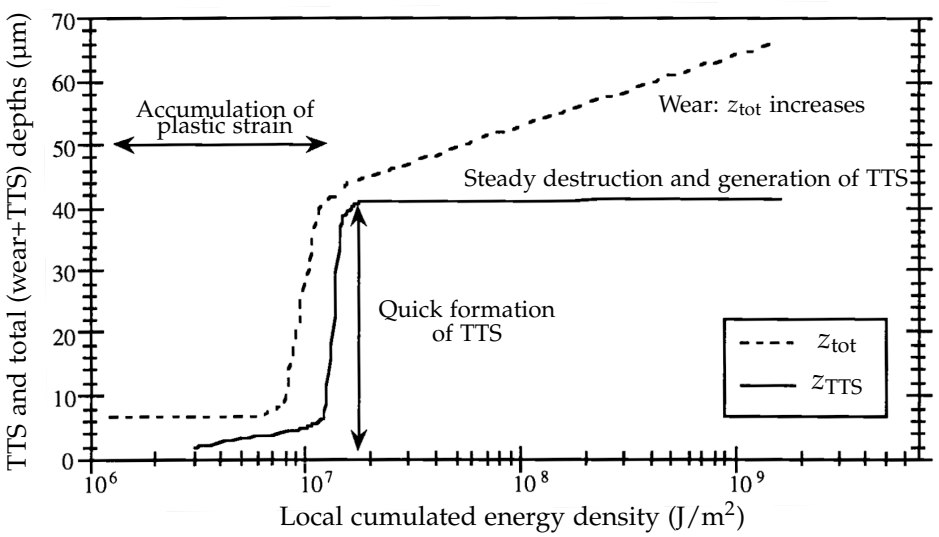

Figure 1.15: Evolution of the TTS layer depth z_{TTS} and total (wear + TTS) depth z_{tot} as functions of the cumulated dissipated energy density [Sauger 1997].

authors for metals under fretting motion [Ko et al. 1997, Kapoor and Franklin 2000, Waterhouse 2000, Fouvry 2001, Marc 2018, Liu et al. 2019]. This suggests that this tribologically transformed structure and its characteristics are key features of fretting wear phenomena.

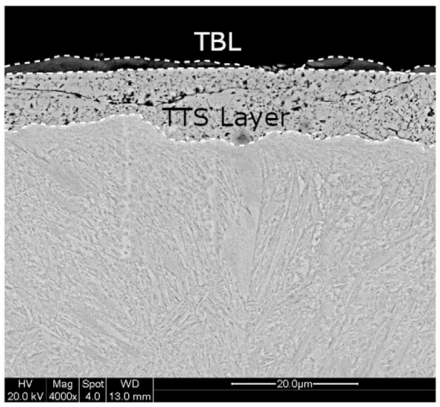

(a) Visualization of the TTS [Kirk et al. 2019]

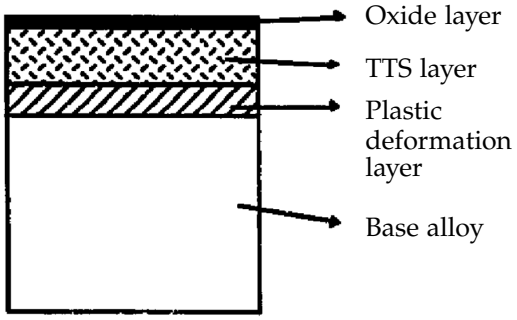

(b) Schematic representation of the TTS [Zhou et al. 1997]

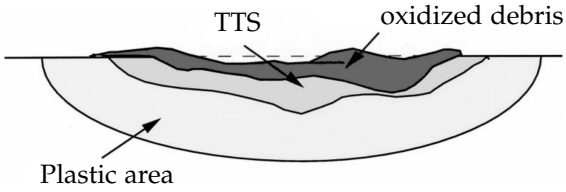

(c) Schematic representation of the TTS [Sauger et al. 2000]

Figure 1.16: Representations of the tribologically transformed structure.

The formation of a TTS layer can be seen as a prerequisite for wear to occur. When a surface is subjected to a fretting loading, TTS is created as an initial step before wear may onset. This can be an explanation for the incubation period sometimes observed in fretting tests. For example, Zhu

et al. realize cylinder-plane fretting tests on high strength steels and note that a certain number of fretting cycles need to be performed before visible wear is observed [Zhu et al. 2023].

1.4.2 Debris ejection and influence of third body

Because fretting motion implies that a part of the contact interface is never exposed, wear debris are likely to remain trapped and a third body layer often develops between the contacting surfaces. The presence of third body has a great impact on the wear process, mainly because it alters the contact pressure distribution [Colombié et al. 1984]. It also has an influence on the shear stresses induced by relative tangential displacement. The presence of an interfacial layer, made of fluid or solid particles, may indeed accommodate the difference of velocity between the primary bodies [Godet 1984, Berthier et al. 1988]. In that case, the third body layer displays a velocity gradient and may behave in an analogous manner to a viscous fluid [Dragon-Louiset 2001].

Factors influencing debris ejection

As mentioned in Section 1.2.3, when considering the presence of a third body the wear rate is no longer defined simply as the debris formation rate but as the debris ejection rate. When debris ejection is easily achieved, the wear rate is governed by the rate at which debris are created. On the opposite, if ejection is more arduous, it may not be possible to expel the debris as fast as they are generated. Based on these considerations, Zhu et al. indicate that wear kinetics depends on the contact width, because when the contact width increases the debris remain trapped within the interface to a greater extent [Zhu et al. 2019]. Their experimental results support this assessment. They realize fretting tests on cylinder-plane steel alloys contacts with different cylinder radii and observe a decreasing wear rate with increasing contact width. The fact that a larger contact surface makes debris ejection slower is well known. In fretting, the contact width increases with time because of the evolution of wear. Consequently, debris ejection may be readily achieved initially, then become more and more difficult as wear proceeds [Shipway et al. 2021].

It has been shown that the displacement amplitude also has an impact on debris ejection. It was observed that a higher displacement amplitude facilitates the ejection, whereas a lower amplitude tends to favor debris retention within the interface [Ding et al. 2007]. Elleuch and Fouvry explain that friction work is used partly to create wear debris and partly to expel them out of the interface [Elleuch and Fouvry 2005]. The bigger the displacement amplitude, the lower the share of friction work used for debris ejection. Increasing the displacement amplitude may then lead to increase the amount of wear per unit friction energy because of the facilitated debris ejection.

The environment plays a role as well in debris ejection. For instance, debris ejection can be easier for fretting operating in an aqueous environment with a fluid flow than in dry air conditions [Marc 2018].

Influence of the third body on wear profiles

The presence of third body debris in the interface has a great influence on fretting damage. It favors the transition from partial slip to gross slip, which activates wear rather than fatigue cracks nucleation and propagation [Zhou and Vincent 1995], and affects the surface stresses [Colombié et al. 1984]. Colombié et al. describe the debris trapped in the interface in fretting and assess their load carrying capacities. Their presence modifies the contact pressure distribution.

When displacement amplitudes are small, a certain amount of debris can more easily remain trapped inside the interface and end up getting compacted under the effect of compressive stress. In this case, after the experiment a compacted bed of debris that adheres to one of the solids may be observed [Ding et al. 2007].

Based on numerical simulations compared with experimental results, Arnaud and Fouvry assess the impact of the presence of a third body layer on wear profiles [Arnaud and Fouvry 2018]. Their model enables the capture of the load-carrying effect of third body which results in a modified contact pressure distribution. Based on their results, they highlight a dependence of the wear profile on the geometry of the third body bed, rather than its mechanical or rheological properties.

Fouvry considers the presence of trapped third body for small displacement amplitudes to be a possible explanation for the formation of *W-shaped* wear profiles [Fouvry 1997]. This typical wear scar morphology is sometimes observed for low amplitude fretting conditions, and it is suggested that it may be the consequence of an imperfect spreading of the debris. For small displacement amplitudes, the debris are not evenly spread in the contact and gather on the edges. This results in a higher contact pressure and higher shear stresses in these surrounding zones, leading to a deeper wear depth on the edges than in the middle of the scar.

W-shaped profiles are observed as well by Marc et al. on fretting tests with stainless steels [Marc et al. 2016]. They also observe a W-shape to V-shape transition when the displacement amplitude increases, and also relate it to the presence of third body. Based on the analysis of oxygen concentration in the wear scar, they infer the presence of a compacted debris cluster at the center of the scar. They conclude that the W-shaped profiles originate from oxidized wear debris stacking in the middle of the scar due to the compressive stress they have undergone. Lower displacement amplitude fretting experiments display W-shaped profiles while for higher displacement amplitudes the fretting tests yield V-shaped profiles, as depicted in Figure 1.17.

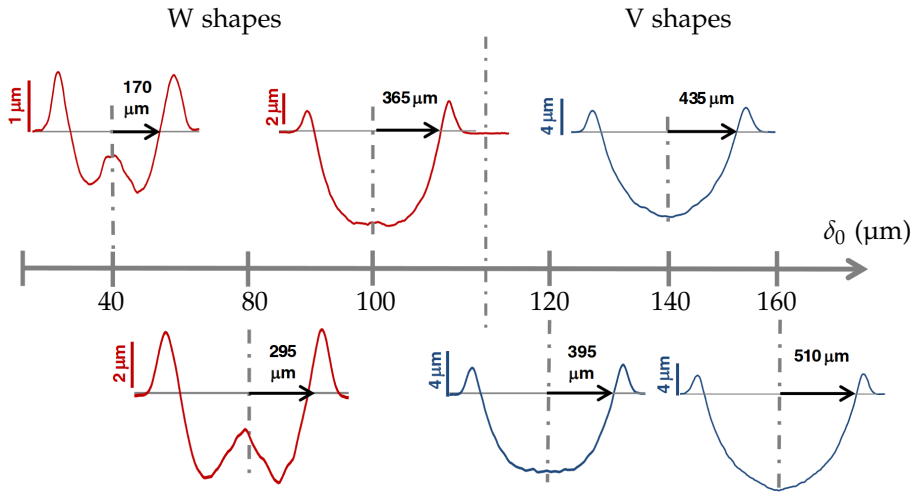

Figure 1.17: Occurrence of W-shaped or V-shaped wear profiles depending on the displacement amplitude [Marc et al. 2016].

The V-to-W wear scar transition is observed by Zhu et al. for an increasing displacement amplitude as well [Zhu et al. 2023]. They also observe this transition when varying the test duration, which they relate to the progressive widening of the wear scar as wear evolves leading to a more difficult debris ejection. They conclude that W-shaped profiles are the result of a higher amount of third body trapped in the interface.

1.4.3 Interaction with corrosion effects

Alternative explanations are also provided regarding the occurrence of W-shaped profiles. Several studies relate this particular shape to the effect of oxidation phenomena. Fouvry suggests that for W-shaped profiles, the local wear depth is correlated to the duration of the surface exposition to the environment, which favors oxidation [Fouvry 1997]. This was later confirmed by Fouvry et al. (2017).

The contact oxygenation concept was formulated by Fouvry et al. and states that the evolution of the local wear depth observed on W shapes is due to a change in the particles detachment mechanism [Fouvry et al. 2017]. They consider that the inner zones in the contact are less subject to corrosion compared to the outer zones, due to the lower concentration in dioxygen. Indeed, dioxygen coming from the environment needs to be transported from the outside to the inside of the contact interface, and the more we get close to the contact center the more the dioxygen concentration decreases. This results in a more facilitated oxidation of the metal surfaces near the contact edges with respect to the contact center. Consequently, the outer zones of the contact are more prone to corrosive and abrasive wear, whereas the inner zones typically suffer from adhesive wear.

The fact that oxidation is more or less facilitated by the access to the environment, which subsequently activates different wear mechanisms, is proposed in several studies as the explanation for the evolution of wear rate. For example, it is suggested that the contact pressure has an influence on the wear kinetics in part because it impacts dioxygen transport through the contact interface [Baydoun 2020]: with high contact pressures, oxygen transport is restrained and adhesive wear prevails, whereas abrasive wear is more predominant in low-pressure contacts. The dependence of wear kinetics to the contact area may be explained in a similar manner [Baydoun et al. 2022]. By the same mechanisms, displacement frequency [Warmuth et al. 2015, Kirk et al. 2019] and displacement amplitude [Marc 2018] reportedly have an influence on the wear kinetics due to the ease with which oxygen reaches the contact surfaces.

It has also been related that tribocorrosion effects may enhance wear because the presence of a surface passive film is likely to increase the subsurface density of dislocations. Before any tribological loading, metallic materials are covered with a thin naturally oxidized layer which is removed as frictional sliding initiates – this is called depassivation. In presence of a corrosive environment, the uncovered metal is subsequently repassivated. The uninterrupted presence of a passive film on the surface prevents the dislocations created by the shear stress to be eliminated when they reach the surface. This results in a higher dislocation density which promotes wear. In addition, the boundary between the passive film and the metal can be a source of dislocation itself [Mischler and Munoz 2018].

1.5 Empirical and phenomenological wear models

The previous sections have highlighted the great diversity of mechanisms and processes underlying fretting wear. Numerous works have attempted to propose models aiming at predicting the occurrence and the kinetics of wear based on the experimental or operational conditions. The number of parameters influencing wear is nevertheless very important. Material parameters, surface characteristics, environmental factors and loading conditions all have an impact [Braunovic 2009]. In their famous work on wear models in 1995, Meng and Ludema outlined the substantial number

of existing models, none of which could be considered general enough so as to provide reasonable predictive capabilities [Meng and Ludema 1995].

Some wear laws have however become the standard in quantitative wear studies. Most of these are empirical laws, namely Archard's law or energy-based models. In this section the focus is on experimental models, whereas Chapter 2 deals with alternative approaches in wear modeling.

1.5.1 Archard's wear law

The most commonly used equation to quantify wear degradation is referred to as Archard's law, or Holm-Archard's law. It was developed in the middle of the 20th century and relates the worn volume – that is the volume of material removed from the surface of a solid – to the normal contacting force and the sliding distance.

This relation was first proposed by Holm, who envisioned wear as an atom removal phenomenon [Holm 1946]. Later, Burwell and Strang, then Archard, took over Holm's theory suggesting this time that wear operates at the asperities level [Burwell and Strang 1952, Archard 1953]. This led to the formulation of the well-known equation:

$$V = \frac{K}{H} F_n \, \delta \tag{1.13}$$

where V is the wear volume, K is Archard's wear coefficient, H is the hardness of the solid, F_n is the normal force and δ the sliding distance. In Archard's view, the non-dimensional coefficient K represents the probability that an asperity encounter gives rise to a detachment and the creation of a wear particle. The model was first proposed for adhesive wear, then Rabinowicz et al. showed that is was also valid for abrasion [Rabinowicz et al. 1961]. The observation of adhesive mechanisms in fretting wear situations led to the conclusion that Archard's law may be used to quantify fretting wear [Stowers and Rabinowicz 1973].

The equation is often written under an equivalent local form which states that at any point on the surface, the wear depth h is related to the normal contact pressure p:

$$h = \frac{K}{H} \, p \, \delta. \tag{1.14}$$

The determination of the parameter K derives purely from experimental tests. This parameter is not intrinsic to the couple of materials. Its value may vary a lot under different lubrication conditions, normal forces or displacement amplitudes for example. Therefore, it is not possible to tabulate a value for any couple of contacting materials, and K must be determined for every operating condition via experimental tests.

1.5.2 Energy-based laws

On fretting tests conducted on TiN coatings, Mohrbacher et al. established a correlation between the wear volume and the cumulated dissipated energy throughout the test as shown in Figure 1.18 [Mohrbacher et al. 1995]. The linear relation between the wear volume and the dissipated energy was confirmed by further experimental work by Fouvry et al. (1996), Fouvry (1997), then Huq and Celis (2002). This led to propose a wear equation relating the wear volume to the dissipated energy [Fouvry et al. 2001]:

$$V = \alpha E_d \tag{1.15}$$

where α is an energy wear coefficient and E_d is the cumulated dissipated energy. The coefficient α is a measure of the volume of material worn away per unit energy dissipated due to frictional sliding.

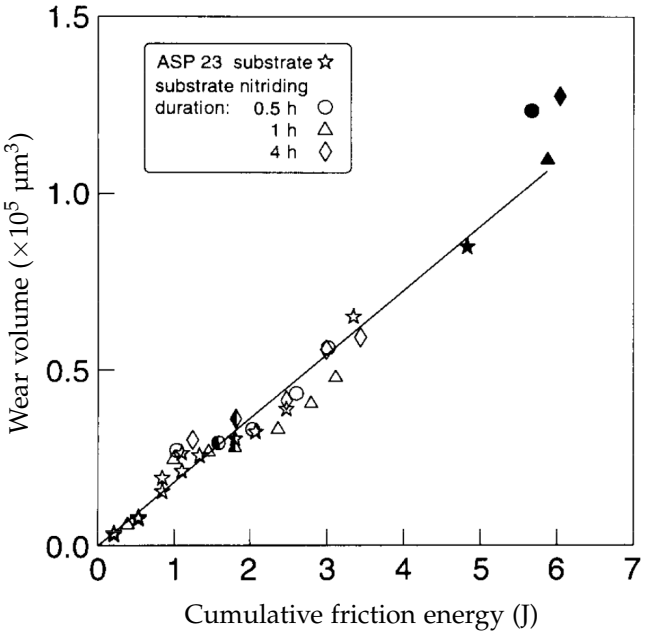

Figure 1.18: Wear volume as a function of the cumulated friction energy [Mohrbacher et al. 1995].

According to Fouvry et al., the wear kinetics of metals is related to the plastic dissipation near the contact surface [Fouvry et al. 2001]. As the knowledge of the plastic dissipation is hardly accessible, they consider that the total dissipated energy can be used as a good proxy of the energy dissipated by plasticity. These considerations are supported by experimental evidences suggesting that this energy approach is more reliable than Archard's model. The energy-based model may actually be seen as an evolution of Archard's law which allows to capture the influence of the coefficient of friction better. The energy description of wear is thus more accurate especially in situations where the coefficient of friction is not constant. Otherwise, when a simple relation exists between the normal force and the tangential friction force, Archard's law and the energy-based law are analogous.

Just as for Archard's law, a local version of the energy model may be derived to express the wear depth h anywhere on the surface [Fouvry et al. 2003]:

$$h = \alpha e_d \tag{1.16}$$

where e_d is the local surface density of energy dissipated by friction.

An evolution of this model allows to account for the TTS formation [Fouvry et al. 2001]. Based on the TTS description given by Sauger et al. (2000)[4], they considered that before the initiation of wear, there is an incubation phase during which, as sliding occurs, all the dissipated energy

[4]See Section 1.4.1.

is related to the TTS formation and no material is being worn. They assume that there exists a threshold dissipated energy E_{th} that needs to be reached before wear starts. The wear law is modified accordingly:

$$V = \begin{cases} 0 & \text{if } E_d < E_{\text{th}} \\ \alpha(E_d - E_{\text{th}}) & \text{if } E_d \geq E_{\text{th}} \end{cases}. \tag{1.17}$$

This modified model taking the TTS formation into account was used for example by Marc (2018) for the determination of the energy wear coefficient α from experimental data.

1.5.3 The limits to these models

Despite the great use of these models due to their simplicity, several studies highlight a number of situations in which they prove to be limited. Although a linear dependency between the wear volume and the dissipated energy is indeed witnessed in numerous experimental works, it has also been reported that the wear kinetics depends on other factors whose effects cannot be captured by either Archard's model or the energy-based model.

First, the wear coefficient may significantly vary by more than one order of magnitude if some test condition is slightly altered. For example, Fouvry relates a great shift in the Archard's coefficient between two fretting tests on a steel-steel cylinder-plane contact with different normal loads [Fouvry 2001]. Denoting $\overline{K} = K/H$, applying Archard's law with the experimental data obtained gives $\overline{K} = 100$ µm^3/J at normal load $F_n = 200$ N and $\overline{K} = 3500$ µm^3/J at $F_n = 1000$ N. Such a transition from mild to severe wear suggests that the underlying wear mechanism has changed, which falls out of reach of Archard's law. A more suitable model in this situation should integrate a deeper insight into the phenomena at stake, perhaps considering the shakedown response of the system as investigated by the author [Fouvry 2001]. Other predominant features such as temperature effects, corrosion or third body interactions should not be neglected either.

As a matter of fact, different studies highlight a dependency of the wear rate to additional parameters which is often understood as a consequence of corrosion or third body effects. In particular, the sliding amplitude in fretting is sometimes found to play a role on wear kinetics. It is observed for example by Fouvry et al. (2004) and Paulin et al. (2005) as depicted in Figure 1.19. They propose to integrate the displacement amplitude into the energy model in order to take that effect into account. Elleuch and Fouvry analyze it in the light of the tribological circuit approach[5] and understand the influence of the displacement amplitude as being a consequence of an easier debris ejection for higher amplitudes [Elleuch and Fouvry 2005]. They suggest that at lower displacement amplitudes, the debris ejection out of the interface is more difficult and requires more energy, which leads to less energy being available to generate debris. On the opposite, increasing the amplitude facilitates debris ejection and increases the wear rate because the proportion of energy dedicated to particle formation is higher.

Marc notices an effect of the displacement amplitude on wear kinetics as well for fretting tests on a stainless steels cylinder-plane contact in an aqueous environment [Marc 2018]. This time however, it is interpreted as a tribocorrosion effect. While acknowledging the results of Elleuch and Fouvry (2005), it is argued that here, debris ejection is facilitated by the presence of an aqueous environment whatever the displacement amplitude. Thus, the correlation of wear rate and displacement amplitude is more likely related to the more prolonged access to the interface the en-

[5] See Section 1.2.3.

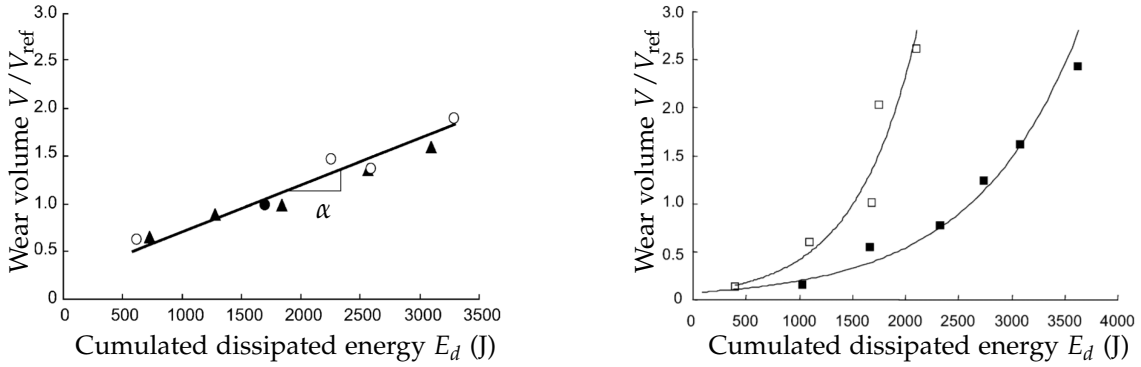

(a) Constant displacement amplitude ($\delta = 75$ µm), variable normal force and number of cycles

(b) Variable displacement amplitude ($\delta \in [25, 100]$ µm), constant normal load and number of cycles

Figure 1.19: Wear volume as a function of the cumulated dissipated energy with (a) the same displacement amplitude for all tests and (b) different displacement amplitudes [Fouvry et al. 2004].

vironment has when the displacement amplitude is higher. Corrosion is then facilitated for higher displacement amplitudes and the wear rate is enhanced. This hypothesis is supported by the fact that an increasing displacement frequency is found to decrease the wear rate, which may be explained in the same way by the time of exposure of the surfaces to the environment, influencing the oxidation. A similar explanation was given by van Peteghem et al. (2011) and Warmuth et al. (2015) who assumed that a higher frequency results in less time for the oxygen transport into the contact interface which lowers the corrosion.

The easiness for the oxygen to be transported within the contact was also brought by Baydoun et al. as an explanation for the variation of wear rate with the contact pressure, the frequency of motion, the displacement amplitude, or the contact width [Baydoun et al. 2019]. In further experimental work, they manage to separately identify the respective contribution of the third body and the oxygenation on the wear rate by considering the effect of the contact dimensions [Baydoun et al. 2022]. This leads to the formulation of an adapted weighted energy-based wear model of the type:

$$V = \alpha \left(\frac{p}{p_{\text{ref}}}\right)^{n_1} \left(\frac{\delta_0}{\delta_{0,\text{ref}}}\right)^{n_2} \left(\frac{f}{f_{\text{ref}}}\right)^{n_3} \left(\frac{L}{L_{\text{ref}}}\right)^{n_4} E_d \tag{1.18}$$

where p is the normal pressure, δ_0 is the displacement amplitude, f is the frequency, L is the contact width and the subscript "ref" indicates an arbitrary reference value[6]. The exponents n_i ($i \in \{1, 2, 3, 4\}$) are determined based on the experimental results. They obtain a good correlation with the experimental results using this equation.

The fact that in several situations the wear model, be it Archard's or an energy-based model, needs to be adapted with convenient additional parameters encourages the search for improvements that could provide a finer apprehension of the processes at stake.

[6]It is clear that the arbitrary choice of a reference value for the different parameters here influences the value determined for the wear coefficient α.

1.5.4 Recent advances

The concept of *rate-determining process* was proposed by Zhu et al. to illustrate the fact that for sufficiently small contact sizes the wear rate is controlled by the debris formation rate, but becomes governed by the debris ejection rate above a critical contact size [Zhu et al. 2019]. Indeed, above this critical value the contact width is so large that debris ejection becomes a bottleneck of the wear process. They rely on experimental tests on a cylinder-plane contact and show that the wear rate is dependent on the contact size which is imputed to debris ejection being the rate-determining process. Assuming that the wear rate is inversely proportional to the wear scar width, they derive from a geometrical basis a relation between the wear volume and the dissipated energy. This relation, which is valid only for a cylinder-plane contact geometry, successfully correlates their experimental data including the contact size dependency.

In a more general case, for non-conforming contact geometries, the contact size increases as wear occurs. Therefore, the wear rate may remain constant to begin with when the contact size is small enough for particles formation to be the rate-determining process, in which case Archard-like wear models may apply. Thereafter, as wear proceeds the wear rate decreases after the contact size has outreached the critical size for debris ejection to become the rate-determining process [Zhu and Shipway 2021]. In that case, Archard-type models are no longer appropriate. Zhu and Shipway propose a modified equation to account for the situation in which the wear rate is governed by debris ejection:

$$V = \alpha \, E_d^n \tag{1.19}$$

where the exponent $n \in [0.67, 0.8]$ depends on the contact geometry.

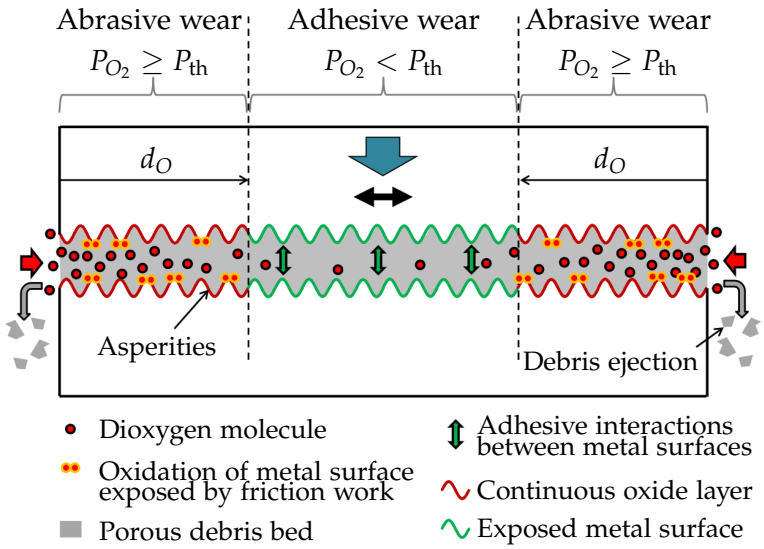

Figure 1.20: Illustration of the advection-dispersion-reaction model [Baydoun et al. 2020].

Another significant contribution was brought by Baydoun et al., this time regarding oxidation [Baydoun et al. 2020]. They use the contact oxygenation concept [Fouvry et al. 2017] which states that because the central area of the contact in fretting has a poor access to the environment, it is less prone to oxidation. Consequently, metal-to-metal contacts are favored in the central area which promotes adhesive wear, unlike the outer zone of the contact in which abrasive wear prevails due to the easier oxidation of the surfaces. On this basis, Baydoun et al. develop an advection-dispersion-

reaction model which aims at representing the transport of dioxygen through the contact interface and its oxidation reaction with iron atoms from the surfaces. Oxygen transport is assumed to operate by diffusion and advection, respectively obeying Fick's and Darcy's laws. The effect of the chemical reaction between iron and dioxygen is represented by considering a sink of dioxygen molecules. A sink term is added to the equation assuming that the vanishing rate is proportional to the concentration of dioxygen. Figure 1.20 illustrates this model. This leads to the derivation of a conservation equation for the partial pressure of dioxygen within the contact interface, which is solved using a finite difference scheme. The solution gives the partial pressure of dioxygen everywhere in the contact which is compared to a threshold value to determine if wear is locally driven by abrasive or adhesive mechanisms. Comparing with experimental results, it is concluded that this model enables the prediction of the transition between the outer abrasive area and the inner adhesive area. The advection-dispersion-reaction model was moreover implemented by Arnaud et al. in finite element simulations of fretting wear [Arnaud et al. 2021]. Using the delimitation between abrasive and adhesive zones, wear simulations are performed considering different wear coefficients related to the different wear mechanisms[7]. This allows to retrieve W-shaped wear profiles as shown in Figure 1.21.

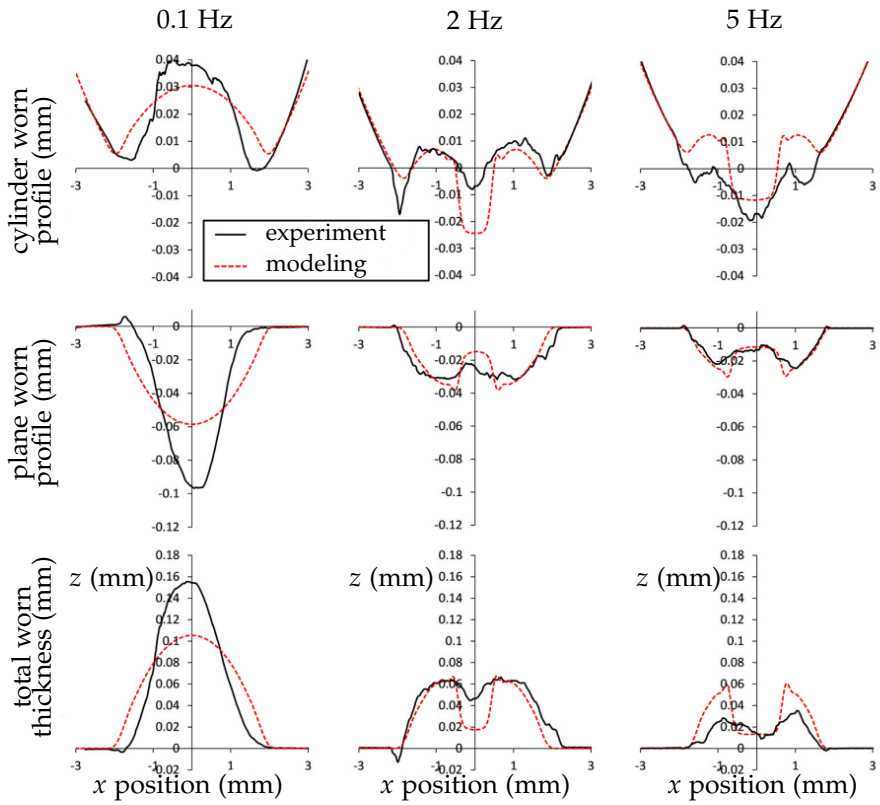

Figure 1.21: Comparison between experimental and simulation results on fretting wear tests at different displacement frequencies displaying V-shaped or W-shaped wear profiles [Arnaud et al. 2021].

Following the work by Baydoun et al., the oxygen transport is integrated by Shipway et al. as a possible rate-determining process [Shipway et al. 2021]. It results in the identification of three possible regimes, as depicted in Figure 1.22:

[7]These simulations also include the evolution of a third body layer and are described in more detail in Chapter 3.

1. For small contact sizes, the wear rate is determined by the particle formation rate. In this case, Archard-like wear laws may apply.
2. When the contact width increases, the rate-determining process becomes debris ejection. The wear rate is inversely proportional to the contact width.
3. For the highest contact sizes, the rate-determining process is oxygen transport. The wear rate is inversely proportional to the square of the contact width.

The observed wear rate is governed by a competition between these three processes.

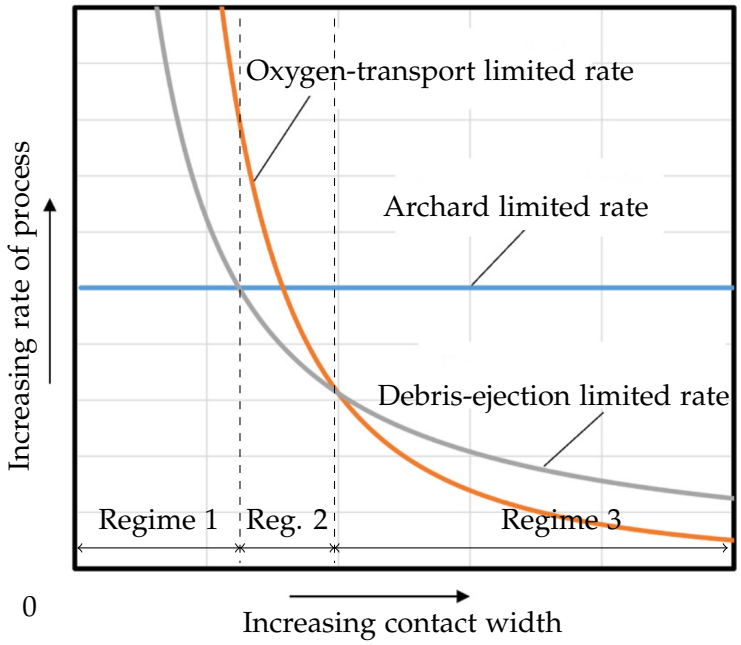

Figure 1.22: Illustration of the evolution of the rates of the three rate-determining processes with the contact width [Shipway et al. 2021].

1.6 Conclusion

The literature review proposed on fretting wear phenomena leads to realize the complexity of the problem. On the one hand, a great diversity of underlying mechanisms is described and makes the problem highly multi-disciplinary. On the other hand, it has a strong multi-scale nature in both time and space. Indeed, the long-term, macroscopic manifestation of material removal is the consequence of an accumulation of repeated microscopic short interactions.

In brief, there seems to be very few principles that can be taken as undeniable truth when dealing with wear. Behind the macroscopic occurrence of surface matter loss lies in fact a diversity of very different microscopic phenomena. Depending on the experimental or operating conditions, different dominant mechanisms can be observed, leading to strong variations of the wear kinetics. The main conclusion drawn from this analysis is that wear cannot be seen as a pure material-dependent response. It must be understood as a system response to a certain loading in which the geometries, the materials, the surface topography, the lubrication and the environment all come into play.

These considerations show the difficulty encountered in wear modeling. The most widespread models are empirical and despite their great use due to their simplicity and their capacity to accurately correlate the experimental results in many cases, they seem limited by their inability to represent the underlying mechanisms governing wear. They suffer in some cases from poor predictability capacities and require to be adjusted by adding various parameters to capture the experimental observations. Alternative models, more of a phenomenological kind, present a great interest for future research because they directly integrate a description of the physical and chemical phenomena that underlie the surface degradation mechanisms.

Overall, this chapter helped understand the major mechanisms at work during fretting wear of metals. The interactions between different processes, such as asperity encounters, the development of high plastic strains, the interactions and ejection of third body or the transport of oxygen leading to chemical reactions have been thoroughly described. The next chapter is devoted to modeling aspects and endeavors to represent the degradation process eventually causing wear particles detachment. Because this work lies mostly in the framework of continuum mechanics, the modeling approach proposed focuses mainly on the material detachment process considering the history of the mechanical state endured by the material. Accordingly, corrosion effects and third body interactions are left aside, despite their actual role in the process.

Chapter recap

In this chapter, some concepts that are central to the rest of the dissertation are defined.

- Wear is defined as the progressive removal of material from a solid surface following tribological loading. It may occur through different surface particles detachment mechanisms, such as abrasion, adhesion, fatigue or delamination.
- Fretting is a type of loading likely to generate wear. It refers to a cyclic sliding motion of small displacement amplitude between two contacting solids.

In addition, the most common features encountered in fretting wear of metals are described.

- Metallic materials are initially covered by a thin oxide film which is removed as fretting occurs. This film may be continuously recreated during the loading due to corrosion; or the metal surface may remain uncovered. In the first case, abrasive wear mechanisms prevail, while metal-to-metal contacts generally lead to adhesion and fatigue phenomena. This latter situation often goes with the development of high plastic strains, delamination phenomena may be observed and a tribologically transformed structure (TTS) layer is created.
- The oxidation of the surface depends on parameters such as the environment, the displacement frequency and amplitude, or the normal load.
- Fretting wear is strongly affected by the presence of third body within the interface. The third body bed alters the contact pressure distribution due to its load-carrying capacities and accommodates the tangential relative velocity.

Finally, several of the most widely used empirical wear models are presented.

- The models used to quantify wear are mostly empirical.
- Archard's wear law is the most widely known equation to quantify wear volume:

$$V = \frac{K}{H} F_n \, s.$$

- Energy-based models enable to better account for the coefficient of friction:

$$V = \alpha \, E_d.$$

- Evolutions of this model integrate an energy required to form TTS, or the dependence on a combination of operating condition parameters. Moreover, adjustments are suggested to capture the effect of the rate-determining process, be it particle detachment, debris ejection or oxidation.
- Alternative models are developed to better account for oxidation.

As a conclusion, the great diversity of processes at stake in wear phenomena is noted. Beside the multi-scale nature of wear, this reveals the challenges faced in modeling.

Chapter 2

Thermodynamical approach of wear modeling

A thermodynamic analysis of a fretting wear problem leading to the formulation of an original model

2.1 Introduction

The modeling of material degradation processes in solid mechanics is usually conducted using continuum thermodynamics principles. This way of doing is justified considering the irreversible nature of these processes. Regarding wear, we have noted that most models were empirical, the main reasons for that being the complexity of the underlying mechanisms involving different space and time scales and various scientific disciplines. Several studies have nevertheless proposed attempts to tackle wear issues from a thermodynamic basis. They endeavored to define thermodynamically consistent theoretical frameworks to develop wear models and relate wear evolution to an energy dissipation. Bridges however still lack between these theoretical works and the empirical knowledge of wear phenomena and the parameters underlying them.

Using a thermodynamical framework in the analysis of a wear problem aims at describing transformations that are physically feasible. One of the main difficulty encountered is that thermodynamic principles are generally expressed for closed systems, whereas wear systems lose mass and are therefore open. A pioneering work was first proposed by Klamecki (1980). They consider that wear evolution being irreversible, it must necessarily be accompanied by a generation of entropy. In other words, wear is a process that transforms a solid body from a more structured state towards a less structured state. They derive a strain energy release rate associated with wear, namely the amount of strain energy which is dissipated as a wear particle is formed. They state that in order to get a loose wear particle, the strain energy contained in the particle must overcome the surface potential of the newly-created surface. Expressions for the entropy generated by different wear-causing mechanisms (overcoming adhesion, ductile fracture of a particle, crack nucleation and propagation, chemical reaction) were proposed by Banjac et al. (2014). In these two contributions, care is taken to tackle the issue that wear systems are open and lose mass. Another significant work was accomplished by Zmitrowicz, who proposed a friction and wear model using thermodynamics equations [Zmitrowicz 1987a,b,c]. Balance equations are thoroughly and carefully derived using a comprehensive set of variables including mechanical, chemical and thermal effects. Thereafter, Strömberg et al. developed a model for contact, friction and wear in the framework of *generalized standard materials*[1] [Strömberg et al. 1996]. They give an expression for a surface free energy and dissipation potential using normal gap, tangential relative displacement and wear depth as surface state variables. They retrieve Coulomb's friction law and Archard's wear law by differentiation of the dissipation potential. A similar approach is conducted by D'Annibale and Luongo (2013). In their work, the friction law integrates a hardening effect: the sliding tangential force evolves with the sliding distance. Wear is governed by a damage-like model: it decreases the stiffness associated with the relation between the surface tangential force and elastic displacement. Finally, a detailed thermodynamic analysis of a wear system is conducted by Dragon-Louiset and Stolz [Dragon-Louiset and Stolz 1999, Dragon-Louiset 2000, Stolz 2010]. They consider a three-body, wear-prone system in which moving boundaries delimitate the primary bodies from the interfacial third body. The analysis relies on previous work by Pradeilles-Duval and Stolz (1995) on problems involving moving boundaries. The moving boundaries are treated as discontinuity surfaces between a sound body with unaltered mechanical characteristics and a third body endowed with its own specific

[1] Generalized standard materials is a class of material models used to represent inelastic transformations. It was introduced by Halphen and Nguyen for elastoviscoplastic materials and relies on the assumption of existence of a convex dissipation potential such that the normal dissipativity hypothesis is verified with every dissipative variable [Halphen and Nguyen 1975].

behavior. The propagation of the boundary represents the evolution of wear: as the surface progresses, mass is transferred from the primary body to the third body. Balance equations and laws of thermodynamics are expressed for this system and the expression of the entropy generation brings out a thermodynamic generalized force associated with wear. This force is related to the discontinuity of free energy across the surface and can be seen as an energy release rate, which may be used to propose a Griffith-like wear evolution law. In addition, the dissipative behavior of third body is modeled.

These studies are theoretical works which are meant to ensure that the models proposed are thermodynamically consistent. They can however be accommodated with different forms of criteria to ultimately quantify wear evolution. The choice of a specific criterion should rely on the experimental knowledge of wear phenomena. It is thus necessary to identify which quantities of interest are the most suitable to capture wear evolution. Beside the most common laws presented in Chapter 1, some alternatives can be found in the literature. First, in line with the thermodynamic approaches mentioned, some studies exhibit an experimental correlation between the wear rate and the entropy generated by the transformations of the system. Doelling et al. measure the entropy flow on unidirectional sliding tests on a copper-steel contact using a calorimeter and thermocouples [Doelling et al. 2000]. A linear relation is observed between the entropy released by the system – inferred from the measured heat flow and temperature – and the wear volume. This relation may be conciliated with energy-based wear models by relating the entropy flow to the power dissipated by friction. This idea was brought further by Bryant et al. (2008) and Lijesh et al. (2018). The correlation is well verified when wear is the only dissipative process at work. In that case all the entropy generated is indeed related to irreversible wear degradation. However, the system may undergo additional dissipative mechanisms which are unrelated to wear. In such cases, only a share of the entropy generation is associated with wear. Consequently, the quantification of wear requires to accurately know which proportion of the entropy generation is related to the other dissipative mechanisms.

Following a different approach, several studies propose to consider a wear law related to plastic strain. This is consistent with the observations presented in Section 1.4.1 that wear of ductile materials is often correlated to a high amount of plastic strain in a subsurface layer and the development of TTS. Stalin-Muller and Dang Van use finite element simulations to compute plastic deformation and correlate their results with the surface degradation observed on experimental data [Stalin Muller and Dang Van 1997]. They carry out unidirectional sliding experiments and observe an accumulation of plastic deformation near the surface. They propose a wear model that relates the number of cycles before the surface material is worn to the plastic strain increment per cycle. The form of the proposed law is similar to a fatigue law. A similar law is given by Boher et al. (2009). Nélias et al. realize finite element simulations to compute plastic deformation as well, in which they assume that the material located in surface gets worn out as soon as the equivalent plastic strain outreaches a threshold [Nélias et al. 2006]. The surface geometry is updated accordingly.

The work reported in the present chapter aims at providing a methodology for wear modeling in a thermodynamical framework. The idea is to attempt to give a wear evolution law which is related to the actual mechanical processes at work in the material. In other words, it relies on the assumption that the knowledge of the mechanical state history in a near-surface material layer is a key information to capture wear evolution.

The purpose is more to define a class of models that we think may reliably represent the main features governing fretting wear, than presenting a fully validated and identified model. It should

be understood as a suggestion for a rather general methodology that can be adapted according to actual empirical observations, but which is thought to integrate general features encountered in the mechanical degradation witnessed under fretting wear. The purpose is also to propose a model that is quite simple to deal with and to implement in numerical simulations.

As focus is on the mechanical degradation ultimately leading to particle detachment, corrosion and third body effects are set aside. It is assumed that wear debris are easily expelled out of the interface, meaning that contact occurs between the two wear surfaces. Taking the third body into account would lead to an altered contact pressure distribution and would require to assess the velocity accommodation capacities and the dissipative behavior of the third body layer[2]. Moreover, no chemical effect is considered here. A finer description of the problem including oxidation would model the oxygen transport[3] and the energy transformations associated with the chemical reactions occurring at the surface.

In Section 2.2, a thermodynamic analysis of a wear system is conducted. It is inspired by the work of Dragon-Louiset and Stolz but is adapted to suit our working hypotheses [Dragon-Louiset and Stolz 1999, Dragon-Louiset 2000, Stolz 2010]. The energy dissipation related to wear evolution is derived, involving a thermodynamic generalized force associated with wear. In Section 2.3, a damage-based wear evolution model is proposed. A damage variable is introduced which serves as a measure of the accumulated material degradation eventually leading to debris formation. The approach presented in this section is rather general and can be adapted with different local damage laws. Finally, an example of application using a specific local damage law is presented in Section 2.4. The damage law is chosen so as to represent a cyclic damage apt to occur in fretting.

2.2 Thermodynamic analysis of a wear problem

2.2.1 Description of the studied system

Let us consider a system Ω composed of two sound, wear-prone bodies Ω_1 and Ω_2 separated by a domain Ω_3 that contains third body trapped in the contact interface. Because it is more convenient to work on a closed system, we consider a domain Ω_{out} that contains the matter ejected out of the interface. Thus, $\Omega = \Omega_1 \cup \Omega_2 \cup \Omega_3 \cup \Omega_{\text{out}}$ is a system with no mass transfer with its outer environment. The mass exchanges within Ω between the different subsystems characterize the tribological circuit [Godet 1984]: there is a positive mass flux from the primary bodies Ω_i ($i \in \{1,2\}$) to the third body Ω_3, which represents the wear particles formation rate, and a positive mass flux from the third body Ω_3 to the outer environment Ω_{out} which represents the particles ejection rate. Let us denote $\Gamma_{i,3}$ ($i \in \{1,2\}$) the surfaces between Ω_i and Ω_3. Across these surfaces, $\underline{j_{\text{m},i}}$ is the *mass flux* per unit surface. As wear occurs, there is a positive mass transfer from Ω_i to Ω_3 so, with $\underline{n_i}$ the surface unit normal vector directed towards the inside of Ω_i,

$$j_{\text{m},i} = -\underline{j_{\text{m},i}} \cdot \underline{n_i} \geq 0. \tag{2.1}$$

Let us also define J_{eject} the total mass flow from the third body to the exterior. It is a positive quantity as well. The tribological system is represented in Figure 2.1.

[2] Such modeling approach is specifically tackled by Dragon-Louiset (2000).
[3] See for example the work of Baydoun (2020).

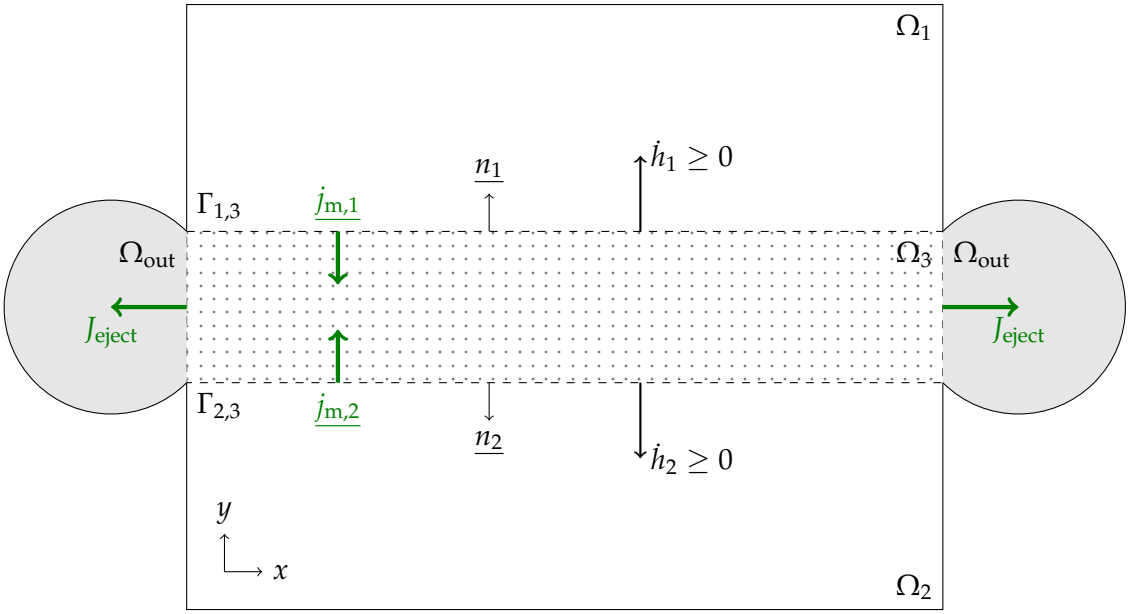

Figure 2.1: Schematic representation of the tribological system studied.

In this problem, the surfaces $\Gamma_{i,3}$ ($i \in \{1,2\}$) are considered as discontinuity boundaries propagating through the bodies with a velocity $\dot{h}_i$. This type of problem was studied by Pradeilles-Duval and Stolz (1995). The boundaries separate the domain Ω_i from the domain Ω_3, each possibly having different material properties. These discontinuity surfaces define the *wear front* whose displacement represents the evolution of wear. The *wear depth* at some point of the surface $\Gamma_{i,3}$ is then its total propagation distance h_i. We recall the formula for the time derivative of the integral over the domain $\Omega_i \cup \Omega_3$ of an arbitrary volume quantity b with a discontinuity boundary $\Gamma_{i,3}$ moving at velocity $\dot{h}_i$ [Maitournam 2017]:

$$\frac{d}{dt}\int_{\Omega_i \cup \Omega_3} b \, d\Omega = \int_{\Omega_i \cup \Omega_3} (\dot{b} + b\mathrm{div}(\underline{U})) \, d\Omega - \int_{\Gamma_{i,3}} [\![b\underline{\dot{h}_i} \cdot \underline{n_i}]\!]_i \, dS \tag{2.2}$$

where $\underline{U}$ is the local material velocity, div is the divergence operator and $[\![b]\!]_i$ is the discontinuity of b across $\Gamma_{i,3}$:

$$\forall x \in \Gamma_{i,3}, \; [\![b(x)]\!]_i = \lim_{x_i \to x} b(x_i) - \lim_{x_3 \to x} b(x_3) \tag{2.3}$$

where x_i is in Ω_i and x_3 is in Ω_3.

2.2.2 Mass conservation

As Ω is a closed system, the mass conservation equation gives, with ρ the density:

$$\frac{d}{dt}\int_{\Omega} \rho \, d\Omega = 0 \tag{2.4}$$

which yields, in every subsystem according to Equation 2.2:

$$\dot{\rho} + \rho \mathrm{div}(\underline{U}) = 0 \text{ in } \Omega_i \ (i \in \{1,2,3\}), \tag{2.5}$$

$$[\![\rho \underline{\dot{h}_i} \cdot \underline{n_i}]\!]_i = 0 \text{ on } \Gamma_{i,3} \ (i \in \{1,2\}). \tag{2.6}$$

Equation 2.6 indicates that the mass flux is conserved across the discontinuity, where the mass flux is expressed:

$$j_{\mathrm{m},i} = \rho \underline{\dot{h}_i} \cdot \underline{n_i} = \rho \dot{h}_i. \tag{2.7}$$

In other words, mass does not disappear while crossing the boundary: all the mass leaving a body enters the adjacent one. Then, for any quantity per unit mass b' (a specific energy for example), the time derivative of its integral over Ω reads:

$$\frac{d}{dt}\int_\Omega \rho b' \, d\Omega = \int_\Omega \rho \dot{b}' \, d\Omega - \sum_{i=1}^{2} \int_{\Gamma_{i,3}} j_{\mathrm{m},i} [\![b']\!]_i \, dS + J_{\mathrm{eject}} [\![b']\!]_{\mathrm{out}}. \tag{2.8}$$

The term related to the ejection flow J_{eject} is intentionally not detailed. As mentioned in the introduction, it is decided not to model the third body behavior. Consequently, we assume that the material detached from the bodies Ω_1 and Ω_2 is instantaneously ejected. As a result, contact is assumed to take place between the wear surfaces $\Gamma_{1,3}$ and $\Gamma_{2,3}$. Because the processes of interest here are related to the propagation of the surfaces $\Gamma_{1,3}$ and $\Gamma_{2,3}$, we simplify the Equation 2.8 into:

$$\frac{d}{dt}\int_\Omega \rho b' \, d\Omega = \int_\Omega \rho \dot{b}' \, d\Omega - \sum_{i=1}^{2} \int_{\Gamma_{i,3}} j_{\mathrm{m},i} [\![b']\!]_i \, dS \tag{2.9}$$

by neglecting the energy transformations occurring within the third body and during its ejection. The simplified system is represented in Figure 2.2, in which Ω_3 is assumed to be very thin. We use this simplified representation to express the laws of thermodynamics on the system Ω, taking the motion of the surfaces of discontinuity into account.

2.2.3 First and second laws of thermodynamics

The first law of thermodynamics states that the evolution of the total energy of a closed system is the result of work and heat exchanges with the surrounding environment. The total energy of the system is the sum of the internal energy $\mathcal{E}$ and the kinetic energy $\mathcal{K}$. The power of external forces on the system is denoted $\mathcal{P}_{\mathrm{ext}}$ and the heat quantity provided to the system is denoted $\mathcal{Q}$, so the first law of thermodynamics reads:

$$\dot{\mathcal{E}} + \dot{\mathcal{K}} = \mathcal{P}_{\mathrm{ext}} + \dot{\mathcal{Q}}. \tag{2.10}$$

In the present problem, the evolution is assumed to be quasistatic, so the time derivative of the kinetic energy is zero:

$$\dot{\mathcal{K}} = 0. \tag{2.11}$$

The rate of internal energy can be expressed by introducing the specific internal energy e and

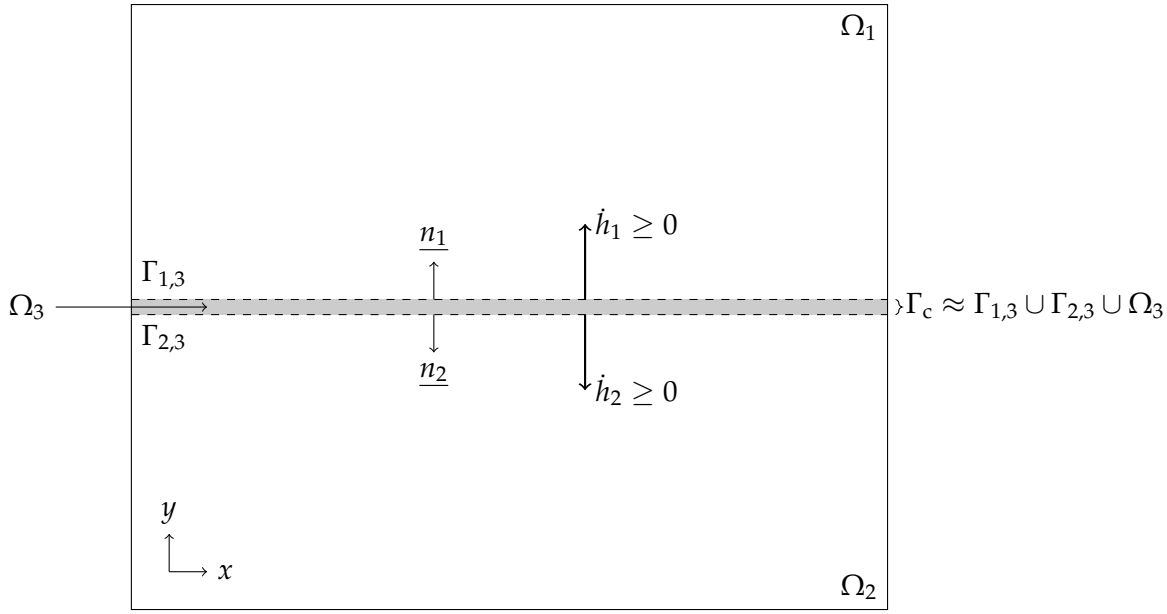

Figure 2.2: Schematic representation of the simplified system of wear-prone contacting solids.

by using Equation 2.9:

$$\dot{\mathcal{E}} = \frac{d}{dt}\int_\Omega \rho e \, d\Omega = \int_\Omega \rho \dot{e} \, d\Omega - \sum_{i=1}^{2} \int_{\Gamma_{i,3}} j_{\mathrm{m},i} [\![e]\!]_i \, dS \tag{2.12}$$

According to the work-energy theorem, the sum of the power of external and internal forces is equal to the rate of kinetic energy which is zero here:

$$\mathcal{P}_{\mathrm{ext}} + \mathcal{P}_{\mathrm{int}} = 0. \tag{2.13}$$

The power of internal forces in Ω is the power of deformation forces and the power of frictional contact forces[4]:

$$\mathcal{P}_{\mathrm{int}} = -\int_\Omega \underline{\underline{\sigma}} : \underline{\underline{\dot{\varepsilon}}} \, d\Omega - \int_{\Gamma_{1,3}} -\underline{T_1} \cdot [\![\underline{\dot{u}}]\!]_1 \, dS - \int_{\Gamma_{2,3}} -\underline{T_2} \cdot [\![\underline{\dot{u}}]\!]_2 \, dS \tag{2.14}$$

where $\underline{\underline{\sigma}}$ and $\underline{\underline{\varepsilon}}$ are the stress tensor and linearized strain tensor, $\underline{T_i} = -\underline{\underline{\sigma}} \cdot \underline{n_i}$ the stress vector defined on the surface $\Gamma_{i,3}$, and $\underline{\dot{u}}$ the velocity. Because Ω_3 is very thin, we make the hypothesis that the velocity is constant over its thickness and equal to the mean between velocities on the surfaces $\Gamma_{1,3}$ and $\Gamma_{2,3}$:

$$\forall x \in \Omega_3, \ \underline{\dot{u}}(x) = \frac{1}{2}\left(\underline{\dot{u}}(x_1) + \underline{\dot{u}}(x_2)\right) \tag{2.15}$$

$\underline{\dot{u}}(x_i)$ being the velocity on the surface $\Gamma_{i,3} \cap \Omega_i$ ($i \in \{1,2\}$). Moreover, stress is assumed to be constant across Ω_3 as well, such that

$$\underline{T_2} = -\underline{T_1}. \tag{2.16}$$

As a result, the contact interface $\Gamma_{1,3} \cup \Gamma_{2,3} \cup \Omega_3$ is considered as a contact surface Γ_c, and the power

[4]Considering additional effects such as chemical reactions would require to include extra terms in this expression.

of internal forces becomes:

$$\mathcal{P}_{\text{int}} = -\int_\Omega \underline{\underline{\sigma}} : \underline{\underline{\dot{\varepsilon}}}\, d\Omega - \int_{\Gamma_c} \underline{T_1} \cdot [\![\underline{\dot{u}}]\!]_2 - \underline{T_1} \cdot [\![\underline{\dot{u}}]\!]_1\, dS \tag{2.17}$$

$$= -\int_\Omega \underline{\underline{\sigma}} : \underline{\underline{\dot{\varepsilon}}}\, d\Omega - \int_{\Gamma_c} \underline{T} \cdot [\![\underline{\dot{u}}]\!]_c\, dS \tag{2.18}$$

where we denoted $\underline{T} = \underline{T_1}$ and $[\![\underline{u}]\!]_c = \underline{u}(x_2) - \underline{u}(x_1)$ the discontinuity of displacement between the two wear surfaces (x_1 is on $\Gamma_{1,3}$ and x_2 is on $\Gamma_{2,3}$). Assuming that the system exchanges a surface heat flux $\underline{q}$ on its exterior boundary $\partial\Omega$ and is provided a volume heat supply r, the total heat supply rate reads:

$$\dot{\mathcal{Q}} = \int_\Omega r\, d\Omega - \int_{\partial\Omega} \underline{q} \cdot \underline{n}\, dS. \tag{2.19}$$

Thus, by detailing Equation 2.10 and using Ostrogradsky's divergence theorem with Equation 2.19, the first principle of thermodynamics yields:

$$\rho \dot{e} = \underline{\underline{\sigma}} : \underline{\underline{\dot{\varepsilon}}} + r - \operatorname{div}(\underline{q}) \text{ in } \Omega_i \ (i \in \{1,2,3\}) \tag{2.20}$$

$$-j_{\text{m},1}[\![e]\!]_1 - j_{\text{m},2}[\![e]\!]_2 = \underline{T} \cdot [\![\underline{\dot{u}}]\!]_c - [\![\underline{q} \cdot \underline{n_1}]\!]_1 - [\![\underline{q} \cdot \underline{n_2}]\!]_2 \text{ on } \Gamma_c. \tag{2.21}$$

The second law of thermodynamics states that the entropy generation is always positive – or zero in case of a reversible transformation. Let us denote $\mathcal{S}$ the total entropy of the system. The entropy supplied to the system is the heat supplied divided by the temperature θ, so the variation of entropy in Ω must verify:

$$\dot{\mathcal{S}} \geq \int_\Omega \frac{r}{\theta}\, d\Omega - \int_{\partial\Omega} \frac{\underline{q} \cdot \underline{n}}{\theta}\, dS. \tag{2.22}$$

By introducing the specific entropy s and following the same steps as for the first principle, we get the Clausius-Duhem inequality both in the solids and on the surface:

$$\rho\theta\dot{s} \geq r - \operatorname{div}(\underline{q}) + \frac{\underline{q} \cdot \underline{\nabla\theta}}{\theta} \text{ in } \Omega_i \ (i \in \{1,2,3\}) \tag{2.23}$$

$$-j_{\text{m},1}\theta[\![s]\!]_1 - j_{\text{m},2}\theta[\![s]\!]_2 \geq -[\![\underline{q} \cdot \underline{n_1}]\!]_1 - [\![\underline{q} \cdot \underline{n_2}]\!]_2 \text{ on } \Gamma_c. \tag{2.24}$$

2.2.4 Energy dissipation

The second law of thermodynamics implies that the dissipation power $\mathcal{D}$ is always non-negative:

$$\mathcal{D} \geq 0. \tag{2.25}$$

Let us introduce the Helmholtz free energy ψ as:

$$\psi = e - \theta s. \tag{2.26}$$

Because the transformation is supposed isothermal, the time derivative of the free energy is simply

$$\dot{\psi} = \dot{e} - \theta\dot{s}. \tag{2.27}$$

By combining the expressions of the first and second laws of thermodynamics, the dissipation can be written as the sum of a volume dissipation d in the bulks and a surface dissipations D on the contact surface:

$$\mathcal{D} = \int_\Omega \mathrm{d}\, d\Omega + \int_{\Gamma_c} D\, dS \geq 0 \tag{2.28}$$

where all terms are independently positive, and can be expressed with the free energy:

$$\mathrm{d} = \underline{\underline{\sigma}} : \dot{\underline{\underline{\varepsilon}}} - \rho\dot{\psi} - \frac{\underline{q}\cdot\underline{\nabla\theta}}{\theta} \geq 0 \tag{2.29}$$

$$D = \underline{T}\cdot[\![\underline{\dot{u}}]\!]_\mathrm{c} + j_{\mathrm{m},1}[\![\psi]\!]_1 + j_{\mathrm{m},2}[\![\psi]\!]_2 \geq 0. \tag{2.30}$$

The volume term is often decomposed into an intrinsic dissipation d_1 resulting from the irreversible mechanisms taking place inside the bodies, and a thermal dissipation d_2 resulting from heat diffusion, both assumed to be independently positive:

$$\mathrm{d}_1 = \underline{\underline{\sigma}} : \dot{\underline{\underline{\varepsilon}}} - \rho\dot{\psi} \geq 0 \tag{2.31}$$

$$\mathrm{d}_2 = -\frac{\underline{q}\cdot\underline{\nabla\theta}}{\theta} \geq 0. \tag{2.32}$$

Equation 2.30 can be written as a function of the wear rate, as the mass flux across the surface $\Gamma_{i,3}$ directly depends on the motion of the wear front: $j_{\mathrm{m},i} = \rho\dot{h}_i$, thus

$$D = \underline{T}\cdot[\![\underline{\dot{u}}]\!]_\mathrm{c} + \rho[\![\psi]\!]_1\dot{h}_1 + \rho[\![\psi]\!]_2\dot{h}_2 \geq 0. \tag{2.33}$$

The expression of the surface dissipation indicates that two different dissipative mechanisms exist on the surface, namely friction and wear fronts propagation. When the wear depth h_i increases, the wear front $\Gamma_{i,3}$ moves and a certain amount of material is detached. During the process, it dissipates a part of its free energy which is represented by the discontinuity term $[\![\psi]\!]_i = \psi(x_i) - \psi(x_3)$. Let us denote $\mathcal{G}_i$ the *energy release rate* related to the wear front propagation – in other words, $\mathcal{G}_i$ is the surface density of energy that is dissipated per unit incremental wear depth. It is expressed

$$\mathcal{G}_i = \rho[\![\psi]\!]_i \tag{2.34}$$

and the dissipation D_i related to wear front $\Gamma_{i,3}$ propagation reads

$$D_i = \mathcal{G}_i\dot{h}_i \tag{2.35}$$

where $\mathcal{G}_i$ appears as the *thermodynamic generalized force* associated with the wear depth h_i. This expression of the surface dissipation is consistent with the derivation carried out by Dragon-Louiset and Stolz[5] [Dragon-Louiset and Stolz 1999, Dragon-Louiset 2000, Stolz 2010].

The surface dissipation sheds light on the difference between the Archard-type wear equations

[5]The expression they obtain for the energy release rate is similar albeit slightly different. In their model, they indeed include the description of interfacial third body which was neglected here. As a result, they assume the continuity of displacement across wear surfaces between the primary bodies and third body. Using Hadamard's relation, they express the friction term as a function of the boundary velocity, yielding an energy release rate encompassing both the discontinuity of free energy and a friction component between the primary body and the third body [Dragon-Louiset 2000].

and the approach followed here. According to Archard's model or, equivalently, the friction-energy-based wear models, the wear dissipation is part of the friction dissipation and the wear mechanisms are assumed to be included within the description of friction. As a result, the wear rate is governed by the friction energy. On the opposite, the evolution of wear is assumed here to dissipate energy aside from friction. This is in line with the objective of this study, which is to attempt to give a description of wear based not only on the friction term but on the history of the mechanical state of the solid near its surface.

From this point forward, evolution laws are required to quantify the motion of the wear fronts. These complementary laws must relate the wear evolution rate to the thermodynamic force, and may be based upon a Griffith-like criterion as suggested by Dragon-Louiset for instance [Dragon-Louiset 2000]:

$$\dot{h}_i \geq 0 \; ; \; \mathcal{G}_i - \mathcal{G}_c \leq 0 \; ; \; \dot{h}_i \left(\mathcal{G}_i - \mathcal{G}_c \right) = 0 \tag{2.36}$$

where we introduced a critical wear energy $\mathcal{G}_c$. This criterion, expressed under the form of a Karush-Kuhn-Tucker condition, implies that the wear front moves at velocity $\dot{h}_i > 0$ only if the driving force $\mathcal{G}_i$ has reached the threshold value $\mathcal{G}_c$.

In the next section, another approach is explored in which we consider wear to be the consequence of a progressive accumulation of degradation in a near-surface material layer. In this description, the thermodynamic driving force is no longer restricted to a surface term but is expressed on this material layer instead. It can however be shown that the approach proposed hereafter is consistent with the analysis carried out in the present section.

2.3 Derivation of a damage-based wear model

The analysis conducted in Section 2.2 considers wear particle detachment to be governed by a surface thermodynamic force. However, the phenomenological descriptions of fretting wear mechanisms analyzed in Chapter 1 suggest that material detachment is the consequence of a progressive degradation process which spans a subsurface layer of several tens of micrometers depth. In this regard, the characteristic scale of the degradation process is about one order of magnitude greater than the surface asperities typical size.

Consequently, we propose in this section to introduce a slight paradigm shift with respect to Section 2.2. Wear is hereafter assumed to be the consequence of a progressive degradation taking place in a near-surface processing layer. This processing layer can possibly be seen as a tribologically transformed structure (TTS) which progressively develops and ultimately leads to particle detachment. In the following, we introduce a scalar variable denoted d which is analogous to a damage variable. This variable d is used as a proxy to quantify the amount of wear damage cumulated near the surface during the loading. The idea is to assume that this wear damage gradually increases and that wear occurs as soon as the cumulated damage reaches a threshold. This approach may be seen as a regularization of the analysis conducted in the previous section: the wear surface is no longer regarded as a localized discontinuity surface, but is expanded into a processing layer with a certain thickness.

The use of damage mechanics to quantify the surface degradation occurring under fretting motion was considered for example by Beyer et al. (2019). In their study, they perform fretting simulations using a local damage model either in partial slip or in gross slip. Their results emphasize the influence of the fretting regime on damage evolution: in gross slip, damage is spread all over

the contact surface while in partial slip damage only develops in the outer slip annulus.

2.3.1 Damage mechanics

Principles of continuum damage mechanics

Continuum damage mechanics is the study of the loss of stiffness endured by a material. This loss of stiffness is generally the macroscopic consequence of microcracks and microvoids arising in the microstructure. The first mechanical description of such phenomena is often attributed to Kachanov who introduced the use of a continuous variable measuring the loss of stiffness [Kachanov 1958]. If damage is assumed to be isotropic, it can indeed be represented using a scalar variable $d \in [0,1]$. The state $d = 0$ represents the original, supposedly undamaged material, while $d = 1$ accounts for a fully damaged material. Considering a representative elementary volume, d may be understood based on the ratio between the effective surface S_{eff} (namely the resistive surface that effectively supports stress) and the total surface S:

$$d = 1 - \frac{S_{\text{eff}}}{S}. \tag{2.37}$$

Damage modeling is done within the framework of irreversible thermodynamics [Lemaitre et al. 2009]. For the sake of simplicity, let us assume that the undamaged material behavior is linear elastic. We take as state variables the deformation $\underline{\underline{\varepsilon}}$ and the damage variable d, and chose as state potential the free energy, generally expressed[6]:

$$\rho\psi(\underline{\underline{\varepsilon}}, d) = \frac{1}{2}\underline{\underline{\varepsilon}} : \underline{\underline{\underline{\underline{C}}}}(d) : \underline{\underline{\varepsilon}} + I_{[0,1]}(d). \tag{2.38}$$

Here, the fourth order elasticity tensor is a function of d. It represents the loss of stiffness associated with the evolution of d, which is often taken into account by introducing a positive decreasing function g such that the elasticity tensor verifies:

$$\underline{\underline{\underline{\underline{C}}}}(d) = g(d)\underline{\underline{\underline{\underline{C}}}}(0). \tag{2.39}$$

Moreover, the term $I_{[0,1]}(d)$ is introduced in the expression of the free energy to prescribe the constraint $d \in [0,1]$. $I_{[0,1]}$ is the indicator function of the segment $[0,1]$:

$$I_{[0,1]}(d) = \begin{cases} 0 & \text{if } d \in [0,1] \\ +\infty & \text{if } d \notin [0,1]. \end{cases} \tag{2.40}$$

The state equations relate the state variables $\underline{\underline{\varepsilon}}$ and d to their respective driving forces $\underline{\underline{\sigma}}$ and Y

[6]Sometimes the damage gradient $\underline{\nabla d}$ is considered as a state variable as well. It introduces non-local terms that take the influence of the vicinity of a point on its damage into account [Nedjar 1995].

and are obtained by differentiation of the state potential:

$$\underline{\underline{\sigma}} = \rho \frac{\partial \psi}{\partial \underline{\underline{\varepsilon}}} \tag{2.41}$$

$$Y \in -\rho \partial_d \psi. \tag{2.42}$$

In Equation 2.42, $\partial_d \psi$ designates the subderivative of ψ with respect to d[7]. It gives:

$$\underline{\underline{\sigma}} = g(d) \underline{\underline{\underline{\underline{C}}}}(0) : \underline{\underline{\varepsilon}} \tag{2.43}$$

$$Y \in -\frac{1}{2} \underline{\underline{\varepsilon}} : g'(d) \underline{\underline{\underline{\underline{C}}}}(0) : \underline{\underline{\varepsilon}} - \partial_d I_{[0,1]}(d) \tag{2.44}$$

where

$$\partial_d I_{[0,1]}(d) = \begin{cases} \{0\} & \text{if } d \in]0,1[\\ \mathbb{R}^+ & \text{if } d = 1 \\ \mathbb{R}^- & \text{if } d = 0 \\ \emptyset & \text{if } d \notin [0,1]. \end{cases} \tag{2.45}$$

The intrinsic dissipation related to the evolution of damage is:

$$\mathrm{d}_1 = Y \dot{d} \geq 0. \tag{2.46}$$

Complementary laws are then required to give the evolution rate of d depending on Y. It is generally given using a dissipation potential φ which is a convex function of $\dot{d}$. The evolution law is then obtained by:

$$Y \in \partial_{\dot{d}} \varphi(\dot{d}). \tag{2.47}$$

The evolution law can equivalently be given considering the dual dissipation potential φ^*, obtained by the Legendre-Fenchel transformation:

$$Y \in \partial_{\dot{d}} \varphi(\dot{d}) \Leftrightarrow \dot{d} \in \partial_Y \varphi^*(Y) \Leftrightarrow \varphi(\dot{d}) + \varphi^*(Y) - Y\dot{d} = 0. \tag{2.48}$$

Decoupling between volumetric and deviatoric contributions

In the specific case of wear modeling we are interested in here, we propose to introduce a decoupling between volumetric and deviatoric contributions to damage. Indeed, we seek to express a damage evolution that is representative of the accumulation of degradation prior to wear particle detachment. The evolution of damage must thus occur following loading types that are likely to generate wear. Decoupling deviatoric loading from volumetric loading seems relevant then; wear degradation being arguably more related to deviatoric stress than volumetric stress. This is consistent with the observation that wear is often accompanied by high plastic strains which, in the general case, are considered to occur only due to deviatoric stress.

[7] The concept of subderivative is used as a generalization of differentiation for convex, non-differentiable functions. It is defined as:

$$\partial \psi(d) = \{d^* \mid \forall d',\ d^*(d' - d) \leq \psi(d') - \psi(d)\}$$

and is employed here because the indicator function $I_{[0,1]}$ is non-differentiable. For differentiable functions, the subderivative is equivalent to the classical derivative [Maitournam 2017].

For simplicity, let us assimilate the damage force Y with its regular term:

$$Y = Y^{\text{reg}} = -\frac{1}{2}\underline{\underline{\varepsilon}} : g'(d)\underline{\underline{\underline{\underline{C}}}}(0) : \underline{\underline{\varepsilon}}. \tag{2.49}$$

We decompose the strain tensor into a volumetric term $\underline{\underline{\varepsilon^{\text{v}}}}$ and a deviatoric term $\underline{\underline{\varepsilon^{\text{d}}}}$:

$$\underline{\underline{\varepsilon}} = \underline{\underline{\varepsilon^{\text{v}}}} + \underline{\underline{\varepsilon^{\text{d}}}} \tag{2.50}$$

where

$$\underline{\underline{\varepsilon^{\text{v}}}} = \frac{1}{3}\text{Tr}(\underline{\underline{\varepsilon}})\underline{\underline{I}} \tag{2.51}$$

$$\underline{\underline{\varepsilon^{\text{d}}}} = \underline{\underline{\varepsilon}} - \underline{\underline{\varepsilon^{\text{v}}}} = \underline{\underline{\varepsilon}} - \frac{1}{3}\text{Tr}(\underline{\underline{\varepsilon}})\underline{\underline{I}} \tag{2.52}$$

with Tr the trace operator and $\underline{\underline{I}}$ the second order identity tensor. Because $\underline{\underline{\varepsilon^{\text{v}}}} : \underline{\underline{\varepsilon^{\text{d}}}} = 0$, we have in the case of isotropic linear elasticity:

$$\underline{\underline{\varepsilon}} : \underline{\underline{\underline{\underline{C}}}} : \underline{\underline{\varepsilon}} = (\underline{\underline{\varepsilon^{\text{v}}}} + \underline{\underline{\varepsilon^{\text{d}}}}) : \underline{\underline{\underline{\underline{C}}}} : (\underline{\underline{\varepsilon^{\text{v}}}} + \underline{\underline{\varepsilon^{\text{d}}}}) = \underline{\underline{\varepsilon^{\text{v}}}} : \underline{\underline{\underline{\underline{C}}}} : \underline{\underline{\varepsilon^{\text{v}}}} + \underline{\underline{\varepsilon^{\text{d}}}} : \underline{\underline{\underline{\underline{C}}}} : \underline{\underline{\varepsilon^{\text{d}}}}. \tag{2.53}$$

Hence, instead of considering a function g, we introduce two positive decreasing functions g_1 and g_2 respectively affecting the volumetric and deviatoric contributions. As a result, the damage driving force can be written

$$Y = -\frac{1}{2}\underline{\underline{\varepsilon^{\text{v}}}} : g_1'(d)\underline{\underline{\underline{\underline{C}}}}(0) : \underline{\underline{\varepsilon^{\text{v}}}} - \frac{1}{2}\underline{\underline{\varepsilon^{\text{d}}}} : g_2'(d)\underline{\underline{\underline{\underline{C}}}}(0) : \underline{\underline{\varepsilon^{\text{d}}}}. \tag{2.54}$$

In this way, the damage law can be adapted for example to depend exclusively on deviatoric stress and strain, or on any combination of deviatoric and volumetric contributions.

2.3.2 The thick level set approach

In accordance with the analysis carried out in Section 2.2, we seek to model wear evolution as a propagating front delimiting unworn material from worn material. In the present section, this approach is enriched by considering that wear results from a progressive degradation occurring within a partially damaged layer of non-zero thickness. In order to model this kind of transformations, we consider using the *thick level set* (TLS) approach. All the following developments are conducted in a two-dimensional case.

General principle of the thick level set

The TLS approach was developed by Moës et al. as a regularization strategy for local damage models in the study of fracture [Moës et al. 2011]. It enhances the concept of level set in which damage evolution is represented by the propagation of a level set front delimiting damaged and undamaged material. In the TLS approach, the level set is supplemented by a transition zone in its wake, in which damage continuously evolves from 0 to 1. In this partially damaged transition zone, the damage variable evolves following a prescribed function which is a parameter of the model. Following this approach, damage growth is no longer governed by a local evolution law

but is the result of the propagation of the level set instead. The level set propagation is driven by a non-local force which is averaged over the thickness of the transition zone.

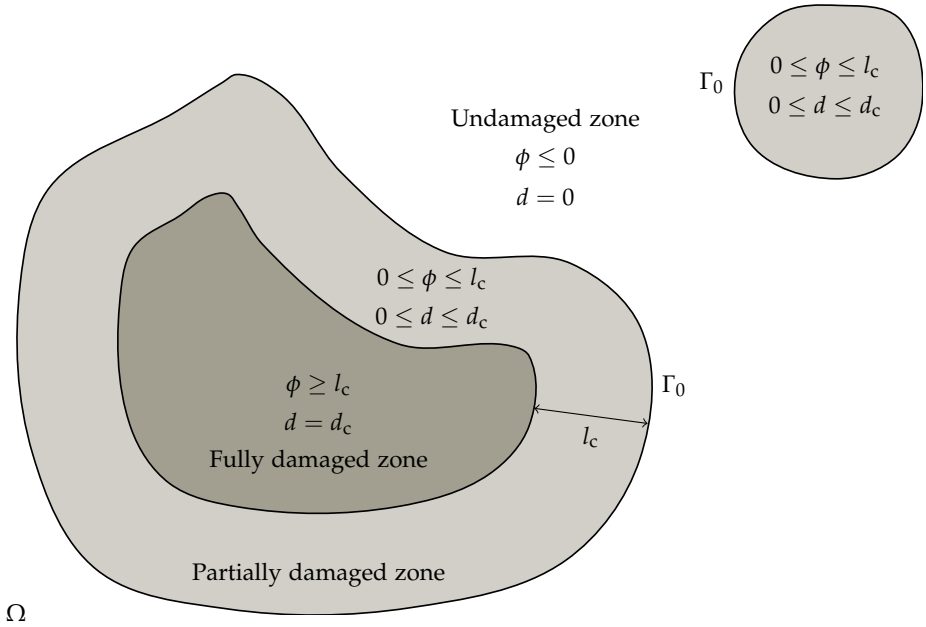

Figure 2.3: Domain containing undamaged, partially damaged and totally damaged zones represented using a thick level set (adapted from Moës et al. (2011)).

Assume a domain Ω containing damaged zones and undamaged zones (Figure 2.3). The boundary between damaged zones and undamaged zones is denoted Γ_0 and is defined by the level set $\phi = 0$ where the function ϕ is defined on Ω as the signed distance to the level set: in undamaged zones, $\phi < 0$ while in damaged zones, $\phi > 0$. In addition, a critical length l_c is introduced and the damage value is explicitly defined in Ω as a function of ϕ:

$$\forall \phi \leq 0,\ d(\phi) = 0 \tag{2.55}$$

$$\forall \phi \in [0, l_c],\ d(\phi) \in [0, d_c] \text{ and } d'(\phi) \geq 0 \tag{2.56}$$

$$\forall \phi \geq l_c,\ d(\phi) = d_c \tag{2.57}$$

in which d_c is a critical damage value (usually $d_c = 1$), and d is a prescribed increasing function of ϕ for $\phi \in [0, l_c]$. For example, with $d_c = 1$ and $d(\phi) = \phi / l_c$ for $\phi \in [0, l_c]$, the graph of the function d is represented in Figure 2.4.

Because ϕ is a signed distance function, it must satisfy an eikonal equation:

$$\|\underline{\nabla \phi}\| = 1 \tag{2.58}$$

and any variation of ϕ must be constant along the direction of the gradient of ϕ (i.e. the normal direction to the level set). In other words, any variation of ϕ in the domain Ω can be reduced to the normal propagation of the level set $\phi = 0$. Moreover, the level set propagation must satisfy the consistency condition such that:

$$\frac{\partial \phi}{\partial t} + v_n \underline{\nabla \phi} \cdot \underline{n} = 0 \tag{2.59}$$

where $\underline{n}$ is the unit normal vector to the level set and v_n is its propagation velocity along that

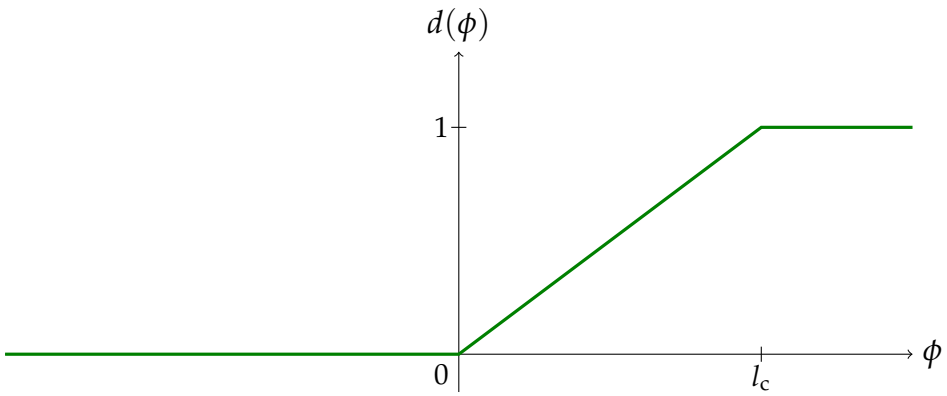

Figure 2.4: Example of a graph of a suitable damage function d. In the thick level set framework, ϕ is the signed distance to the level set, and the function d and the critical length l_c are parameters of the model.

normal. This consistency condition is equivalently given with respect to the damage variable:

$$\dot{d} = d'(\phi) v_n \tag{2.60}$$

in which d' is the derivative of d with respect to ϕ. Considering these conditions, the aim is to formulate a propagation law on the level set which is based on the local damage evolution law and enables to determine the appropriate propagation velocity v_n regarding damage growth.

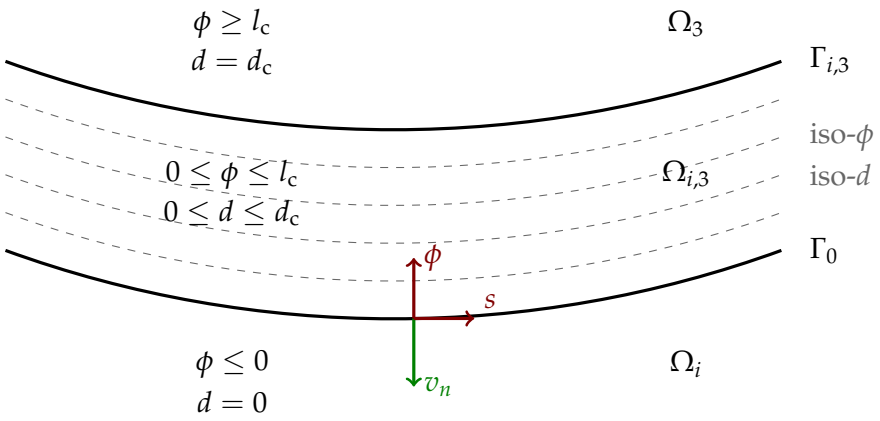

Figure 2.5: Representation of a partially damaged layer using a thick level set, aiming at representing a wear processing layer.

Propagation law

Let us consider a partially damaged layer as depicted in Figure 2.5, which is similar to the representation of the wear problem described in Section 2.2. Ω_i designates the undamaged domain, $\Omega_{i,3}$ is the partially damaged layer, and Ω_3 is the totally damaged, or worn, domain. The surface Γ_0 is the level set $\phi = 0$ and separates the undamaged Ω_i from the partially damaged $\Omega_{i,3}$, while $\Gamma_{i,3}$ is the wear surface and separates the partially damaged domain from the worn domain Ω_3 (which is supposedly not taking part in the contact). The level set Γ_0 is propagating towards Ω_i at velocity v_n while the wear surface $\Gamma_{i,3}$ moves at the wear velocity $\dot{h}_i$. Moreover, the partially damaged domain

$\Omega_{i,3}$ is endowed with a curvilinear coordinate system (s, ϕ). As a result, the velocity v_n is expressed as a function of s along the level set.

As a first step, we express the dissipation power associated with the propagation of the level set at velocity $v_n(s)$. The total dissipation over Ω is:

$$\mathcal{D} = \int_\Omega Y\dot{d}\, d\Omega. \tag{2.61}$$

Because damage growth occurs only in the partially damaged layer $\Omega_{i,3}$ and using the consistency condition (2.60), we get

$$\mathcal{D} = \int_{\Omega_{i,3}} Y d'(\phi) v_n\, d\Omega. \tag{2.62}$$

Then we express the integral using the curvilinear coordinates (ϕ, s). The integration element becomes:

$$d\Omega = \left(1 - \frac{\phi}{r(s)}\right) d\phi\, ds \tag{2.63}$$

where $r(s)$ is the radius of curvature of the level set Γ_0 at the coordinate s. The dissipation can then be expressed:

$$\mathcal{D} = \int_{\Gamma_0} \int_0^l Y(\phi, s) d'(\phi) \left(1 - \frac{\phi}{r(s)}\right) v_n(s)\, d\phi\, ds \tag{2.64}$$

where $l \leq l_c$ is the thickness of the partially damaged layer. Let us introduce $\overline{\mathcal{G}}$ such that:

$$\overline{\mathcal{G}}(s) = \int_0^l Y(\phi, s) d'(\phi) \left(1 - \frac{\phi}{r(s)}\right) d\phi. \tag{2.65}$$

This enables to write the dissipation as an integral over the level set Γ_0 of terms depending only on s:

$$\mathcal{D} = \int_{\Gamma_0} \overline{\mathcal{G}}(s) v_n(s)\, ds. \tag{2.66}$$

In this expression of the dissipation, $\overline{\mathcal{G}}$ appears as the driving force governing the propagation of the level set front. This driving force arises from an average of the damage driving force over the partially damaged domain thickness. By doing that, the damage problem that was initially expressed in the volume Ω is reduced to a propagation problem expressed on the surface Γ_0.

One can note the similarity between this averaged level set propagation driving force $\overline{\mathcal{G}}$ and the wear front driving force introduced in Equation 2.35. This shows that the approach conducted here is consistent with the analysis carried out in Section 2.2.

The next step is to provide an evolution law for the level set propagation in order to be able to derive $v_n(s)$. Considering the local damage evolution law expressed as in Equation 2.48, we search v_n that minimizes the following integral under the constraint of the consistency condition (2.60):

$$\inf_{\dot{d}=d'(\phi)v_n} \int_{\Omega_{i,3}} (\varphi(\dot{d}) + \varphi^*(Y) - Y\dot{d})\, d\Omega. \tag{2.67}$$

This is equivalent to searching v_n minimizing:

$$\inf_{v_n} \int_{\Omega_{i,3}} (\varphi(d'(\phi)v_n) - Yd'(\phi)v_n)\, d\Omega. \tag{2.68}$$

We define a homogenized dissipation potential $\overline{\varphi}$ such that

$$\int_{\Omega_{i,3}} \varphi(d'(\phi)v_n)\, d\Omega = \int_{\Gamma_0} \overline{\varphi}(v_n, s)\, ds. \tag{2.69}$$

Using the dissipation equation (2.66) the problem is reduced to finding v_n on Γ_0 with:

$$\inf_{v_n} \int_{\Gamma_0} (\overline{\varphi}(v_n, s) - \overline{\mathcal{G}}(s)v_n(s))\, ds \Leftrightarrow \sup_{v_n} \int_{\Gamma_0} (\overline{\mathcal{G}}(s)v_n(s) - \overline{\varphi}(v_n, s))\, ds = \int_{\Gamma_0} \overline{\varphi^*}(\overline{\mathcal{G}}, s)\, ds \tag{2.70}$$

where $\overline{\varphi^*}$ is a homogenized dual dissipation potential defined through a Legendre-Fenchel transformation. This development is completed in Section 2.4 using a specific damage evolution law, which eventually enables to derive the level set propagation velocity v_n.

Finally, the wear rate $\dot{h}_i$ is easily obtained from v_n. Assuming that wear occurs when d reaches d_c, it follows that the distance between the wear surface and the level set must be lower than l_c. As a first step, when the material is not sufficiently damaged yet, the level set propagates and damage grows but no wear occurs. Then, when the damage value in surface reaches $d = d_c$, wear occurs and the wear surface propagates at iso $d = d_c$ and iso $\phi = l_c$. Consequently, the wear rate may be expressed:

$$\dot{h}_i = \begin{cases} v_n & \text{if } l = l_c \\ 0 & \text{if } l < l_c. \end{cases} \tag{2.71}$$

The approach chosen here is one possibility among others to regularize a local damage law. Different alternatives exist [Valoroso and Stolz 2022] but the thick level set approach seems appropriate regarding the actual mechanisms at stake in fretting wear. It allows to represent the progressive growth of a partially damage layer before wear onsets, followed by a steady-state wear phase in which the processing layer keeps a constant depth. In particular, these characteristics appear to be prone to reproduce the behavior of a tribologically transformed structure (TTS) layer, including the incubation time sometimes observed prior to the start of wear.

2.4 Example of application with a specific damage law

2.4.1 Identification of a fretting wear damage law

In order to be able to derive wear evolution, one still has to identify a suitable local damage evolution law to be included within the thick level set framework. This is done through the definition of a dissipation potential from which the evolution law derives. Here, we endeavor to propose a simple damage law that is able to account for the progressive accumulation of degradation under fretting motion. Because the aim is to keep the approach rather general, the damage law is chosen as simple as possible. However, it is obviously possible to adapt the proposed methodology with different, more complex damage laws.

The most simple form for the free energy in an elastic material with damage is as follows:

$$\rho\psi(\underline{\underline{\varepsilon}}, d) = \frac{1}{2} g(d) \underline{\underline{\varepsilon}} : \underline{\underline{\underline{\underline{C}}}} : \underline{\underline{\varepsilon}} \tag{2.72}$$

with $g(d) = 1 - d$. The state laws are then:

$$\underline{\underline{\sigma}} = (1-d)\underline{\underline{\underline{\underline{C}}}} : \underline{\underline{\varepsilon}} \tag{2.73}$$

$$Y = \frac{1}{2} \underline{\underline{\varepsilon}} : \underline{\underline{\underline{\underline{C}}}} : \underline{\underline{\varepsilon}}. \tag{2.74}$$

Alternatives include more complex forms for the function g, or even a decoupling between deviatoric and volumetric terms as proposed in Section 2.3.1. For example, if we consider that damage is only related to deviatoric loading, the state laws may become:

$$\underline{\underline{\sigma}} = (1-d)\underline{\underline{\underline{\underline{C}}}} : \underline{\underline{\varepsilon^{\mathrm{d}}}} + \underline{\underline{\underline{\underline{C}}}} : \underline{\underline{\varepsilon^{\mathrm{v}}}} = \underline{\underline{\underline{\underline{C}}}} : \underline{\underline{\varepsilon}} - d\underline{\underline{\underline{\underline{C}}}} : \underline{\underline{\varepsilon^{\mathrm{d}}}} \tag{2.75}$$

$$Y = \frac{1}{2} \underline{\underline{\varepsilon^{\mathrm{d}}}} : \underline{\underline{\underline{\underline{C}}}} : \underline{\underline{\varepsilon^{\mathrm{d}}}}. \tag{2.76}$$

Then, we consider a simple damage evolution law [Lemaitre et al. 2009]:

$$\varphi^*(Y, d) = I_{\mathcal{C}}(Y, d) \tag{2.77}$$

where $I_{\mathcal{C}}$ is the indicator function of the convex set $\mathcal{C}$:

$$\mathcal{C} = \{(Y, d) \mid f(Y, d) = Y - Y_0 - Y_1 d \leq 0\}. \tag{2.78}$$

The differentiation of the dual pseudo-potential φ^* gives the damage evolution law as:

$$\exists \dot{\lambda} \geq 0 \text{ s.t. } \dot{d} = \dot{\lambda} \; ; \; Y - Y_0 - Y_1 d \leq 0 \; ; \; \dot{\lambda}(Y - Y_0 - Y_1 d) = 0. \tag{2.79}$$

The consistency condition gives:

$$\dot{d} > 0 \Rightarrow \dot{Y} = Y_1 \dot{d}. \tag{2.80}$$

Thus, the damage evolution law may be written as:

$$\dot{d} = \begin{cases} 0 & \text{if } Y < Y_0 + Y_1 d \\ \frac{\langle \dot{Y} \rangle_+}{Y_1} & \text{if } Y = Y_0 + Y_1 d \end{cases} \tag{2.81}$$

where the Macaulay bracket notation $\langle x \rangle_+ = \frac{1}{2}(x + |x|)$ designates the positive part.

This law implies that damage evolves only when the driving force Y reaches a threshold. The initial threshold value is set to Y_0, then it increases as damage grows. As a result, damage may not grow if Y does not outreach its previous maximal value. This property implies that a repeated loading in which Y is bounded results in a bounded damage evolution. As it was outlined first by Marigo, then by Mai et al., this damage law is suitable to represent a brittle damage, but fails to account for fatigue damage in which damage progressively increases cycle-by-cycle [Marigo

1985, Mai et al. 2012]. Consequently, they propose to use a slightly modified version of the law (2.81) in which damage is assumed to evolve for values of Y even below the threshold. By doing that, they introduce a so-called loading/unloading irreversibility concept assuming that damage may increase even with a driving force below the yield surface. The brittle damage law (2.81) is modified accordingly into:

$$\forall Y,\ \dot{d} = \beta(Y,d)^n \frac{\langle \dot{Y} \rangle_+}{Y_1} \tag{2.82}$$

where $n > 0$ and β is any increasing function of Y such that $\beta(0,d) = 0$ and $\beta(Y,d) = 1$ if $Y = Y_0 + Y_1 d$. This modified law may be seen as a regularization of the brittle law, which is retrieved for $n \to +\infty$.[8] For example, let us choose $n = 1$ and

$$\beta(Y,d) = \frac{Y}{Y_0 + Y_1 d}. \tag{2.83}$$

In this case, the local damage law becomes:

$$\forall Y,\ \dot{d} = \frac{Y}{Y_1(Y_0 + dY_1)} \langle \dot{Y} \rangle_+. \tag{2.84}$$

In order to assess the difference of behavior between the brittle damage law (2.81) and the regularized damage law (2.84), let us consider the following simple test case. We assume a tension test with two different loadings: (a) monotonic tension with imposed tensile strain $\varepsilon_{xx}(t) = K_0 t$, and (b) loading/unloading cycles with imposed tensile strain $\varepsilon_{xx}(t) = \frac{1}{2} K_1 \left(1 - \cos(2\pi f t)\right)$. The damage driving force is derived as

$$Y(t) = \frac{1}{2} E \varepsilon_{xx}(t)^2 \tag{2.85}$$

E being the initial Young's modulus. Damage evolution is derived using either the brittle damage law (2.81), or the regularized damage law (2.84). Figure 2.6 shows the stress-strain response with both loadings and both damage laws. One notes that considering the brittle law through loading/unloading cycles leads to no damage evolution after the first cycle, which was expected as the driving force never outreaches its previous maximal value. On the opposite, the regularized law leads to a progressive damage increase throughout the cycles. The evolution of the damage value in the different cases is depicted in Figure 2.7.

The results obtained on this simple tension test case indicate that the brittle damage law (2.81) fails to represent a cyclic increasing damage, whereas the regularized law (2.84) is better suited for that. As a consequence, we seek to integrate this damage law into the TLS framework. However, the considered evolution law does not derive from a dissipation potential and falls outside of the generalized standard framework. Therefore, an adaptation is required for its integration within the TLS approach.

[8] This regularized law can be accommodated to integrate a threshold as well, such that:

$$\dot{d} = \begin{cases} 0 & \text{if } Y < Y_0 \\ \beta(Y,d)^n \frac{\langle \dot{Y} \rangle_+}{Y_1} & \text{if } Y \geq Y_0. \end{cases}$$

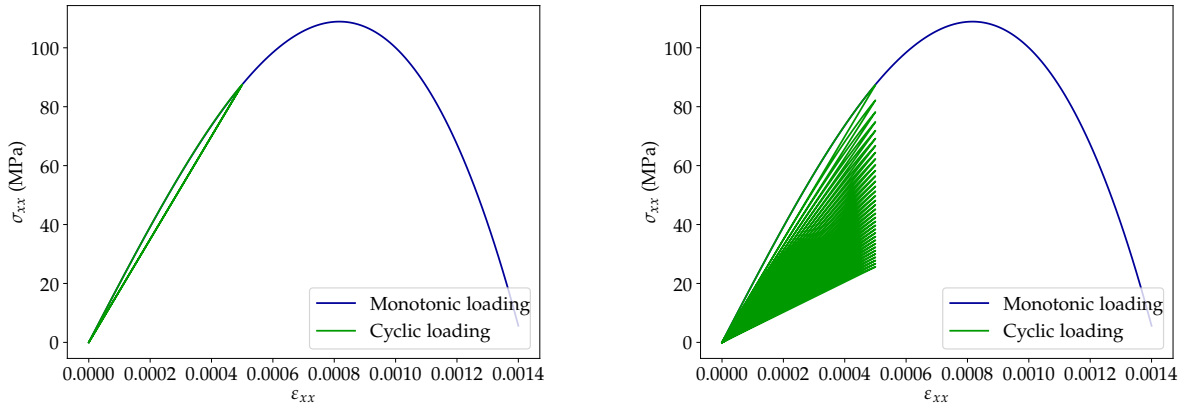

(a) Brittle damage law **(b)** Regularized damage law

Figure 2.6: Comparison of the stress-strain responses to a monotonic or cyclic imposed tensile strain using (a) the brittle damage law (2.81) or (b) the regularized damage law (2.84); with parameters $E = 200$ MPa, $Y_0 = 0$ MPa, $Y_1 = 0.2$ MPa, $K_0 = 1 \times 10^{-4}$ s^{-1}, $K_1 = 5 \times 10^{-4}$, $f = 5$ Hz.

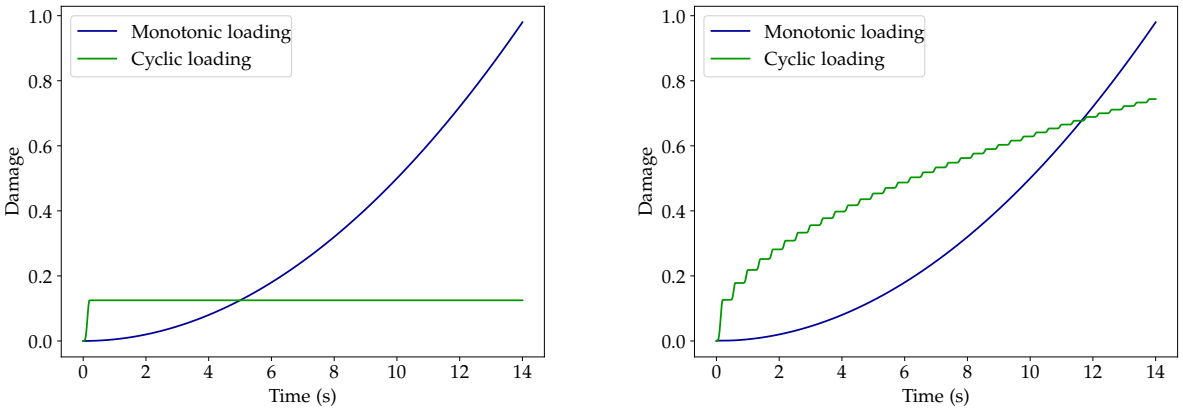

(a) Brittle damage law **(b)** Regularized damage law

Figure 2.7: Comparison of the damage evolution with a monotonic or cyclic imposed tensile strain using (a) the brittle damage law (2.81) or (b) the regularized damage law (2.84); with parameters $E = 200$ MPa, $Y_0 = 0$ MPa, $Y_0 = 0.2$ MPa, $K_0 = 1 \times 10^{-4}$ s^{-1}, $K_1 = 5 \times 10^{-4}$ s^{-1}, $f = 5$ Hz.

2.4.2 Integration within the thick level set framework

Using Equation 2.66, we propose to find the level set propagation velocity v_n such that the dissipation resulting from the level set front propagation equals the dissipation generated by damage evolution in the processing zone considering the local damage law:

$$\mathcal{D} = \int_{\Gamma_0} \overline{\mathcal{G}}(s) v_n(s)\, ds = \int_{\Omega_{i,3}} Y \dot{d}\, d\Omega \tag{2.86}$$

where $\dot{d}$ stems from the local damage law (2.84) and the homogenized driving force $\overline{\mathcal{G}}$ is expressed in Equation 2.65. This gives:

$$\int_{\Gamma_0} v_n(s) \int_0^l Y(\phi,s) d'(\phi) \left(1-\frac{\phi}{r(s)}\right) d\phi\, ds = \int_{\Gamma_0} \int_0^l \frac{Y^2(\phi,s)}{Y_1(Y_0+d(\phi)Y_1)} \langle \dot{Y}(\phi,s)\rangle_+ \left(1-\frac{\phi}{r(s)}\right) d\phi\, ds. \tag{2.87}$$

We obtain an equation to find v_n. Let us first introduce a time discretization, and assume we solve the problem on a time step Δt. We denote $\Delta a(s) = v_n(s)\Delta t$ the propagation increment and $\Delta Y(\phi,s) = \dot{Y}(\phi,s)\Delta t$ the local driving force increment. TLS problems are generally solved explicitly, decoupling the elastic problem computation and the damage evolution [Bernard et al. 2012]. The static equilibrium problem is solved as a first step considering a fixed damage field, then the level set propagation problem is solved. Let us then assume that we search $\Delta a(s)$ at fixed $d(\phi)$. We transform Equation 2.87 into a weak formulation and use a Galerkin method to convert it into a discretized system. We introduce a discretization of the level set Γ_0 into n_s nodes $(s_i)_{1\leq i\leq n_s}$. A set of basis functions $(N_i)_{1\leq i\leq n_s}$ defined on Γ_0 is considered which satisfy:

$$\forall (i,j) \in \{1,\dots n_s\}\times\{1,\dots n_s\},\ N_i(s_j) = \delta_{ij} \tag{2.88}$$

where δ_{ij} is Kronecker's symbol. A simple example for linear basis functions is represented in Figure 2.8. The level set propagation increment $\Delta a(s)$ is then projected into the basis functions space as

$$\forall s \in \Gamma_0,\ \Delta a(s) = \sum_{i=1}^{n_s} \Delta a_i N_i(s). \tag{2.89}$$

It finally leads to the system:

$$\forall i \in \{1,\dots n_s\},\ \sum_{j=1}^{n_s} \int_{\Gamma_0} \int_0^l Y(\phi,s) d'(\phi) \left(1-\frac{\phi}{r(s)}\right) d\phi\, N_i(s) N_j(s)\, ds\, \Delta a_j = \int_{\Gamma_0} \int_0^l \frac{Y^2(\phi,s)}{Y_1(Y_0+d(\phi)Y_1)} \langle \Delta Y(\phi,s)\rangle_+ \left(1-\frac{\phi}{r(s)}\right) d\phi\, N_i(s)\, ds \tag{2.90}$$

which can be written in a matrix form:

$$\boldsymbol{K}\,\boldsymbol{\Delta a} = \boldsymbol{\Delta F} \tag{2.91}$$

where $\boldsymbol{K}$, $\boldsymbol{\Delta a}$ and $\boldsymbol{\Delta F}$ are respectively $n_s \times n_s$, $n_s \times 1$ and $n_s \times 1$ matrices whose coefficients are:

$$K_{ij} = \int_{\Gamma_0} \int_0^l Y(\phi,s) d'(\phi) \left(1-\frac{\phi}{r(s)}\right) d\phi\, N_i(s) N_j(s)\, ds \tag{2.92}$$

$$\Delta F_i = \int_{\Gamma_0} \int_0^l \frac{Y^2(\phi,s)}{Y_1(Y_0+d(\phi)Y_1)} \langle \Delta Y(\phi,s)\rangle_+ \left(1-\frac{\phi}{r(s)}\right) d\phi\, N_i(s)\, ds. \tag{2.93}$$

The resolution of the system (2.91) enables to compute the propagation of the level set. Using an explicit scheme which decouples elastic resolution at fixed damage and level set propagation, a simple step-by-step algorithm may be implemented to compute wear evolution. Examples of wear computations using this strategy are provided in Chapter 3.

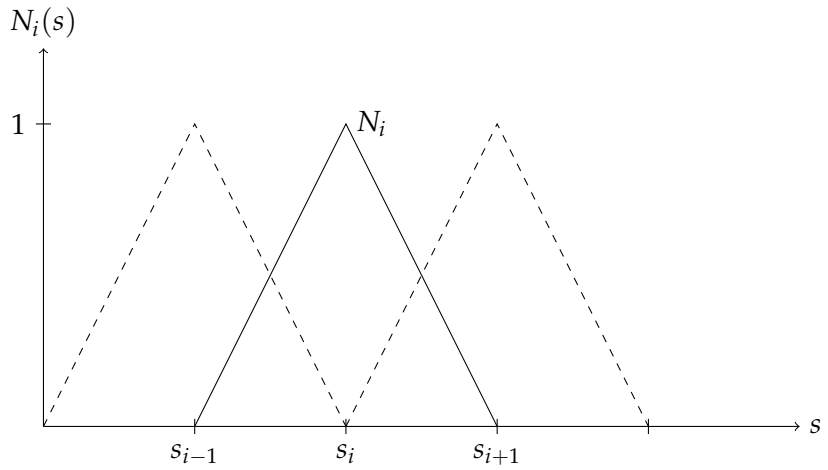

Figure 2.8: Example of basis functions used for level set propagation resolution.

2.5 Conclusion

While the most widespread wear models are empirical, it can be supposed that models relying upon the history of the mechanical state of the near-surface material could provide better predictive capabilities. For that, a certain amount of theoretical studies developed modeling frameworks based on sound thermodynamical principles. To this day however, no unified description of wear mechanics has been widely adopted. The work reported in this chapter relies on these past studies and attempts to provide a description of fretting wear based on damage accumulation.

The idea here was to provide a methodology for deriving such models, which includes common features of fretting wear. The precise identification of a wear law that accurately captures experimentally observed wear kinetics is not tackled here. The proposed model however integrates several levers enabling it to be customized to fit experimental data. First, it can be adapted to integrate any damage law, including the choice of a local damage driving force. For instance, it could be chosen to depend on deviatoric stress only. In addition, the thick level set approach contains its own tailoring parameters, such as the prescribed damage evolution function and the critical length. The existence of various adaptation possibilities offers a great versatility which is a valuable asset for the model. It can indeed be accommodated to integrate a threshold beneath which wear is not triggered for example. In addition, this model may be used regardless of the surface loading. It could for example possibly be used to represent the surface degradation under impact-sliding loadings. On another note, accounting for wear using a scalar variable quantifying the accumulation of damage might help provide a formalism able to integrate more general features of wear. It could for example be imagined to introduce a damage evolution related to oxidation or other external causes.

Some questions raised by the proposed models may however be highlighted, especially regarding the legitimacy of a wear model based on damage mechanics. In the first place, the idea of a damage-like variable arose to quantify the progressive accumulation of degradation near the surface. While this seems consistent with the mechanisms described for fretting wear, in this model wear damage is associated with a stiffness drop as in regular damage mechanics. But does this stiffness decrease faithfully represent the actual degradation mechanism occurring in fretting wear? Or should the pseudo-damage variable remain instead a purely fictitious proxy accounting for the ac-

cumulation of degradation? In the bigger picture, this question concerns the physical meaning of this modeling approach.

Another interrogation concerns the identification of the law chosen for wear damage. Measuring the local mechanical properties of a thin surface layer seems challenging to say the least, and tracking their evolution throughout the experiment would require complicated interrupted tests. Coupled approaches involving both experimental and numerical studies are needed to perform experimental data fit and numerically retrieve experimentally observed wear kinetics.

In the next chapter, numerical methods are described for the simulation of fretting wear using either usual energy-based wear models or a damage-based model with the thick level set approach.

Chapter recap

Based on previous theoretical studies, a thermodynamic analysis of a fretting wear problem is conducted.

- Wear evolution is represented through the propagation of a wear front.
- The dissipation associated with the wear front propagation is related to the discontinuity of free energy across the front.
- It brings out a thermodynamic force associated with wear, which is seen as an energy release rate. This is the surface density of free energy that is dissipated per unit wear depth growth.

A wear model based on damage accumulation is suggested.

- Wear is assumed to occur at $d = d_c$.
- It is proposed to make damage evolution depend on deviatoric stress to better capture wear degradation.
- Damage evolution is represented using a thick level set approach: damage evolution is governed by the propagation of a level set front.
- The chosen local damage evolution law is a regularization of a brittle damage law, initially intended to represent fatigue degradation.
- The level set propagation law is obtained as a homogenization of the local damage law over the processing zone.
- A simple step-by-step algorithm may be implemented to compute wear evolution based on thick level set damage:
  1. Assuming a fixed damage field, the resolution of the elastic problem enables the computation of the local driving force Y.
  2. The level set propagation law (2.91) is used to get the level set evolution over the time step.
  3. The level set propagation governs damage evolution; the damage field is updated accordingly.
  4. We assume that the material wears out at iso $d = d_c$; the wear front propagation increment over the time step is computed accordingly.

Chapter 3

Numerical simulation of fretting wear problems

A finite element framework for the simulation of fretting wear problems including either Archard-like or damage-based wear models

3.1 Introduction

Over the past few decades, numerical approaches have become an integral part of studying structural and material mechanics. The continuous progress in computational capacities, coupled with the emergence of groundbreaking numerical methods like the finite element method (FEM), have provided researchers with the means to study intricate problems and extract detailed mechanical information from large and complex structures.

Concerning the study of wear, experimental approaches still prevail especially because of the lack of widely accepted unified wear models. In addition, numerical simulation of wear is a challenging issue. The main difficulty lies in the multi-time-scale nature of wear which imposes to compute high amounts of time steps to capture its progressive evolution. Moreover, it must deal with several non-linearities, including frictional contact, surface geometry evolution, or material non-linearities such as plasticity. Numerical strategies have however been developed to tackle these questions and improved over the past years.

Johansson published an early study in 1994 on wear simulations enabling to compute the evolution of contact pressure as wear occurs, governed by Archard's law [Johansson 1994]. In the aftermath of this work, numerical studies of wear have essentially relied on the finite element method. In this framework, the evolution of the surface geometry due to wear is generally taken into account through a fictitious nodal displacement on the wear surfaces. Earliest studies used Archard's law and assumed a frictionless contact [Põdra and Andersson 1999], then integrated friction [Oqvist 2001, McColl et al. 2004] which enabled to use an energy wear model [Mary and Fouvry 2007, Paulin et al. 2008, Garcin et al. 2015]. Most studies are conducted in two dimensions, but three-dimensional problems have been considered [Kim et al. 2005] which is limiting in terms of number of loading cycles able to be computed due to the high computational cost. The computational efficiency is generally tackled assuming a time scales decoupling between the deformation response and wear evolution [Lengiewicz and Stupkiewicz 2012], which allows to introduce an acceleration factor on wear evolution. This acceleration factor is used to extrapolate wear evolution computed on a limited time interval (say a loading cycle) over a greater time interval [McColl et al. 2004, Mary and Fouvry 2007]. The use of an acceleration factor or, equivalently, a cycle jump technique, is extensively discussed in Chapter 4. In addition, it raises some difficulties when an inelastic material behavior is considered [Mohd Tobi et al. 2009, Basseville et al. 2013]. The related issues are especially dealt with in Chapter 5.

Beyond these classical studies that consider smooth evolutions of wear on two-body systems obeying Archard's or energy laws, additional phenomenological aspects of wear have been introduced in the simulations, starting with third body. Third body particles can be explicitly represented within the finite element model as a set of small bodies in frictional sliding contact between the two primary bodies [Basseville et al. 2011, 2013]. Alternatively, it is more often modeled as a homogeneous interfacial layer endowed with a specific material behavior, either elastic [Done et al. 2017, Arnaud et al. 2017, Arnaud and Fouvry 2018] or elastoplastic [Ding et al. 2007]. In all cases its thickness evolves concomitantly with material removal. Arnaud et al. show that the third body layer alters the contact pressure distribution, which is more concentrated towards the center of the contact surface. It gives wear profiles much closer to experimental observation [Arnaud et al. 2017]. Other experimentally observed features were included within numerical studies of wear, such as the presence of pores in the bulk material near the surface [Basseville et al. 2013, Proudhon et al. 2014] or the transport and reaction of oxygen within the contact interface [Arnaud et al. 2021].

Assuming that high dioxygen concentrations promote abrasive wear while adhesive wear prevails under low concentrations, Arnaud et al. retrieve W-shaped wear profiles in their numerical results as observed experimentally.

Whereas all these numerical studies are based on the finite element method and use classical contact formulations, alternatives have been explored. First, in the continuity of the modeling work by Dragon-Louiset and Stolz (1999), Peigney computes the evolution of wear based on semi-analytical solutions for the contact problem using a Griffith-like wear criterion. Wear evolution is tackled as a minimization problem targeting the dissipated energy to compute the stabilized state under a prescribed vertical and cyclic horizontal displacement [Peigney 2004]. Gallego et al. also use a semi-analytical contact model for linear elastic bodies based on the integration of Boussinesq and Cerruti's potentials [Gallego and Nélias 2007, Gallego et al. 2010]. Firstly introduced as a FEM-free method, it was then coupled with the finite element method to compute the evolution of wear on a complex three-dimensional dynamic structure in an efficient way [Lemoine et al. 2020]. In the same computational cost mitigation purpose, the use of a Winkler elastic contact model was proposed [Garcin et al. 2022]. Both these semi-analytical contact solvers enable a much more efficient computation of wear evolution than using the finite element method. Finally, an original so-called MorteX framework was proposed to solve wear problems [Akula 2019]. It couples the X-FEM[1] approach and a mortar[2] treatment of contact conditions and is used to solve contact problems between a real and a virtual embedded surface. In this approach, unilateral wear is represented by the propagation of a virtual embedded surface within the solid. Contact conditions are enforced between this virtual surface and the real, non-wearing contact surface of the counterpart body. This approach enables to mitigate the numerical complexity by getting rid of the mesh update step for the whole finite element model.

In line with the modeling aspects tackled in the previous chapter, this chapter aims at providing numerical strategies to compute the evolution of wear using a damage-based wear model relying upon the thick level set approach. The results are compared with wear evolution computed using a more classical energy-based wear model. First, the governing equations of the problem are given along with some preliminary, semi-analytical results for wear evolution. Then the finite element model used is described together with the computation algorithms implemented to simulate wear using either a damage-based or an energy-based law. Finally, the results obtained with both wear models are analyzed and compared.

3.2 Governing equations

As a first step, we express the governing equations for a quasistatic problem including two bodies in contact with friction and wear. The description of a two-body frictional contact problem may for example be found in a monograph by Wriggers (2006). Let us consider two bodies Ω_1 and Ω_2 as depicted in Figure 3.1. Their respective boundaries $\partial\Omega_i$ ($i \in \{1,2\}$) are decomposed into a Neumann boundary $\partial\Omega_i^t$ with prescribed traction $\underline{T_0}$, a Dirichlet boundary $\partial\Omega_i^u$ with prescribed displacement $\underline{u_0}$, and a potential contact surface $\partial\Omega_i^c$. These latter contact surfaces are not necessarily in contact, but are susceptible to get in contact. When they are not, they are considered as Neumann boundaries with zero prescribed traction. The fact that it is not possible to exactly know a priori which surface will get in contact makes contact problems non-linear.

[1] eXtended Finite Element Method.
[2] See Section 3.4.1.

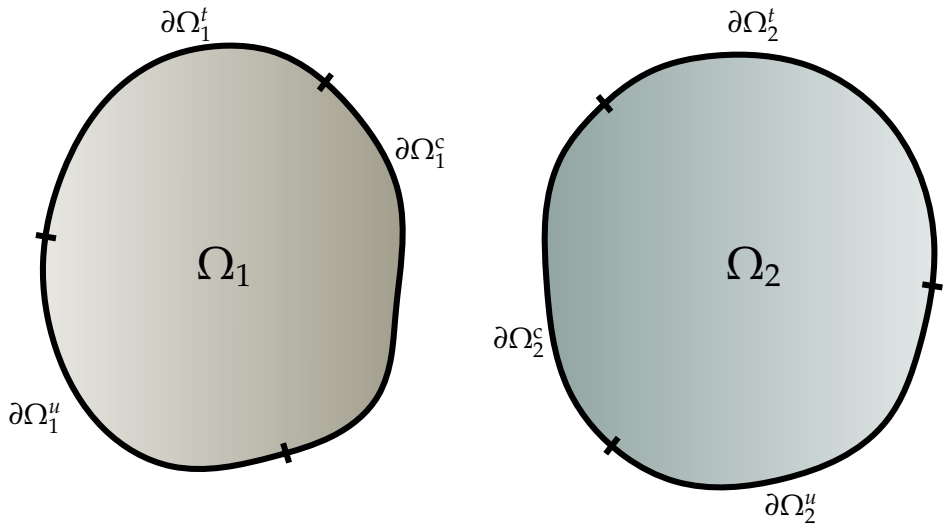

Figure 3.1: Schematic representation of a two-body contact problem.

3.2.1 Static equilibrium

Let us write the static equilibrium conditions in Ω_1 and Ω_2 to begin with. Static equilibrium implies that in any subsystem $\widetilde{\Omega} \subset \Omega_i$ ($i \in \{1,2\}$), forces must be balanced. We denote $\underline{f}$ the volume forces and $\underline{T}$ the surface forces on $\widetilde{\Omega}$ and write:

$$\int_{\widetilde{\Omega}} \underline{f}\, d\Omega + \int_{\partial\widetilde{\Omega}} \underline{T}\, dS = 0. \tag{3.1}$$

Cauchy's stress tensor $\underline{\underline{\sigma}}$ is introduced considering the outward unit normal vector $\underline{n}$ to the boundary $\partial\widetilde{\Omega}$:

$$\underline{T} = \underline{\underline{\sigma}} \cdot \underline{n} \tag{3.2}$$

and using Ostrogradsky's divergence theorem,

$$\int_{\widetilde{\Omega}} \left(\underline{f} + \underline{\mathrm{div}}(\underline{\underline{\sigma}}) \right) d\Omega = 0. \tag{3.3}$$

Because this equality holds for any $\widetilde{\Omega} \subset \Omega_i$, and considering the boundary conditions, we can write locally:

$$\underline{\mathrm{div}}(\underline{\underline{\sigma}}) + \underline{f} = 0 \text{ in } \Omega_i \tag{3.4}$$

$$\underline{\underline{\sigma}} \cdot \underline{n} = \underline{T_0} \text{ on } \partial\Omega_i^t \tag{3.5}$$

$$\underline{u} = \underline{u_0} \text{ on } \partial\Omega_i^u \tag{3.6}$$

where $\underline{u}$ is the displacement field. Here, the material behavior is assumed linear elastic, so the stress tensor verifies the following constitutive equation introducing a fourth-order elasticity tensor $\underline{\underline{\underline{\underline{C}}}}$:

$$\underline{\underline{\sigma}} = \underline{\underline{\underline{\underline{C}}}} : \underline{\underline{\varepsilon}} \tag{3.7}$$

where $\underline{\underline{\varepsilon}}$ is the linearized strain tensor:

$$\underline{\underline{\varepsilon}} = \frac{1}{2}\left(\underline{\underline{\nabla u}} + \underline{\underline{\nabla u}}^T\right). \tag{3.8}$$

When damage is considered, the material behavior is affected by the evolution of the damage variable d, and in this case:

$$\underline{\underline{\sigma}} = \underline{\underline{\underline{\underline{C}}}}(d) : \underline{\underline{\varepsilon}} \tag{3.9}$$

with, in the following:

$$\underline{\underline{\sigma}} = (1-d)\underline{\underline{\underline{\underline{C}}}}(0) : \underline{\underline{\varepsilon}}. \tag{3.10}$$

3.2.2 Frictional contact

Then we write the frictional contact conditions expressed on the surfaces $\partial\Omega_i^c$. Let us consider a point $\underline{x_1^c} \in \partial\Omega_1^c$ and chose a projection operator[3] $\underline{\Pi}$ from the surface $\partial\Omega_1^c$ onto the counterpart surface $\overline{\partial\Omega_2^c}$. Let us define the displacement discontinuity $[\![\underline{u}]\!]_c$ as:

$$[\![\underline{u}(\underline{x_1})]\!]_c = \underline{u}(\underline{x_1}) - \underline{u}(\underline{\Pi}(\underline{x_1})) \tag{3.11}$$

and the normal displacement discontinuity $[\![u_n]\!]_c$:

$$[\![u_n]\!]_c = [\![\underline{u}]\!]_c \cdot \underline{n_2} \tag{3.12}$$

where $\underline{n_2}$ is the unit normal vector to the surface $\partial\Omega_2^c$ at the point $\underline{\Pi}(\underline{x_1})$. In order to enforce the non-interpenetration, the normal displacement discontinuity must verify:

$$g_n = [\![u_n]\!]_c + g_0 \geq 0 \tag{3.13}$$

g_0 and g_n being the initial and current normal gaps. In addition, contact can only transmit compressive stress so the contact pressure can only be negative:

$$\sigma_n(\underline{x_1}) = \left(\underline{\underline{\sigma}}(\underline{\Pi}(\underline{x_1})) \cdot \underline{n_2}\right) \cdot \underline{n_2} \leq 0. \tag{3.14}$$

A last condition states that either the normal gap is zero, that means the surfaces are in contact and the normal pressure can be negative, or there is no contact and the contact pressure is necessarily zero. This set of conditions are known as Hertz-Signorini-Moreau's conditions and usually written:

$$[\![u_n]\!]_c + g_0 \geq 0 \tag{3.15}$$

$$\sigma_n \leq 0 \tag{3.16}$$

$$([\![u_n]\!]_c + g_0)\,\sigma_n = 0. \tag{3.17}$$

The possible values for (g_n, σ_n) allowed by these conditions are depicted in Figure 3.2a. In addition, friction is assumed to follow Coulomb's law. Let us introduce Coulomb's coefficient of friction μ

[3] This projection operator should be chosen so as to give for any point from $\partial\Omega_1^c$ the closest point from $\partial\Omega_2^c$, which is not always trivial [Yastrebov 2011].

and denote $\underline{\tau}$ the tangential contact traction:

$$\underline{\tau} = \underline{\underline{\sigma}} \cdot \underline{n_2} - \sigma_n \underline{n_2}. \tag{3.18}$$

The tangential part of displacement discontinuity is denoted $[\![\underline{u_t}]\!]_c$ and Coulomb's friction law reads:

$$\exists \dot{\lambda} \geq 0 \text{ s.t. } [\![\underline{\dot{u}_t}]\!]_c = \dot{\lambda} \frac{\underline{\tau}}{\|\underline{\tau}\|} \tag{3.19}$$

$$\|\underline{\tau}\| - \mu|\sigma_n| \leq 0 \tag{3.20}$$

$$[\![\underline{\dot{u}_t}]\!]_c \left(\|\underline{\tau}\| - \mu|\sigma_n|\right) = 0. \tag{3.21}$$

These conditions impose that the tangential relative displacement is colinear with the tangential contact traction whose norm is necessarily lower than a threshold proportional to the normal stress. Sliding may occur only if the threshold is reached.

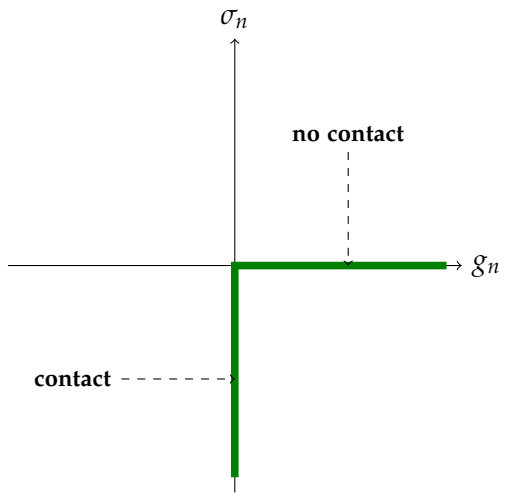

(a) Normal gap and contact pressure values verifying Hertz-Signorini-Moreau's conditions.

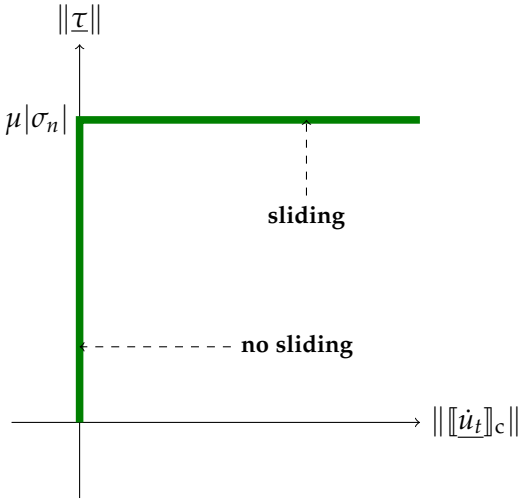

(b) Tangential stress and sliding velocity verifying Coulomb's friction law.

Figure 3.2: Representation of Hertz-Signorini-Moreau's contact conditions and Coulomb's friction law.

3.2.3 Wear evolution

Finally, the contact surface geometry is assumed to evolve according to wear evolution. We explore the use of different wear laws. The first possibility considered is an energy-based wear law which states that wear volume is proportional to the total amount of dissipated energy. We use a local version of this law, which relates the local wear rate $\dot{h}$ (namely the wear depth evolution rate) to the surface density of power dissipated by frictional forces. This law uses an energy wear coefficient α and reads:

$$\dot{h} = \alpha \underline{\tau} \cdot [\![\underline{\dot{u}_t}]\!]_c. \tag{3.22}$$

The other possibility explored is the use of a damaged-based wear model using the thick level set approach as described in Chapter 2. We recall the expression for the local wear rate:

$$\dot{h}_i = \begin{cases} v_n & \text{if } l = l_c \\ 0 & \text{if } l < l_c \end{cases} \tag{3.23}$$

where v_n is the propagation velocity of the level set and l and l_c are respectively the current thickness and the critical thickness of the partially damaged layer. The propagation increment Δa of the level set over a time step Δt is computed through the resolution of a system of the form:

$$\boldsymbol{K}\,\boldsymbol{\Delta a} = \boldsymbol{\Delta F} \tag{3.24}$$

where possible expressions for $\boldsymbol{K}$ and $\boldsymbol{\Delta F}$ are given in Chapter 2.

3.2.4 Time scales decoupling

The elastic deformation response of a solid to a certain loading and the evolution of wear following repeated contacts operate on very different time scales. Wear processes are indeed very slow with respect to the deformation rates. Consequently, a very convenient yet appropriate assumption is that wear is sufficiently slow to decouple the resolution of the wear problem from the resolution of the deformation problem. This is equivalent to introducing two time scales: a *short time scale* accounting for the deformation of the solids and a *long time scale* describing wear evolution.

This principle was formalized by Lengiewicz and Stupkiewicz and is generally assumed in most numerical studies on wear, although often not explicitly stated [Lengiewicz and Stupkiewicz 2012]. Lengiewicz and Stupkiewicz consider the existence of three configurations describing a wear problem: an initial, undeformed and unworn configuration; a current, deformed and worn configuration; and an intermediate, worn but undeformed configuration. This allows to properly take into account the surface geometry evolution due to wear. The mapping between the initial and intermediate configurations is governed by the wear evolution law, whereas static equilibrium, boundary conditions (including contact and friction) and constitutive equations are used between the intermediate and current configurations.

These two transformations are then assumed to operate in a decoupled manner, on different time scales. Let us denote t the variable representing physical time, whose evolution describes the short time scale. In the case of fretting, we chose as a pseudo-time variable the fretting cycle number n, whose evolution governs the long time scale. Denoting N_{cyc} the total number of fretting cycles, the pseudo-time variable n is a real number lying within the interval $[0, N_{\text{cyc}}]$. For the resolution of the wear evolution problem, this interval is decomposed into a set of K time steps $(n_k)_{1\leq k\leq K}$. The cycle increment Δn between two wear resolution steps is referred to as the *cycle jump*, or *acceleration factor*:

$$\Delta n = n_{k+1} - n_k. \tag{3.25}$$

The deformation problem is analyzed at fixed n and fixed wear over the interval $t \in [t_0(n), t_0(n) + T]$ using a time increment Δt, T being the cycle period. This reduces the problem to a classical frictional contact problem. Over this cycle, the frictional contact problem is solved for every time step t_j. Wear rate is evaluated at the end of the cycle as a postprocessing quantity of the short time scale

resolution. Instead of considering the instantaneous wear rate $\dot{h} = \frac{\partial h}{\partial t}$, we use the cyclic wear rate $\partial_n h = \frac{\partial h}{\partial n}$ calculated as:

$$\partial_n h(x,n) = \frac{\partial h}{\partial n}(x,n) = \int_{t_0(n)}^{t_0(n)+T} \dot{h}(x,t)\, dt. \tag{3.26}$$

The cyclic wear rate, hereafter simply designated as "wear rate", is defined as the wear depth increment generated per fretting cycle.

The two time steps principle is schematically depicted in Figure 3.3. This assumption is valid if wear evolution over the pseudo-time step Δn is small enough to be considered negligible on the deformation response.

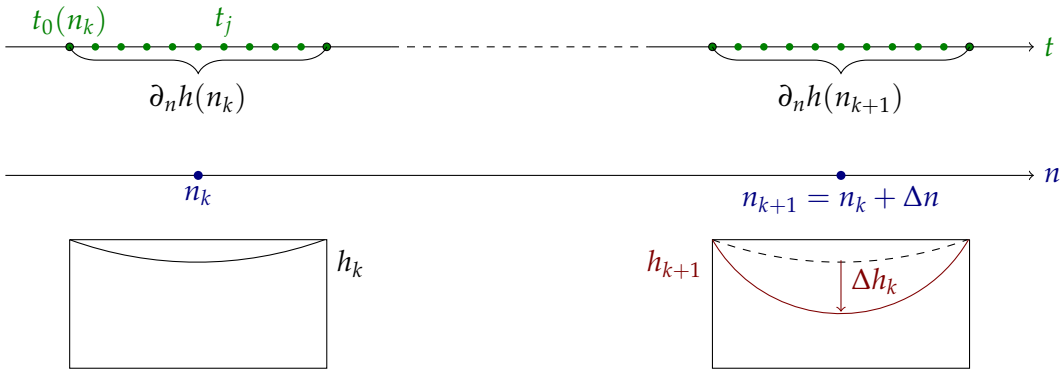

Figure 3.3: Schematic representation of the two time scales principle.

As outlined by Lengiewicz and Stupkiewicz (2012), this two time scales assumption is very convenient because it allows a great flexibility in the choice of resolution schemes for the wear problem. This aspect is specifically tackled in Chapter 4. They also mention that adapting this principle to path-dependent material behaviors such as elastoplasticity is not straightforward except for the case $\Delta n = 1$. Specific strategies need to be introduced to represent the evolution of internal variables over the cycle jump. An attempt to deal with this issue is proposed in Chapter 5.

3.3 Preliminary computations

3.3.1 Presentation of the loading case

In this section, we propose to compute the initial wear rate on a plane surface subjected to a surface loading, reflecting a contact with a cylinder in fretting motion. We consider the plane body to be a semi-infinite elastic solid occupying the two-dimensional half-space $y \leq 0$. In this case, the two time scales principle may be employed to derive wear rate, based on simple solutions for the set of governing equations. Let us consider that the free surface is subjected to a pressure field reflecting a hertzian contact. The pressure distribution is of the form:

$$p(x,t) = p_{\max}\sqrt{1 - \left(\frac{x - \delta(t)}{a}\right)^2} \text{ if } |x - \delta(t)| \leq a \tag{3.27}$$

where a is the contact half-width and $p_{\max}$ is the maximum contact pressure. The tangential displacement δ is assumed to be cyclic of amplitude δ_0. The evolution of this displacement over time is depicted in Figure 3.4. This tangential displacement is accompanied with a tangential surface traction obeying Coulomb's friction law under the gross slip assumption:

$$q(x,t) = \frac{\dot{\delta}(t)}{|\dot{\delta}(t)|}\mu p(x,t) \tag{3.28}$$

where μ is Coulomb's coefficient of friction. Considering such cyclic loading, we seek to derive wear rate using one or other wear model. In the following, numerical applications are carried out with reference to experimental tests realized by Marc (2018). In this regard, the following values are used: normal force $F_n = 3\ \mathrm{N\,mm^{-1}}$, tangential displacement of amplitude $\delta_0 = 80$ µm, coefficient of friction $\mu = 0.9$. Considering a contact with a $R = 4.85$ mm radius cylinder and considering the elastic properties $E = 200 \times 10^3$ MPa and $\nu = 0.3$ corresponding to the 304L and 316L stainless steels used by Marc (2018), Hertz's theory gives $a = 9.2 \times 10^{-3}$ mm and $p_{\max} = 208$ MPa. Moreover, using an energy wear law, the wear coefficient is $\alpha = 3.14 \times 10^{-8}\ \mathrm{mm^3\,mJ^{-1}}$. Regarding the damage-based wear model, we chose for the parameters of the thick level set a critical length $l_c = 10 \times 10^{-3}$ mm and an initial level set depth $a_{\mathrm{ini}} = 0.5 \times 10^{-3}$ mm – resulting in an initial maximum damage $d = 0.05$. The damage law parameters are set to $Y_0 = 0$ MPa, $Y_1 = 300$ MPa. Thus chosen, this set of parameters leads to a level set propagation rate of the same order of magnitude as wear evolution rate in the first test case with an energy law.

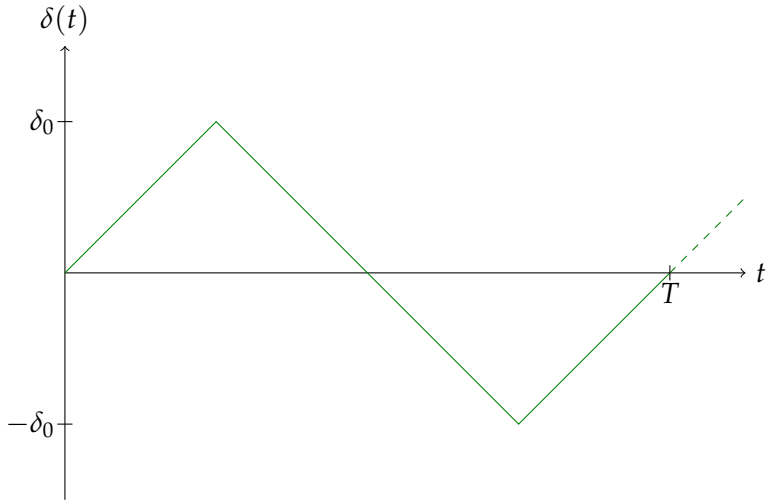

Figure 3.4: Cyclic tangential displacement $\delta(t)$.

3.3.2 Energy-based wear law

Using the energy wear law (3.22), the instantaneous wear rate is:

$$\dot{h}(x,t) = \alpha q(x,t)\dot{\delta}(t) \tag{3.29}$$

which enables to compute the cyclic wear rate:

$$\partial_n h(x) = \int_0^T \dot{h}(x,t)\, dt. \tag{3.30}$$

Depending on the position x on the surface, three different situations are distinguished. If $|x| \leq \langle \delta_0 - a \rangle_+$, this point undergoes two full loading passes per cycle (one way and back). Then,

$$\begin{aligned}
\int_0^T \dot{h}(x,t)\, dt &= \alpha\mu p_{\max} \int_0^T \sqrt{1 - \left(\frac{x-\delta(t)}{a}\right)^2} |\dot{\delta}(t)|\, dt \\
&= 2\alpha\mu p_{\max} \int_{-a}^{a} \sqrt{1 - \left(\frac{x}{a}\right)^2}\, dx \\
&= 2\alpha\mu p_{\max} a \int_{-\pi/2}^{\pi/2} \cos^2(u)\, du \\
&= \alpha\mu p_{\max} a \int_{-\pi/2}^{\pi/2} (1 + \cos(2u))\ du
\end{aligned}$$

which gives:

$$\forall |x| \leq \langle \delta_0 - a \rangle_+,\ \partial_n h(x) = \alpha\mu p_{\max} a \pi. \tag{3.31}$$

Else, if $\langle \delta_0 - a \rangle_+ \leq |x| \leq \delta_0 + a$, this point sees only a part of the loading, yielding:

$$\begin{aligned}
\int_0^T \dot{h}(x,t)\, dt &= 2\alpha\mu p_{\max} \int_{|x|-\delta_0}^{a} \sqrt{1 - \left(\frac{x}{a}\right)^2}\, dx \\
&= \alpha\mu p_{\max} a \int_{-\arcsin\left(\frac{|x|-\delta_0}{a}\right)}^{\pi/2} (1 + \cos(2u))\ du
\end{aligned}$$

which gives:

$$\forall \langle \delta_0 - a \rangle_+ \leq |x| \leq \delta_0 + a,\ \partial_n h(x) = \alpha\mu p_{\max} a \left(\frac{\pi}{2} - \arcsin\left(\frac{|x|-\delta_0}{a}\right) - \frac{1}{2}\frac{|x|-\delta_0}{a}\sqrt{1 - \left(\frac{|x|-\delta_0}{a}\right)^2} \right). \tag{3.32}$$

Finally,

$$\forall |x| \geq \delta_0 + a,\ \partial_n h(x) = 0. \tag{3.33}$$

The resulting wear rate profile is represented in Figure 3.5.

This wear rate profile applies to a plane, unworn surface. As wear occurs, the surface geometry evolves and the pressure distribution changes accordingly, which in turn modifies the wear rate profile.

3.3.3 Damage-based wear model

An equivalent approach can be followed considering the damage-based wear model with the thick level set approach derived in Section 2.3.2. As already stated in Section 1.3.3, the stress fields

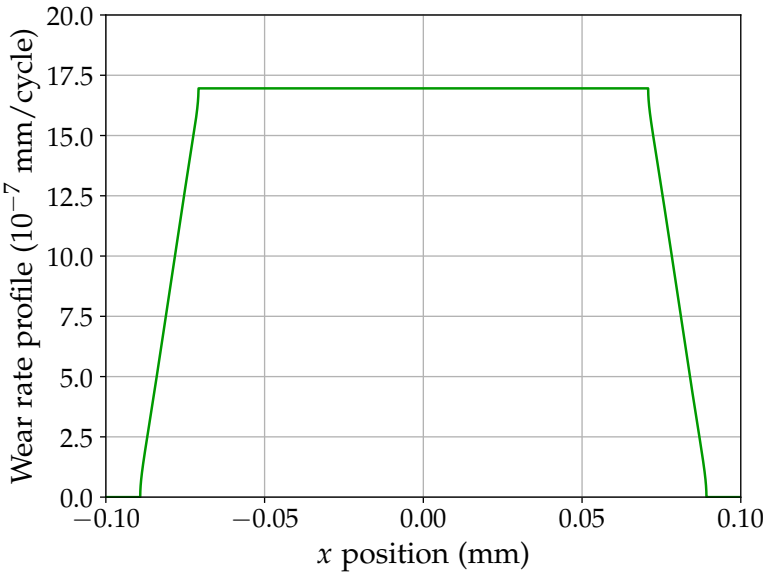

Figure 3.5: Wear rate profile derived for a hertzian contact. The parameter values used correspond to a fretting test conducted by Marc (2018).

generated in the bulk material by the considered loading can be integrated as:

$$\sigma_{xx}(x,y,t) = -\frac{2y}{\pi}\int_{-a+\delta(t)}^{a+\delta(t)} \frac{p(s,t)(x-s)^2}{((x-s)^2+y^2)^2}ds - \frac{2}{\pi}\int_{-a+\delta(t)}^{a+\delta(t)} \frac{q(s,t)(x-s)^3}{((x-s)^2+y^2)^2}ds \tag{3.34}$$

$$\sigma_{yy}(x,y,t) = -\frac{2y^3}{\pi}\int_{-a+\delta(t)}^{a+\delta(t)} \frac{p(s,t)}{((x-s)^2+y^2)^2}ds - \frac{2y^2}{\pi}\int_{-a+\delta(t)}^{a+\delta(t)} \frac{q(s,t)(x-s)}{((x-s)^2+y^2)^2}ds \tag{3.35}$$

$$\sigma_{xy}(x,y,t) = -\frac{2y^2}{\pi}\int_{-a+\delta(t)}^{a+\delta(t)} \frac{p(s,t)(x-s)}{((x-s)^2+y^2)^2}ds - \frac{2y}{\pi}\int_{-a+\delta(t)}^{a+\delta(t)} \frac{q(s,t)(x-s)^2}{((x-s)^2+y^2)^2}ds \tag{3.36}$$

$$\sigma_{zz}(x,y,t) = \nu(\sigma_{xx}(x,y,t) + \sigma_{yy}(x,y,t)). \tag{3.37}$$

These integrals are computed numerically using the SciPy library of Python. We prescribe the same tangential displacement $\delta(t)$ as previously (Figure 3.4) and solve the problem incrementally.

Initialization

As a first step, the level set front Γ_0 is discretized into n_s nodes $(s_i)_{1\leq i\leq n_s}$, and is initialized in the half-plane at a certain depth a_{ini} from the surface. This gives access to the initial damage field $d(t_0)$ which directly depends on the distance ϕ to Γ_0:

$$\forall \phi \leq 0,\ d(\phi) = 0 \tag{3.38}$$

$$\forall \phi \in [0, l_c],\ d(\phi) = \frac{\phi}{l_c} \tag{3.39}$$

$$\forall \phi \geq l_c,\ d(\phi) = 1. \tag{3.40}$$

Time step increments

Then, the problem is solved recursively. Suppose we know the damage field at time step t_j. At time step t_{j+1}, the thermodynamic force Y is:

$$\begin{aligned} Y(t_{j+1}) &= \frac{1}{2}\underline{\underline{\varepsilon}}(t_{j+1}) : \underline{\underline{\underline{\underline{C}}}}(0) : \underline{\underline{\varepsilon}}(t_{j+1}) \\ &= \frac{1}{2(1-d(t_j))}\underline{\underline{\sigma}}(t_{j+1}) : \underline{\underline{\varepsilon}}(t_{j+1}) \\ &= \frac{1}{2(1-d(t_j))^2 E}\left((1+\nu)\underline{\underline{\sigma}}(t_{j+1}) : \underline{\underline{\sigma}}(t_{j+1}) - \nu \mathrm{Tr}(\underline{\underline{\sigma}}(t_{j+1}))^2\right). \end{aligned}$$

This also enables to calculate the thermodynamic force increment ΔY over the time step:

$$\Delta Y(t_{j+1}) = Y(t_{j+1}) - Y(t_j). \tag{3.41}$$

The matrices $\boldsymbol{K}$ and $\boldsymbol{\Delta F}$ need to be built at each time step, where

$$K_{ij} = \int_{\Gamma_0}\int_0^l Y(\phi,s)d'(\phi)\left(1-\frac{\phi}{r(s)}\right)d\phi\, N_i(s)N_j(s)\,ds \tag{3.42}$$

$$\Delta F_i = \int_{\Gamma_0}\int_0^l \frac{Y^2(\phi,s)}{Y_1(Y_0+d(\phi)Y_1)}\langle \Delta Y(\phi,s)\rangle_+ \left(1-\frac{\phi}{r(s)}\right)d\phi\, N_i(s)\,ds. \tag{3.43}$$

We make the simplifying assumption that the level set is flat, so $r(s) \to +\infty$, and $d'(\phi) = 1/l_c$ is constant, following the linear prescribed form assumed for $d(\phi)$. The basis functions N_i are chosen linear as depicted in Figure 2.8. The terms of the matrices may thus be simplified into

$$K_{ij} = \frac{1}{l_c}\int_{\Gamma_0}\int_0^l Y(\phi,s)\,d\phi\, N_i(s)N_j(s)\,ds \tag{3.44}$$

$$\Delta F_i = \int_{\Gamma_0}\int_0^l \frac{Y^2(\phi,s)}{Y_1(Y_0+d(\phi)Y_1)}\langle \Delta Y(\phi,s)\rangle_+ \,d\phi\, N_i(s)\,ds \tag{3.45}$$

with

$$\forall 1 \le i \le n_s,\ N_i(s) = \begin{cases} 1-\frac{|s-s_i|}{ds} & \text{if } |s-s_i| \le ds \\ 0 & \text{if } |s-s_i| \ge ds. \end{cases} \tag{3.46}$$

The integrals are computed numerically using the SciPy library of Python as well. Once the matrices $\boldsymbol{K}$ and $\boldsymbol{\Delta F}$ are built, the level set propagation increment $\boldsymbol{\Delta a}$ over the time step is computed through the resolution of the following system:

$$\boldsymbol{K}\,\boldsymbol{\Delta a} = \boldsymbol{\Delta F}. \tag{3.47}$$

The level set position is finally updated accordingly, which gives the evolution of the damage field.

Results

This iterative computation process is applied to the same test case as for the energy wear law. Here, 10,000 loading cycles are computed during which the level set progressively propagates until the point where wear should onset – in other words, a critical damage $d = 1$ is reached. Figure 3.6

depicts the evolution of the level set position throughout the cycles. The corresponding damage fields are depicted in Figure 3.7. Finally, the evolution of the maximum damage value is shown in Figure 3.8. These results show the progressive evolution of the damage field evolution throughout the loading cycles following the level set displacement.

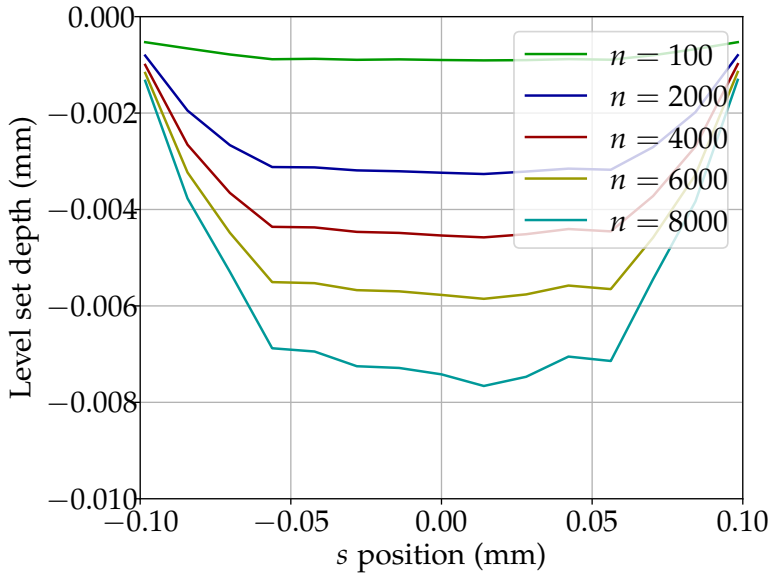

Figure 3.6: Evolution of the level set position using a thick level set damage model on a simple hertzian fretting loading.

In this test case, wear rate is not computed as such. The process described indeed only gives access to the level set propagation until the moment wear onsets. In the aftermath, the occurrence of wear modifies the surface geometry and the resulting contact is no longer hertzian. Consequently, the simple approach proposed here is no longer valid. Since wear evolution results from level set propagation, the propagation profiles of the level set however give an idea of what wear profiles would look like if they were actually computed. In this regard, the primary results obtained on this simple test case with the thick level set approach are encouraging in terms of the ability of the model to represent fretting wear problems. It is demonstrated here that the model enables to represent the progressive accumulation of damage in a near-surface layer prior to wear, which results in the existence of an incubation time before wear onsets.

In order to go further in the computation of wear evolution, numerical processes enabling to calculate contact pressure evolution together with surface geometry evolution are required. This will extend the computation processes proposed to non-hertzian situations. For this purpose, the finite element method is used.

3.4 Finite element modeling

3.4.1 Variational formulation

The set of governing equations derived in Section 3.2 need to be written under a weak form in order to be solved using the finite element method. In virtue of the decoupling assumed between the deformation problem and the wear evolution problem, we only need to solve a classical frictional contact problem. Here, the imposed constraints are enforced using the Lagrange multipliers

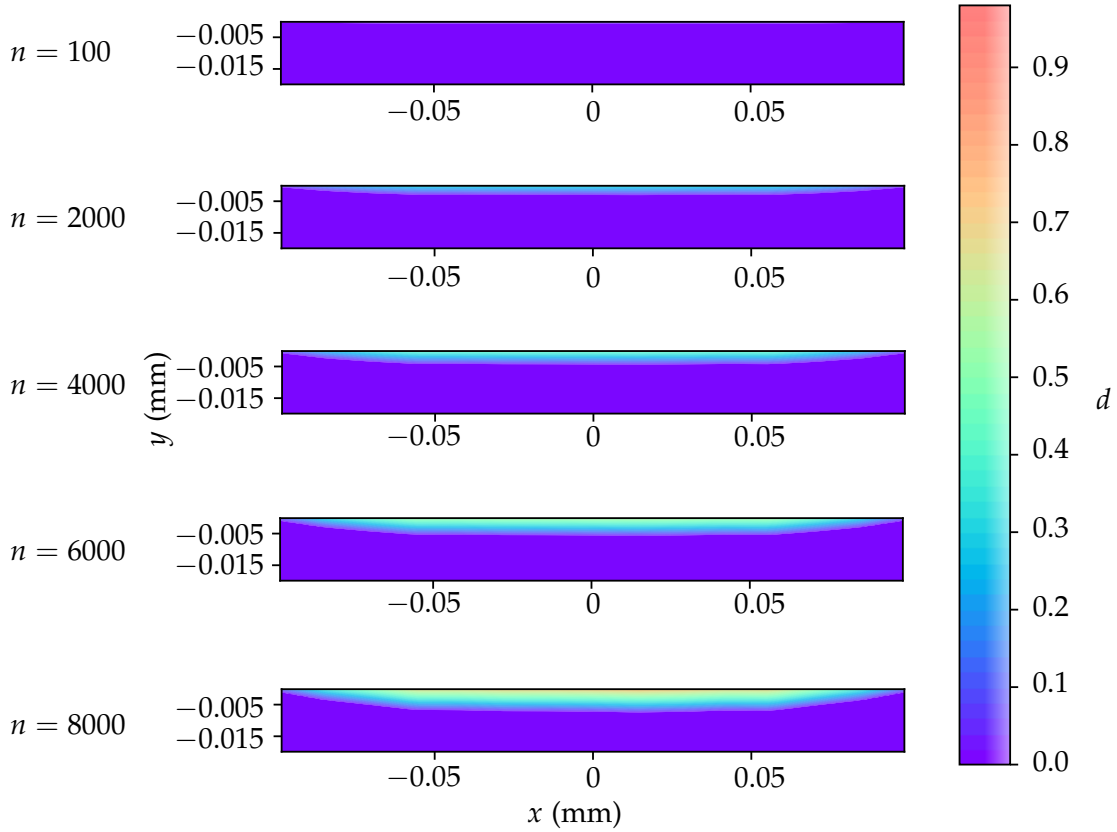

Figure 3.7: Evolution of the damage field following level set progression on a simple hertzian fretting loading.

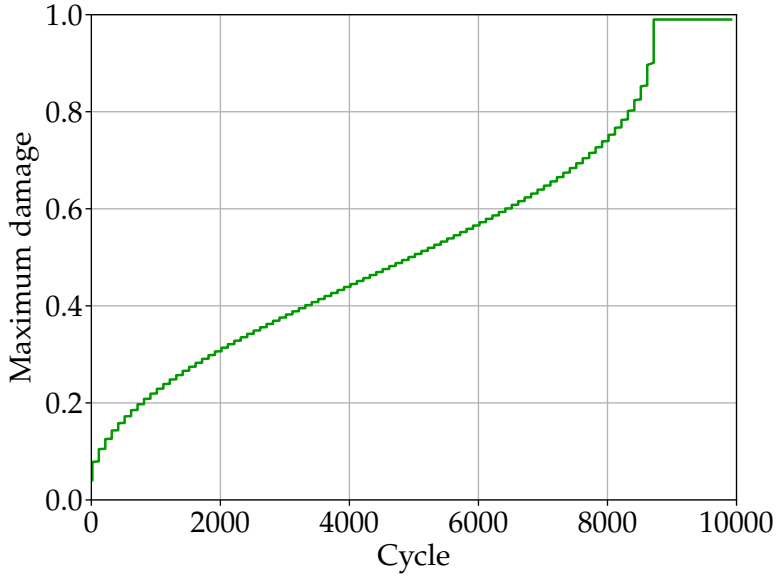

Figure 3.8: Evolution of the maximum damage value on a simple hertzian fretting loading with a thick level set damage model.

method. Let us consider a virtual displacement field $\underline{u^*} \in \mathcal{U}$ with:

$$\mathcal{U} = \{\underline{u^*} \mid \underline{u^*} = 0 \text{ on } \partial\Omega_1^u \cup \partial\Omega_2^u\}. \tag{3.48}$$

Considering the static equilibrium equation with zero volume force $\underline{f}$ for simplicity, the problem is transformed into finding the displacement field $\underline{u}$ verifying:

$$\forall \underline{u^*} \in \mathcal{U},\ \int_{\Omega_1 \cup \Omega_2} \underline{\mathrm{div}}(\underline{\underline{\sigma}}(\underline{u})) \cdot \underline{u^*}\, d\Omega = 0 \tag{3.49}$$

which becomes using the divergence theorem:

$$\forall \underline{u^*} \in \mathcal{U},\ \int_{\Omega_1 \cup \Omega_2} \underline{\underline{\sigma}}(\underline{u}) : \underline{\underline{\nabla u^*}}\, d\Omega = \int_{\partial\Omega_1 \cup \partial\Omega_2} \left(\underline{\underline{\sigma}}(\underline{u}) \cdot \underline{n}\right) \cdot \underline{u^*}\, dS. \tag{3.50}$$

Because $\underline{\underline{\sigma}}$ is a symmetric tensor,

$$\underline{\underline{\sigma}} : \underline{\underline{\nabla u^*}} = \underline{\underline{\sigma}} : \underline{\underline{\nabla u^{*S}}} = \underline{\underline{\sigma}} : \underline{\underline{\varepsilon}}(\underline{u^*}). \tag{3.51}$$

For simplicity, let us assume we have frictionless contact so only the normal contact conditions on the surfaces $\partial\Omega_i^c$ are considered. The problem now reads:

$$\forall \underline{u^*} \in \mathcal{U},\ \int_{\Omega_1 \cup \Omega_2} \underline{\underline{\sigma}}(\underline{u}) : \underline{\underline{\varepsilon}}(\underline{u^*})\, d\Omega = \int_{\partial\Omega_1^t \cup \partial\Omega_2^t} \underline{T_0} \cdot \underline{u^*}\, dS + \int_{\partial\Omega_1^u \cup \partial\Omega_2^u} \underline{\lambda_u} \cdot \underline{u_0}\, dS + \int_{\partial\Omega_1^c \cup \partial\Omega_2^c} \lambda_n u_n^*\, dS \tag{3.52}$$

where $\underline{\lambda_u}$ and λ_n are the Lagrange multipliers respectively associated with Dirichlet boundary conditions and normal contact conditions. This variational equation needs to be solved for the unknowns $\left(\underline{u}, \underline{\lambda_u}, \lambda_n\right)$ considering the additional constraints that must hold for any virtual Lagrange multiplier $\underline{\lambda_u^*}$ and $\lambda_n^* \leq 0$:

$$\int_{\partial\Omega_1^u \cup \partial\Omega_2^u} (\underline{u} - \underline{u_0}) \cdot \underline{\lambda_u^*}\, dS = 0 \tag{3.53}$$

$$\int_{\partial\Omega_1^c \cup \partial\Omega_2^c} (\llbracket u_n \rrbracket_c + g_0)\lambda_n^*\, dS = 0. \tag{3.54}$$

The introduction of a spatial discretization together with basis functions for the unknown fields leads to the formulation of this problem under a matrix form. Regarding the contact conditions enforcement, different formulations exist [Wriggers 2006]. The simplest one is a node-to-node formulation in which contact conditions are expressed on node pairs from each of the opposing surfaces. This formulation however requires to have conformal meshes for the opposing surfaces with nodes facing each other.

Node-to-segment formulations overcome this drawback by enforcing contact conditions on contact elements composed of an *impactor* node from one surface and a *target* element from the opposing one. The impactor node is projected onto the target element in order to evaluate the normal gap. This results in the formulation of a relation between the displacement of the impactor node and the displacements of the nodes from the target surface. These methods, albeit widely used in finite element codes, are known to pass with little success the patch test which consists in transmitting a

uniform pressure through a plane contact [Wriggers 2006].

The patch-test performances are improved using a surface-to-surface contact formulation, such as mortar methods [Popp and Wall 2014]. In mortar methods, contact conditions are enforced on contact elements composed of two opposing surface elements on which the Lagrange multipliers are interpolated using a specific set of basis functions. These basis functions may be the same as the displacement's, but it was shown that a wise alternative choice ensures the verification of the *inf-sup* or Babuška-Brezzi condition, leading to the so-called dual mortar method [Wohlmuth 2001].

Node-to-segment contact formulation and mortar contact formulation are briefly presented in Appendix A.

Unless otherwise specified, node-to-segment contact formulations will be used in the following developments. It should be kept in mind that the possibly non-smooth contact pressure fields computed using these methods may be a source of error. This is of particular importance in the resolution of wear problems since wear evolution laws depend more or less directly on the contact pressure field, and will be discussed in Chapter 4.

3.4.2 Presentation of the finite element model

Reference experimental tests

Throughout the document, fretting wear simulations are conducted in reference to experimental tests conducted by Marc (2018). They carried out fretting tests on a cylinder-plane contact at room temperature, either in a dry air environment or in a lithium-boron aqueous solution (Figure 3.9). The cylinder is made of 316L stainless steel, while the plane is made of 304L stainless steel. The cylinder has a radius $R = 4.85$ mm. A normal load is applied and an oscillating tangential displacement at frequency $f = 5$ Hz is enforced. Different tests are run at various normal loads between 2 N/mm and 5 N/mm, displacement amplitudes between 40 µm and 160 µm, and number of fretting cycles between 25,000 and 1,500,000.

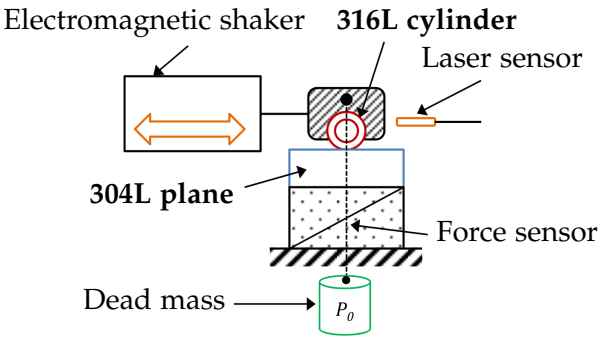

Figure 3.9: Experimental setup for the fretting wear tests [Marc 2018].

The tangential force and horizontal displacement are recorded through the tests. Coulomb's coefficient of friction is inferred from the measures using the friction energy dissipation. After the tests, the depth in the three-dimensional wear scars is measured and averaged along the cylinder axis to get equivalent wear profiles. The tests conducted in a dry air environment yield bilateral wear on both the plane and cylinder surfaces, while water environment tests only show wear on the plane surface. The wear volume is measured which enables the determination of a friction energy wear coefficient.

Finite element model

The finite element computations are conducted using the finite element code Cast3M. A two-dimensional plane-strain finite element model is defined using 4-nodes bilinear elements. In the vicinity of the contact zone, the element size is around 6 µm. By similarity with Marc's experimental tests, the cylinder radius is 4.85 mm. The material behavior is assumed to be linear elastic.

A zero-displacement condition is imposed on the bottom and side lines of the plane, and the vertical displacement of all the cylinder top line nodes is imposed to be equal (thus preventing rigid body rotations). Moreover, a uniformly distributed normal pressure is applied on top of the cylinder to account for the normal load F_n, and a cyclic triangular horizontal displacement is imposed on the cylinder with an amplitude δ_0. Frictional contact conditions are enforced at the interface using the Lagrange multipliers method and a node-to-segment formulation. The contact surface of the cylinder is defined as the impactor surface while the top surface of the plane is defined as the target surface. The finite element mesh is represented in Figure 3.10.

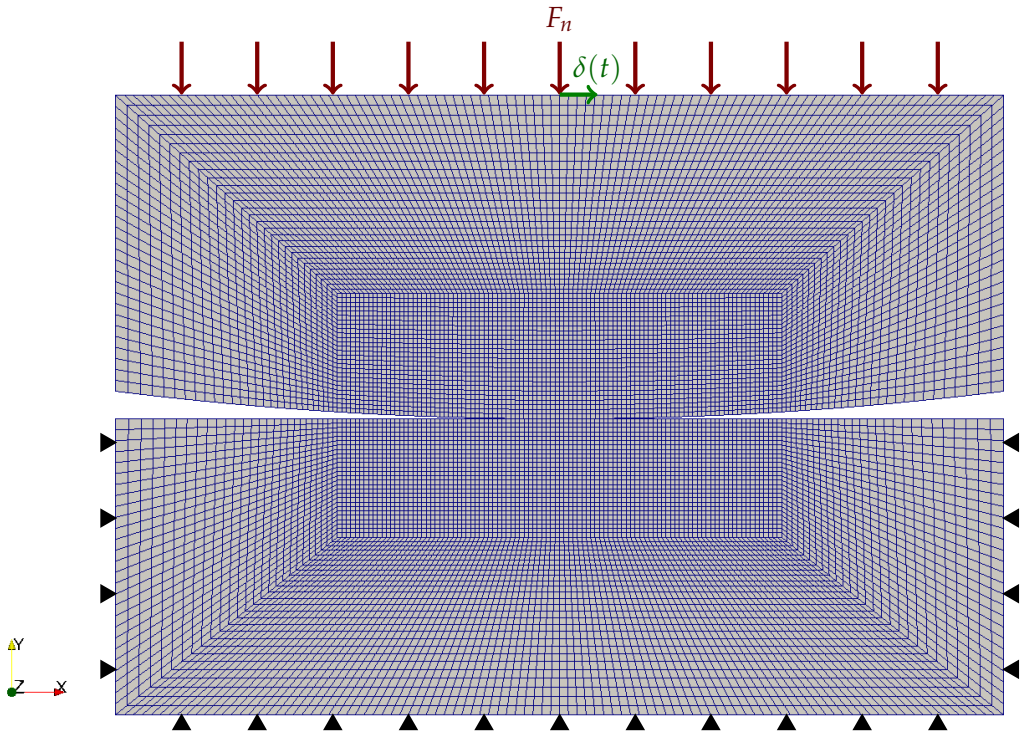

Figure 3.10: Finite element mesh of the cylinder-plane contact model.

Preliminary computations are performed using this finite element model. A single displacement cycle is imposed to begin with, in order to illustrate the ability of the model to represent the cyclic frictional contact problem. This preliminary computation is performed using the same elastic material properties as in Section 3.3. The coefficient of friction is $\mu = 0.95$ and the cylinder is subjected to a constant normal force[4] $F_n = 15$ N/mm and a displacement cycle of amplitude $\delta_0 = 80$ µm. The computed cycle is decomposed into 128 time steps. Prior to starting the tangential displace-

[4]The normal force is expressed as a force per unit out-of-plane length due to the 2D assumption. In the same way, the dissipated energy is expressed as an energy per unit out-of-plane length.

ment loading, 10 initial time steps are performed to progressively initiate the normal loading – this progressive initialization is necessary because of the path-dependent nature of friction.

As a first step, the normal and tangential contact tractions are computed on the first time step following the start of tangential displacement (Figure 3.11). The normal contact pressure profile has a typical hertzian shape, and the tangential stress indicates that the contact is in gross slip. The strain and stress fields induced by this loading are computed and displayed on the first time step as well. Figure 3.12 and Figure 3.13 respectively show the $xx-$, $yy-$, $xy-$ and $zz-$components of the strain tensor and stress tensor. The stress state computed analytically on a semi-infinite elastic body (Figure 1.10) is retrieved. Expected observations can be made on the strain and stress fields. First, the contact effectively yields compressive normal yy stress. Moreover, due to the frictional relative displacement, the edges of the contact zone on each solid undergoes tangential xx stress. The leading edge (front edge in the solid's motion direction) endures tension while the trailing edge endures compression. In accordance with the plane-strain assumption, the out-of-plane zz strain is zero.

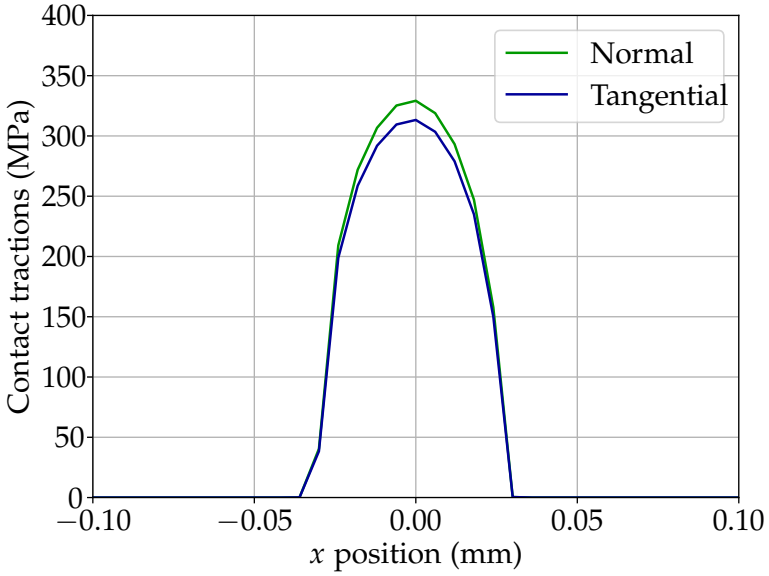

Figure 3.11: Normal and tangential contact tractions on the plane surface due to a frictional cylinder-plane contact.

A full horizontal displacement loading cycle is computed, which enables to compile the fretting loop (Figure 3.14a). It reflects a gross slip fretting regime with almost vertical slopes at the changes of direction. The integral of the fretting loop gives the friction energy dissipated throughout the cycle $E_\mathrm{d} = 4.53$ mJ/mm. This value is very close to the following approximation:

$$E_\mathrm{d} \approx 4\,\mu\,F_n\,\delta_0 = 4.56 \text{ mJ/mm}. \tag{3.55}$$

The distribution of dissipated energy over the plane surface is depicted in Figure 3.14b showing the profile of surface density of dissipated energy.

3.4.3 Wear computation processes

Wear evolution is computed using an incremental process which integrates the time scales decoupling principle and uses the finite element method to solve the frictional contact problem. The

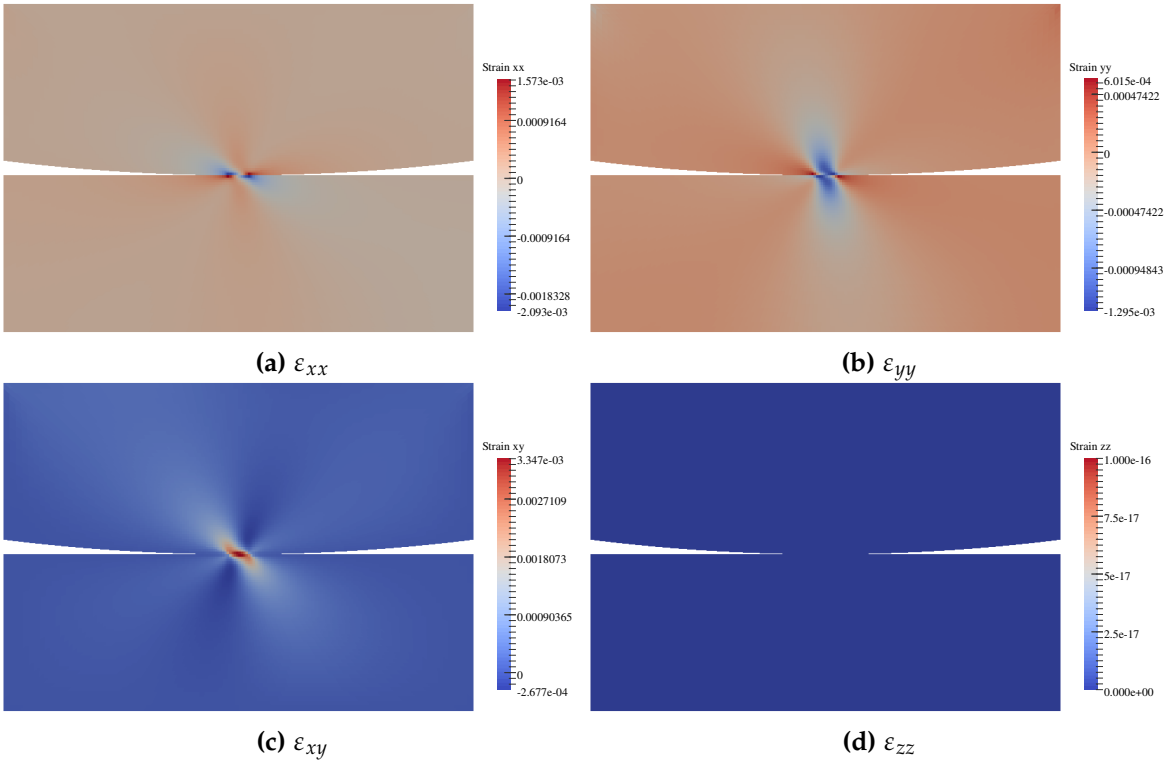

(a) ε_{xx} **(b)** ε_{yy}

(c) ε_{xy} **(d)** ε_{zz}

Figure 3.12: Strain field on a frictional cylinder-plane contact subjected to a normal load and tangential relative displacement.

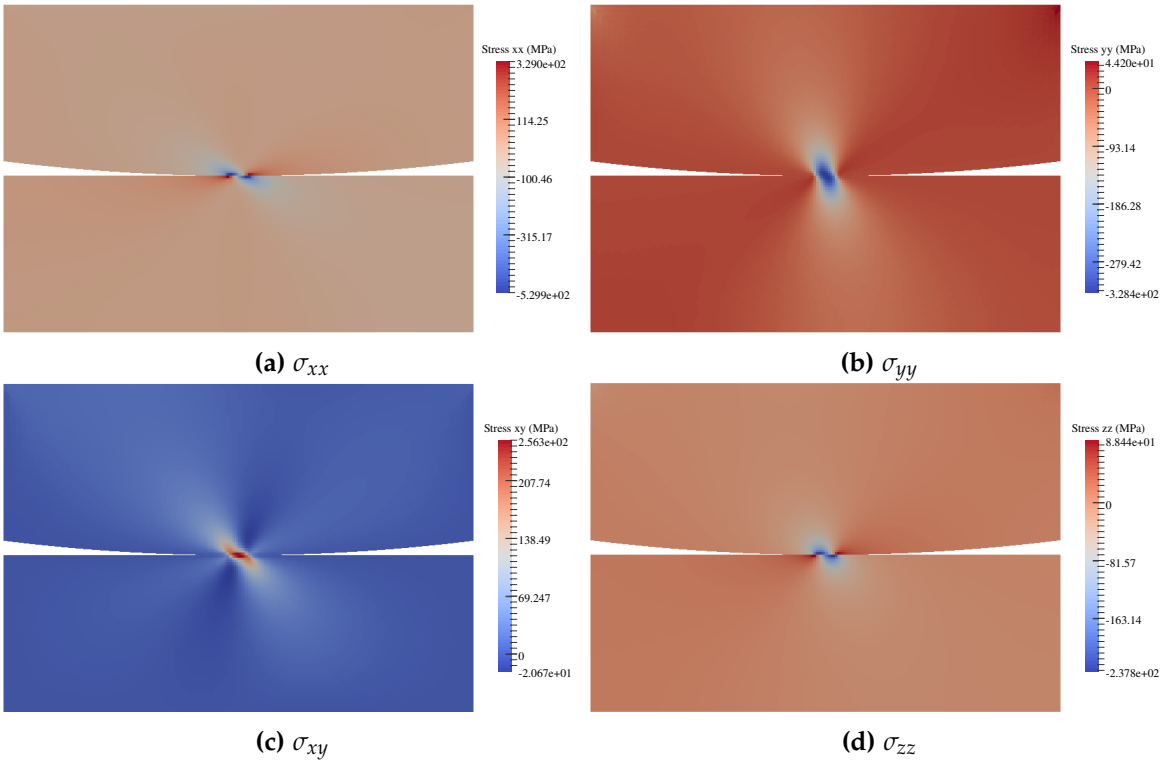

(a) σ_{xx} **(b)** σ_{yy}

(c) σ_{xy} **(d)** σ_{zz}

Figure 3.13: Stress field on a frictional cylinder-plane contact subjected to a normal load and tangential relative displacement.

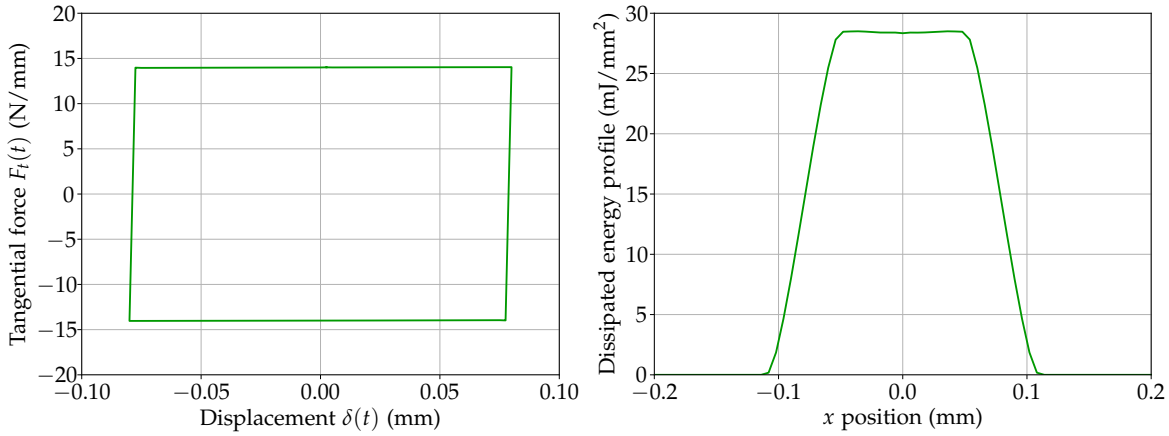

(a) Fretting loop **(b)** Surface density of dissipated energy

Figure 3.14: Fretting loop and surface density of dissipated energy profile over the plane surface, computed on a frictional cylinder-plane contact subjected to a cyclic horizontal displacement.

methods implemented also integrate a simple explicit cycle jump, considering an acceleration factor Δn. The two wear computation strategies using one or other wear evolution law are described here. Using the spatial discretization introduced with the finite element model, wear profile is denoted as a column matrix $\boldsymbol{h} = (h_1 \ \dots \ h_{n_x})^T$ whose components are the surface nodal values of wear depth: for each surface node x_i, $h_i = h(x_i)$. The same goes for every quantity expressed on the surface – wear rate, friction energy, etc. $\boldsymbol{h}$, $\boldsymbol{\partial_n h}$, $\boldsymbol{e}_\mathrm{d}$, $\boldsymbol{\partial_n e}_\mathrm{d}$ are matrices of size $n_x \times 1$ with n_x the number of surface nodes while $\boldsymbol{\Delta a}$, $\boldsymbol{\partial_n a}$ are matrices of size $n_s \times 1$ with n_s the number of level set nodes.

Energy-based wear model

First, a classical simulation routine is used with an energy wear law. This is very similar to the computational processes presented in several articles on the topic [Mary and Fouvry 2007, Paulin et al. 2008]. In brief, it consists in solving the incremental frictional contact problem for each time step of a cycle. The friction energy is calculated at each time step as a nodal quantity defined on the contact surface, and is cumulated over the cycle. At the end of the cycle, the cyclic wear rate $\boldsymbol{\partial_n h}$ – namely the wear depth increment generated over the cycle – is derived as a nodal quantity defined on the surface as well using the energy-based wear law (3.22). The use of an explicit cycle jump implies to multiply the cyclic wear rate by the acceleration factor Δn, yielding the wear depth increment over a range of Δn cycles. Finally, the surface geometry is updated accordingly by imposing a fictitious displacement field on it. In order not to distort the elements too much, this surface displacement field induces a displacement of the whole mesh in the bulk material which is gradually decreasing from the contact surface towards the other end, as depicted in Figure 3.15. Then, the next cycle is computed. This incremental wear simulation process is described in Algorithm 3.1. The same process may be employed to simulate wear using various Archard-like wear laws.

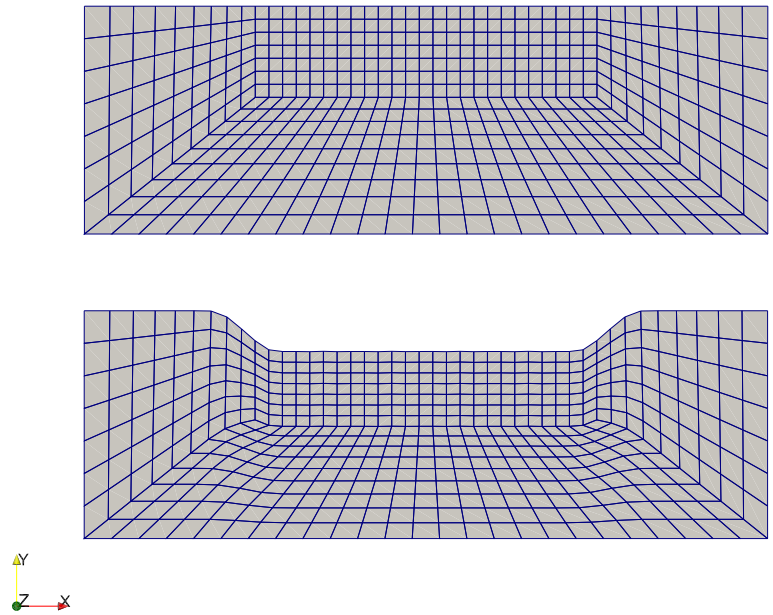

Figure 3.15: Reference mesh (top) and displaced mesh (bottom) to account for surface geometry evolution due to wear.

Algorithm 3.1: Cyclic wear computation process using an energy-based law.

I - Parameters definition
Set values for α, μ, δ_0, F_0, N_{cyc}, Δn, T, Δt, E, ν ;
II - Loading definition
Define J time steps per cycle: $\{t_1, \dots t_J\}$;
Define K computed cycles: $\{n_1, \dots n_K\}$;
for j *in* $\{1, \dots J\}$ **do**
    Define $F_n(t_j)$; `// Normal force`
    Define $\delta(t_j)$; `// Tangential displacement`
III - Initialization
Initiate $\boldsymbol{h} \leftarrow 0$; `// Total wear depth`
IV - Iterative process
for k *in* $\{1, \dots K\}$ **do**
    Initiate $\boldsymbol{\partial_n e}_{d,k} \leftarrow 0$; `// Friction energy cumulated over cycle` n_k
    for j *in* $\{1, \dots J\}$ **do**
        Impose loading at t_j ;
        Solve the frictional contact problem at t_j ; `// Finite element problem resolution`
        foreach *contact surface node* x_i **do**
            Get sliding $\Delta s_j(x_i)$ over Δt ;
            Get tangential frictional contact reaction $\lambda_{t,j}(x_i)$; `// Lagrange multiplier`
            Calculate friction energy over Δt: $\Delta e_{d,j}(x_i) \leftarrow \lambda_{t,j}(x_i)\Delta s_j(x_i)$;
        Cumulate friction energy over cycle n_k: $\boldsymbol{\partial_n e}_{d,k} \leftarrow \boldsymbol{\partial_n e}_{d,k} + \boldsymbol{\Delta e}_{d,j}$;
    Calculate wear rate at cycle n_k: $\boldsymbol{\partial_n h_k} \leftarrow \alpha \boldsymbol{\partial_n e}_{d,k}$;
    Update surface geometry with fictitious displacement $\Delta n\, \boldsymbol{\partial_n h_k}$; `// See Figure 3.15`
    Cumulate total wear depth $\boldsymbol{h} \leftarrow \boldsymbol{h} + \Delta n\, \boldsymbol{\partial_n h_k}$;

Damage-based wear model

A rather similar process is defined considering a damage-based wear model using thick level set. The thick level set formulation requires to be initiated with non-zero damage, so the level set front Γ_0 is initialized at a small incipient depth a_{ini} with respect to the contact surface. This yields an initial distance field ϕ and an initial damage field d. Then, the iterative process consists in incrementally solving the frictional contact problem over a cycle. At each time step of the cycle, the stress and strain fields are computed which yields the local thermodynamic force field Y. This enables to build the matrices $\boldsymbol{K}$ and $\boldsymbol{\Delta F}$ at each time step and solve the system $\boldsymbol{K}\,\boldsymbol{\Delta a} = \boldsymbol{\Delta F}$[5]. Using the time scales decoupling, the level set is not actually propagated at each time step but only at the end of the cycle instead. Thus, the level set propagation increment is cumulated over the cycle, and the level set is accordingly displaced at the end of the cycle. The distance field ϕ and damage field d are then updated, possibly followed by the propagation of the contact surface if required. Indeed, wear is supposed to occur at iso-$\phi = l_{\text{c}}$ and iso-$d = d_{\text{c}}$ which has to be verified after the level set is propagated. If the values of ϕ and d on the contact surface overshoot the threshold values, the surface needs to be displaced in consequence. This wear step is followed by a new update of the distance and damage fields to retrieve the threshold values on the contact surface. The material stiffness is locally updated as well due to the evolution of damage. This routine is repeated over a certain number of cycles, possibly considering an explicit cycle jump as previously. The computation process is described in Algorithm 3.2 and examples of simulations are detailed in Section 3.5.

Note that these processes are written for the case of unilateral wear. When considering multiple wearing surfaces, we just need to define as many wear profiles as there are wearing surfaces and repeat these processes for each of the surfaces.

3.5 Simulation results

In this section, the simulation processes presented are used to compute wear evolution using either an energy-based wear law or the damage-based wear model. We consider a unilateral wear case in which wear only occurs on the plane surface. The normal load is assumed constant with $F_n = 3$ N/mm, and two different displacement amplitudes are used: either $\delta_0 = 80$ µm or $\delta_0 = 120$ µm.

The numbers of cycles simulated here are too low to allow for a comparison of the wear profiles with the experimental data available. This is left for Chapter 4 in which fretting wear simulations are conducted for higher numbers of cycles.

3.5.1 Results using an energy-based wear law

First, simulations are conducted using the friction energy wear law. The energy wear coefficient for the plane surface is extracted from the experimental data of Marc (2018): $\alpha_{\text{pla}} = 3.14 \times 10^{-8}$ mm^3 mJ^{-1}. Two simulations are performed with either of the two displacement amplitude values. The computations are conducted for a total number of $N_{\text{cyc}} = 10{,}000$ cycles using an acceleration factor $\Delta n = 5$, leading to the effective computation of 2,000 cycles.

The simulations are conducted following the process described in Algorithm 3.1. Using this simulation process, the evolutions of the cyclic wear rate profiles are depicted in Figure 3.16, with

[5]The building process of matrices $\boldsymbol{K}$ and $\boldsymbol{\Delta F}$ is detailed in Appendix B, using the finite element code Cast3M.

Algorithm 3.2: Cyclic wear computation process using a damage-based law with the thick level set approach.

I - Parameters definition
Set values for Y_0, Y_1, l_c, d_c, a_{ini}, μ, δ_0, F_0, N_{cyc}, Δn, T, Δt, E_0, ν ;
Define a function $d : \phi \rightarrow d(\phi)$;
II - Loading definition
Define J time steps per cycle: $\{t_1, \dots t_J\}$;
Define K computed cycles: $\{n_1, \dots n_K\}$;
for *j in* $\{1, \dots J\}$ **do**
    Define $F_n(t_j)$; `// Normal force`
    Define $\delta(t_j)$; `// Tangential displacement`
III - Initialization
Initiate $\boldsymbol{h} \leftarrow 0$; `// Total wear depth`
Initiate Γ_0 at depth a_{ini} ;
Compute the initial fields ϕ and $d(\phi)$;
Initiate the material stiffness field $E(d)$;
IV - Iterative process
for *k in* $\{1, \dots K\}$ **do**
    Initiate $\boldsymbol{\partial_n a_k} \leftarrow 0$; `// Level set propagation cumulated over cycle` n_k
    for *j in* $\{1, \dots J\}$ **do**
        Impose loading at t_j ;
        Solve the frictional contact problem at t_j ; `// Finite element problem resolution`
        Compute the field $Y_j(\underline{\underline{\sigma}}, \underline{\underline{\varepsilon}})$; `// Different possible expressions`
        Build the matrices $\boldsymbol{K_j}$ and $\boldsymbol{\Delta F_j}$;
        Solve $\boldsymbol{K_j}\, \boldsymbol{\Delta a_j} = \boldsymbol{\Delta F_j}$;
        Cumulate over cycle n_k: $\boldsymbol{\partial_n a_k} \leftarrow \boldsymbol{\partial_n a_k} + \boldsymbol{\Delta a_j}$;
    Displace Γ_0 by the propagation increment $\Delta n\, \boldsymbol{\partial_n a_k}$ over Δn cycles ;
    Update fields ϕ and $d(\phi)$;
    Calculate wear increment over Δn cycles: $\Delta n\, \partial_n h_k(x_i) \leftarrow \langle \phi(x_i) - d_c l_c \rangle_+$;
    Update surface geometry with fictitious displacement $\Delta n\, \boldsymbol{\partial_n h_k}$; `// See Figure 3.15`
    Cumulate total wear depth $\boldsymbol{h} \leftarrow \boldsymbol{h} + \Delta n\, \boldsymbol{\partial_n h_k}$;
    Update fields ϕ and $d(\phi)$ again ;
    Update the material stiffness field $E(d)$;

either $\delta_0 = 80$ µm or $\delta_0 = 120$ µm. In the early cycles, the wear rate profiles display a parabolic shape with a maximum at the center of the surface. As wear proceeds, the surface geometry evolves and with it the contact pressure distribution. This causes the wear rate profiles to progressively decrease at the center of the surface, and in the meantime to enlarge towards the contact surface edges. One can note that all the profiles have the same integral: this reflects the fact that the amount of friction energy dissipated per cycle is constant, only the distribution over the surface evolves.

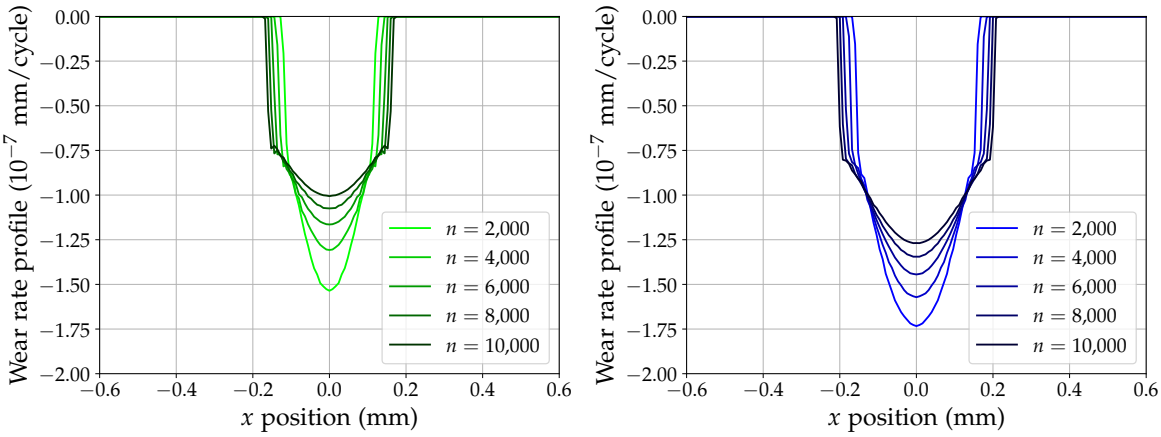

(a) $\delta_0 = 80$ µm **(b)** $\delta_0 = 120$ µm

Figure 3.16: Wear rate profiles computed using an energy wear law.

The resulting evolution of wear depth profiles is shown in Figure 3.17. As expected, the wear profiles expand both in depth and in width over the cycles. After $N_{\text{cyc}} = 10{,}000$ cycles, the maximum wear depth is about $h_{\max} = 1.3$ µm for $\delta_0 = 80$ µm and $h_{\max} = 1.5$ µm for $\delta_0 = 120$ µm.

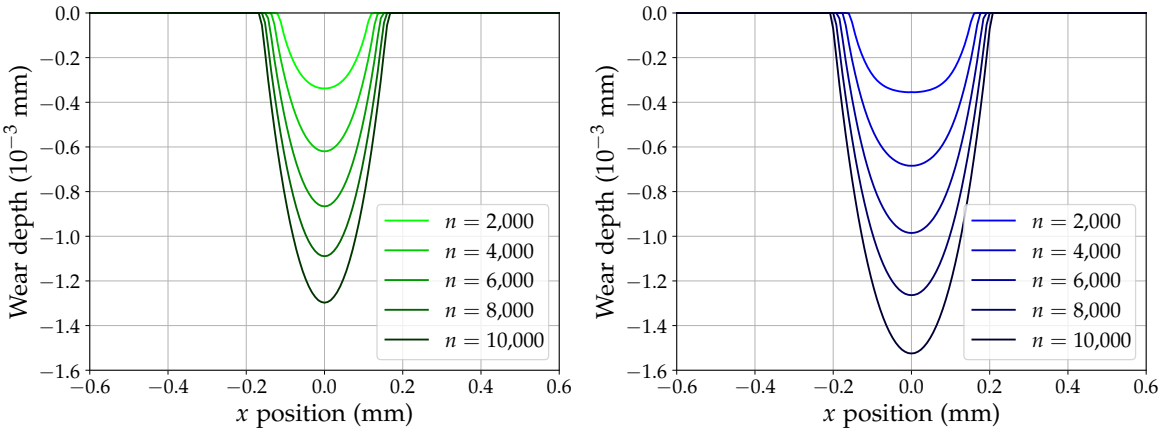

(a) $\delta_0 = 80$ µm **(b)** $\delta_0 = 120$ µm

Figure 3.17: Wear profiles computed using an energy wear law.

Figure 3.18 depicts the evolution over the cycles of the wear profiles width. The evolution is piecewise-constant, which is due to the spatial discretization of the surface: the wear profile width can only increase one node at a time. It turns out that the evolution of the wear profiles width l may be well approximated by a power function $\tilde{l}$ of the form:

$$l(n) \approx \tilde{l}(n) = l_0 + \kappa_1 n^{\kappa_2} \tag{3.56}$$

where l_0, κ_1 and κ_2 are parameters that need to be determined to fit the evolution obtained with the finite element simulation. The evolution of the wear profile width is rather quick during the early cycles, then progressively decreases throughout the cycles. This indicates that the evolution of the wear profile shape is faster at the start than subsequently. The further into the cycles, the more the integration of a new surface node into the contact surface is a rare event.

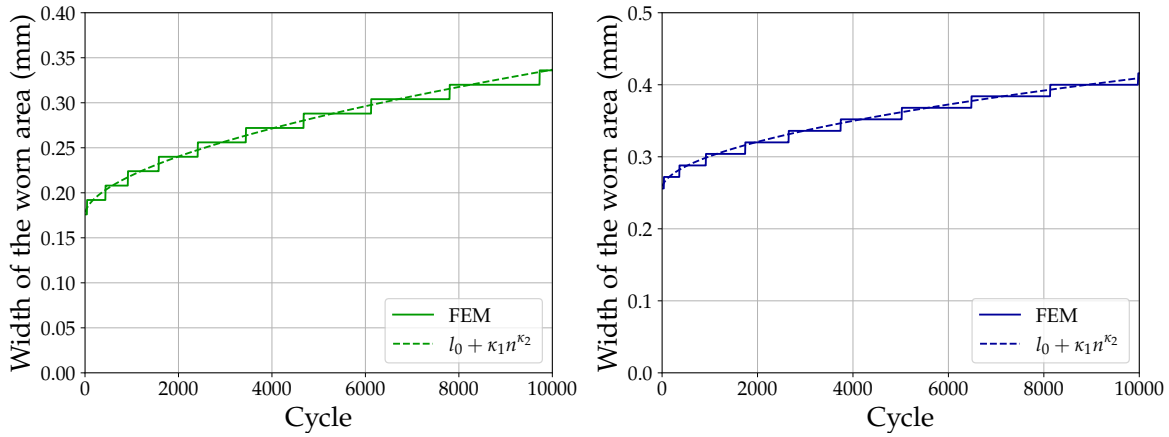

(a) $\delta_0 = 80$ µm **(b)** $\delta_0 = 120$ µm

Figure 3.18: Evolution of the wear profile width computed using an energy wear law.

Finally, the evolution of the wear volume over the cycles is linear (Figure 3.19). This was expected given than the dissipated friction energy is constant from one cycle to another.

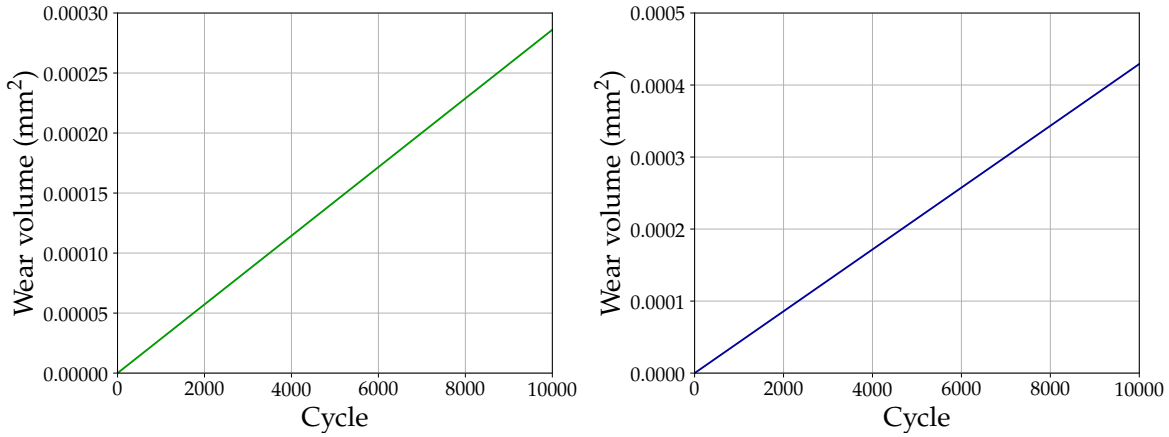

(a) $\delta_0 = 80$ µm **(b)** $\delta_0 = 120$ µm

Figure 3.19: Evolution of the wear volume computed using an energy wear law.

3.5.2 Results using the damaged-based wear model

Thereafter, similar simulations are carried out with the damage-based wear model. As a first step, preliminary simulations are performed in which the initial level set propagation stage prior to the

onset of wear is skipped. In this situation, the level set is initialized in depth at a distance to the surface which corresponds to the critical distance for wear to occur. By doing this, the slightest level set propagation is inevitably followed by wear, thus ensuring the occurrence of wear as soon as the first cycle. First, the model parameters are arbitrarily chosen. The damage law parameters are $Y_0 = 0$ MPa and $Y_1 = 200$ MPa, and we use a critical length $l_c = 40$ µm and a critical damage $d_c = 0.5$ – hence, the level set is initialized at a depth $a_{ini} = 20$ µm which gives an initial damage value $d = d_c = 0.5$ on the surface. The simulation is conducted for $N_{cyc} = 5{,}000$ cycles with an acceleration factor $\Delta n = 5$. Using the results obtained, the value of Y_1 is adjusted in order to fit the energy wear law (for which an experimentally obtained wear coefficient is known) in terms of wear volume evolution.

Using the value thus determined for the coefficient Y_1, subsequent simulations are performed with a lower initial damage value. This allows for a two-stage process: at first, the level set propagates but no wear occurs while the surface damage remains lower than the threshold. Then, as the damage threshold is reached, further propagation of the level set triggers the propagation of the wear surface. In these simulations, the initial level set depth is chosen as $a_{ini} = 10$ µm. Because the propagation of the level set is pretty linear during the initial wear-free stage, a high acceleration factor is used at the start: Δn is comprised between 100 and 2,500 – it decreases progressively as the surface damage value tends towards the critical value. As wear occurs, the acceleration factor is reduced to $\Delta n = 5$. The simulation is run for a total number of $N_{cyc} = 50{,}000$ cycles.

Preliminary simulations: skipped initial level set propagation stage

Simulations using the damage-based wear model with the thick level set approach are first realized skipping the initial level set propagation stage. The initial position of the level set together with the associated damage field in the plane are depicted in Figure 3.20. The level set is positioned such that the damage value on the surface is $d = d_c = 0.5$.

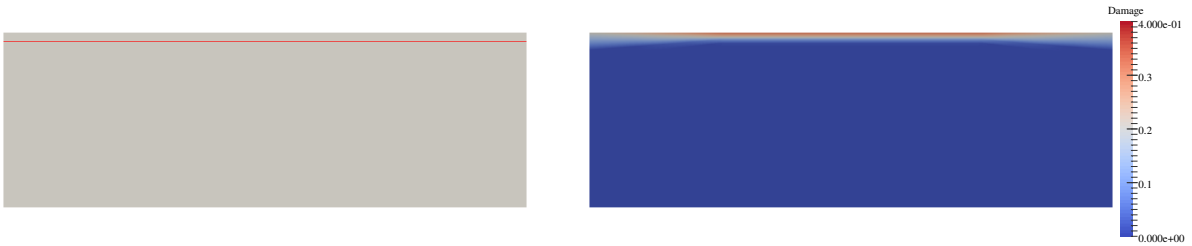

(a) Level set (red line) position in the plane **(b)** Damage field

Figure 3.20: Initial level set position and damage field for a simulation with a skipped wear-free level set propagation stage. The values indicated for damage in the color map refer to the values at the Gauss points, the maximum value for damage on the surface is therefore higher.

At first, a simulation is run with a displacement amplitude $\delta_0 = 80$ µm and choosing arbitrary values for the parameters of the damage model. Considering such initialization at $d = d_c = 0.5$, wear occurs as soon as the first cycle. The evolution of the wear volume is depicted in Figure 3.21. It shows that the wear volume evolution is linear with respect to the number of cycles, but the rate is higher in the TLS simulation result than the evolution with an energy wear law, taken as a reference. Based on this result, it is proposed to adjust the parameter Y_1 to fit the reference evolution. Equation 2.91, governing the propagation of the level set, indicates that the propagation rate should be inversely proportional to Y_1^2. As a result, a corrected $Y_{1,corr}$ is determined to fit the

reference evolution: $Y_{1,\text{corr}} = 249.47$ MPa instead of the arbitrary $Y_1 = 200$ MPa used in the first instance – all other parameters remaining unchanged.

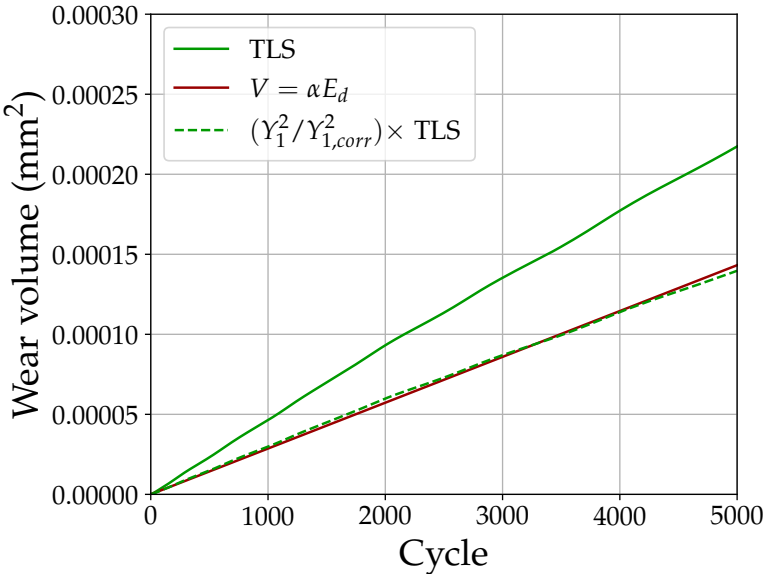

Figure 3.21: Wear volume evolution computed using a damage-based wear model with a thick level set (TLS) approach. The evolution is compared with the linear evolution yielded by the energy wear law for which the coefficient is known from experimental data. A correction of the parameter Y_1 is determined to fit the linear evolution from the energy wear law.

Using the corrected value $Y_{1,\text{corr}}$, two simulations are run with either $\delta_0 = 80$ µm or $\delta_0 = 120$ µm. The results show indeed a wear volume evolution very close to the friction energy wear, as depicted in Figure 3.22. The wear depth profiles are very similar as well, except that using the damage-based model the wear profiles are slightly wider and less deep than with a friction energy wear law (Figure 3.23).

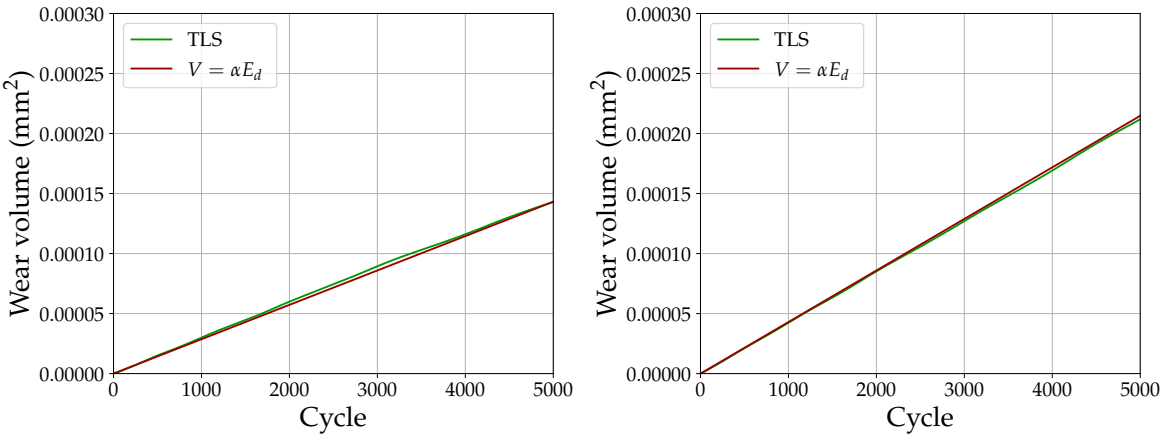

(a) $\delta_0 = 80$ µm **(b)** $\delta_0 = 120$ µm

Figure 3.22: Evolution of the wear volume computed using a damage-based wear model using the thick level set (TLS) approach, compared with an energy wear law.

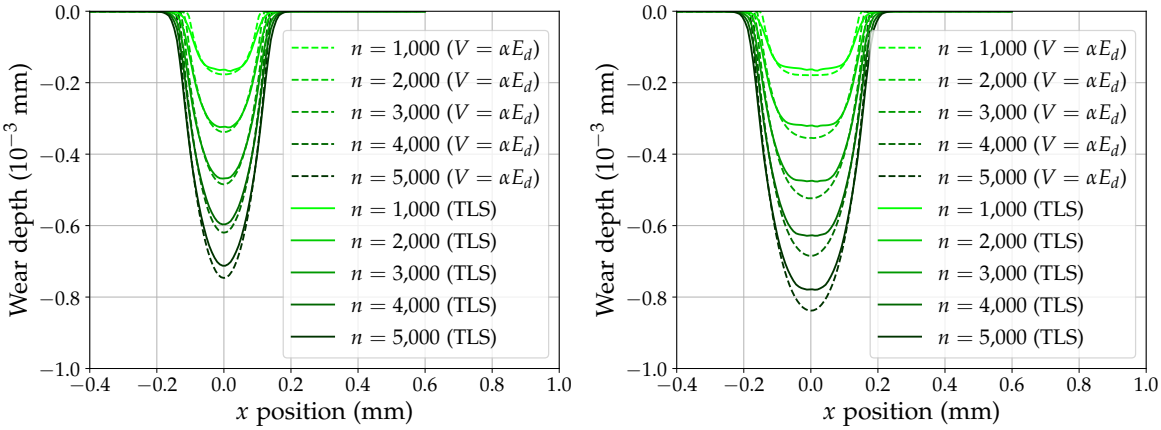

(a) $\delta_0 = 80$ µm **(b)** $\delta_0 = 120$ µm

Figure 3.23: Wear profiles computed using a damage-based wear model using the thick level set (TLS) approach, compared with an energy wear law.

Complete simulations: two-stage evolution

Considering the same set of parameters for the damage model, including the corrected value for Y_1, two complete simulations are run with either $\delta_0 = 80$ µm or $\delta_0 = 120$ µm. This time, the level set is initialized in such a way that the surface damage is below the threshold, allowing for the existence of an initial wear-free level set propagation stage. The initial position of the level set and the associated damage field are shown in Figure 3.24. The initial damage value on the surface is $d = 0.25$.

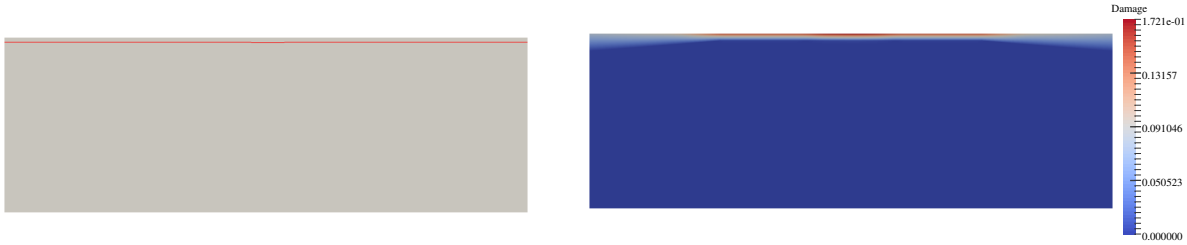

(a) Level set (red line) position in the plane **(b)** Damage field

Figure 3.24: Initial level set position and damage field for a simulation with a two-stage evolution. The values indicated for damage in the color map refer to the values at the Gauss points, the maximum value for damage on the surface is therefore higher.

The simulations are then conducted as previously, however with a slight modification. The primary computation of the level set propagation increment over a cycle can include very small perturbations. These perturbations, which are negligible in the first place, accumulate over the set of cycles during which the level set propagates prior to the onset of wear. As a result, the level set position may be disturbed at the start of the wear surface propagation stage leading to a disturbed wear evolution. In order to tackle this effect, a Gaussian smoothing is applied at the end of each cycle to the level set propagation increment. For each node s_i on the level set, the propagation

increment $\Delta a(s_i)$ is replaced by $\overline{\Delta a}(s_i)$ with:

$$\overline{\Delta a}(s_i) = \frac{\sum_{s_j} \Delta a(s_j) \mathrm{e}^{-(d_{ij}/R)^2}}{\sum_{s_j} \mathrm{e}^{-(d_{ij}/R)^2}} \tag{3.57}$$

where d_{ij} is the euclidean distance between the nodes s_i and s_j, and R is a parameter governing the bandwidth of the decreasing exponential smoothing function. This smoothing step was proposed by Basseville et al. (2019) in fretting wear simulations using an energy wear law. By doing this, the possible irregularities on the level set propagation are mitigated. Smoothing the level set propagation appeared to be necessary in the simulation presented here. The need for smoothing the propagation increments might be related to the discretization chosen for the level set. Choosing different numbers of nodes in the level set or basis functions shapes may possibly improve the situation.

Following this process, the initial wear-free level set propagation stage produces a displacement of the level set depicted in Figure 3.25. This shows the positions of the level set for both simulations just before wear onsets. This occurs at cycle $N_0 = 42{,}440$ in the case $\delta_0 = 80$ µm and $N_0 = 42{,}360$ in the case $\delta_0 = 120$ µm. The resulting damage fields in the plane are shown in Figure 3.26. In each case, the maximum damage value on the surface is $d = d_c = 0.5$.

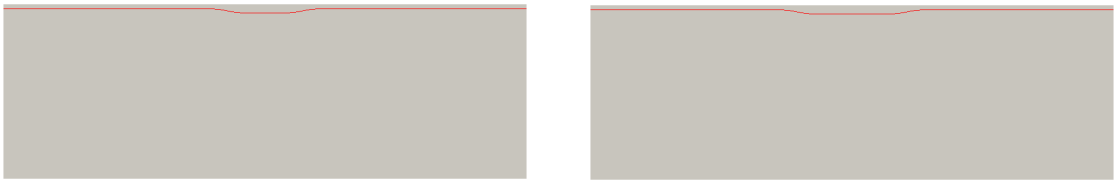

(a) $\delta_0 = 80$ µm, $N_0 = 42{,}440$ **(b)** $\delta_0 = 120$ µm, $N_0 = 42{,}360$

Figure 3.25: Level set (red line) position after N_0 cycles, just before wear onsets, for a simulation with a two-stage evolution.

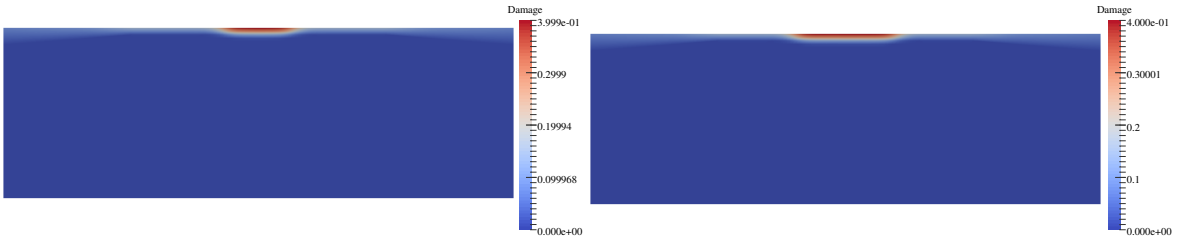

(a) $\delta_0 = 80$ µm, $N_0 = 42{,}440$ **(b)** $\delta_0 = 120$ µm, $N_0 = 42{,}360$

Figure 3.26: Damage field after N_0 cycles, just before wear onsets, for a simulation with a two-stage evolution. The values indicated for damage in the color map refer to the values at the Gauss points, the maximum value for damage on the surface is therefore higher.

From this point forward, wear evolves up to cycle $N_{\mathrm{cyc}} = 50{,}000$. The level set position at the end of the simulations is depicted in Figure 3.27, and the final damage fields in Figure 3.28. It is clear that further propagation of the level set causes the propagation of the wear surface in such a way that the surface damage value remains constant. This can also be seen in Figure 3.29 which shows the evolution over the cycles of the maximum damage value. Damage progressively

increases during the initial wear-free propagation stage, until it reaches the critical value. From this point on, the maximum surface damage value is constant: $d = 0.5$.

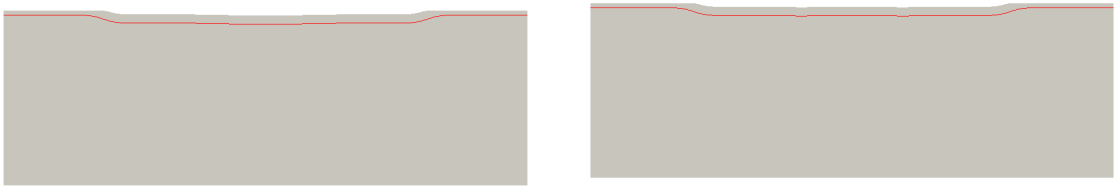

(a) $\delta_0 = 80$ µm **(b)** $\delta_0 = 120$ µm

Figure 3.27: Level set (red line) position after $N_{cyc} = 50{,}000$ cycles for a simulation with a two-stage evolution.

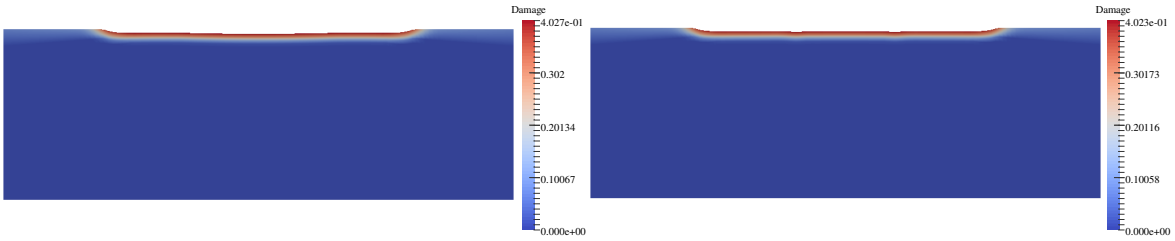

(a) $\delta_0 = 80$ µm **(b)** $\delta_0 = 120$ µm

Figure 3.28: Damage field after $N_{cyc} = 50{,}000$ cycles for a simulation with a two-stage evolution. The values indicated for damage in the color map refer to the values at the Gauss points, the maximum value for damage on the surface is therefore higher.

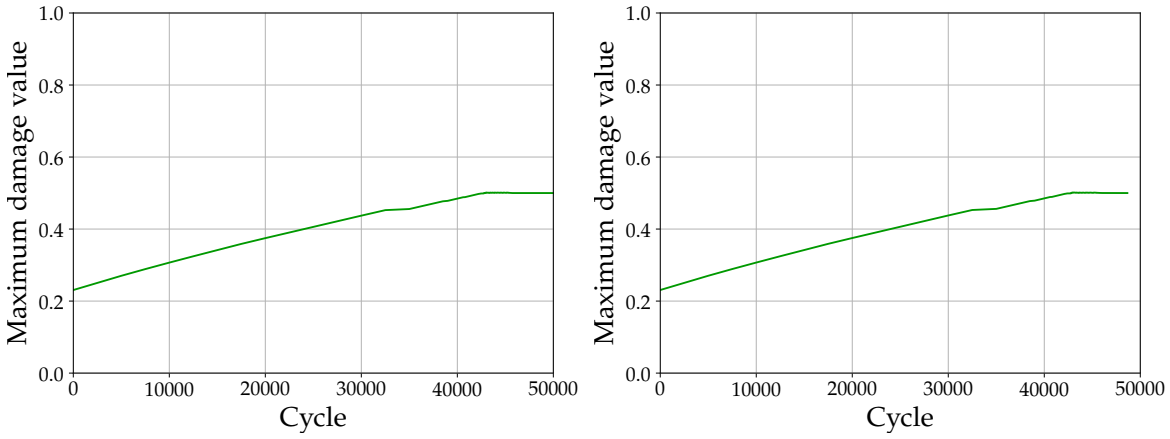

(a) $\delta_0 = 80$ µm **(b)** $\delta_0 = 120$ µm

Figure 3.29: Evolution of the maximum damage value.

The evolution of the wear profiles is depicted in Figure 3.30. First, a very rapid evolution of wear appears during the first cycles. This evolution is driven by a substantial growth of wear depth near the contact surface edges, initially forming W-shaped profiles. Thereafter, wear evolution seems to progressively stabilize in a shape that resembles more a V shape, with a more limited wear rate.

Figure 3.31 shows the evolution of the wear volume over the cycles, compared to the evolution obtained with an energy wear law. The initial wear-free propagation stage can clearly be seen here.

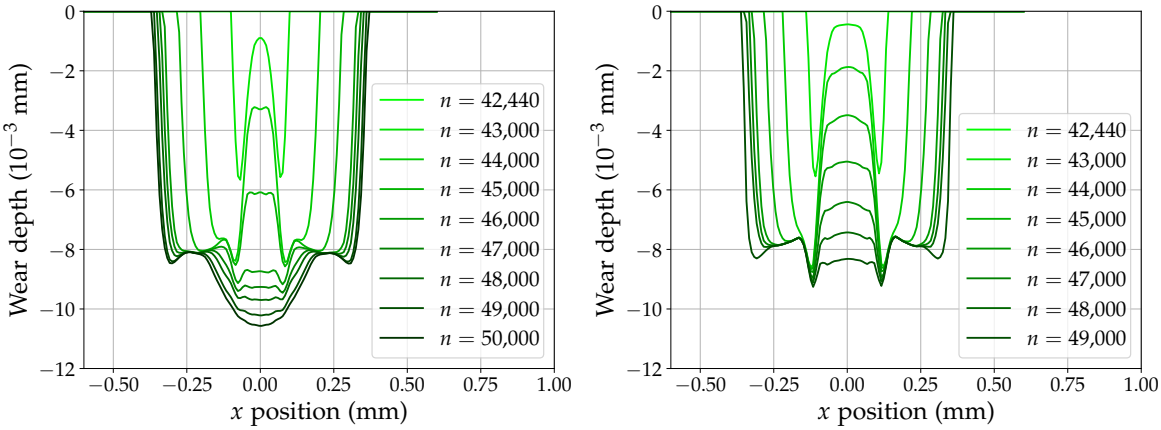

(a) $\delta_0 = 80$ µm **(b)** $\delta_0 = 120$ µm

Figure 3.30: Evolution of the wear profiles on the plane surface using a damage-based wear model.

Once wear onsets, the evolution of the wear volume is very different from what could be expected. The wear volume growth rate is much higher than what was obtained in the previous simulations skipping the initial damage propagation stage. This confirms the initially sharp evolution of wear once it onsets, followed by a progressive decrease in the wear evolution rate. As the wear profile evolves towards a V shape, the wear rate seems to tend towards a value closer to the expected wear rate. The number of cycles computed here is however not sufficient to assess the long-term evolution of wear rate with any certainty.

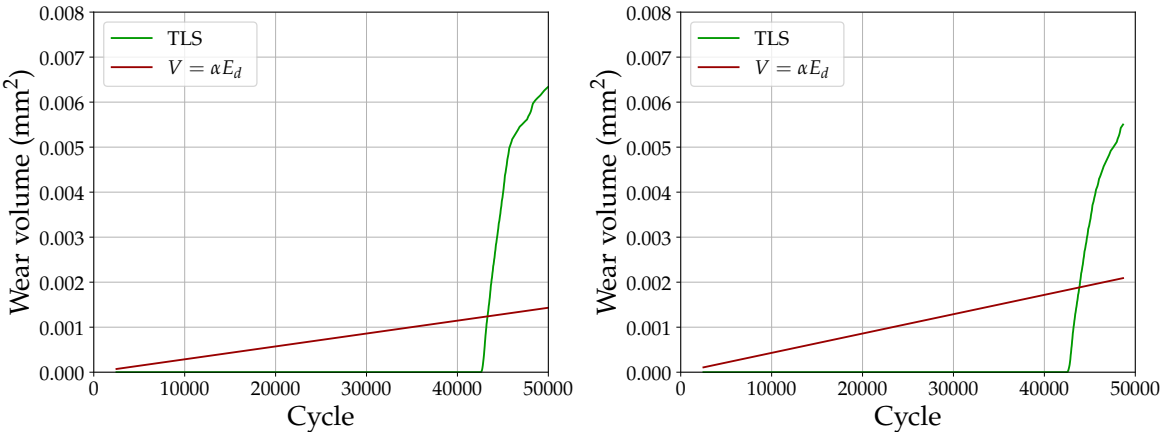

(a) $\delta_0 = 80$ µm **(b)** $\delta_0 = 120$ µm

Figure 3.31: Evolution of the wear volume using a damage-based wear model.

Discussion

Such a difference between the results obtained with or without the initial wear-free propagation stage may seem surprising. The calculated wear rate could have been expected to be roughly similar to the propagation rate of the level set that preceded wear evolution. This is not the case here: while the initial propagation of the level set is very stable from one cycle to another and

progresses at the expected rate, the subsequent propagation of the wear surface shows a very quick enlargement accompanied with significant wear in the vicinity of the surface edges.

This is presumably related to the delay between the moment a certain point of the surface experiences loading and the moment it starts to wear, which is inherent to the model developed. At first, only a small number of surface nodes, located at the center of the surface, undergoes contact stress and the level set propagates only in this area. The initial propagation stage may take several thousands cycles before wear starts to occur, causing then a modification of the surface geometry. Wear evolution first concerns only the few points at the center of the surface which experienced loading, leading to an enlargement of the contact surface which results in newer surface points, previously out of the contact surface bounds, experiencing contact stress. These newly-stressed points, however, do not start to wear right away. There is a delay related to the propagation time of the level set. This level set propagation can take several hundreds or thousands cycles, during which wear goes on for the center points of the surface, which creates always sharper edges and higher stress on the newly-stressed points. This higher stress increases the propagation rate in these areas, and when wear finally occurs at the nodes in question the wear rate is quite high, creating a wear profile with a W shape. This evolution, which could be qualified as unstable, is repeated upon further enlargement of the wear profile with an increasing intensity, up to a point where the wear profile has become sufficiently large to retrieve a more stable wear evolution.

The understanding of such unstable evolution using the thick level set model needs to be improved by exploring its use further and performing additional simulations, varying the different parameters such as the critical length, the level set discretization, or the damage law. In addition, simulations on larger numbers of cycles should enable a better assessment of the long-term behavior of wear evolution using this model.

Because the issues mentioned here are seemingly related to the delay between the surface loading and the start of wear, reducing the incubation time of wear could be worth a try. The initial stage seems indeed quite long here: more than 40,000 cycles. This could be done for example by the modification of the relation $d(\phi)$ which governs the spatial evolution of damage in the partially damaged zone. For now, a linear evolution was considered for the sake of simplicity. Choosing a different function would affect the propagation rate of the level set prior to the onset of wear.

3.6 Conclusion

The work described in this chapter enabled the implementation of the damage-based wear model presented in Chapter 2 in order to simulate wear evolution. Preliminary, semi-analytical computations are proposed and show the initial level set propagation stage prior to the start of wear. As wear occurs, the surface geometry is altered which makes the computation of contact stresses more complicated. In this regard, the finite element method is used. A two-dimensional model of a cylinder-plane system is defined and a simulation routine is presented to account for the progressive evolution of the level set followed by the propagation of the wear surface.

Beside that, a classical simulation process is employed to simulate wear evolution obeying a friction energy law. These simulation processes are based on a decoupling assumption between the elastic response of the system and wear evolution. This hypothesis is made considering that both processes evolve on very different time scales. This enables the introduction of an acceleration factor on wear evolution, which decreases the number of cycles that needs to be effectively computed.

As expected, the damage-based wear model using the thick level set approach implies the existence of an incubation period before wear onsets. In a first stage, the level set propagates without causing wear, until the surface damage value reaches the defined threshold. When it does, further propagation of the level set leads to a propagation of the wear surface. The simulation results presented here show a higher than expected wear rate, driven by a fast evolution of wear in the vicinity of the wear profile edges. This is likely related to the delay between the moment a surface point experiences loading and the moment it starts to wear. The use of this model needs to be explored further, with different model parameters and computing higher numbers of cycles.

The need to simulate high numbers of cycles is especially discussed in the next chapter. This will allow for a comparison of the simulation results with experimental data. In the remainder of the document, the simulations are carried out using a friction energy wear law.

Chapter recap

This chapter deals with the simulation of wear evolution using either an energy-based law or the damage-based wear model developed in the previous chapter.

- The simulation processes defined rely upon a time scales decoupling between wear evolution and the elastic response to the frictional contact problem.
- Preliminary computations are performed, but they are limited by the need to compute contact stresses for arbitrary surface geometries. Surface geometries are initially regular but are altered as soon as wear occurs.
- To this end, the finite element method is used. A two-dimensional finite element model of a cylinder-plane system is defined.

Simulation processes are implemented to assess the progressive evolution of wear.

- Considering a friction energy wear law, a classical simulation routine is used. It is based on the incremental, step-by-step simulation of fretting cycles, yielding the dissipated friction energy over each cycle and, using the wear law, the cyclic wear rate. Wear is accounted for through the displacement of the contact surface.
- Using the damage-based model with the thick level set approach, the level set propagation increment is calculated at each cycle. When the level set reaches a critical distance to the surface, it causes the propagation of the wear surface.

Simulation results are presented using these two processes.

- The friction energy wear law yields V-shaped wear profiles, progressively expanding both in depth and width. The wear profile width evolution may be well approximated by a power function.
- The damage-based wear model with the thick level set approach generates a two-stage wear evolution. First, a wear-free level set propagation stage, followed by the evolution of the wear surface. Once it has started, wear evolution is faster than expected, with high wear rates near the edges of the wear profile.
- This fast wear evolution is likely related to the delay between the start of loading and the start of wear. Performing additional simulations trying to reduce the initial propagation stage could help investigate the reasons behind that behavior.

Chapter 4

Cycle jump methods for high-cycle fretting wear simulations

An investigation on the most appropriate numerical schemes in a computational cost mitigation purpose

4.1 Introduction

Due to the slow nature of wear, its numerical simulation is known to be very computationally expensive. In order to capture the progressive evolution of surface geometry, it is indeed necessary to compute high amounts of time steps. As it was stated in the previous chapter, the numerical studies on the topic generally deal with this issue by assuming a time scales decoupling between wear evolution and the deformation of the structure [Lengiewicz and Stupkiewicz 2012] together with the introduction of an acceleration factor, or cycle jump, on wear evolution [Põdra and Andersson 1999, McColl et al. 2004, Mary and Fouvry 2007]. The idea is to compute wear evolution on a single loading cycle, and to extrapolate it over a certain range of subsequent cycles.

However, the size of the cycle jump is limited by the need to compute a smooth and stable evolution of wear. It has indeed been widely documented that choosing a too high value for the acceleration factor leads to the emergence of spurious oscillations on the computed wear profiles [Oqvist 2001, McColl et al. 2004, Mary and Fouvry 2007]. They originate from a too harsh surface geometry modification when the acceleration is too fast, leading to unstable wear computations. Palliative strategies such as smoothing wear profiles have been proposed to avoid unexpected instabilities [Basseville et al. 2019, Arnaud and Fouvry 2018].

This chapter investigates the use of alternative numerical integration schemes for the cycle jump. The use of various integration schemes to perform a cycle jump has already been studied for example in the simulation of fatigue crack propagation [Loew et al. 2020]. Regarding wear simulation, implicit methods remain uncommon although they have been suggested by a few authors [Ben Dhia and Torkhani 2011, Stupkiewicz 2013]. The classically used cycle jump method is hereafter referred to as *forward Euler explicit* cycle jump, in contrast with the alternative cycle jump schemes proposed in this chapter. The use of other explicit integration schemes of the Runge-Kutta family is investigated and the stability domain of these different explicit schemes is determined. Thereafter, the use of a *backward Euler implicit* scheme is suggested for the cycle jump which proves to be unconditionally stable.

In addition, an original strategy is proposed to integrate a variable cycle jump throughout the computation. The local wear depth rate is generally quite high at the start of the simulation, then decreases as wear evolves and spans a larger surface. This leads to the idea that it is possible to progressively increase the acceleration factor throughout the computation. This is usually done based on a criterion related to the maximum wear depth increment per cycle [Põdra and Andersson 1999, McColl et al. 2004]. It is argued here that the wear profile enlargement rate probably provides a more suitable indicator to govern the acceleration factor evolution.

These developments are conducted assuming that wear obeys an energy-based law. This type of model is indeed much more mature in terms of numerical simulations than the alternative damage-based wear model proposed, which allows an easier implementation of the different cycle jump schemes. In addition, wear coefficient values identified on experimental tests using an energy wear law are available in the literature, enabling to compare the simulation results with experimental data more easily.

Overall, the strategies suggested in this chapter enable the simulation of wear evolution on high-cycle fretting wear in a more efficient manner. They are especially designed to be effective when the number of cycles to compute is important, which is interesting considering the typically high numbers of cycles performed in experimental tests. The simulation results with the different suggested numerical schemes are compared with experimental data obtained by Marc (2018) on

cylinder-plane fretting tests on high numbers of cycles, demonstrating the suitability of the computation processes proposed in this type of situation. The work reported in this chapter is the subject of a published article [Caradec et al. 2023].

4.2 Explicit cycle jump

Let us assume we want to compute wear evolution over a total number of N_{cyc} fretting cycles. The current fretting cycle number is denoted n, and we seek to compute the wear depth $h(x,n)$ for each point x of the contact surface and for n in $[0, N_{\text{cyc}}]$. Here, n is considered to be a continuous pseudo-time variable in accordance with the two time scales principle[1]. For the resolution, the interval $[0, N_{\text{cyc}}]$ is discretized into a set of K computed cycles $(n_k)_{1\leq k\leq K}$. An acceleration factor Δn is defined as the step between two consecutive computed cycles:

$$\Delta n = n_{k+1} - n_k. \tag{4.1}$$

Note that here, n_k and Δn are considered to be real numbers and not necessarily integers. This reduces the problem to the computation of only K fretting cycles. For now, the acceleration factor Δn is assumed to be constant.

Wear evolution is computed recursively on this set of cycles. The wear profile at cycle n_k is denoted $\boldsymbol{h_k} = \boldsymbol{h}(n_k)$[2]. An initial wear state $\boldsymbol{h_0}$ is defined, typically $h_0(x_i) = 0$ for every surface node x_i. Then, the recursive process is written:

$$\forall k \in \{0,1,\dots K-1\},\ \boldsymbol{h_{k+1}} = \boldsymbol{h_k} + \int_{n_k}^{n_{k+1}} \boldsymbol{\partial_n h}(n)\, dn, \tag{4.2}$$

$\boldsymbol{\partial_n h}$ being the cyclic wear rate, namely the incremental wear depth profile generated per fretting cycle. This relation defines the integral form of the cycle jump method.

4.2.1 Forward Euler explicit scheme

In practice, a variety of numerical schemes may be employed to approximate the integral term in Equation 4.2. The simplest one is the forward Euler explicit method which was already used in Chapter 3. The forward Euler explicit cycle jump reads:

$$\forall k \in \{0,1,\dots K-1\},\ \boldsymbol{h_{k+1}} = \boldsymbol{h_k} + \Delta n\, \boldsymbol{\partial_n h_k} \tag{4.3}$$

where $\boldsymbol{\partial_n h_k}$ is the cyclic wear rate computed at cycle n_k. This relation indeed defines an explicit scheme: based on the knowledge of the wear profile $\boldsymbol{h_k}$ at cycle n_k, the computation of a fretting cycle yields the wear rate $\boldsymbol{\partial_n h_k}$ which directly gives access to the wear profile $\boldsymbol{h_{k+1}}$ at cycle n_{k+1} using the acceleration factor Δn. Wear rate $\boldsymbol{\partial_n h_k}$ is computed through the incremental step-by-step simulation of one loading cycle, as it was described in Algorithm 3.1 (Chapter 3). This cycle jump

[1] See Section 3.2.4.

[2] As in Section 3.4.3, $\boldsymbol{h}$ designates the matrix of size $n_x \times 1$ with n_x the number of surface nodes, whose components are the nodal wear depth values.

method is a first-order method and it requires a single evaluation of the wear rate to go from cycle n_k to cycle n_{k+1}.

The performances of this simple explicit cycle jump method are assessed on preliminary computations conducted on a low number of cycles. Fretting wear simulations are carried out on the cylinder-plane contact model presented hereinbefore, assuming bilateral wear on both cylinder and plane surfaces. Wear evolution is computed over $N_{\text{cyc}} = 300$ cycles. The parameters used are extracted from the experimental data of Marc (2018). The cylinder is subjected to a normal force $F_n = 3$ N/mm and the cyclic tangential displacement has an amplitude $\delta_0 = 80$ µm. The coefficient of friction experimentally measured is $\mu = 0.95$, and the energy wear coefficients are $\alpha_{\text{cyl}} = 2.32 \times 10^{-8}$ mm^3/mJ and $\alpha_{\text{pla}} = 3.14 \times 10^{-8}$ mm^3/mJ for the cylinder and the plane. The elastic properties are identical to those used in Chapter 3: $E = 200 \times 10^3$ MPa and $\nu = 0.3$.

Several computations are conducted with different acceleration factor values from $\Delta n = 1$ to $\Delta n = 30$ and different mesh refinements with element sizes from 1 µm to 12 µm. Depending on the acceleration factor and the mesh refinement, unexpected oscillations may arise on the mean contact pressure profiles computed at each cycle. Figure 4.1 shows that a computation run with $\Delta n = 3$ and mesh elements of 5 µm side yields smooth contact pressure profiles. On the opposite, strong disturbances appear with the same mesh size but an acceleration factor $\Delta n = 10$, or same acceleration factor but refined mesh with 1 µm elements.

These instabilities are observed in both space and time. They are indeed visible as well on the evolution of the local wear rate observed at different nodes from the plane surface throughout the 300 cycles. Figure 4.2 shows, for the same three computations, a stable case in which local wear rate evolves smoothly throughout the cycles unlike two unstable cases with strong variations from one computed cycle to the next.

These spurious instabilities originate from an imperfect computation of the contact pressure which is eventually reverberated on the dissipated energy distribution and the wear profile. These perturbations are enhanced by the use of an acceleration factor, and the modification of the surface geometry following a disturbed wear profile leads to an increasingly erroneous pressure computation, ultimately generating instabilities. The results obtained here show that there exists a critical acceleration factor value under which no oscillation is observed, and above which sharp oscillations quickly appear on the pressure profile. This critical value depends on the mesh refinement, and a finer mesh is detrimental regarding the instabilities.

4.2.2 Explicit Runge-Kutta methods

In an attempt to mitigate the instabilities, the use of higher-order explicit schemes is explored. We propose to investigate the use of Runge-Kutta schemes of order 2 and 4. Using a second-order Runge-Kutta scheme, the evolution of wear over the cycle jump reads:

$$\forall k \in \{0, 1, \dots K-1\},\ \boldsymbol{h_{k+1}} = \boldsymbol{h_k} + \Delta n\, \boldsymbol{\partial_n h_{k+1/2}} \tag{4.4}$$

where

$$\boldsymbol{\partial_n h_{k+1/2}} = \boldsymbol{\partial_n h}\left(\boldsymbol{h_k} + \frac{1}{2}\Delta n\, \boldsymbol{\partial_n h_k}\right). \tag{4.5}$$

This method requires to evaluate the wear rate profile twice, which leads to the effective computation of two fretting cycles in order to go from cycle n_k to cycle n_{k+1}. Regarding the fourth-order

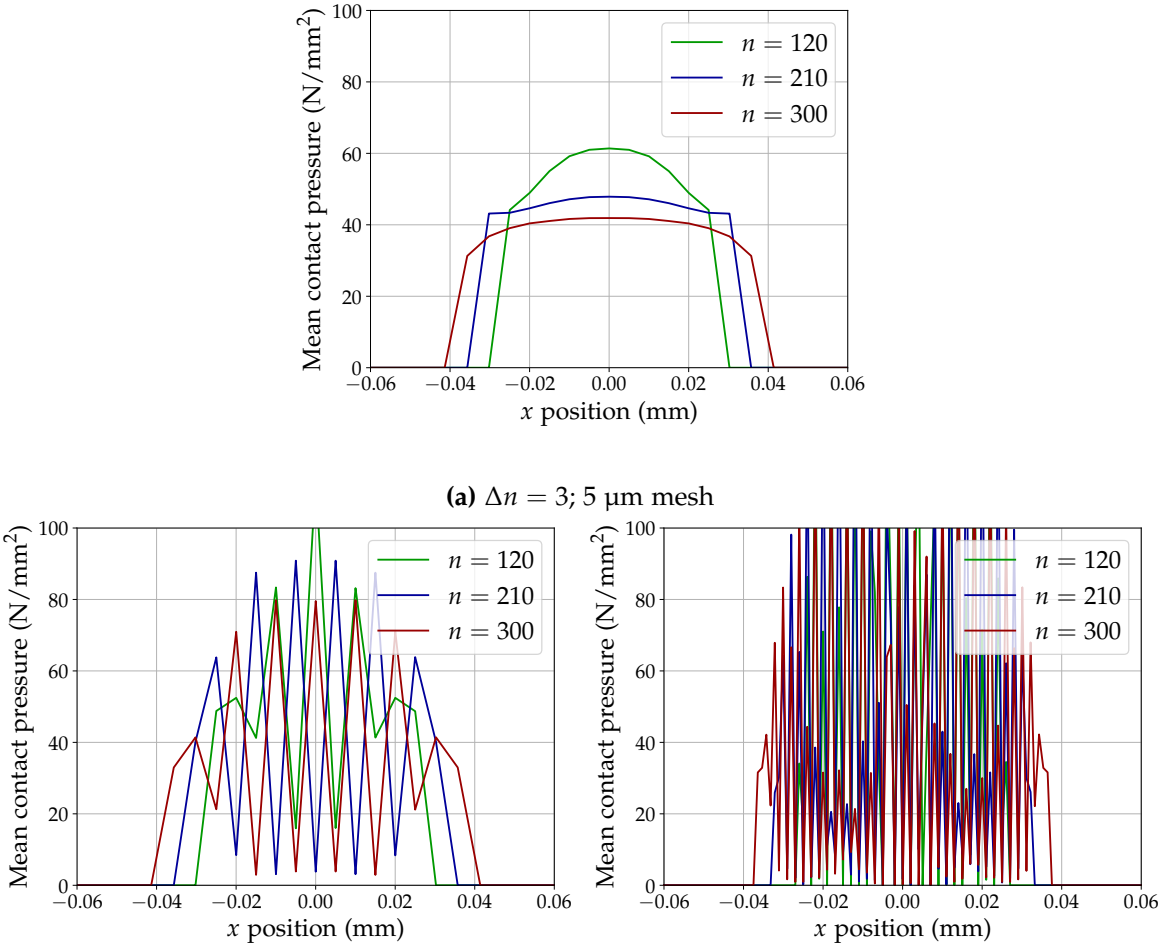

(a) $\Delta n = 3$; 5 µm mesh

(b) $\Delta n = 10$; 5 µm mesh

(c) $\Delta n = 3$; 1 µm mesh

Figure 4.1: Mean contact pressure profiles on the plane surface over cycles $n = 120$, $n = 210$, $n = 300$, computed with different acceleration factors and mesh refinements. (a) stable computation, (b), (c) unstable computations.

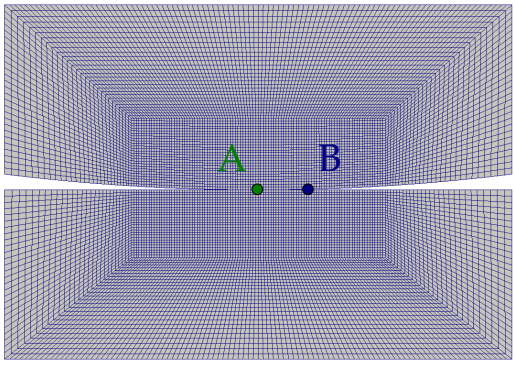

(a) Nodes A and B on the plane surface

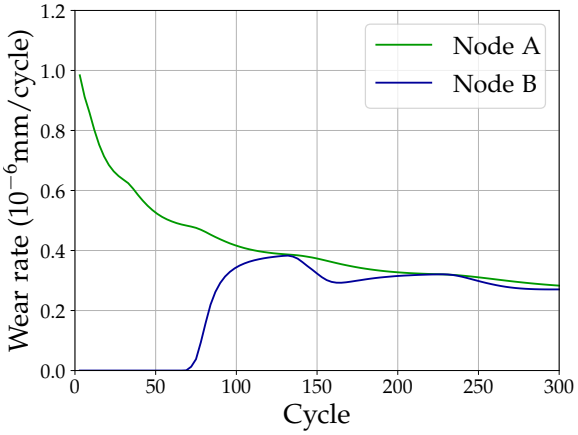

(b) $\Delta n = 3$; 5 µm mesh

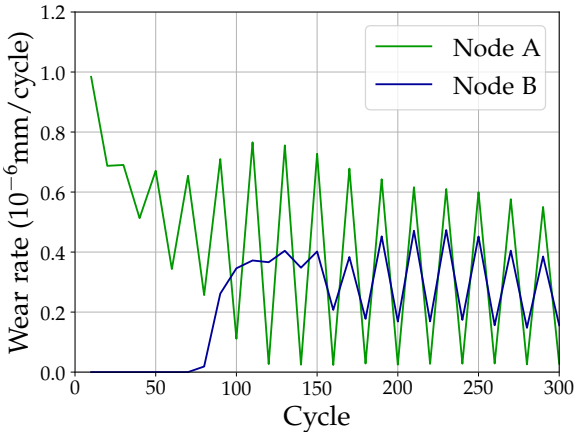

(c) $\Delta n = 10$; 5 µm mesh

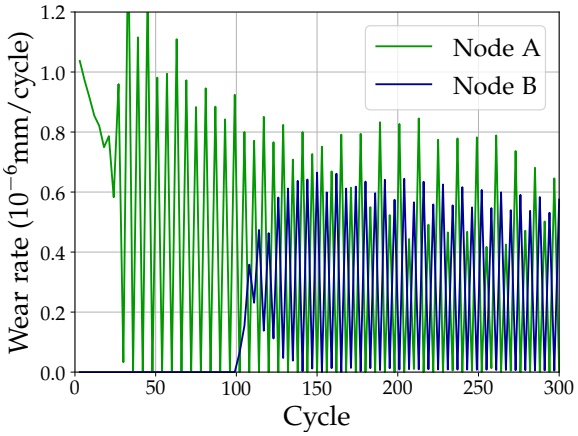

(d) $\Delta n = 3$; 1 µm mesh

Figure 4.2: Nodal wear rate evolution computed on two plane surface nodes with different acceleration factors and mesh refinements. (b) stable computation, (c), (d) unstable computations.

Runge-Kutta scheme, the computation of four fretting cycles is required:

$$\forall k \in \{0, 1, \dots K-1\},\ \boldsymbol{h_{k+1}} = \boldsymbol{h_k} + \frac{1}{6}\Delta n \left(\boldsymbol{\partial_n h_{k,1}} + 2\boldsymbol{\partial_n h_{k,2}} + 2\boldsymbol{\partial_n h_{k,3}} + \boldsymbol{\partial_n h_{k,4}}\right) \tag{4.6}$$

where

$$\boldsymbol{\partial_n h_{k,1}} = \boldsymbol{\partial_n h_k} \tag{4.7}$$

$$\boldsymbol{\partial_n h_{k,2}} = \boldsymbol{\partial_n h}\left(\boldsymbol{h_k} + \frac{1}{2}\Delta n\, \boldsymbol{\partial_n h_{k,1}}\right) \tag{4.8}$$

$$\boldsymbol{\partial_n h_{k,3}} = \boldsymbol{\partial_n h}\left(\boldsymbol{h_k} + \frac{1}{2}\Delta n\, \boldsymbol{\partial_n h_{k,2}}\right) \tag{4.9}$$

$$\boldsymbol{\partial_n h_{k,4}} = \boldsymbol{\partial_n h}\left(\boldsymbol{h_k} + \Delta n\, \boldsymbol{\partial_n h_{k,3}}\right). \tag{4.10}$$

These schemes are more time-consuming than the forward Euler scheme, as they require to compute respectively two or four times more fretting cycles. In return, we can expect them to be more reliable especially when a high acceleration factor is used.

In order to compare the stability of the different explicit schemes, we map their respective stability domains in terms of acceleration factor and mesh refinement. For this purpose, a computation run with a certain acceleration factor Δn is said to be unstable when the root mean square (RMS) error of the pressure profile of the 300^{th} cycle compared to the same computation with $\Delta n = 1$ exceeds 5%. It is shown in the literature that in case of instabilities, they appear as early as the first fretting cycles, which is observed here as well [McColl et al. 2004, Mary and Fouvry 2007]. This leads to the assumption that if no instability appears during the first 300 cycles, it will not appear later.

With a forward Euler explicit scheme, a linear relation is observed between the critical acceleration factor and the mesh size, which is depicted in Figure 4.3. This indeed shows that refining the finite element mesh is detrimental regarding stability. This is in line with the conclusions of Johansson (1994), according to whom the critical time increment for stability in wear simulations is proportional to the size of the elements, and inversely proportional to the elastic modulus. Using higher-order Runge-Kutta schemes, the simulation results show instabilities as well beyond a certain critical acceleration factor. The critical acceleration factor is higher than with a forward Euler scheme. However, the stability domains show that even though they are more stable than the forward Euler scheme, they are not worth the computational cost increase. Indeed, these schemes require respectively two or four times more computations, and do not ensure a critical acceleration factor respectively two or four times greater than with the forward Euler scheme (Figure 4.3).

In order to mitigate or prevent the instabilities, palliative solutions may be envisioned. Basseville et al. proposed to use a Gaussian smoothing function in order to eliminate the perturbations [Basseville et al. 2019]. This showed good results in removing the instabilities, but the method has the disadvantage of slightly altering the shape of the profile. In particular, the smoothing may induce an undesired expansion of the wear profile toward the edges. Moreover, it requires to wisely choose the parameters the smoothing function: a moving average with a too large bandwidth will alter the profile shape too much, while a too narrow one will not remove the instabilities. Here, the choice is made not to use smoothing techniques.

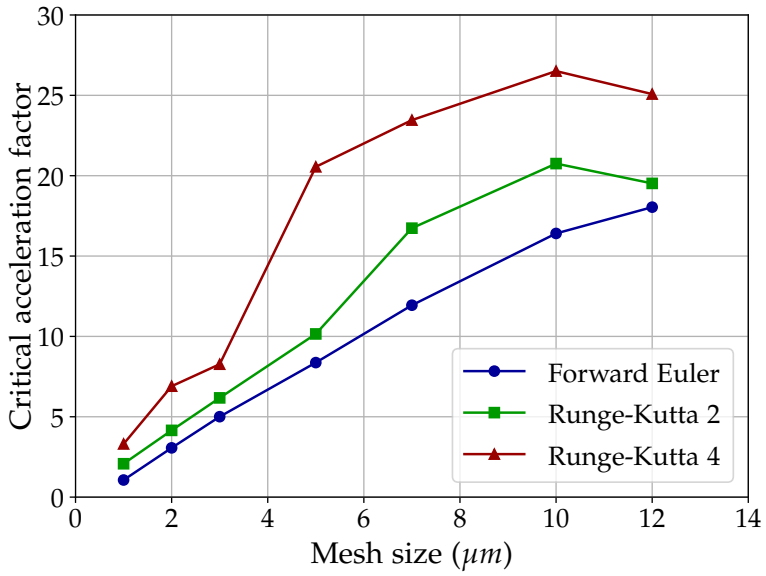

Figure 4.3: Stability limit for the different explicit cycle jump schemes in terms of critical acceleration factor with respect to the mesh size.

4.2.3 Influence of the contact formulation on instabilities

As the root cause of these spurious instabilities is a slightly flawed computation of contact pressure, it seems natural to attempt to improve its accuracy. It was mentioned in Section 3.4.1 that the contact conditions are enforced using a Lagrange multiplier method with a node-to-segment formulation. It is well-known that node-to-segment formulations are likely to deliver slightly oscillating contact pressure profiles, and that other formulations such as surface-to-surface mortar methods provide better results in this respect. As a consequence, a change in the contact formulation is attempted and the use of a mortar method is considered for wear simulations. Mortar methods were initially not available in the finite element code Cast3M employed here, so it was implemented for the sake of this study in the two-dimensional frictional contact case using linear elements only[3].

Wear simulations are conducted using a mortar method for contact conditions enforcement with a forward Euler explicit cycle jump scheme, and compared with the simulations presented in the previous section using a node-to-segment contact formulation. The simulations are performed using an acceleration factor $\Delta n = 10$ and a mesh of 2 µm elements size, which is a highly unstable situation with a node-to-segment contact formulation. Using a mortar method, the existence of spurious numerical instabilities is also exhibited. The analysis of the results however show that the oscillations magnitude in the contact pressure profiles is substantially reduced (Figure 4.4). A concordant observation is made on the evolution of nodal wear rate (Figure 4.5).

It is concluded that the use of a mortar method does not prevent the instabilities from occurring, although they are more limited. The use of mortar methods for frictional contact conditions enforcement is still appropriate in wear simulations because it enables to chose a higher acceleration factor while keeping a more stable explicit wear computation than with a node-to-segment formulation. In the following, the simulations presented are nevertheless being run using a node-to-segment contact formulation. This choice will not affect the conclusions drawn from the subsequent investigations presented.

[3]See Appendix A.

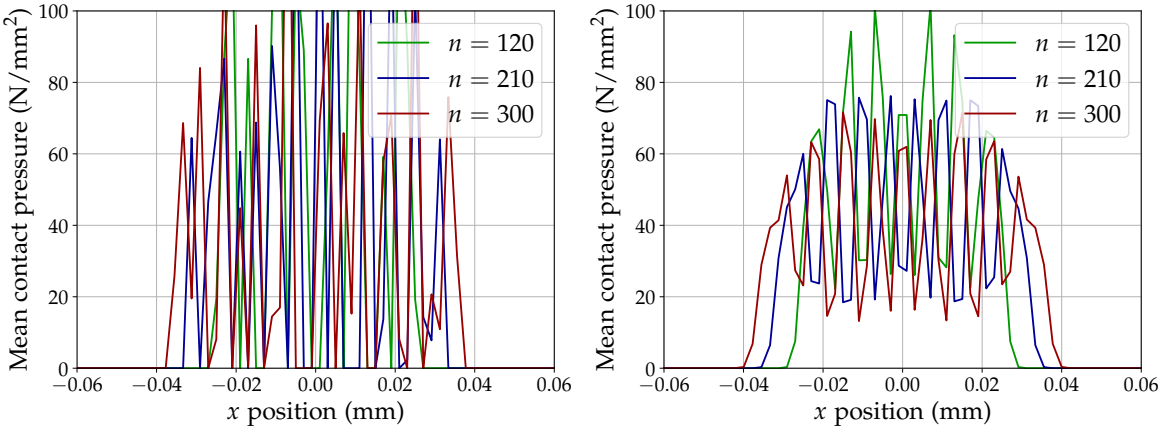

(a) Node-to-segment **(b)** Mortar

Figure 4.4: Mean contact pressure profiles on the plane surface over cycles $n = 120$, $n = 210$, $n = 300$, computed with $\Delta n = 10$ and 2 µm mesh. Comparison between (a) node-to-segment and (b) mortar contact conditions enforcement formulation.

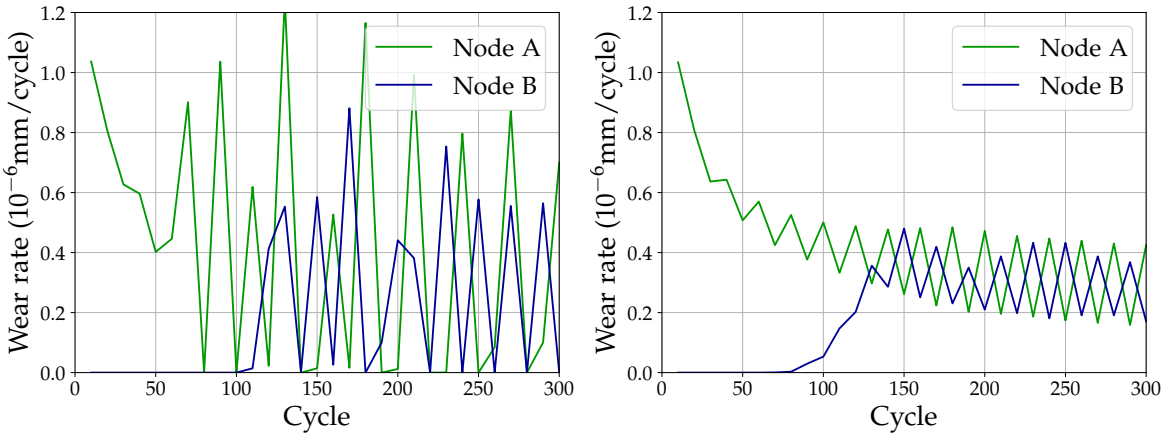

(a) Node-to-segment **(b)** Mortar

Figure 4.5: Nodal wear rate evolution computed on two plane surface nodes with $\Delta n = 10$ and 2 µm mesh. Comparison between (a) node-to-segment and (b) mortar contact conditions enforcement formulation.

4.3 Implicit cycle jump

4.3.1 Backward Euler implicit cycle jump scheme

Facing stability issues using explicit (pseudo-)time integration schemes, the use of implicit schemes is reasonably investigated. They are known to provide stable evolutions of the computed quantities and have been used in cycle jump methods for example by Loew et al. (2020) for the simulation of fatigue cracks propagation. In the case of wear simulations, they could help eliminate the instabilities from which explicit simulations suffer. Considering a backward Euler implicit scheme, the cycle jump relation reads:

$$\forall k \in \{0, 1, \dots K-1\},\ \boldsymbol{h_{k+1}} = \boldsymbol{h_k} + \Delta n\, \boldsymbol{\partial_n h_{k+1}}. \tag{4.11}$$

Here, the cycle jump relies on the wear rate $\boldsymbol{\partial_n h_{k+1}}$ computed at cycle n_{k+1} to calculate wear evolution between cycles n_k and n_{k+1}. Because the computation of $\boldsymbol{\partial_n h_{k+1}}$ requires the knowledge of $\boldsymbol{h_{k+1}}$, this scheme is indeed implicit and must involve the use of an iterative process to go from cycle n_k to n_{k+1}.

The iterative resolution of implicit schemes is often performed using a Newton-Raphson algorithm, which requires to compute a tangent term defined here as the Jacobian matrix of the wear rate, namely the derivative of the wear rate $\boldsymbol{\partial_n h}$ with respect to the wear depth $\boldsymbol{h}$. This computation is not straightforward and can be costly. Hence, a simpler fixed-point iteration scheme is used instead, which has the advantage of being a Jacobian-free method. In order to prevent non-convergence situations, a relaxation method is used along with the fixed-point scheme. This consists in progressively relaxing, or alleviating, the increment between two consecutive iterations of the fixed-point algorithm. As a result, the iterative algorithm for solving the backward Euler implicit scheme reads as follows.

- The first iteration is performed just as an explicit scheme: for $i = 0$,

$$\boldsymbol{h^0_{k+1}} = \boldsymbol{h_k} + \Delta n\, \boldsymbol{\partial_n h_k}. \tag{4.12}$$

- At each iteration i, we compute the wear rate $\boldsymbol{\partial_n h^i_{k+1}}$ based on the knowledge of the wear profile $\boldsymbol{h^i_{k+1}}$. The unrelaxed wear increment is then expressed

$$\boldsymbol{\delta h^i_{k+1}} = \boldsymbol{h_k} + \Delta n\, \boldsymbol{\partial_n h^i_{k+1}} - \boldsymbol{h^i_{k+1}}. \tag{4.13}$$

  Considering a relaxation exponent p_i, we prescribe

$$\boldsymbol{h^{i+1}_{k+1}} = \boldsymbol{h^i_{k+1}} + \frac{1}{2^{p_i}}\, \boldsymbol{\delta h^i_{k+1}}. \tag{4.14}$$

- Convergence is reached when

$$\frac{\|\boldsymbol{\delta h^i_{k+1}}\|}{\|\Delta n\, \boldsymbol{\partial_n h_k}\|} \leq \eta_0 \tag{4.15}$$

  where η_0 is the convergence tolerance.

Here, the relaxation exponent p_i is set to 0 for the first iteration, to 1 for the next two iterations, to 2 for the next four iterations, ..., to k for the next 2^k iterations, etc. It is noteworthy that if the relaxation exponent is equal to 0, then the classical expression for the fixed-point algorithm is retrieved. A fretting wear simulation process using this cycle jump scheme is described in Algorithm 4.1. It is obvious that with such an iterative algorithm, each iteration before convergence requires the finite element computation of one fretting cycle. As a consequence, the computational cost of the implicit scheme highly depends on the convergence rate of the iterative scheme.

Algorithm 4.1: Wear simulation process involving a backward Euler implicit cycle jump scheme.

I - Parameters definition
Set values for α, μ, δ_0, F_0, N_{cyc}, Δn, T, Δt, E, ν ;
II - Loading definition
Define J time steps per cycle: $\{t_1, \dots t_J\}$;
Define K computed cycles: $\{n_1, \dots n_K\}$;
for j *in* $\{1, \dots J\}$ **do**
  Define $F_n(t_j)$; `// Normal force`
  Define $\delta(t_j)$; `// Tangential displacement`
III - Initialization
Initiate $\boldsymbol{h_0} \leftarrow 0$; `// Total wear depth`
Perform one loading cycle to compute $\boldsymbol{\partial_n h_0}$; `// See Algorithm 3.1, IV`
IV - Iterative process
for k *in* $\{0, \dots K-1\}$ **do**
  Initiate iterative process: $i \leftarrow 0$;
  $\boldsymbol{h^0_{k+1}} \leftarrow \boldsymbol{h_k} + \Delta n\, \boldsymbol{\partial_n h_k}$;
  Update surface geometry with fictitious displacement $\Delta n\, \boldsymbol{\partial_n h_k}$; `// See Figure 3.15`
  Perform one loading cycle to compute $\boldsymbol{\partial_n h^0_{k+1}}$; `// See Algorithm 3.1, IV`
  $\boldsymbol{\delta h^0_{k+1}} \leftarrow \boldsymbol{h_k} + \Delta n\, \boldsymbol{\partial_n h^0_{k+1}} - \boldsymbol{h^0_{k+1}}$;
  while $\frac{\|\boldsymbol{\delta h^i_{k+1}}\|}{\|\Delta n\, \boldsymbol{\partial_n h_k}\|} > \eta_0$ **do**
    Set value of relaxation exponent p_i ;
    $\boldsymbol{h^{i+1}_{k+1}} \leftarrow \boldsymbol{h^i_{k+1}} + \frac{1}{2^{p_i}}\, \boldsymbol{\delta h^i_{k+1}}$;
    Update surface geometry with fictitious displacement $\frac{1}{2^{p_i}}\, \boldsymbol{\delta h^i_{k+1}}$;
    Perform one loading cycle to compute $\boldsymbol{\partial_n h^{i+1}_{k+1}}$; `// See Algorithm 3.1, IV`
    $\boldsymbol{\delta h^{i+1}_{k+1}} \leftarrow \boldsymbol{h_k} + \Delta n\, \boldsymbol{\partial_n h^{i+1}_{k+1}} - \boldsymbol{h^{i+1}_{k+1}}$;
    $i \leftarrow i+1$;
  After convergence: $\boldsymbol{h_{k+1}} \leftarrow \boldsymbol{h^i_{k+1}}$;
  $\boldsymbol{\partial_n h_{k+1}} \leftarrow \boldsymbol{\partial_n h^i_{k+1}}$;

Note that this way of solving the implicit scheme may not be optimal, as the fixed-point iterative algorithm does not ensure a quadratic convergence, which is the case for Newton-Raphson. In order to improve the convergence rate, other algorithms than the simple fixed-point scheme could be investigated.

Preliminary computations identical to those presented in Section 4.2 are carried out using the implicit scheme described. Results show that no instability has arisen as far as it has been tried. For example, as depicted in Figure 4.6, a computation with a mesh size of 5 µm and an acceleration factor $\Delta n = 30$ is highly unstable with the forward Euler scheme, but stable with the backward

Euler scheme. The use of a backward Euler implicit scheme thus allows to take an acceleration factor beyond the stability limit of the forward Euler scheme. However, a certain number of iterations are required for the scheme to converge, which increases the computational cost. The issue is then to determine whether the convergence is fast enough to compete with the forward Euler scheme. This will be assessed based on the results obtained on high-cycle fretting simulations dedicated to represented actual experimental tests.

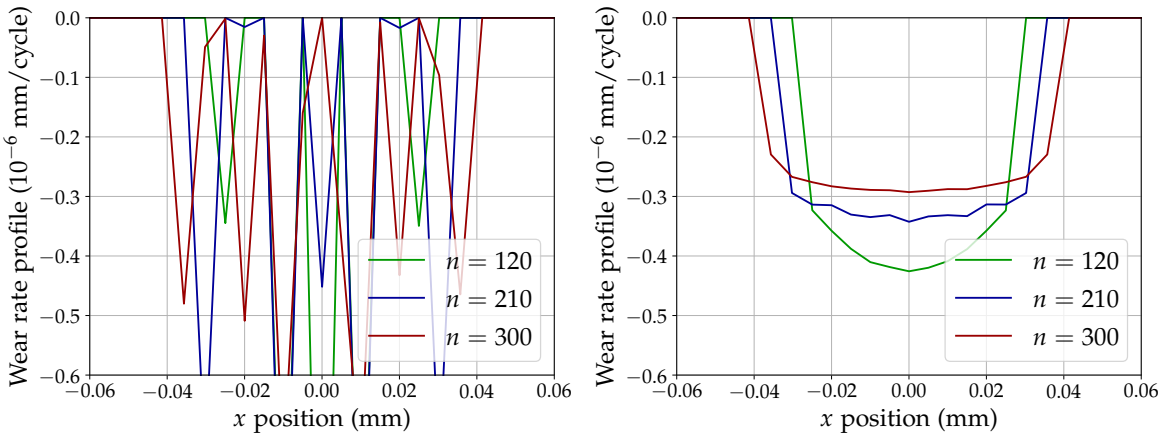

(a) Explicit cycle jump

(b) Implicit cycle jump

Figure 4.6: Wear rate profiles computed on the plane surface over cycles $n = 120$, $n = 210$, $n = 300$, with $\Delta n = 30$ and 5 µm mesh. Comparison between (a) an explicit cycle jump and (b) an implicit cycle jump.

4.3.2 Adaptive cycle jump

In addition to the implicit cycle jump method proposed, a strategy to use an adaptive cycle jump is explored. The idea behind the adaptive cycle jump is that local wear depth growth rate is rather high at the start, then progressively decreases as fretting cycles proceed. Thus, we may arguably think that a wise choice is to take a limited value for the acceleration factor at the start, then let it increase gradually over the cycles. In the literature, such feature is often introduced based on the maximal wear depth increase rate per cycle [Põdra and Andersson 1999, McColl et al. 2004]. The adaptive strategy is used together with the implicit scheme only, taking advantage of the unconditional stability it provides regardless of the acceleration factor value. Considering an adaptive acceleration factor, we denote Δn_k its value at cycle n_k. In the case of a criterion based on the maximal wear depth increment, we introduce $\Delta h_{0,\max}$ the maximum wear depth increment allowed between two consecutive computed cycles. The adaptive acceleration factor is then calculated as:

$$\Delta n_k = \frac{\Delta h_{0,\max}}{\max(\partial_n h_k)}. \tag{4.16}$$

Here, the adaptive acceleration factor is assumed to be computed based on an estimate of the wear profile enlargement rate instead. The faster the wear profile widens, the lower the acceleration factor. The wear profile width is denoted l, and its cyclic widening rate is

$$\partial_n l = \frac{\partial l}{\partial n}. \tag{4.17}$$

The adaptive acceleration factor is then assumed to be governed by

$$\Delta n_k = \frac{\Delta l_0}{\partial_n l_k} \tag{4.18}$$

where Δl_0 is the average width increment expected between two consecutive computed cycles.

Using this strategy requires to assess the enlargement rate at each computed cycle. For this purpose, the approximation of the wear profile width evolution introduced in Section 3.5.1 is used:

$$l(n) = l_0 + \kappa_1 n^{\kappa_2} \tag{4.19}$$

l_0, κ_1 and κ_2 being parameters of the approximation law. As a result, the enlargement rate is expressed:

$$\partial_n l(n) = \kappa_1 \, \kappa_2 \, n^{\kappa_2 - 1} \tag{4.20}$$

which yields for the acceleration factor:

$$\Delta n_k = \frac{\Delta l_0}{\kappa_1 \, \kappa_2} n^{1-\kappa_2} \tag{4.21}$$

The parameters κ_1 and κ_2 are estimated and reevaluated on a regular basis throughout the simulation using a Levenberg-Marquardt algorithm. This algorithm aims at solving non-linear least square problems and is used here to find the best fit κ_1 and κ_2 parameters with respect to the effectively computed wear profile width evolution.

Because this method would give very low values for the acceleration factor during the early cycles, a lower bound $\Delta n_{\min}$ is defined. In the end, the value used for the acceleration factor is derived as follows:

$$\Delta n_k = \max\left(\frac{\Delta l_0}{\kappa_1 \, \kappa_2} n^{1-\kappa_2}, \Delta n_{\min} \right). \tag{4.22}$$

4.4 Results and discussion

In order to investigate the performances of the different numerical schemes proposed, they are tried on two test cases aiming at simulating experimental tests carried out by Marc (2018). In their work, fretting tests are conducted on a cylinder-plane contact either in air or in an aqueous lithium-boron environment at atmospheric pressure and room temperature. The plane is made of 304L stainless steel while the cylinder is made of 316L stainless steel and is nitrided. Fretting tests conducted in air yield bilateral wear on both counterparts, whereas in a water environment wear is observed on the plane surface only.

The first test case considered here reproduces a bilateral wear situation obtained in a dry environment. A total number of $N_{\text{cyc}} = 100{,}000$ fretting cycles is performed under a normal load $F_n = 3 \text{ N mm}^{-1}$ with a displacement amplitude $\delta_0 = 80$ µm. A friction energy wear law is used. Based on the experimental measures, the coefficient of friction is $\mu = 0.95$ and the wear coefficients are respectively for the cylinder and the plane $\alpha_{\text{cyl}} = 2.32 \times 10^{-8}$ mm^3 mJ^{-1} and $\alpha_{\text{pla}} = 3.14 \times 10^{-8}$ mm^3 mJ^{-1}. The elastic properties for both solids are $E = 200 \times 10^3$ MPa and $\nu = 0.3$. In the finite element model, a mesh with 6 µm size elements is used. Three different computations are run: at first, a forward Euler explicit scheme is used with an acceleration factor

$\Delta n = 3$ in order to ensure a stable computation (see Figure 4.3). Thereafter, a backward Euler implicit scheme is used with a fixed acceleration factor $\Delta n = 30$. Finally, another implicit simulation is carried out with an adaptive cycle jump. The acceleration factor is set to $\Delta n_{\min} = 30$ at the start of the simulation, then is allowed to increase following Equation 4.22.

A second test case is presented in this section. It aims at simulating a fretting wear test conducted in an aqueous environment yielding unilateral wear on the plane surface. A total number of $N_{\text{cyc}} = 1{,}000{,}000$ fretting cycles is performed under a normal load $F_n = 3\ \text{N mm}^{-1}$ with a displacement amplitude $\delta_0 = 80$ µm. This time , the coefficient of friction is $\mu = 0.66$ and the wear coefficient on the plane is $\alpha_{\text{pla}} = 4.72 \times 10^{-9}\ \text{mm}^3\,\text{mJ}^{-1}$. The elastic properties remain unchanged. A slightly coarser mesh element size is used: 8 µm. In this case, a single simulation is run with a backward Euler implicit scheme and an adaptive cycle jump. The initial value for the acceleration factor is set to $\Delta n_{\min} = 40$.

The different simulations conducted are summarized in Table 4.1.

Table 4.1: Recap of the four simulations presented.

Sim.	Wear	N_{cyc}	F_n (N mm^{-1})	δ_0 (µm)	μ	α_{cyl} ($\text{mm}^3\,\text{mJ}^{-1}$)	α_{pla} ($\text{mm}^3\,\text{mJ}^{-1}$)	...
1	Bilat.	100,000	3	80	0.95	2.32×10^{-8}	3.14×10^{-8}	...
2	Bilat.	100,000	3	80	0.95	2.32×10^{-8}	3.14×10^{-8}	...
3	Bilat.	100,000	3	80	0.95	2.32×10^{-8}	3.14×10^{-8}	...
4	Unilat.	1,000,000	3	80	0.66	0	4.72×10^{-9}	...

...	Mesh size (µm)	Cycle jump	Δn
...	6	Explicit	3
...	6	Implicit	30
...	6	Implicit	Variable
...	8	Implicit	Variable

4.4.1 Numerical performances

As a first step, the computational cost of the different simulations conducted is assessed. At first order, the runtime is determined by the number of cycles effectively computed. As a result, the total number of fretting cycles effectively computed (including the cycles computed within the iterative process to solve the implicit scheme: each iteration involves one cycle computation) is considered here as a measure of the computational cost and is used to compare the simulations with one another.

Bilateral wear

Using a forward Euler explicit scheme with a fixed acceleration factor, the number of cycles computed overall is simply $N_{\text{cyc}}/\Delta n$ which gives $33,334$ cycles effectively computed for the considered case. Using a backward Euler implicit scheme, it depends on the number of iterations for convergence needed at every cycle. With a fixed acceleration factor $\Delta n = 30$, the evolution of the number of iterations per cycle throughout the computation is depicted in Figure 4.7a. First, one can note

that a few cycles do not reach convergence: when convergence has not been reached after 40 iterations, it is decided to jump to the next cycle even though the current cycle has not converged. The few unconverged cycles are checked a posteriori and it is ensured that the residual, albeit higher than the convergence criterion, is reasonably small. As they represent less than 10 computed cycles out of several thousands, we propose to leave these non-convergences aside. Apart from these few cycles, the number of iterations per cycle jump is between 5 and 10 for the early cycles, and decreases quickly: after a few hundred cycles, the implicit scheme converges often in one or two iterations. However, as it can be seen in Figure 4.7a, some cycles converge more slowly (4 or 5 iterations). These slowly converging cycles are regularly spaced and perfectly match the cycles at which the wear profiles enlarge. In other words, the cycles at which the implicit scheme converges slowly are the same as the cycles at which the evolution of the wear profile width has a discontinuity. This can be observed in Figure 4.7. These discontinuities happen frequently in the early cycles, and then occur less and less often. These remarks support the idea of using an adaptive acceleration factor based on the wear profile enlargement rate: the faster the wear profile enlarges, the lower the acceleration factor, and vice-versa. The cumulated number of cycles computed overall, including the cycle computation required for each iteration, is 7,353, yielding an equivalent acceleration factor $\Delta n_{\text{eq}} = 13.6$.

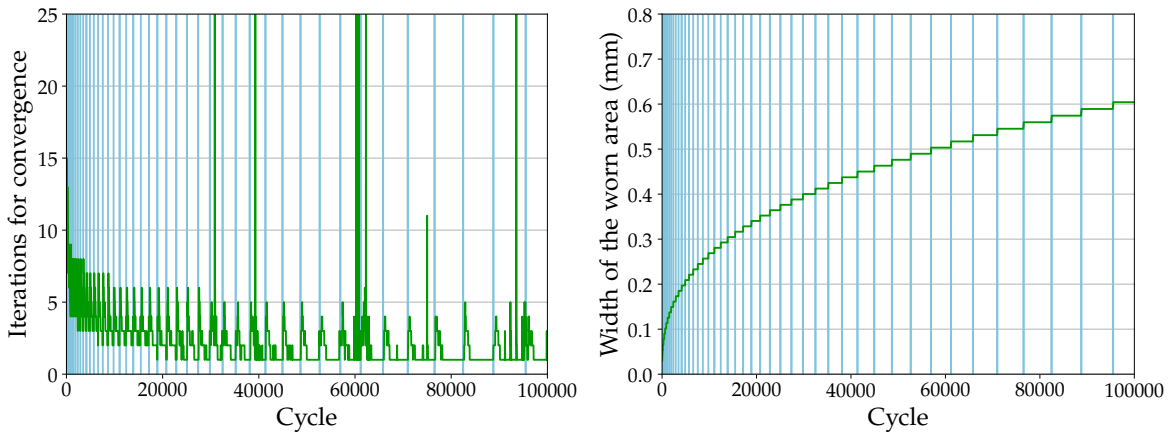

(a) Number of iterations per cycle **(b)** Evolution of the cylinder wear profile width

Figure 4.7: Evolution of (a) the number of iterations per cycle for convergence and of (b) the width of the wear profile on the cylinder surface, for a bilateral wear simulation conducted on 100,000 cycles with an implicit cycle jump. The blue vertical lines on both figures show the discontinuities in the wear profile width evolution. They are determined based on (b) and then reported on (a).

Using an adaptive cycle jump, the evolution of the acceleration factor is depicted in Figure 4.8. Its value is initialized with $\Delta n_{\text{min}} = 30$ and then increases gradually to reach over 80 at the end of the simulation. The evolution of the number of iterations for convergence and the evolution of the cumulated number of cycles effectively computed are shown in Figure 4.9. Overall, a total number of 6,704 cycles has been computed leading to $\Delta n_{\text{eq}} = 14.9$. Figure 4.9 illustrates the efficiency of the implicit scheme to compute a high number of cycles. The greater the number of computed cycles, the lower the computational cost per cycle. Moreover, using an adaptive cycle jump is beneficial for high cycle computations.

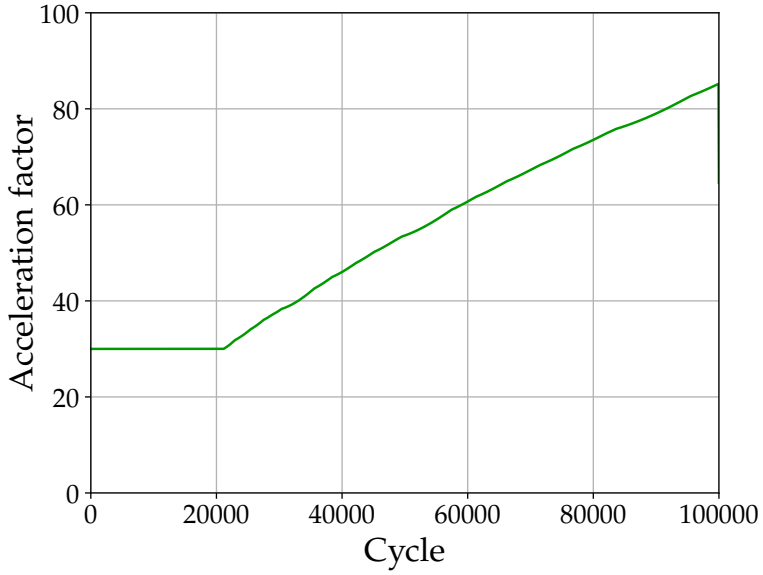

Figure 4.8: Evolution of the acceleration factor for a bilateral wear simulation conducted on 100,000 cycles with an adaptive implicit cycle jump.

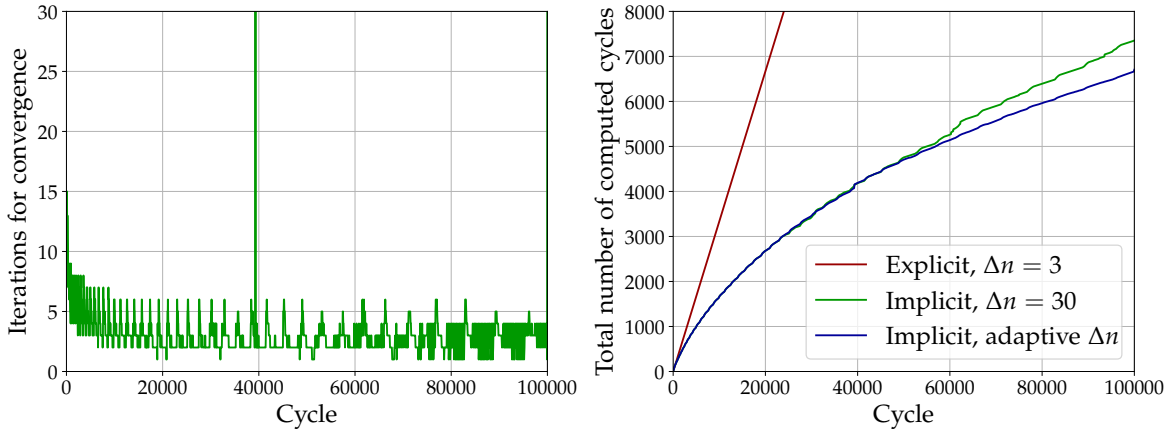

(a) Number of iterations per cycle **(b)** Cumulated number of cycles computed

Figure 4.9: Evolution of (a) the number of iterations per cycle for convergence and of (b) the cumulated number of cycles effectively computed, for a bilateral wear simulation conducted on 100,000 cycles with an adaptive implicit cycle jump.

Unilateral wear

The unilateral wear simulation on 1,000,000 cycles conducted with an adaptive implicit cycle jump confirms that the implicit scheme combined with a variable acceleration factor is relevant for high-cycle computations. The acceleration factor increases throughout the simulation to reach more than 1,300 at the end (Figure 4.10). The evolution of the number of iterations per cycle is depicted in Figure 4.11a and the cumulated number of cycles effectively computed is shown in Figure 4.11b. Overall, a total of 4,960 cycles has been computed to simulate 1,000,000 cycles leading to an equivalent acceleration factor $\Delta n_{\text{eq}} = 201.6$.

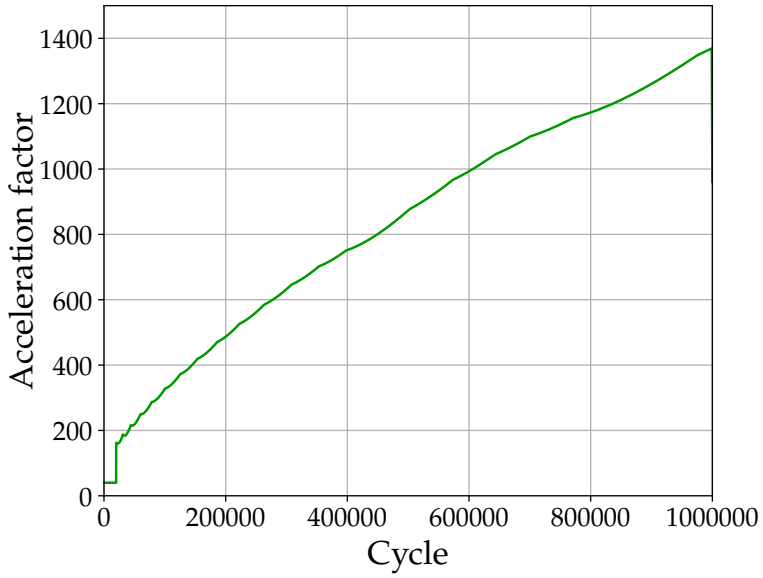

Figure 4.10: Evolution of the acceleration factor for a unilateral wear simulation conducted on 1,000,000 cycles with an adaptive implicit cycle jump.

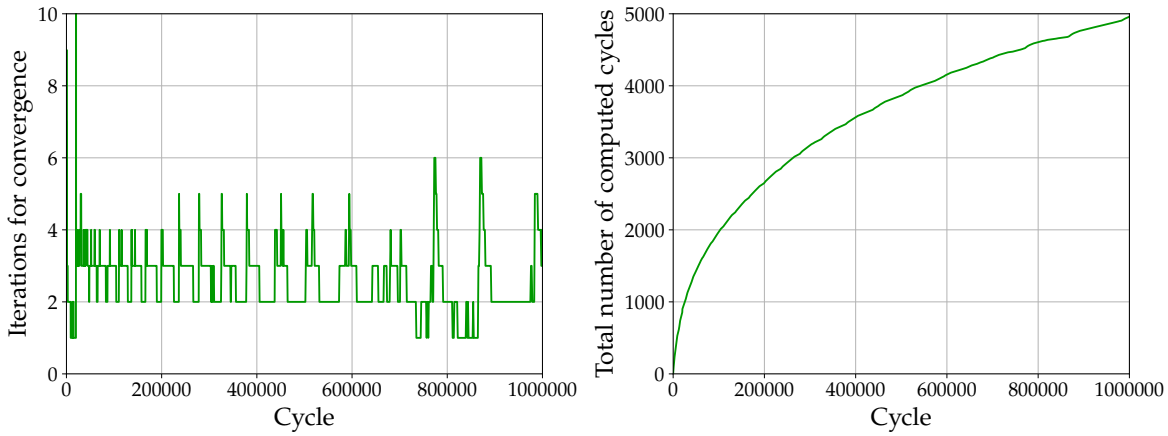

(a) Number of iterations per cycle **(b)** Cumulated number of cycles computed

Figure 4.11: Evolution of (a) the number of iterations per cycle for convergence and of (b) the cumulated number of cycles effectively computed, for a unilateral wear simulation conducted on 1,000,000 cycles with an adaptive implicit cycle jump.

As a conclusion, it is noted that the more cycles we need to compute, the more an implicit scheme is beneficial compared with an explicit scheme. Moreover, considering an adaptive cycle

jump based on the wear profile enlargement rate is relevant with an implicit cycle jump.

4.4.2 Numerical results analysis

Wear evolutions computed for both bilateral and unilateral wear cases are described in this section. In the bilateral wear case, all three simulations delivered identical results in terms of wear profile. The results presented here are extracted from the explicit simulation. As for the unilateral wear simulation, they were obtained using an implicit cycle jump.

Bilateral wear

First, the evolution of wear rate profiles is shown in the bilateral wear case on both cylinder and plane surfaces (Figure 4.12). During the early cycles, wear rate is concentrated in a limited central zone of the contact surface and the local wear depth increment per cycle is quite high. As cycles proceed, the incremental wear volume per cycle is constant but is distributed more uniformly on the surface: wear rate profiles expand and the local wear depth increment per cycle is lower. The resulting evolution of total wear depth profiles throughout the cycles is presented in Figure 4.13 for both surfaces.

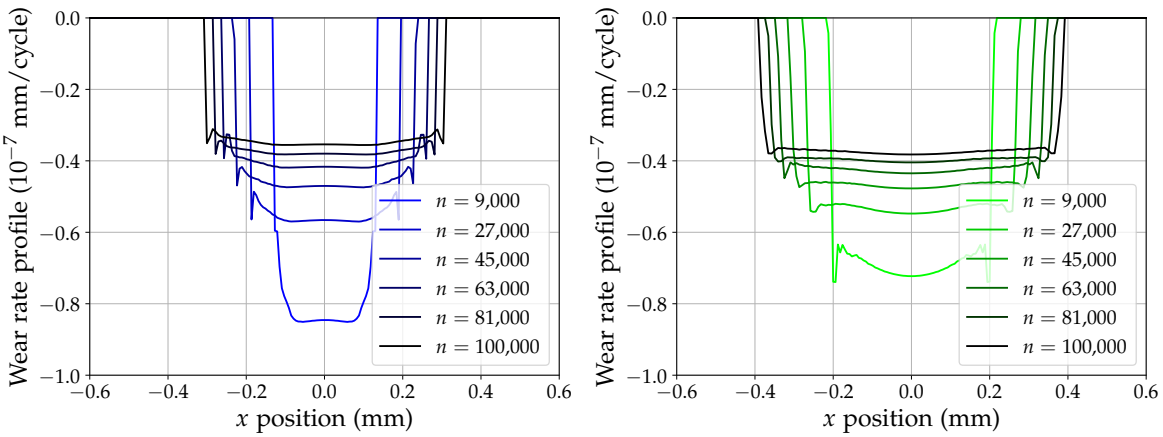

(a) Cylinder **(b)** Plane

Figure 4.12: Evolution of wear rate profiles on (a) the cylinder surface and (b) the plane surface, for a bilateral wear simulation conducted on 100,000 cycles.

After 100,000 fretting cycles, the surface geometries have changed generating altered contact conditions compared with the initial situation. Figure 4.14 compares the stress states computed in the initial unworn cylinder-plane configuration with respect to the worn configuration after 100,000 cycles. On can note that the contact spans a larger area after wear has occurred, leading to a lower maximum von Mises stress. After 100,000 cycles, the maximum von Mises stress is divided by nearly four.

Unilateral wear

A similar evolution of wear profiles is computed in the unilateral wear case. The evolution of wear rate profiles on the plane surface is depicted in Figure 4.15a and wear depth profiles in

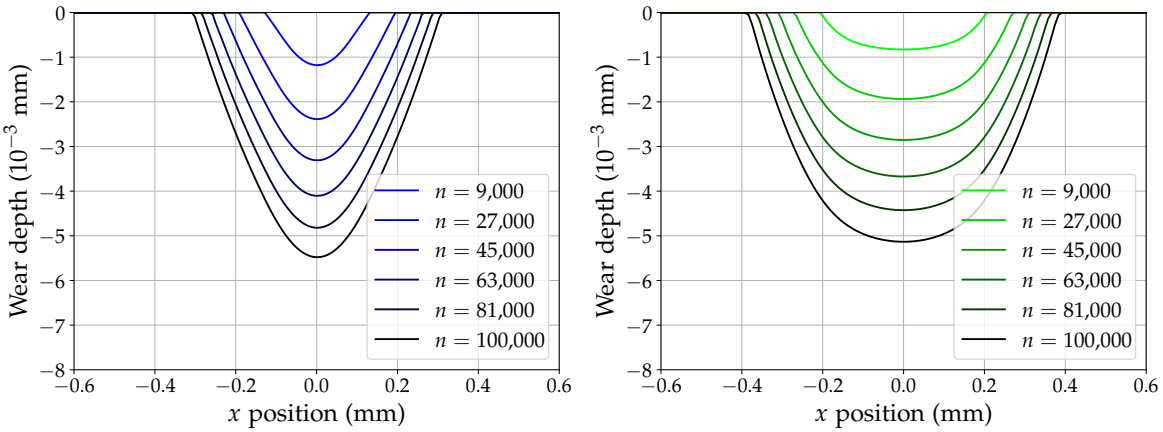

(a) Cylinder **(b)** Plane

Figure 4.13: Evolution of wear profiles on (a) the cylinder surface and (b) the plane surface, for a bilateral wear simulation conducted on 100,000 cycles.

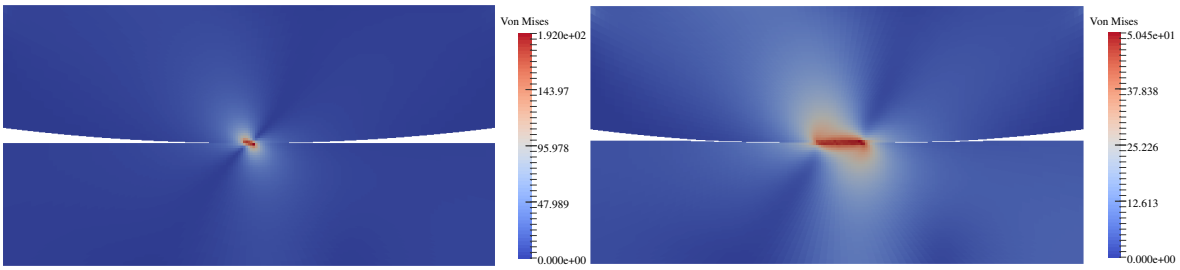

(a) Initial state **(b)** After 100,000 cycles

Figure 4.14: Von Mises equivalent stress computed (a) in the initial configuration and (b) in the worn configuration, for a bilateral wear simulation conducted on 100,000 cycles.

Figure 4.15b. Wear rate is about one order of magnitude lower here than in the previous bilateral test case, generating after 1,000,000 cycles a wear depth of the same order of magnitude as in the previous case after 100,000 cycles. The maximum wear depth is about 7 µm here. A similar wear profile expansion both in depth and width is captured here as well throughout the simulation.

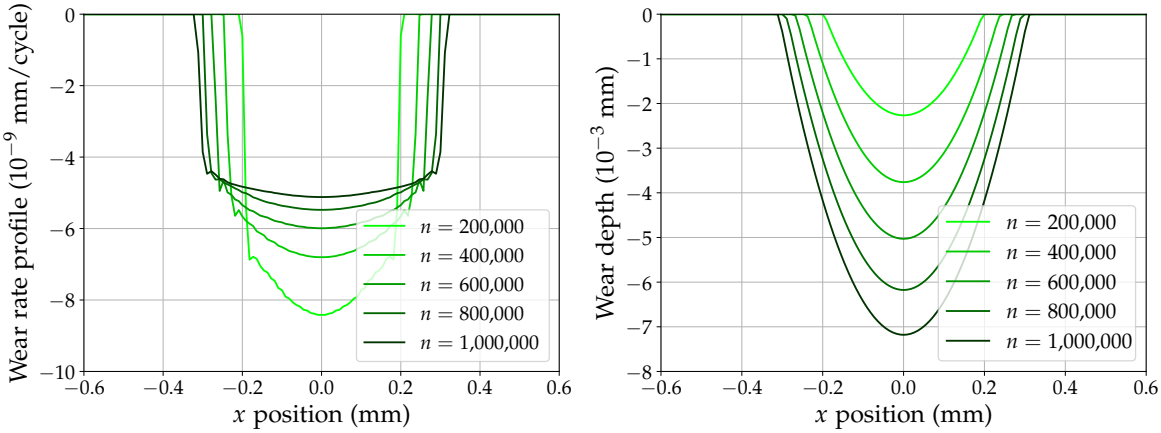

(a) Wear rate profiles **(b)** Wear profiles

Figure 4.15: Evolution of (a) wear rate profiles and (b) wear profiles on the plane surface for a unilateral wear simulation conducted on 1,000,000 cycles.

Von Mises equivalent stress is computed in the worn configuration and compared with the initial configuration (Figure 4.16). In this case as well the enlargement of the contact area is noted, leading to a reduced maximum stress.

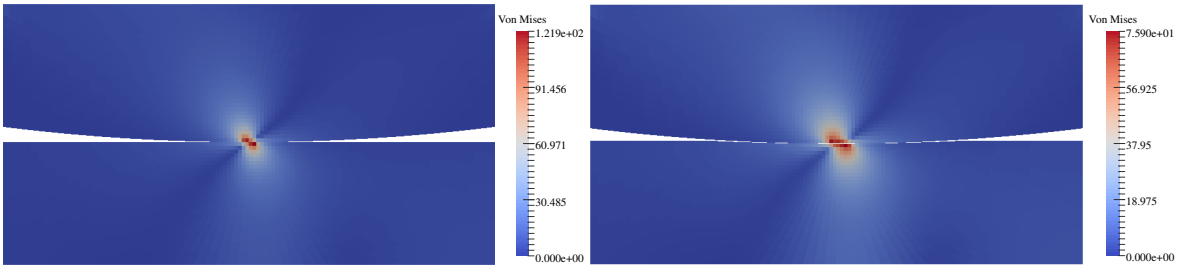

(a) Initial state **(b)** After 1,000,000 cycles

Figure 4.16: Von Mises equivalent stress computed (a) in the initial configuration and (b) in the worn configuration, for a unilateral wear simulation conducted on 1,000,000 cycles.

4.4.3 Comparison with experimental data

The results of the finite element simulations are compared with experimental data. The experimental data available are the evolution throughout the test of the tangential displacement and tangential force, and the final wear profile. The knowledge of tangential displacement and force enables to build fretting loops throughout the experiment and to infer the evolution of the energy dissipated per cycle. In the following, the evolution of the energy dissipated per cycle, the mean fretting loop over the experiment and the final wear profiles are compared with the numerical results for both bilateral and unilateral wear tests.

Bilateral wear

In the bilateral wear case, the evolution of the energy dissipated per cycle is depicted in Figure 4.17a. The comparison between experimental and numerical results shows a good correlation: the dissipated energy measured experimentally is relatively steady and is close to the energy computed numerically which is constant throughout the simulation. In addition, the numerical result is accurately captured by the approximation $E_d = 4\mu F_n \delta_0$. This is consistent with the form of the fretting loop (Figure 4.17b) which indicates a gross slip fretting regime with a high slope at the direction changes.

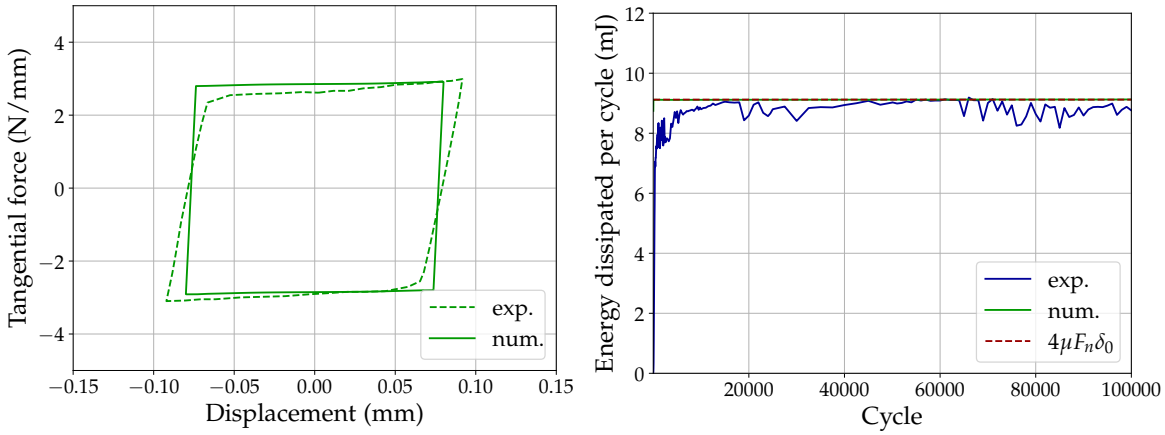

(a) Mean fretting loop

(b) Energy dissipated per cycle

Figure 4.17: (a) Mean fretting loop and (b) evolution of the energy dissipated per cycle, for a bilateral wear simulation conducted on 100,000 cycles.

The comparison of the experimental and numerical wear profiles is shown in Figure 4.18. On the cylinder surface, the computed wear profile has the same V shape as in the experiment, though slightly deeper and wider. On the plane surface however, the W-shaped profile obtained experimentally could not be represented by this numerical model. This was expected, given that the model presented here does not integrate a plastic behavior on the one hand, which makes the simulation of the plastic edge bumps impossible. On the other hand, the W shape is presented by Marc (2018) as resulting from a pile-up of compacted third body debris at the center of the wear scar, which is not represented here either.

Unilateral wear

In the aqueous environment unilateral wear test case, we do not dispose of the experimental data for the evolution of the fretting loops and dissipated energy. Only the numerical and experimental wear profiles are compared. Wear profiles after 1,000,000 fretting cycles are compared in Figure 4.19. In this case, the experimental wear profile on the plane surface displays a V shape which is accurately retrieved numerically.

The comparison between experimental and numerical results shows that the simulation processes enable to reproduce experimental wear profiles to a certain extent. If experimental profiles display a V shape, the comparison with the numerical results shows a good accuracy. However, some experimental profiles show a W shape that our simulation process has more trouble representing.

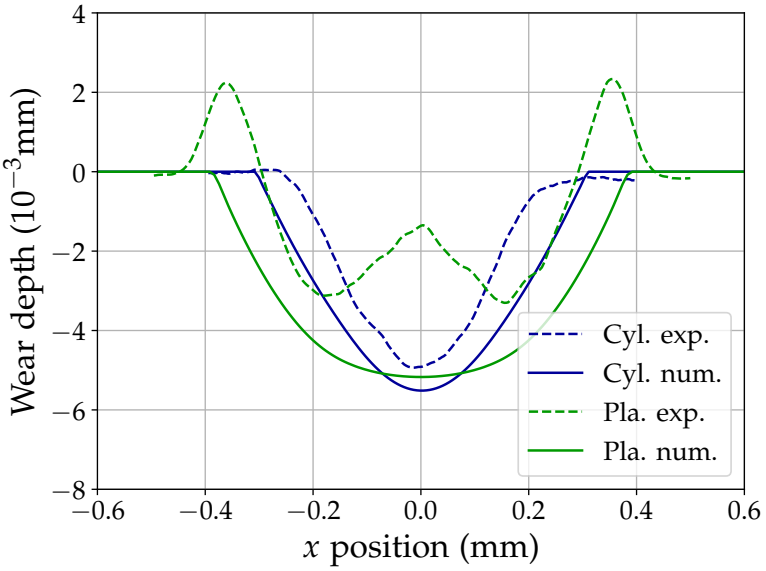

Figure 4.18: Comparison of the experimental and numerical wear profiles obtained in the bilateral wear case on the plane surface after 100,000 cycles.

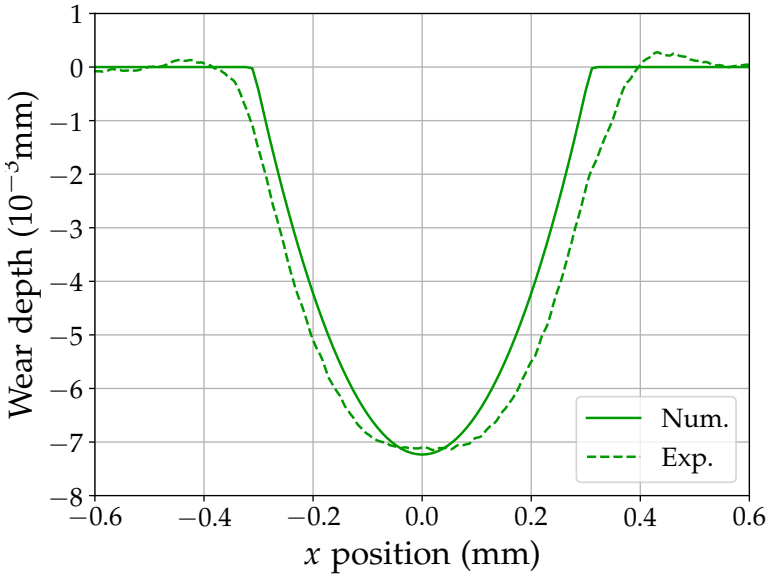

Figure 4.19: Comparison of the experimental and numerical wear profiles obtained in the unilateral wear case on the plane surface after 1,000,000 cycles.

4.5 Conclusion

The simulation framework presented here aims at efficiently simulating wear occurring at the contact between two solids under a fretting loading. The cycle jump classically used in finite element simulations of wear which was introduced in the previous chapter is extensively studied in the present chapter. The use of different integration schemes for the cycle jump is explored. As it was already observed in previous studies, it is confirmed here that using an explicit scheme can lead to unexpected oscillations which limits the acceleration factor value. On the opposite, results show that an implicit scheme succeeds to prevent these instabilities, and its convergence is fast enough to decrease the computational cost. This is especially true when the simulation of high numbers of cycles is needed, in which case the use of an implicit cycle jump integration scheme is recommended. In addition, choosing an adaptive acceleration factor based on the wear profile enlargement rate is beneficial for high-cycle computations. Such criterion for an adaptive acceleration factor has the additional advantage of removing the need for the user to chose an appropriate acceleration factor value. This choice may be tricky and relies entirely on the experience of the user. Using an adaptive acceleration factor based on the wear profile enlargement rate helps overcome this difficulty by providing a parameter that one can easily relate to the mesh elements size. It is also noted that although these conclusions were drawn using a friction energy wear law, they are likely to hold true with different wear laws.

On this basis, outlooks include investigating alternative integration schemes that might be used. One might for example consider higher-order numerical resolution schemes for the cycle jump, or hybrid implicit-explicit methods such as Crank-Nicolson. In addition, alternative iterative algorithms may be considered for the resolution of the implicit cycle jump. While the fixed-point algorithm has the advantage of being a Jacobian-free method, other choices can be made and may improve the convergence.

The ability of the numerical model presented to simulate experimental fretting wear tests is also assessed. The numerical processes implemented allow for the simulation of high-cycle experimental fretting tests and the numerical results are compared with experimental data. The wear profiles obtained numerically and experimentally match to some extent. The interest of this kind of simulation lies in the fact that it enables to derive local quantities (wear depth distribution, contact stresses, distribution of dissipated energy density, etc.) based on the experimental measure of global quantities (total wear volume, total dissipated energy, etc.). Some experimentally observed features may however not be represented using such numerical models in which third body is not represented. As a result, the simulation framework developed is especially suitable when debris transport out of the contact is easily achieved. In order to better capture the complex processes involved in wear damage, including the effects of third body and plastic behavior would be a valuable asset. Regarding plasticity, being able to simulate smooth surface geometry evolutions following wear is of utmost importance to accurately compute plastic strains. In this respect, the numerical methods implemented demonstrate their relevance. Taking plasticity into account is however not straightforward when using a cycle jump. As a matter of fact, the knowledge of the plastic strains evolution during one cycle gives little to no information on how it will evolve through the next cycles and extrapolating the behavior of a single cycle seems expeditious.

Chapter recap

In virtue of the time scales decoupling introduced in Chapter 3, a cycle jump method is used in wear simulations. The use of different integration schemes is explored together with it.

- Wear simulation processes presented in the literature typically use a forward Euler explicit scheme. It is well-known that it generates spurious instabilities when the acceleration factor is too high, which is witnessed here as well. The critical acceleration factor for stability is found to be proportional to the mesh elements size: a finer mesh is detrimental regarding cycle jump stability.
- The use of explicit Runge-Kutta schemes of order 2 and 4 is also investigated. While they prove to be slightly more stable than the forward Euler explicit scheme, they are not worth the computational cost increase related to the need to perform respectively two or four cycle computations on each cycle jump.
- A backward Euler implicit scheme succeeds to remove the instabilities. The implicit scheme is solved using a fixed-point iterative algorithm with a relaxation strategy.

The numerical performances of the implicit scheme are assessed on high-cycle test cases enabling to simulate experimental tests from the literature.

- In the simulations carried out, the implicit scheme converges most of the time in less than 5 or 6 iterations using an acceleration factor several times higher than the explicit stability limit, which demonstrates its benefits over the explicit method.
- The convergence of the implicit scheme is more costly during the early cycles. The further the cycles proceed, the faster the implicit scheme converges, which shows that the method is especially well suited to simulate high numbers of cycles.
- On a regular basis, some cycles take longer to converge. It turns out that these cycles correspond to the cycles for which the wear profile expands: each time a previously unworn surface node gets integrated to the wear profile, more iterations are required to converge. Because wear profiles expand quickly during the early cycles then more and more slowly, the idea of choosing an adaptive acceleration factor governed by the wear profile enlargement rate emerges. By doing this, the acceleration factor value is limited at first, then progressively increases throughout the computation. This enables to accelerate the simulation compared with a fixed acceleration factor.

Finally, the numerical results are compared with experimental data.

- The experimental data available may be retrieved numerically to some extent. In the unilateral wear situation, the experimental wear profile obtained in an aqueous environment displays a V shape and is accurately calculated using the computational methods presented.
- In the bilateral wear situation however, fretting tests conducted in dry air yield a W-shaped wear profile on the plane surface with plastic bumps on the edges. These features may not be reproduced by the numerical methods used here.

Chapter 5

Wear simulation with an elastoplastic material behavior

A numerical strategy to compute the evolution of plastic strain together with wear

5.1 Introduction

The major role played by plastic deformation in fretting wear mechanisms of ductile metals has been highlighted in Chapter 1. Surface degradation leading to particles detachment is often correlated with an accumulation of near-surface plastic strains [Waterhouse 2000, Fouvry et al. 2001]. Maouche et al. associate wear occurring under gross slip fretting regimes with plastic shakedown or ratchetting cyclic plasticity[1] [Maouche et al. 1997]. The accumulation of plastic strain is described as the source of the development of a material layer that has undergone significant microstructural transformations, known as a tribologically transformed structure (TTS) layer [Rigney et al. 1984, Sauger et al. 2000]. In addition, fretting motion may induce a plowing effect resulting in the formation of plastic deformation bumps on the edges of the wear scar [Elleuch and Fouvry 2002]. As a consequence, being able to simulate the evolution of plastic strain together with wear would be a great asset in the understanding of fretting wear degradation mechanisms.

The integration of path-dependent material behavior models into the wear simulation frameworks presented so far raises however some issues. This is mainly related to the systematic use of a cycle jump, as it was outlined by Lengiewicz and Stupkiewicz (2012). Indeed, a specific treatment needs to be considered for the possibly non-linear evolution of additional internal variables over the cycle jump. Regarding plasticity, Johnson's shakedown theory indicates that several regimes may be identified for the cyclic evolution of plastic strain [Johnson 1985]. One has to manage the evolution of the plastic strain state over the cycle jump depending on the cyclic plasticity regime in question. This explains why few numerical studies on wear integrate a material behavior with plasticity.

In this regard, one may still mention numerical studies by Feng and Xu (2006) and Basseville et al. (2013) that take into account plasticity in fretting wear simulations. These studies do not integrate a cycle jump, which limits the number of fretting cycles that may be computed. Mohd Tobi et al. (2009) propose to integrate an elastoplastic material behavior model within a fretting wear finite element simulation framework initially developed by McColl et al. (2004). They aim at simulating a plowing effect observed experimentally. They use a cycle jump on wear profile evolution, but the evolution of plastic strain and hardening variables over the cycle jump is not described. In a subsequent article, they simulate the accumulation of plastic strain as a post-processing treatment of a fretting wear simulation [Mohd Tobi et al. 2017]. In this work, a fretting wear simulation is conducted as a first step using a cycle jump. Thereafter, a few cycles are selected with the corresponding wear profiles and additional computations are carried out to simulate the accumulation of plastic strain in the worn configurations. The subsequent computations are run on 5 consecutive fretting cycles with no cycle jump and without considering further evolution of wear during these 5 cycles. In a more recent study, Zhang et al. (2019) perform fretting wear simulations including the presence of a third body debris bed and assuming an elastoplastic material behavior. The purpose is to investigate the effect of ratchetting on wear evolution. They use a cycle jump to compute wear profile evolution, which is applied to the evolution of cumulative plastic strain as well. However, all these studies do not fully tackle the issue of plastic strain evolution over the cycle jump. Indeed, when cyclic plasticity occurs the use of a cycle jump should integrate a description of the extrapolation performed on all the internal variables [Kiewel et al. 2000, Cojocaru and Karlsson 2006].

The present chapter attempts to tackle this question and suggests strategies for a proper treat-

[1] See Section 1.3.3 for the definition of elastic, elastic shakedown, plastic shakedown and ratchetting regimes.

ment of plastic strain and hardening variables evolution along with wear over large cycle jumps. Both plastic strain evolution and wear profile evolution interact because of the contact pressure alteration they induce. As a first step, an appropriate elastoplastic material behavior model is defined and identified. In order to represent the behavior of 304L and 316L stainless steels used in fretting tests conducted by Marc (2018), a Chaboche elastoplastic model accounting for non-linear isotropic and non-linear kinematic hardening is employed. In Section 5.3, a first approach to simulate fretting wear in elastoplasticity using a cycle jump is explored. In this framework, the same explicit cycle jump method is considered for both wear depth and plastic variables extrapolation. Based on the simulation of a single cycle, plastic strain and hardening variables are linearly extrapolated together with wear depth over a certain amount of subsequent cycles. Thereafter, an alternative approach is suggested in Section 5.4 which is based on the stabilized cyclic state for plasticity. It is assumed that the number of cycles for the structure to reach a stabilized state in terms of plastic strain is small compared with the characteristic number of cycles for significant wear evolution, allowing to estimate the stabilized plastic state at fixed wear. The asymptotic stabilized state is computed using the direct cyclic method (DCM).

The overall objective is to enable a finer description of wear degradation processes by providing methods for a proper estimation of plastic strain evolution throughout fretting cycles. The ability to simulate the coupled evolution of wear profiles and plastic strain not only allows for a more detailed knowledge of the mechanical state during fretting wear but could also enable to investigate the possible correlation between wear kinetics and accumulation of plastic strain.

5.2 Elastoplastic behavior model

5.2.1 Chaboche elastoplastic model

Plasticity designates a deformation mechanism that originates from the presence of dislocations in the crystal lattice on a microscopic scale and results in permanent deformations on a macroscopic scale. The behavior of ductile metals is often described using an elastoplastic model, which assumes that the behavior remains elastic for sufficiently low mechanical loadings and that plastic deformation occurs beyond a stress threshold. Various models exist that integrate different forms of hardening, leading to an evolution of the elastic domain depending on the material history. Elastoplastic models are path-dependent and rate-independent.

Let us express the total strain tensor $\underline{\underline{\varepsilon}}$ as the combination of an elastic strain $\underline{\underline{\varepsilon}}^{\mathrm{e}}$ and a plastic strain $\underline{\underline{\varepsilon}}^{\mathrm{p}}$:

$$\underline{\underline{\varepsilon}} = \underline{\underline{\varepsilon}}^{\mathrm{e}} + \underline{\underline{\varepsilon}}^{\mathrm{p}}. \tag{5.1}$$

To describe the transformations of the materials, the state variables considered here are the total strain $\underline{\underline{\varepsilon}}$, the plastic strain $\underline{\underline{\varepsilon}}^{\mathrm{p}}$ and a set of additional internal variables $\boldsymbol{\alpha}$. The state potential, chosen as the free energy ψ, is considered to be the sum of an elastic contribution ψ^{e} and a blocked free energy ψ^{α}:

$$\rho\psi(\underline{\underline{\varepsilon}}, \underline{\underline{\varepsilon}}^{\mathrm{p}}, \boldsymbol{\alpha}) = \rho\psi^{\mathrm{e}}(\underline{\underline{\varepsilon}} - \underline{\underline{\varepsilon}}^{\mathrm{p}}) + \rho\psi^{\alpha}(\underline{\underline{\varepsilon}}^{\mathrm{p}}, \boldsymbol{\alpha}) \tag{5.2}$$

where ρ is the density. For linear elasticity,

$$\rho\psi^{\mathrm{e}}(\underline{\underline{\varepsilon}} - \underline{\underline{\varepsilon}}^{\mathrm{p}}) = \frac{1}{2}\left(\underline{\underline{\varepsilon}} - \underline{\underline{\varepsilon}}^{\mathrm{p}}\right) : \underline{\underline{\underline{\underline{C}}}} : \left(\underline{\underline{\varepsilon}} - \underline{\underline{\varepsilon}}^{\mathrm{p}}\right) \tag{5.3}$$

yielding[2]

$$\underline{\underline{\sigma}} = \rho \frac{\partial \psi}{\partial \underline{\underline{\varepsilon}}} = \underline{\underline{\underline{\underline{C}}}} : \left(\underline{\underline{\varepsilon}} - \underline{\underline{\varepsilon^{\mathrm{p}}}}\right) = \underline{\underline{\underline{\underline{C}}}} : \underline{\underline{\varepsilon^{\mathrm{e}}}} \tag{5.4}$$

$\underline{\underline{\sigma}}$ being Cauchy's stress tensor and $\underline{\underline{\underline{\underline{C}}}}$ the fourth-order elasticity tensor.

Then, the flow rule governing plastic strain evolution is defined by giving a yield function, which in the case of von Mises J_2-plasticity is a function of the second invariant of the deviatoric stress tensor $J_2(\underline{\underline{\sigma}})$. Let us write $\underline{\underline{\sigma^{\mathrm{d}}}}$ the deviatoric stress tensor:

$$\underline{\underline{\sigma^{\mathrm{d}}}} = \underline{\underline{\sigma}} - \frac{1}{3}\mathrm{Tr}(\underline{\underline{\sigma}})\underline{\underline{I}}. \tag{5.5}$$

We have

$$J_2(\underline{\underline{\sigma}}) = \frac{1}{2}\underline{\underline{\sigma^{\mathrm{d}}}} : \underline{\underline{\sigma^{\mathrm{d}}}} \tag{5.6}$$

and von Mises equivalent stress is

$$\sigma_{\mathrm{VM}} = \sqrt{3J_2(\underline{\underline{\sigma}})}. \tag{5.7}$$

A frequently used model to represent the cyclic behavior of ductile steels is Chaboche elasto-plastic model [Chaboche 1986]. It was used for example by Vor (2009), Lê (2013) and Dhahri (2019) to model the cyclic behavior of 304L and 316L stainless steels. It allows to account for both non-linear isotropic and non-linear kinematic hardening, respectively representing an expansion of the elastic domain size and a displacement of the elastic domain center. In this case, the yield function f is defined by:

$$f(\underline{\underline{\sigma}}, \underline{\underline{X}}, R) = \sqrt{\frac{3}{2}(\underline{\underline{\sigma^{\mathrm{d}}}} - \underline{\underline{X}}) : (\underline{\underline{\sigma^{\mathrm{d}}}} - \underline{\underline{X}})} - R \leq 0. \tag{5.8}$$

Here, $\underline{\underline{X}}$ is the *backstress* tensor and represents the displacement of the elastic domain center, and R is the elastic domain radius.

In the following, we use a two-center non-linear kinematic hardening with an evolution of the backstress verifying:

$$\underline{\underline{\dot{X}}} = \sum_{i=1}^{2} \underline{\underline{\dot{X}_i}} \tag{5.9}$$

and

$$\forall i \in \{1,2\},\ \underline{\underline{\dot{X}_i}} = C_i \left(\frac{2}{3} A_i \underline{\underline{\dot{\varepsilon}^{\mathrm{p}}}} - \dot{\varepsilon}_{\mathrm{c}}^{\mathrm{p}} \underline{\underline{X_i}}\right) \tag{5.10}$$

in which C_i and A_i are parameters to identify and $\varepsilon_{\mathrm{c}}^{\mathrm{p}}$ is the *cumulative plastic strain*:

$$\dot{\varepsilon}_{\mathrm{c}}^{\mathrm{p}} = \sqrt{\frac{2}{3}\underline{\underline{\dot{\varepsilon}^{\mathrm{p}}}} : \underline{\underline{\dot{\varepsilon}^{\mathrm{p}}}}}. \tag{5.11}$$

Non-linear isotropic hardening is governed by the evolution of the radius R, which is assumed to be a function of the cumulative plastic strain:

[2] See Equation 2.41.

$$R(\varepsilon_c^p) = \sigma_0 + R_M \left(1 - e^{-b\varepsilon_c^p}\right) \tag{5.12}$$

with σ_0 the initial elastic limit, and R_M and b parameters of the model. In addition, we also define the *equivalent plastic strain* as

$$\varepsilon_{eq}^p = \sqrt{\frac{2}{3}\underline{\underline{\varepsilon^p}} : \underline{\underline{\varepsilon^p}}}. \tag{5.13}$$

5.2.2 Parameters identification

We seek to identify the parameters of Chaboche elastoplastic model for 304L and 316L stainless steels at room temperature. For that, we use experimental data obtained by Vor (2009) on 304L stainless steel and by Lê (2013) on 316L stainless steel. In both cases, cyclic tension-compression tests were carried out with an imposed strain of amplitude $\Delta\varepsilon/2$ up to stabilization.

The identification process is as follows. We consider experimental tests conducted with $\Delta\varepsilon = 2\%$, and from the experimental stress-strain cyclic evolution we extract the first and last (stabilized) cycles. Then, a two-dimensional, axially symmetric finite element model of a cylindrical specimen is built (Figure 5.1a) and a cyclic axial tension-compression deformation is prescribed (Figure 5.1b). The material behavior model is a Chaboche model as described in Section 5.2.1, whose parameters are optimization variables of a Levenberg-Marquardt algorithm. The finite element simulation is run for a certain amount of cycles until stabilization of the cyclic state, and the optimization process aims at matching the target quantities which are the first and stabilized experimental cycles. Within the Levenberg-Marquardt optimization process, each iteration requires to run the finite element computation of the stabilized state once for each of the optimization parameters, in order to build the Jacobian matrix of the objective function.

Except for the parameter b driving the exponential decay in the isotropic hardening function, whose value was set to $b = 20$ to roughly match the number of cycles to stabilization, all other Chaboche model parameters are considered as optimization variables. The values obtained for 304L and 316L stainless steels are given in Table 5.1. The elastic properties values are set as usual to $E = 200$ GPa and $\nu = 0.3$ for both materials.

Table 5.1: Parameters identified for Chaboche elastoplastic model for 304L and 316L stainless steels.

Parameter	304L	316L
A_1 (MPa)	40.27	140.8
C_1	1090	285.5
A_2 (MPa)	138.9	27.88
C_2	209.4	286.6
σ_0 (MPa)	126.7	153.9
R_M (MPa)	203.2	244.4
b	20	20

Using the identified set of parameters, the cyclic stress-strain evolutions are depicted in Figure 5.2 and compared with the first and stabilized experimental cycles based on which they were

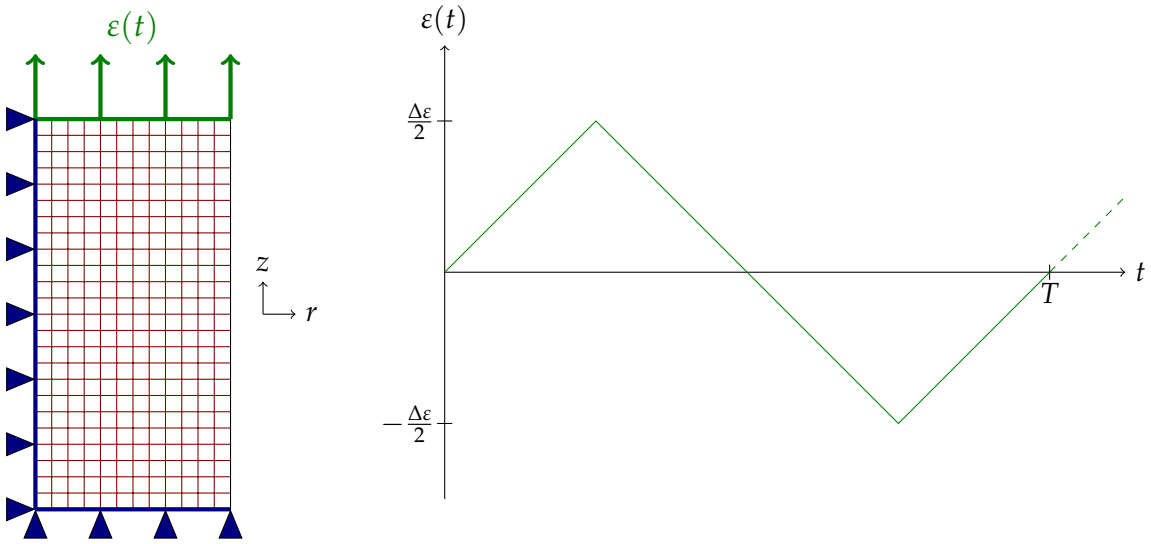

(a) FE model **(b)** Evolution of the prescribed deformation

Figure 5.1: Two-dimensional finite element model of an axially symmetric cylindrical specimen loaded with a cyclic prescribed deformation, used to identify parameters of Chaboche elastoplastic model for 304L and 316L stainless steels.

identified. In addition, Figure 5.3 shows the comparison between the stabilized cycle numerically simulated and experimentally obtained by Dhahri (2019) for 316L stainless steel for $\Delta\varepsilon = 0.8\%$. This elastoplastic model with the determined parameter values will be used in the remainder of the chapter.

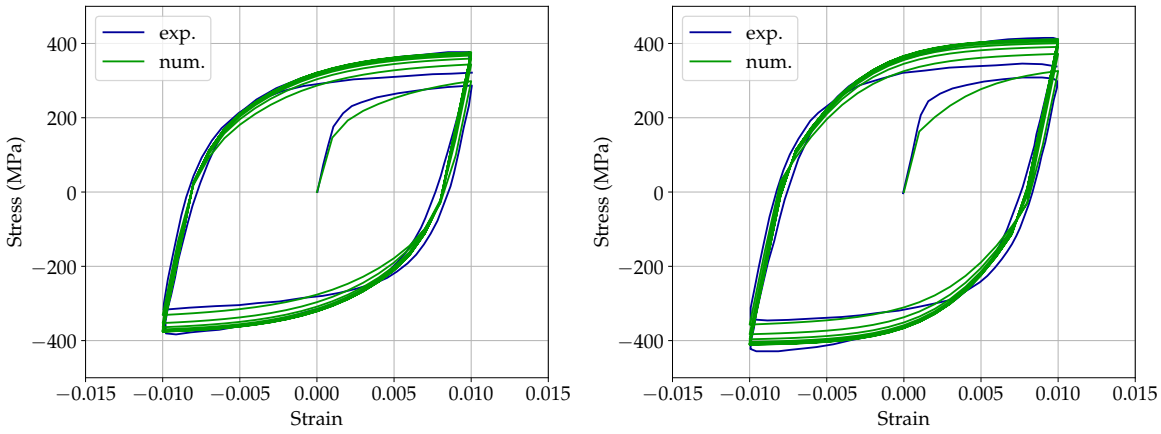

(a) 304L **(b)** 316L

Figure 5.2: Comparison of the cyclic response simulated with a Chaboche elastoplastic model with the experimental data that served for the identification, for (a) 304L stainless steel identified with data from Vor (2009) and (b) 316L stainless steel identified with data from Lê (2013).

5.2.3 Preliminary no-wear fretting simulation

Using the parameters thus identified for Chaboche elastoplastic model, a preliminary simulation is conducted on a cylinder-plane contact under fretting motion. The finite element model employed

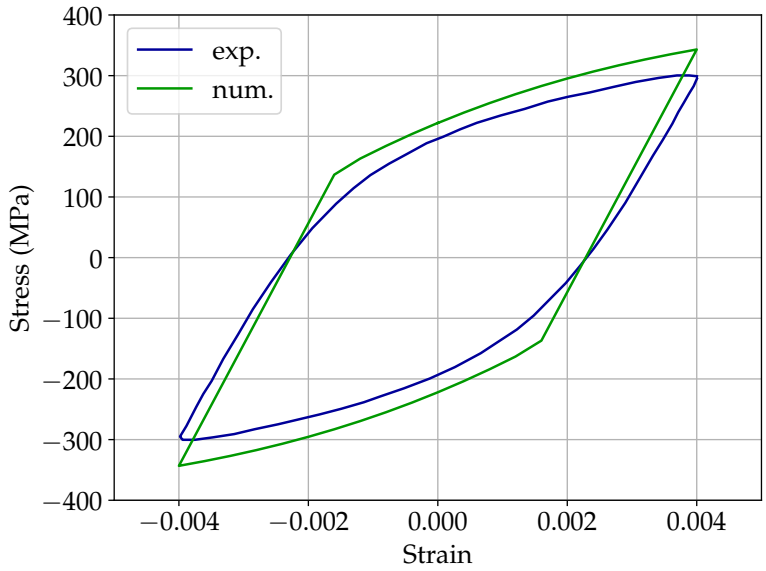

Figure 5.3: Comparison of the stabilized cycle simulated with a Chaboche elastoplastic model for 316L stainless steel with experimental stabilized cycle obtained by Dhahri (2019).

is similar to the model used in the previous chapters[3], and the simulation is run on $N_{\text{cyc}} = 100$ cycles. The cylinder is subjected to a normal load $F_n = 3\ \text{N mm}^{-1}$ and a tangential displacement of amplitude $\delta_0 = 80\ \mu\text{m}$. The coefficient of friction is $\mu = 0.95$. Here, no wear occurs and no cycle jump is used.

At the end of the first loading cycle, plastic yield has occurred in the vicinity of the surfaces (Figure 5.4). Plastic strains are very localized in a near surface layer and spread over the contact area. They are higher near the fretting contact edges than at the center of the surfaces. Figure 5.5 shows the evolution of plastic strains in the plane depth at the central position of the surface ($x = 0$). It can be observed that they span a layer of about 10 µm depth.

The simulation is conducted on 100 cycles. The evolution of equivalent plastic strain profiles on the cylinder and plane surfaces is depicted in Figure 5.6. This confirms that plastic strains are higher near the edges than at the center of the surfaces. Plastic strain seems to stabilize over the cycles. The cyclic evolution of equivalent plastic strain monitored on several points of the cylinder and plane surfaces is depicted in Figure 5.7. Six points are shown which are located between $x = 0$ µm and $x = 80$ µm. First, it can be noticed that only the centermost cylinder points undergo plastic strain, while on the plane surface plastic strain spans a larger area. In addition, it is observed that on these points a stabilized state is indeed reached after 100 cycles. On the cylinder, the surface undergoes no further plastic strains: an elastic shakedown is observed. On the plane, cyclic plastic strain is still observed after 100 cycles, but at the end of each cycle plastic strain retrieves the same value as at the start of the cycle – in other words, there is not uncontrolled plastic strain increase cycle after cycle. This is a plastic shakedown situation.

[3]See Section 3.4.2.

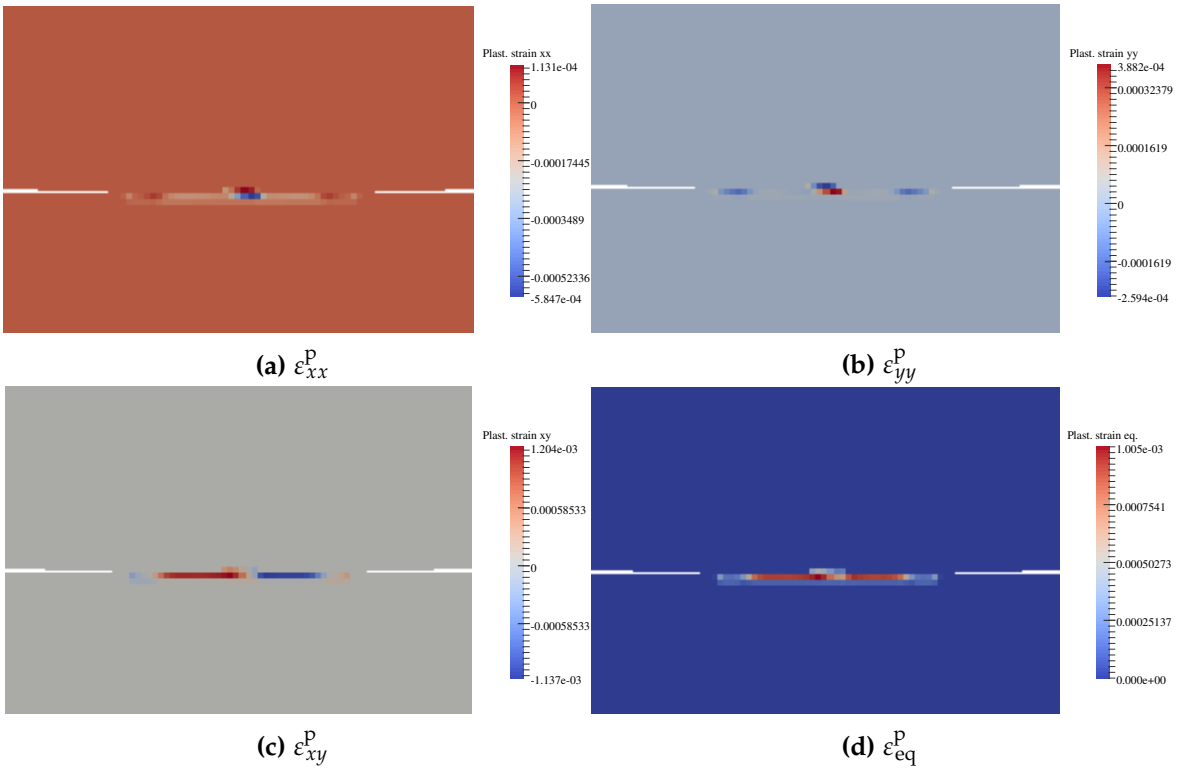

(a) $\varepsilon^{\mathrm{p}}_{xx}$ **(b)** $\varepsilon^{\mathrm{p}}_{yy}$

(c) $\varepsilon^{\mathrm{p}}_{xy}$ **(d)** $\varepsilon^{\mathrm{p}}_{\mathrm{eq}}$

Figure 5.4: Plastic strain fields after one fretting cycle. The view is zoomed in on the contact zone.

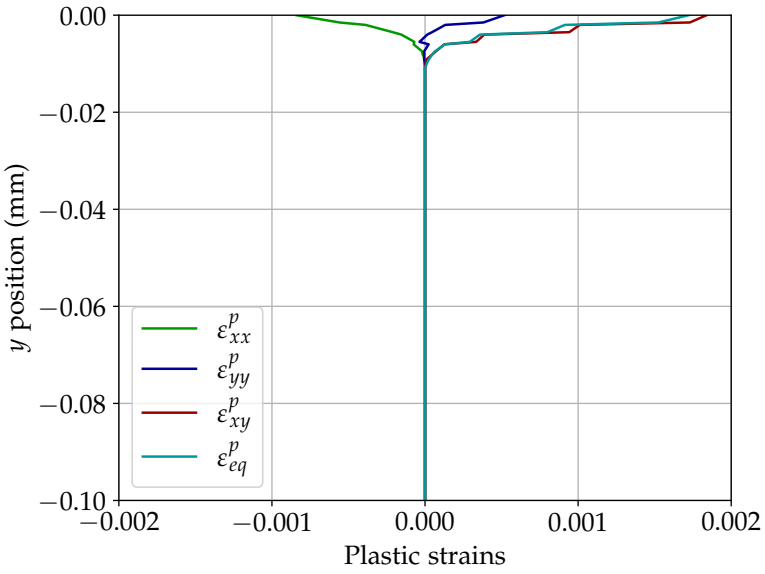

Figure 5.5: Plastic strains evolution in the plane depth, at position $x = 0$ (center of the plane surface).

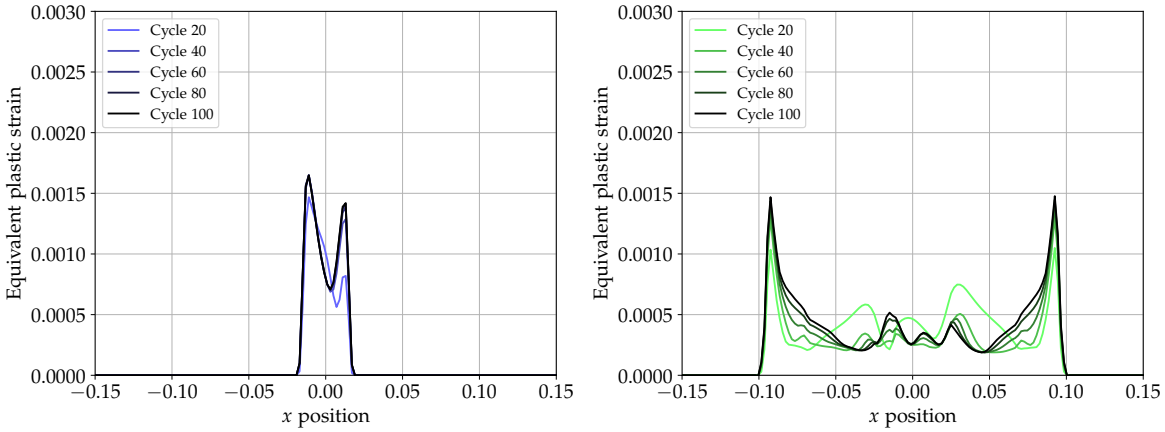

(a) Cylinder **(b)** Plane

Figure 5.6: Evolution of equivalent plastic strain profiles on the cylinder and plane surfaces over 100 fretting cycles.

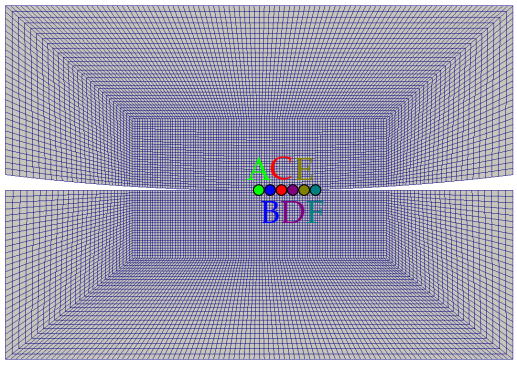

(a) Nodes A to F on the cylinder and plane surfaces

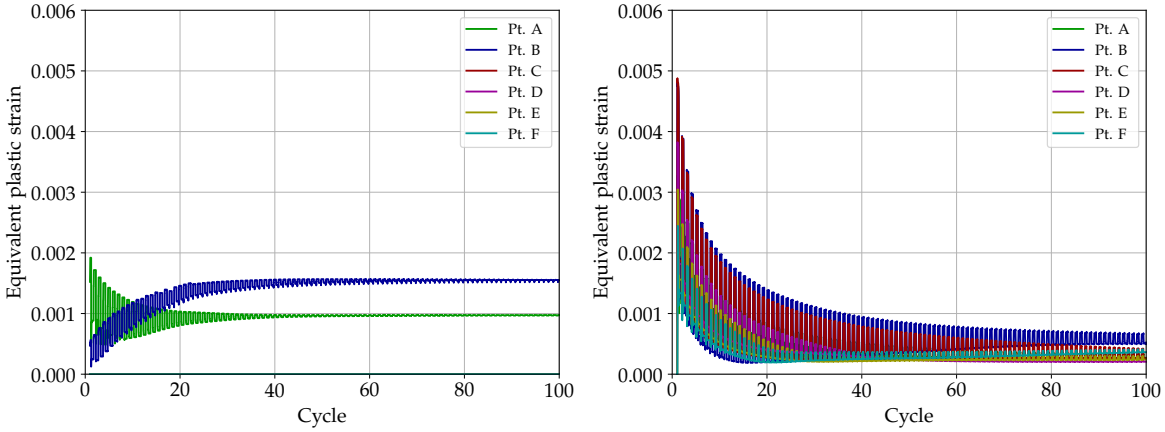

(b) Cylinder **(c)** Plane

Figure 5.7: Evolution of the equivalent plastic strain over 100 fretting cycles on six different points of the cylinder and plane surfaces.

5.3 Cycle jump approach for elastoplastic response in wear simulation

In this section, a first approach is proposed and implemented to simulate plastic strain evolution together with wear. It is part of the continuity of the wear simulation processes presented so far and merely consists in extending the explicit cycle jump method to plastic strain and hardening variables. The application of a cycle jump method in case of elastoplastic or viscoplastic models is described for example by Kiewel et al. (2000) or Cojocaru and Karlsson (2006). The aim is to extrapolate every variable of interest over the cycle jump in order to retrieve an evolution similar to a cycle-by-cycle simulation. The specificity here is that the structure geometry evolves over the cycle jump due to wear, which needs to be taken into account. As a first step, we present the simulation process implemented to simulate wear with an elastoplastic material behavior, without cycle jump. This allows to stress the peculiarities related to surface geometry evolution regarding the internal hardening variables fields. Then, the explicit cycle jump method used for plastic strain and hardening variables is presented and tried on a no-wear case. Finally, these two processes are brought together in order to simulate wear evolution with plastic strains using a cycle jump.

5.3.1 Wear simulation using an elastoplastic material behavior

First, a fretting wear simulation is carried out with no cycle jump. Using an elastoplastic material behavior, the relation between stress and strain is dependent upon the history of the material state and so does the resolution of the static equilibrium equations. One needs then to pay attention to correctly update the surface geometries due to wear, in order not to alter the fields of variables of interest. As a matter of fact, the representation of material removal is made through a fictitious displacement of the mesh, as it was explained in Section 3.4.3. As a consequence, in the absence of further treatment the internal variables and plastic strain fields would be displaced together with the mesh following wear, which is not intended. In order to address this and ensure a correct integration of the behavior constitutive equation after the mesh displacement, a projection step is performed. The need for such step is illustrated in Figure 5.8.

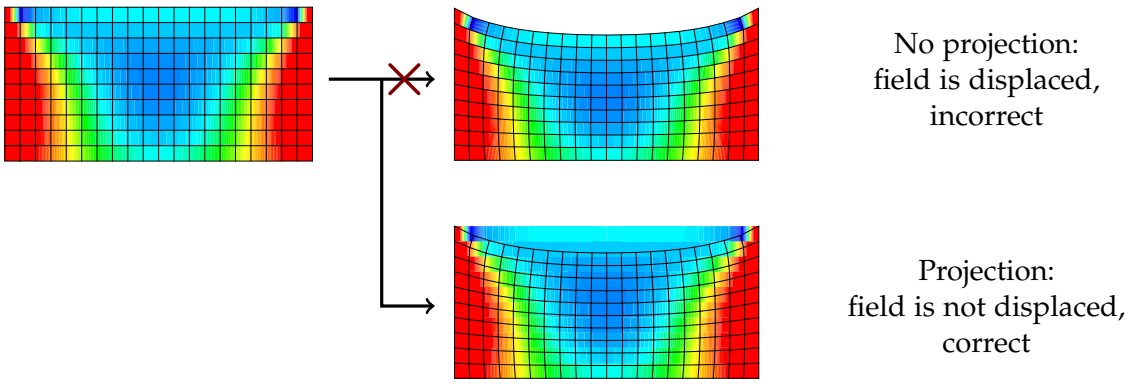

Figure 5.8: Illustration of the necessary projection step after mesh displacement accounting for wear, with an arbitrary field.

Because the integration of the behavior constitutive equation at each time step requires the

knowledge of the stress, strain, plastic strain and hardening internal variables fields at the previous time step, we need to ensure a proper projection of these quantities onto the displaced mesh. The aim is to get the mesh displaced due to wear, but to keep the aforementioned fields in an unchanged position. For that, a dummy mesh is created by copying the actual mesh just before the displacement step. On the dummy mesh are defined the actual, undisplaced fields. The mesh displacement due to wear affects the actual mesh but not the dummy one and is followed by a projection step of the undisplaced fields from the dummy mesh onto the actual one. A similar projection process was for example employed by Gibert (2019) for adaptive mesh refinement. The projection operation uses the interpolation functions of the finite element model to project the field values from the integration points of a mesh onto the integration points of another. This projection step may lead to an equilibrium loss, which is corrected by an additional resolution of static equilibrium at the same time step. Finally, the positivity of the cumulative plastic strain which might have been corrupted due to the interpolation is enforced again.

A wear simulation is conducted with this additional projection step in the simulation process. The simulation is similar to that carried out in Section 5.2.3, except that here bilateral wear is considered on the cylinder and plane surfaces. Wear evolution obeys an energy wear law. The parameters are unchanged with respect to the elastic bilateral wear simulations performed in Chapter 4. For now, no cycle jump is used. The simulation is conducted on $N_{\text{cyc}} = 100$ fretting cycles and the results are compared with the no-wear results of Section 5.2.3.

The evolution of the equivalent plastic strain profiles on the cylinder and plane surfaces is shown in Figure 5.9, with a comparison to the no-wear simulation. Although similar shapes may be observed in both situations, the simulation including wear leads to lower levels of equivalent plastic strain especially near the contact surface edges. Moreover, the progressive expansion of the contact surface towards the sides because of wear may be observed. This can be seen as well on the cumulative plastic strain profiles (Figure 5.10). In all the figures, dotted lines refer to the previous no-wear case while plain lines refer to the current wear case.

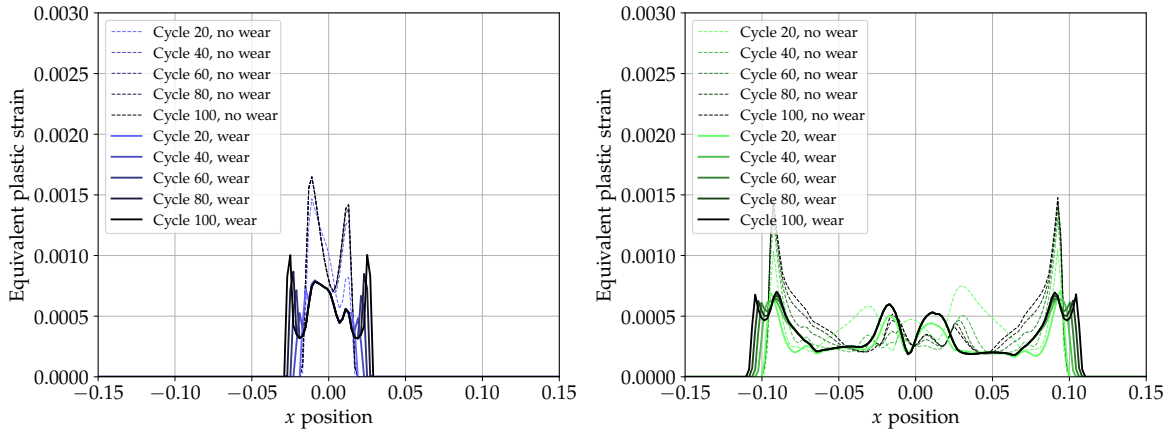

(a) Cylinder **(b)** Plane

Figure 5.9: Evolution of equivalent plastic strain profiles on the cylinder and plane surfaces over 100 fretting cycles, compared between a case with wear and a case without wear.

The evolution of equivalent plastic strain is monitored on six points from both cylinder and plane surfaces over the 100 cycles and is depicted in Figure 5.11. This clearly shows a stabilization due to an elastic shakedown much more quickly than in the absence of wear. Nevertheless, the

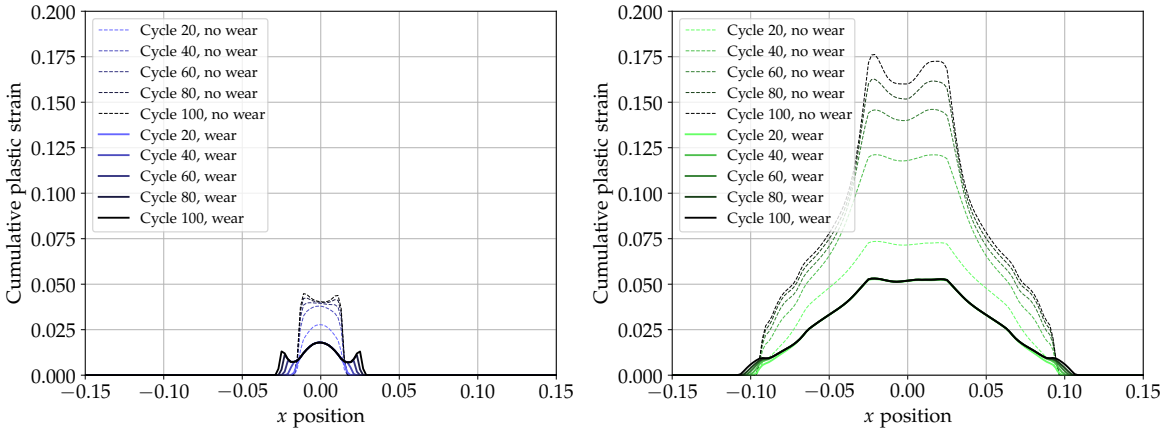

(a) Cylinder **(b)** Plane

Figure 5.10: Evolution of cumulative plastic strain profiles on the cylinder and plane surfaces over 100 fretting cycles, compared between a case with wear and a case without wear.

effect of the profile enlargement is visible on the cylinder surface: the point denoted C, which initially had no plastic strain, starts plastifying after about 40 fretting cycles (Figure 5.11a). It endures cyclic plasticity for a few tens of cycles, then stabilizes due to an elastic shakedown. This can be observed on the cumulative plastic strain evolution as well (Figure 5.12). These results show that the quick stabilization of the cyclic state is continuously disturbed by wear evolution: while the surface points located near the center of the wear profile have a stabilized plastic strain, the wear profile expansion induces further plasticity on the edges, which eventually stabilizes as well upon further enlargement of the wear profile.

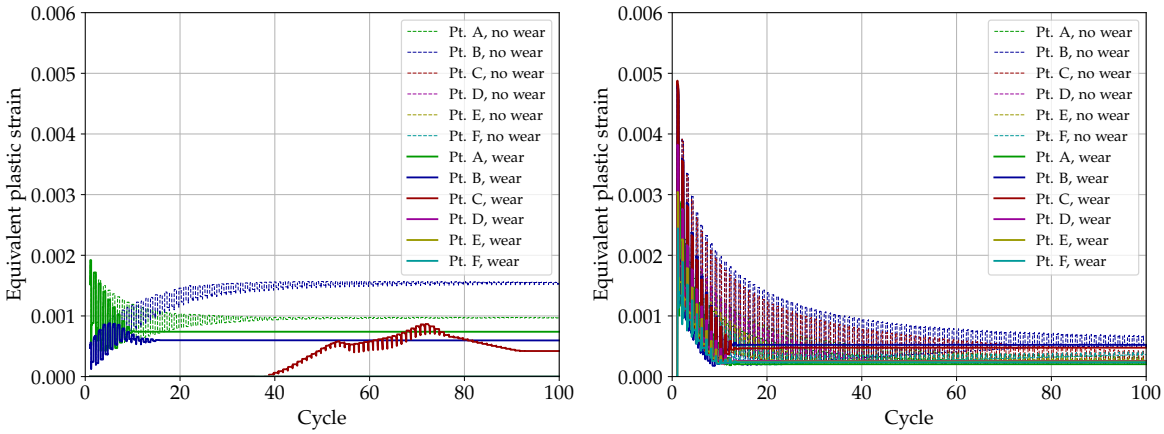

(a) Cylinder **(b)** Plane

Figure 5.11: Evolution of the equivalent plastic strain over 100 fretting cycles on six different points of the cylinder and plane surfaces, compared between a case with wear and a case without wear.

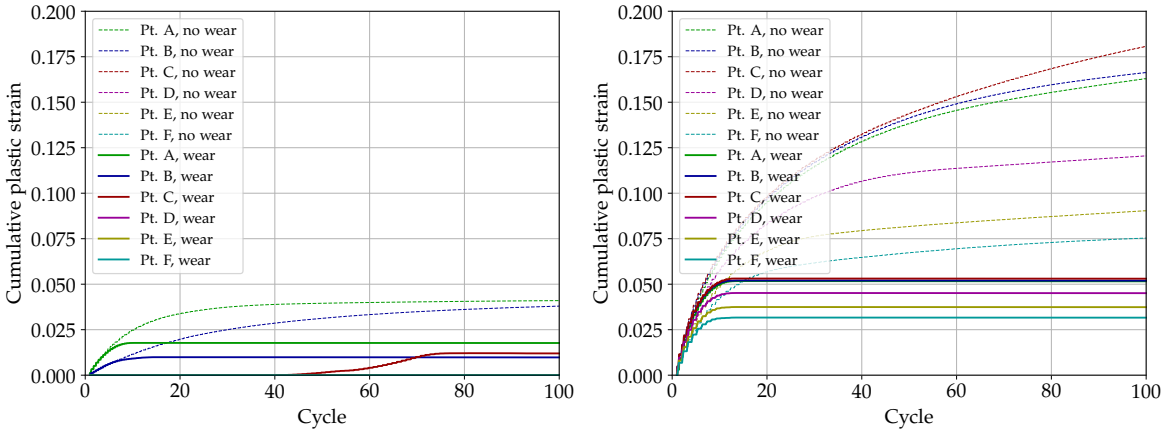

(a) Cylinder **(b)** Plane

Figure 5.12: Evolution of the cumulative plastic strain over 100 fretting cycles on six different points of the cylinder and plane surfaces, compared between a case with wear and a case without wear.

5.3.2 Cycle jump method with an elastoplastic behavior

The following step consists in introducing a cycle jump method adapted for an elastoplastic material behavior. In the first instance, it is presented in the absence of wear. The additional consideration of wear is straightforward given the simulation processes already presented. Here, the cycle jump method relies on a forward Euler explicit integration scheme, meaning that any quantity Y is obtained at cycle n_{k+1} by direct linear extrapolation of the quantity at cycle n_k, using the acceleration factor Δn and having computed the cyclic rate of the quantity $\partial_n Y_k$ at cycle n_k:

$$Y_{k+1} = Y_k + \Delta n \, \partial_n Y_k. \tag{5.14}$$

The cyclic rate $\partial_n Y_k$ of Y at cycle n_k is calculated as the difference between the quantity at the end of cycle n_k and the quantity at the start of cycle n_k:

$$\partial_n Y_k = \frac{\partial Y}{\partial n}(n_k) = Y_k(t_J) - Y_k(t_1) \tag{5.15}$$

where t_1 and t_J are respectively the first and last time steps of the cycle. The quantities extrapolated are the stress, strain, plastic strain and hardening internal variables fields, as well as the displacement field which is used to extrapolate the current geometrical configuration.

Simulations are carried out on the same wearless test case as in Section 5.2.3, this time with a cycle jump using an acceleration factor $\Delta n = 2$ or $\Delta n = 4$. Due to the quick evolution of plastic strains during the early cycles, the 10 initial cycles are simulated with $\Delta n = 1$. Figure 5.13 shows the evolution of the equivalent plastic strain monitored on six points from the cylinder and plane surfaces, simulated with $\Delta n = 2$ and compared with the reference results at $\Delta n = 1$. A very good agreement is found between the two simulations, demonstrating the validity of the method. A good accuracy is observed as well on the evolution of cumulative plastic strain (Figure 5.14).

Using an acceleration factor $\Delta n = 4$ however, a rapid divergence is observed with respect to the reference $\Delta n = 1$ simulation. Figure 5.15 shows the deviation from the reference solution on the

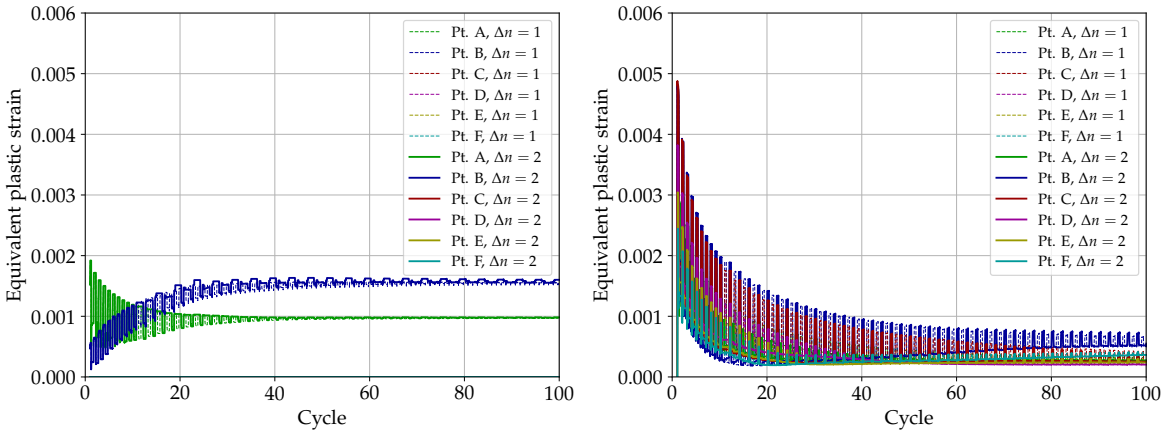

(a) Cylinder **(b)** Plane

Figure 5.13: Evolution of the equivalent plastic strain over 100 fretting cycles on six different points of the cylinder and plane surfaces, using a cycle jump with $\Delta n = 2$.

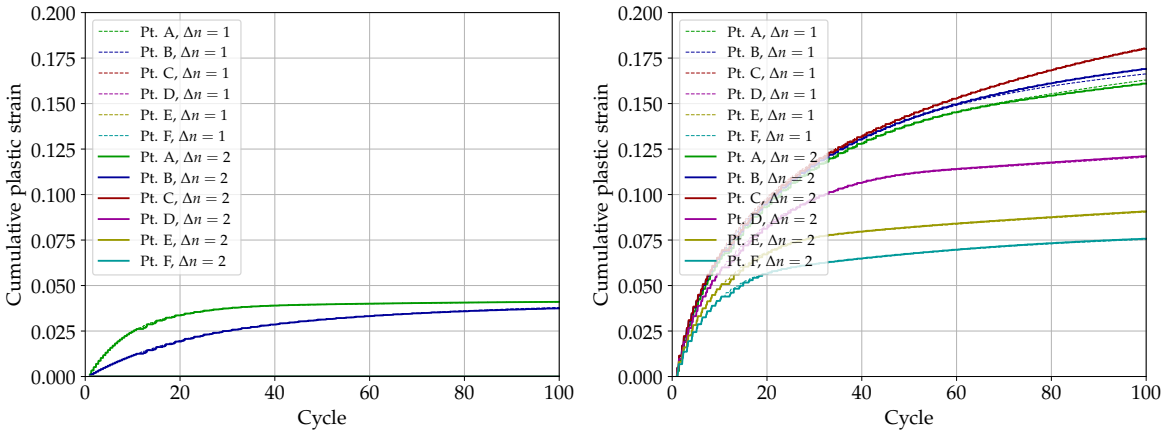

(a) Cylinder **(b)** Plane

Figure 5.14: Evolution of the cumulative plastic strain over 100 fretting cycles on six different points of the cylinder and plane surfaces, using a cycle jump with $\Delta n = 2$.

equivalent plastic strain evolution after only a few cycles computed at $\Delta n = 4$. The divergence is observed on the cumulative plastic strain evolution as well (Figure 5.16). The simulation goes no further than $n = 38$ cycles, after which convergence is no longer reached in the resolution of the behavior constitutive equations.

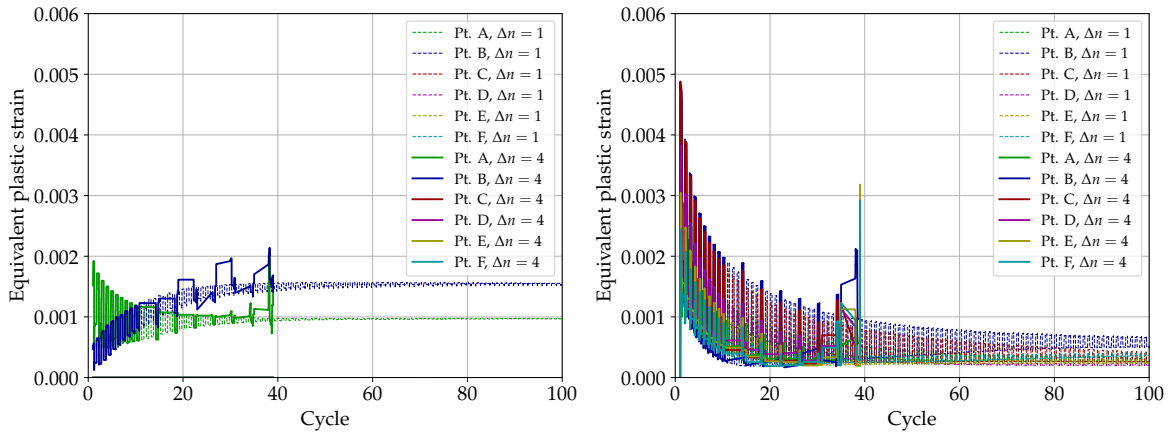

(a) Cylinder **(b)** Plane

Figure 5.15: Evolution of the equivalent plastic strain over 100 fretting cycles on six different points of the cylinder and plane surfaces, using a cycle jump with $\Delta n = 4$.

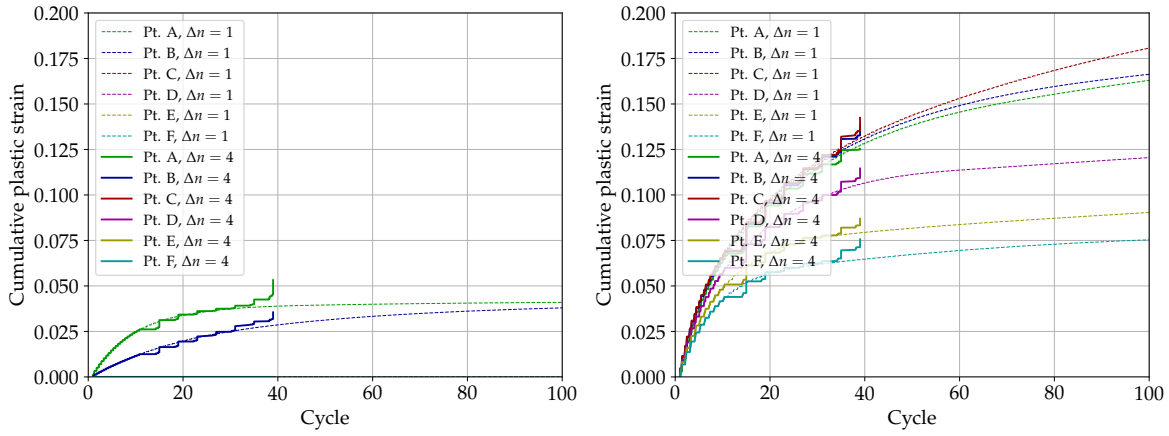

(a) Cylinder **(b)** Plane

Figure 5.16: Evolution of the cumulative plastic strain over 100 fretting cycles on six different points of the cylinder and plane surfaces, using a cycle jump with $\Delta n = 4$.

These results show that although the cycle jump method can effectively reduce the computational cost of elastoplastic fretting simulations, its accuracy is limited to low acceleration factors. This is arguably related to the simple first-order explicit scheme chosen here, which may lead to a divergence of the extrapolated solution. The use of alternative more suitable schemes may be investigated, which was not explored here. Despite this limit, the method is still of great use for low acceleration factors, for which it proves its ability to properly reproduce the cyclic evolution of the plastic deformation state.

5.3.3 Wear simulation results using a cycle jump

At last, a fretting simulation is carried out including bilateral wear and using a cycle jump, bringing together the two simulation processes presented so far in the present section. Considering the developments presented to account for fields projection at the mesh update step and to introduce a cycle jump with an elastoplastic material behavior, connecting both is straightforward. The cycle jump method employed for both wear and plastic internal variables uses the same forward Euler explicit scheme. With an acceleration factor $\Delta n = 2$, the cyclic evolution of equivalent plastic strain is well captured (Figure 5.17). However, as can be seen in Figure 5.18, here again the use of an acceleration factor $\Delta n = 4$ leads to a divergence.

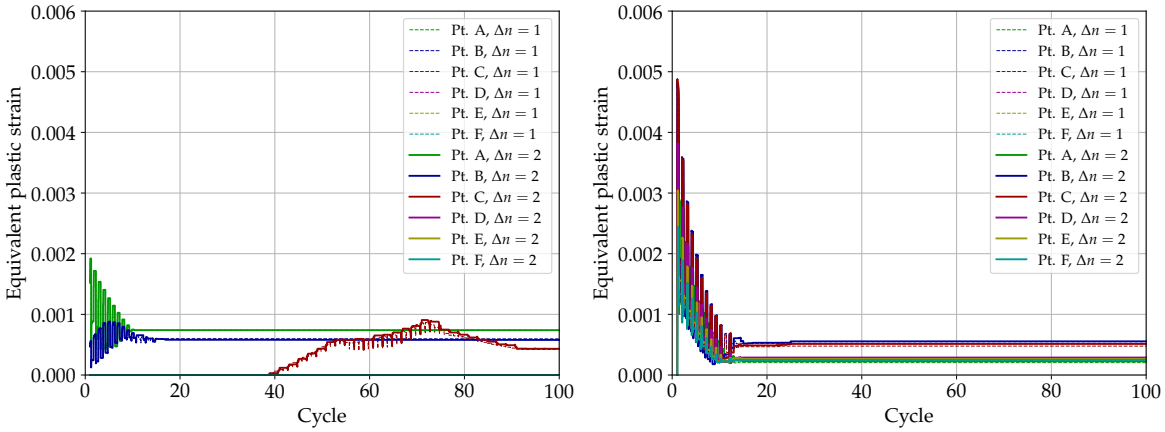

(a) Cylinder **(b)** Plane

Figure 5.17: Evolution of the equivalent plastic strain over 100 fretting cycles on six different points of the cylinder and plane surfaces, using a cycle jump with $\Delta n = 2$ considering bilateral wear.

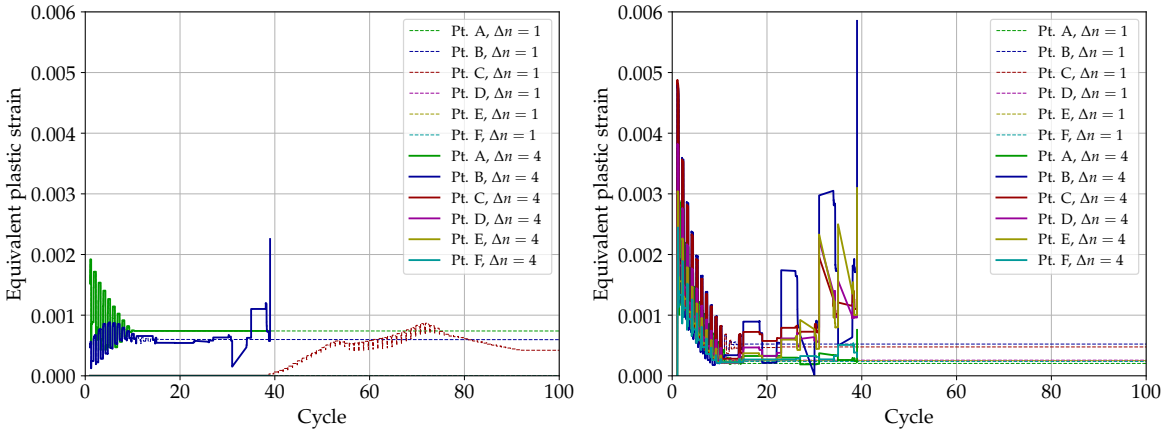

(a) Cylinder **(b)** Plane

Figure 5.18: Evolution of the equivalent plastic strain over 100 fretting cycles on six different points of the cylinder and plane surfaces, using a cycle jump with $\Delta n = 4$ considering bilateral wear.

The same observation is made as in the no-wear case, even though here the plastic strain evo-

lution presents a quicker stabilization. For this reason, a better stability could have been expected when wear is considered than in the absence of wear. Nevertheless, it should not be forgotten that the application of a cycle jump on wear profile evolution may itself lead to instabilities. Indeed, as it was demonstrated in Chapter 4, the use of an explicit cycle jump on wear evolution generates spurious instabilities when the acceleration factor is greater than a stability limit. Here, with the considered mesh elements size, $\Delta n = 2$ is in the stability domain but $\Delta n = 4$ falls beyond the limit. As a result, the divergence observed here on plastic strain evolution may be related to an erroneous computation of contact pressures.

It can be concluded that the cycle jump method effectively enables to accelerate elastoplastic wear simulations, at least by a factor two in our case, and provides a possible way for cheaper fretting wear simulations. However, the simulation processes proposed here do not enable sufficient acceleration capacities to reach the desired high numbers of cycles. Evolutions of these methods could be investigated in order to build more robust acceleration processes. These include alternative extrapolation functions, possibly of higher order. For example, Kiewel et al. (2000) propose a cycle jump method based on the initial simulation of several cycles, followed by the use of spline functions of degree two or three to interpolate each internal variable at each integration point. The spline functions are used to extrapolate the values over a certain range of subsequent cycles. Another possibility involves the use of implicit integration schemes for the cycle jump.

The results obtained in this section highlight the existence of a competition between stabilization of cyclic plastic strain and evolution of wear. The asymptotic stabilized state that the system seemingly tends to reach is constantly affected by wear evolution, which enlarges the contact surface and induces further plastic strain on the edges of the contact area.

5.4 Direct cyclic approach for elastoplastic response in wear simulation

In this section, another approach is proposed for the simulation of fretting wear considering an elastoplastic material behavior. It relies on a decoupling between the determination of cyclic plasticity and the computation of wear profiles evolution. This decoupling is proposed upon the assumption that plastic strain reaches a stabilized cycle much quicker than the characteristic time for wear to significantly evolve. We have seen in the previous section that whereas the structure indeed seems to tend towards a cyclic stabilized state, this stabilized state is continuously disturbed by the evolution of wear which enlarges the contact surface, thus generating plasticity on the surface points initially located out of the contact area. Consequently, the cyclic stabilized state mentioned here is to be understood as the asymptotic state the system would reach without further evolution of wear (i.e. at fixed wear). Similarly, the "characteristic time for wear to significantly evolve" is defined as the duration needed for wear to noticeably affect the stabilized state. In this chapter, the cyclic stabilized state of the system is determined by use of the *direct cyclic method* (DCM).

5.4.1 Presentation of the direct cyclic method

The direct cyclic method was developed by Maouche et al. and aims at evaluating the asymptotic response of an inelastic structure subjected to an arbitrary cyclic loading [Maouche et al. 1997,

Maouche 1997, Maitournam et al. 2002]. If the cyclic response asymptotically reaches a stabilized state in an elastic or plastic shakedown regime, the method consists in directly seeking this stabilized state without following the whole loading path. Consequently, it does not give access to the complete response history over the cyclic loading but only enables to get the stabilized cycle, if it exists. In case of ratchetting, the method is not appropriate. The direct research of a stabilized state relies upon a separate treatment of, on the one hand, local constitutive equations governing the material behavior, and on the other hand the global static equilibrium equations. This kind of approach was first proposed by Ladevèze (1985) in the large time increment method, then by Akel and Nguyen (1989). In brief, the process is an iterated succession of a local stage, which aims at verifying the local constitutive equations, and a global stage ensuring the static and kinematic admissibility of the solution. It was proposed to provide a way to compute the stabilized state quicker than with a classical incremental step-by-step method, in which the solution is determined following the whole loading path using small time increments. The direct cyclic method is especially useful when the asymptotic state is reached only after a large number of cycles.

Description of the process

Let us consider an elastoplastic structure subjected to a cyclic loading. The loading cycle is defined on a time interval $[0, T]$ which is decomposed into a set of discrete time steps $\{t_1, \dots t_J\}$. At each time step t_j ($j \in \{1, \dots J\}$) is associated a loading F_j with, necessarily, $F_J = F_1$ – here, loading may refer to diverse thermomechanical loading conditions: surface or volume forces, prescribed displacement, temperature, etc. The iterative process for the direct cyclic method is as follows.

1. **Initialization:** for each time step $t_j \in \{t_1, \dots t_J\}$, plastic strain $\underline{\underline{\varepsilon^p}}(t_j)$ and internal hardening variables $\boldsymbol{\alpha}(t_j)$ are initialized.

2. **Global stage:** the static equilibrium equation is solved incrementally at each time step $t_j \in \{t_1, \dots t_J\}$ considering the loading F_j, boundary conditions and, in our case, frictional contact conditions to get kinematically admissible strain fields $\underline{\underline{\varepsilon}}(t_j)$. The material behavior constitutive equation is not solved and statically admissible stress fields are calculated as:

$$\underline{\underline{\sigma}}(t_j) = \underline{\underline{\underline{\underline{C}}}} : \left(\underline{\underline{\varepsilon}}(t_j) - \underline{\underline{\varepsilon^p}}(t_j)\right). \tag{5.16}$$

3. **Convergence test:** the process has converged if the stresses obtained in the global stage verify, at each time step, the plasticity criterion given the internal variables:

$$\text{convergence} \Leftrightarrow \forall j \in \{1, \dots J\},\ f(\underline{\underline{\sigma}}(t_j), \underline{\underline{\varepsilon^p}}(t_j), \boldsymbol{\alpha}(t_j)) \leq 0. \tag{5.17}$$

   In this case, the solution $(\underline{\underline{\varepsilon}}(t_j), \underline{\underline{\sigma}}(t_j), \underline{\underline{\varepsilon^p}}(t_j))$ is, for each time step t_j, kinematically, statically and plastically admissible. If not,

4. **Local stage:** the material behavior constitutive equation is integrated for each time step:

$$\forall j \in \{1, \dots J-1\},\ (\underline{\underline{\sigma}}(t_{j+1}), \underline{\underline{\varepsilon^p}}(t_{j+1}), \boldsymbol{\alpha}(t_{j+1})) = \mathcal{F}(\underline{\underline{\sigma}}(t_j), \underline{\underline{\varepsilon}}(t_j), \underline{\underline{\varepsilon^p}}(t_j), \boldsymbol{\alpha}(t_j)) \tag{5.18}$$

   in which $\mathcal{F}$ is a generic notation for the operation enforcing the constitutive equation satisfac-

tion, which is not detailed here[4].

5. **Periodicity:** the periodicity of plastic strain and hardening variables is enforced by taking $\underline{\underline{\varepsilon^{\mathrm{p}}}}(t_1) = \underline{\underline{\varepsilon^{\mathrm{p}}}}(t_J)$ and $\boldsymbol{\alpha}(t_1) = \boldsymbol{\alpha}(t_J)$. Then, the process is iterated back to the global stage.

It should also be noted that this process, because it does not follow the response history, cannot deliver true values for hardening variables – such as cumulative plastic strain for example. The computation process is described in Algorithm 5.1, and examples of application are presented next.

Algorithm 5.1: Direct cyclic method.

I - Loading definition
Define n time steps: $\{t_1, \dots t_J\}$;
Define loading: $\{F_1, \dots F_J\}$;
II - Initialization
for j *in* $\{1, \dots J\}$ **do**
  Initialize $\underline{\underline{\varepsilon^{\mathrm{p}}}}(t_j) \leftarrow \underline{\underline{\varepsilon^{\mathrm{p}}}}_{0,j}$;
  Initialize $\boldsymbol{\alpha}(t_j) \leftarrow \boldsymbol{\alpha}_{0,j}$;
  Solve the static equilibrium problem at t_j and get $\underline{\varepsilon}(t_j)$ kinematically admissible ;
  Compute $\underline{\sigma}(t_j) \leftarrow \underline{\underline{\underline{\underline{C}}}} : \left(\underline{\varepsilon}(t_j) - \underline{\underline{\varepsilon^{\mathrm{p}}}}(t_j)\right)$;
III - Iterative process
while $\exists j \in \{1, \dots J\}$ *s.t.* $f(\underline{\sigma}(t_j), \underline{\varepsilon^{p}}(t_j), \boldsymbol{\alpha}(t_j)) > 0$ **do**
  (1) Local stage
  for j *in* $\{1, \dots J-1\}$ **do**
    $(\underline{\sigma}(t_{j+1}), \underline{\underline{\varepsilon^{\mathrm{p}}}}(t_{j+1}), \boldsymbol{\alpha}(t_{j+1})) \leftarrow \mathcal{F}(\underline{\sigma}(t_j), \underline{\varepsilon}(t_j), \underline{\underline{\varepsilon^{\mathrm{p}}}}(t_j), \boldsymbol{\alpha}(t_j))$; `// Integrate behavior constitutive equation`
  $(\underline{\underline{\varepsilon^{\mathrm{p}}}}(t_1), \boldsymbol{\alpha}(t_1)) \leftarrow (\underline{\underline{\varepsilon^{\mathrm{p}}}}(t_J), \boldsymbol{\alpha}(t_J))$; `// Enforce periodicity`
  (2) Global stage
  for j *in* $\{1, \dots J\}$ **do**
    Solve the static equilibrium problem at t_j and get $\underline{\varepsilon}(t_j)$ kinematically admissible ;
    Compute $\underline{\sigma}(t_j) \leftarrow \underline{\underline{\underline{\underline{C}}}} : \left(\underline{\varepsilon}(t_j) - \underline{\underline{\varepsilon^{\mathrm{p}}}}(t_j)\right)$;

Examples of application

The use of the direct cyclic method is presented as a first step on a simple axial tension-compression test case. A two-dimensional, axially symmetric finite element model of a cylindrical specimen is built which is identical to that used for the identification of Chaboche model parameters (see Figure 5.1, Section 5.2.2). A Chaboche elastoplastic model is used for the material behavior, whose parameters correspond to a 304L stainless steel as in Table 5.1. An axial tension-compression cyclic strain is prescribed with an amplitude $\Delta\varepsilon/2 = 0.2\%$. First, a classical incremental simulation is conducted up to stabilization of the stress-strain cyclic response. Thereafter, another simulation is performed using the direct cyclic method. Figure 5.19 depicts the results obtained with both methods: using the incremental method, the progressive cycle-by-cycle evolution of the stress-strain cyclic response is shown until its stabilization. The asymptotically stabilized cycle is well retrieved using the direct cyclic method.

[4]This operation is generally carried out using a radial return algorithm, see for example Simo and Taylor (1985).

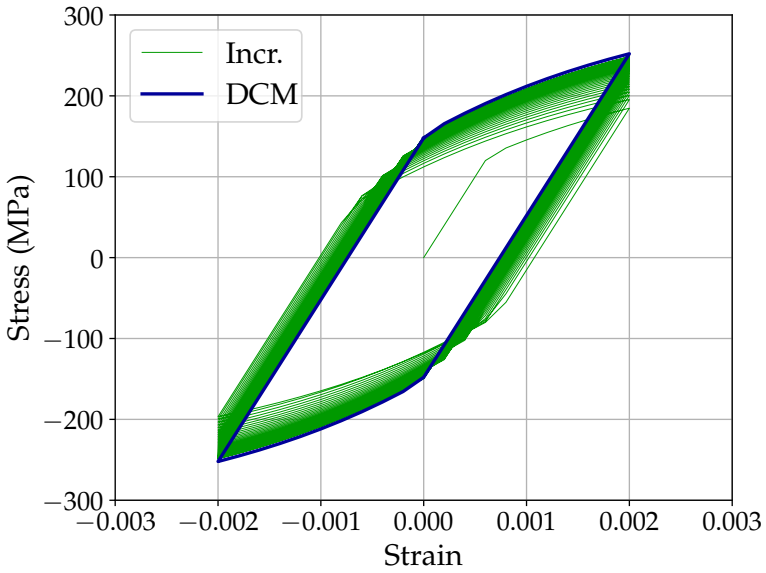

Figure 5.19: Evolution of the cyclic response on a cylindrical elastoplastic specimen loaded with a prescribed cyclic strain. Comparison between the complete response history computed with an incremental method and the stabilized cycle computed with the direct cyclic method.

A second example is presented on the cylinder-plane fretting model used throughout this chapter. As it was shown in Section 5.2.3, in the absence of wear the structure reaches after 100 cycles a stabilized state due to either elastic or plastic shakedown. The direct cyclic method is used to retrieve this stabilized state and the results are compared with those of Section 5.2.3 using an incremental method on 100 fretting cycles. Figure 5.20 compares the xy component of plastic strain and equivalent plastic strain fields obtained after 100 cycles with an incremental method and obtained using the direct cyclic method. The results show a very good agreement between both simulations. The cyclic evolution of the equivalent plastic strain computed on the surfaces with the incremental method is compared with the stabilized results obtained with the direct cyclic method, which demonstrates the ability of the method to capture the asymptotic behavior of the elastoplastic structure (Figure 5.21).

5.4.2 Wear simulation strategy integrating the direct cyclic method

The numerical strategy proposed here to simulate wear evolution with an elastoplastic material behavior relies on the use of the direct cyclic method. As it was stated in Section 5.3, there exists a competition between the stabilization of the cyclic plastic strain state, and the evolution of wear which prevents a complete stabilization by continuously enlarging the contact area. Based on this observation, we make the assumption that stabilization of the cyclic plastic strain state operates on a quicker time scale than wear evolution. In other words, the number of cycles for wear to significantly affect the stabilized state is much greater than the number of cycles for the structure to reach a stabilized state. As a consequence, we consider that the stabilized cyclic plasticity state is a good approximate of the actual plastic strain evolution during a certain amount of cycles over which wear evolves slowly and supposedly not enough to significantly alter the stabilized state.

Let us denote Δn^{p} a characteristic number of cycles required for wear to significantly alter the stabilized cyclic plasticity state. The simulation process is the following. We start by computing the stabilized cyclic plasticity state by means of the direct cyclic method – in this process, wear evolution

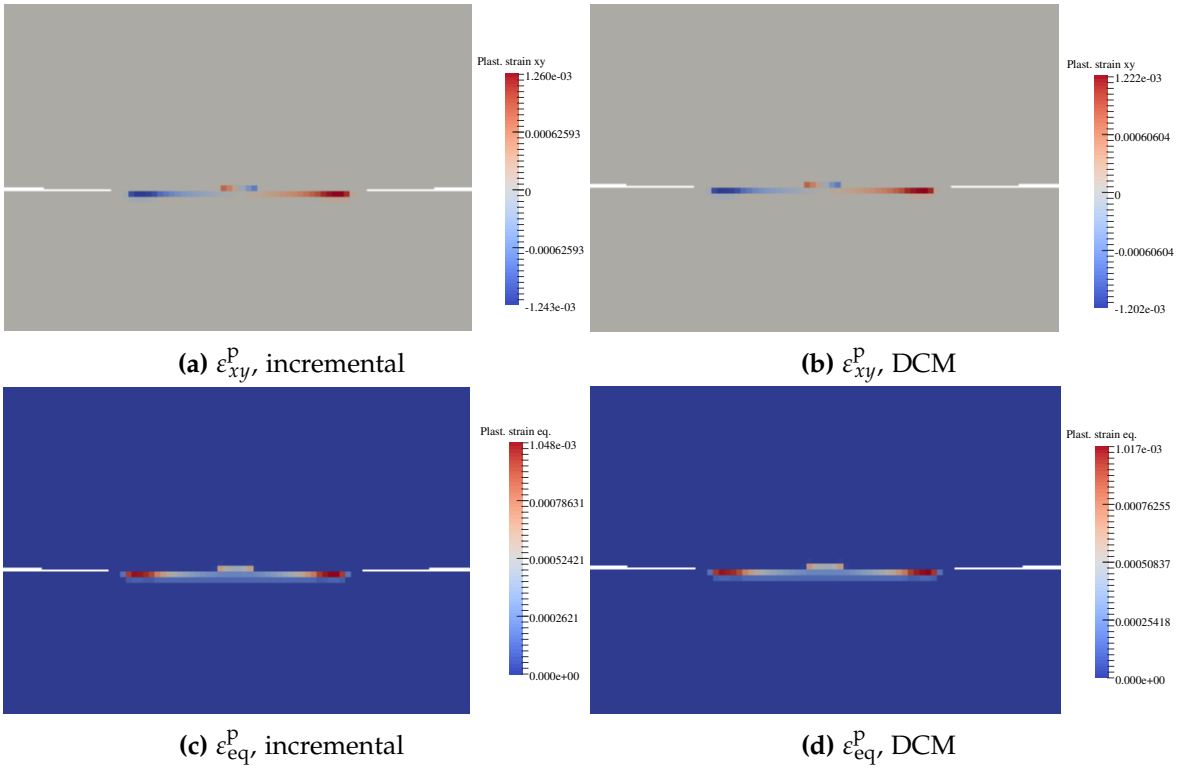

(a) $\varepsilon^{\mathrm{p}}_{xy}$, incremental **(b)** $\varepsilon^{\mathrm{p}}_{xy}$, DCM

(c) $\varepsilon^{\mathrm{p}}_{\mathrm{eq}}$, incremental **(d)** $\varepsilon^{\mathrm{p}}_{\mathrm{eq}}$, DCM

Figure 5.20: Plastic strain fields compared between the incremental method after 100 loading cycles and the direct cyclic method. The view is zoomed in on the contact zone.

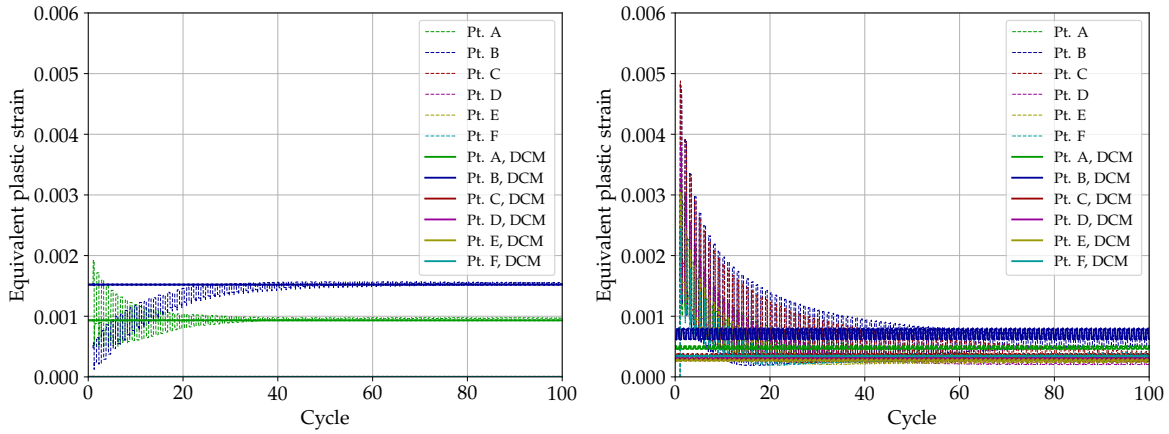

(a) Cylinder **(b)** Plane

Figure 5.21: Evolution of the equivalent plastic strain over 100 fretting cycles on six different points of the cylinder and plane surfaces, compared with the asymptotic response computed using the direct cyclic method. The asymptotic response delivered by the DCM represents a single cycle, which is reported here on each of the 100 fretting cycles to show the convergence of the progressive cyclic plasticity evolution towards the stabilized state.

does not intervene. The cyclic plasticity state thus calculated is assumed to be representative of the actual cyclic plasticity state over the next Δn^{p} fretting cycles. Then, wear evolution is simulated over these Δn^{p} cycles without reconsidering plastic strain evolution from one cycle to the next. In this stage, because plastic strain is not reevaluated, the classical wear simulation processes used in elasticity are employed. They may involve an acceleration factor Δn, and an explicit or implicit treatment of the cycle jump[5]. After Δn^{p} cycles, wear has allegedly sufficiently evolved to modify the stabilized cyclic plasticity state. Consequently, the direct cyclic method is used again to update the stabilized cyclic plasticity state. It is initialized with the previous plastic strain and internal variables fields, which have been projected throughout the wear evolution stage to account for surface material removal. This process is repeated until the desired number of cycles is reached. Overall, it consists in an alternated research of the stabilized state and simulation of wear evolution over a certain amount of cycles Δn^{p}, which are treated as separate problems. This simulation process is represented schematically in Figure 5.22.

5.4.3 Wear simulation results

This method is used to simulate wear and plastic strain evolution on the cylinder-plane fretting case presented throughout this chapter. In the simulation, the stabilized cyclic state for plasticity is computed once every $\Delta n^{\mathrm{p}} = 400$ cycles using the direct cyclic method. Regarding simulation of wear evolution, an implicit cycle jump method is used with an acceleration factor $\Delta n = 25$. Overall, $N_{\mathrm{cyc}} = 30{,}000$ fretting cycles are simulated. The results obtained are presented hereafter.

First, the evolution of equivalent plastic strain profiles on the cylinder and plane surfaces is depicted in Figure 5.23. It shows that plastic strains are the highest on the edges of the contact surface, which widens over the cycles. Equivalent plastic strain is lower in the center of the surfaces. The values observed in the central part are stable throughout the cycles, but get progressively eroded: this is an effect of material removal on the surfaces and appears as a consequence of the projection step performed. Equivalent plastic strain is locally stable, but is at a peak on the surface and decreases with depth. Therefore, as the surface material gets worn away, previously in-depth material with lower plastic strain levels gets uncovered on the surface.

This can be observed as well on the evolution over the cycles of surface equivalent plastic strain, monitored on six surface nodes (Figure 5.24). The further into the cycles, the more the contact area expands and the more side nodes get integrated within the contact area. As they get integrated, these edge locations undergo high plastic strains, which eventually stabilizes to lower levels upon further progression of the contact area expansion. Once stabilized, plastic strain on these locations slowly decreases due to material removal. These observations confirm that the highest plastic strain levels are experienced on the contact surface edges, and constantly move towards the sides. This is consistent with the observations made by Mohd Tobi et al. (2009) on their numerical studies.

After $N_{\mathrm{cyc}} = 30{,}000$ fretting cycles, plastic strain fields indeed show concentrations near the contact surface edges (Figure 5.25). In particular, the yy plastic strain component is positive at the contact surface edges on the plane surface. This suggests an elongation in the vertical direction on the plane surface, which could be interpreted as an indication of a plowing effect.

Finally, the surface normal displacement profiles, which account for both wear depth and permanent surface deformation, are shown in Figure 5.26. Here, vertical deformation due to a plowing

[5]The only difference here in the wear simulation process compared with the elastic case is the projection step of the plastic strain and hardening variables fields, which is needed here to correctly initialize the next direct cyclic method. See Section 5.3.1 for a description of the projection step.

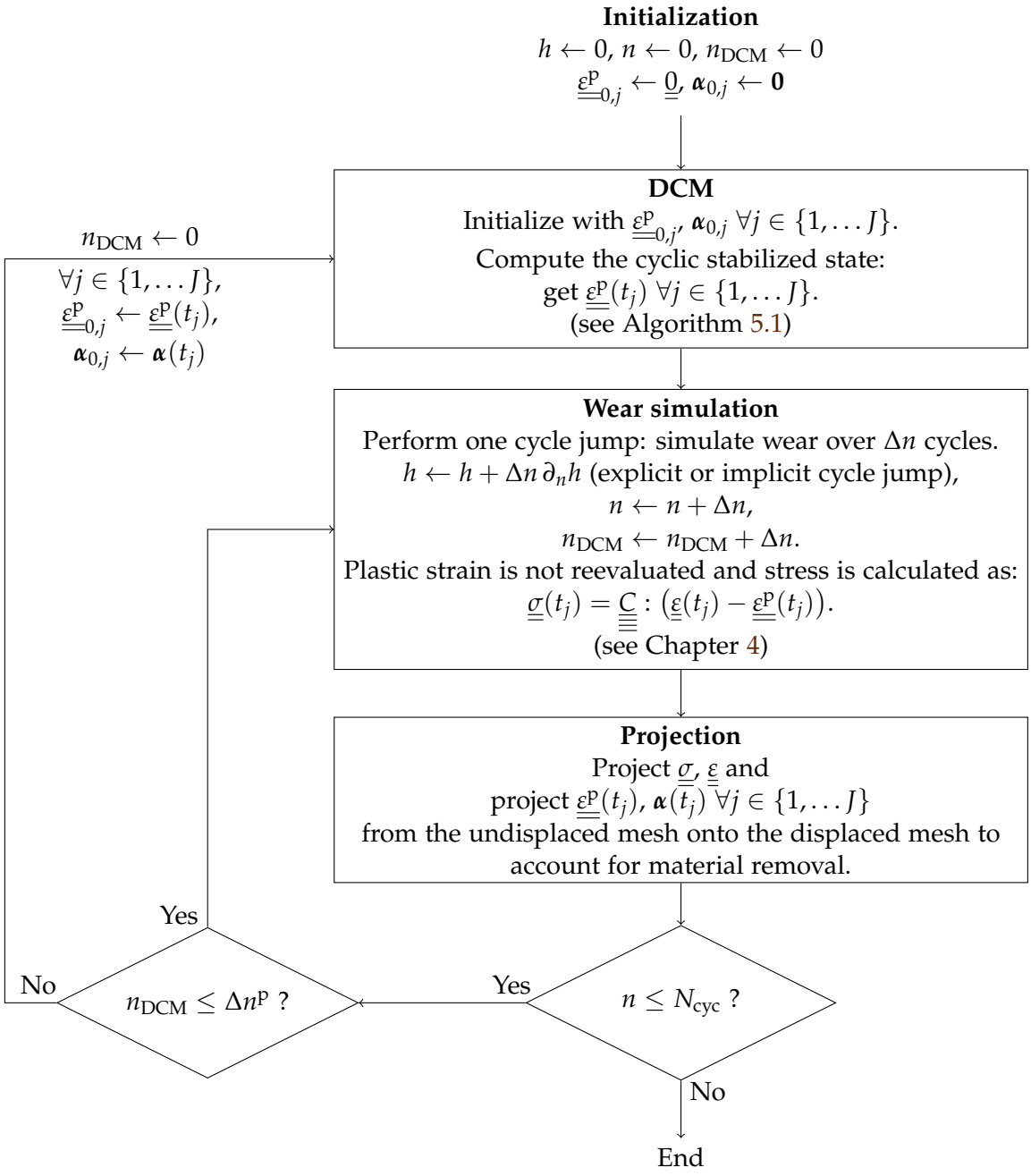

Figure 5.22: Schematic representation of the wear simulation process involving the direct cyclic method for cyclic plasticity computation.

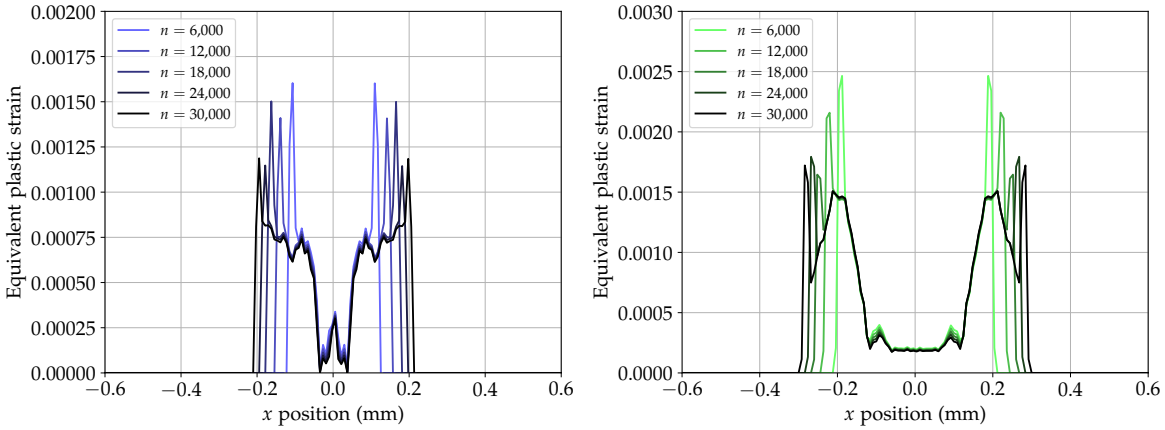

(a) Cylinder **(b)** Plane

Figure 5.23: Evolution of equivalent plastic strain profiles on the cylinder and plane surfaces over 30,000 fretting wear cycles computed using a direct cyclic approach.

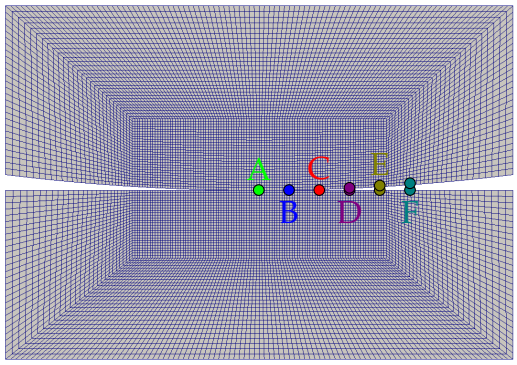

(a) Nodes A to F on the cylinder and plane surfaces

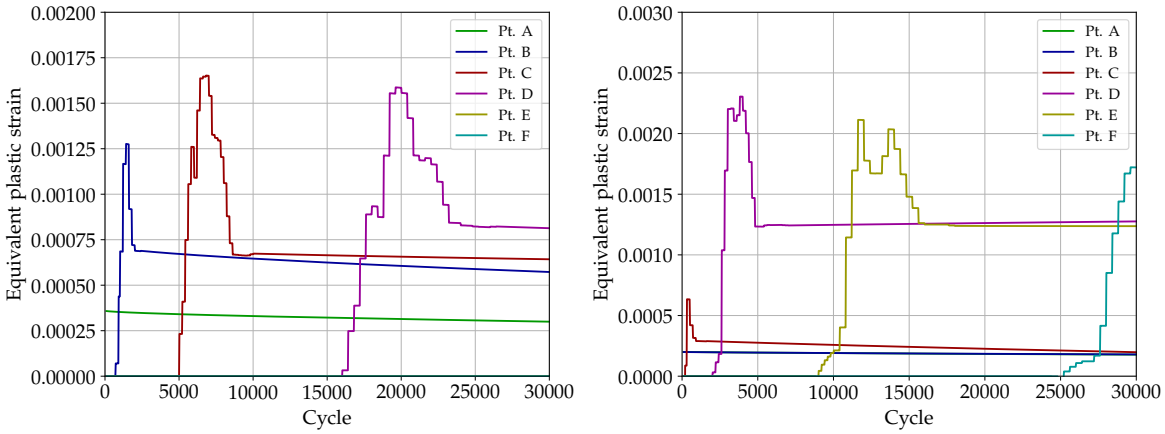

(b) Cylinder **(c)** Plane

Figure 5.24: Evolution of the equivalent plastic strain over 30,000 fretting wear cycles monitored on six different points of the cylinder and plane surfaces.

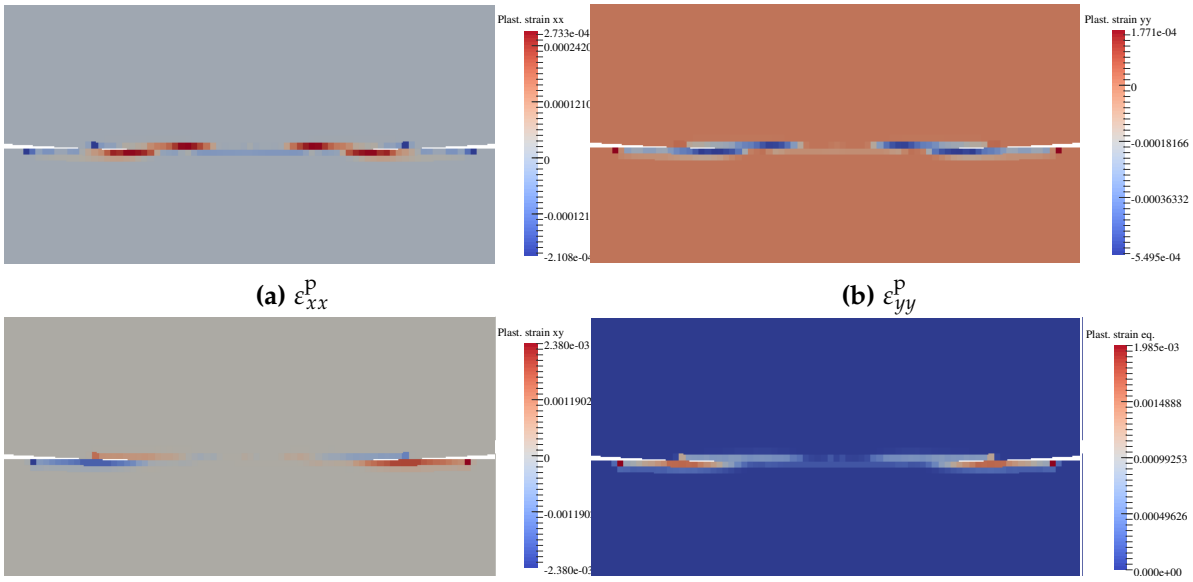

(a) $\varepsilon^{\mathrm{p}}_{xx}$ **(b)** $\varepsilon^{\mathrm{p}}_{yy}$

(c) $\varepsilon^{\mathrm{p}}_{xy}$ **(d)** $\varepsilon^{\mathrm{p}}_{\mathrm{eq}}$

Figure 5.25: Plastic strain fields after 30,000 fretting wear cycles. The view is zoomed in on the contact zone.

effect on the plane surface is hardly visible, although the edge nodes of the profile indeed present a very small vertical displacement.

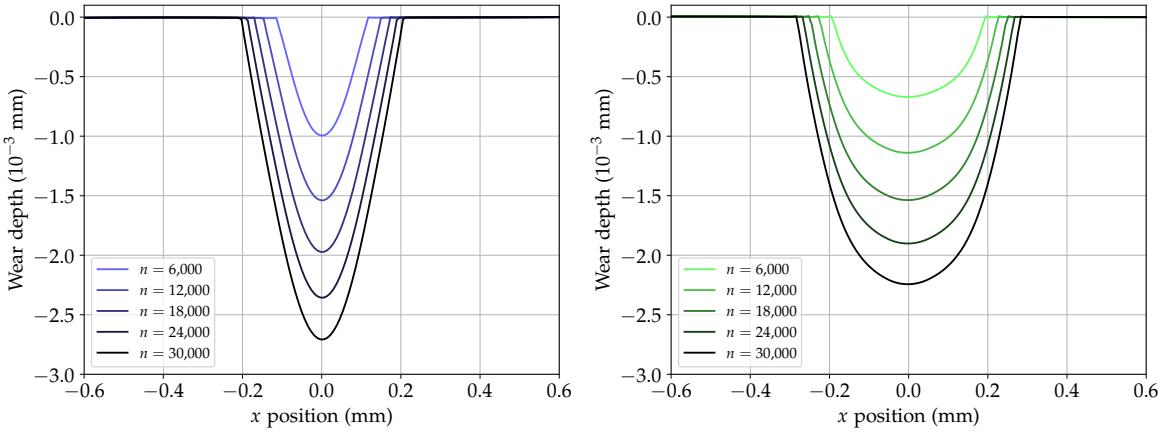

(a) Cylinder **(b)** Plane

Figure 5.26: Evolution of normal displacement profiles on cylinder and plane surfaces over 30,000 fretting wear cycles, accounting for both wear depth and permanent deformation.

5.5 Conclusion

In this chapter, numerical simulation strategies are proposed in order to compute fretting wear evolution considering elastoplastic materials. As a first step, a method involving a cycle jump for plastic strain and hardening variables is proposed, in the continuity of the methods used for wear simulation in elasticity. We use the same linear explicit extrapolation scheme for wear, plastic

strain and hardening variables, which showed to be reliable only for small acceleration factors. Thereafter, an alternative method is proposed which is based on iterated computations of the cyclic stabilized state for plastic strains. The stabilized state is computed using the direct cyclic method. The decoupling between the treatments of wear evolution and cyclic plasticity has the advantage of enabling the use of diverse cycle jump methods for wear evolution, identical to those used in elasticity. This simulation process was proposed based on the assumption that the characteristic time required to reach a stabilized state for plastic strain is small compared to the time for wear to significantly evolve.

The results highlight the existence of a competition between stabilization of cyclic plasticity and contact surface enlargement due to wear. Indeed, whereas cyclic plastic strain seems to tend towards a stabilized state, this stabilized state is continuously disturbed by the integration within the contact area of previously out-of-contact zones. This implies that surfaces subjected to uninterrupted fretting are not likely to reach a fully stabilized state for plastic strain. Surface plastic strains show a stabilization in the central part of the contact surfaces, where plastic strain progressively decreases due to material removal – plastic strain being lower in depth than in surface. Plastic strain levels are at peak near the contact surface edges, indicating the possible existence of a plowing effect. The location of plastic strain peaks on the edges constantly moves outwards due to the contact surface enlargement.

Overall, the great influence of surface geometry evolution due to wear on plastic strains in fretting is outlined. This indicates that a coupled simulation of wear and plasticity is necessary to correctly assess the evolution of plastic strains occurring under fretting motion. Such investigations could provide means to explore the possible correlations between plastic strain accumulation and wear kinetics, enabling a finer understanding of the mechanical processes involved in surface degradation and wear particles detachment.

Chapter recap

This chapter aims at suggesting numerical simulation processes dedicated to the computation of fretting wear considering an elastoplastic material behavior.

- Throughout the chapter, the material behavior is represented using a Chaboche elastoplastic model.

In order to accelerate the simulations, the use of an explicit cycle jump method accounting for plastic strain and hardening variables evolution is explored as a first step.

- Along with wear, plastic strain and hardening variables are extrapolated using a linear explicit scheme.
- Results show a good agreement with the reference simulation when a small acceleration factor is used for the cycle jump.
- For higher values of the acceleration factor, the simulation diverges. As a conclusion, this method is reliable only for sufficiently small acceleration factors.

A second approach is suggested based on the direct determination of a cyclic stabilized state for plastic strain.

- It is assumed that in a hypothetical fixed wear state, a stabilized cyclic state would be reached much faster than the time needed for wear to evolve enough to significantly affect this stabilized state.
- Wear evolution is simulated using the same processes as in elasticity, using an explicit or implicit cycle jump, without constantly reevaluating cyclic plastic strain. Cyclic plastic strain is approximated by the asymptotic cycle, which is computed using the direct cyclic method.
- The asymptotic cycle is updated on a regular basis when wear is expected to have sufficiently evolved to modify it.

The proposed simulation processes enable the simulation of plastic strain evolution throughout fretting cycles considering surface geometry evolution due to wear.

- Wear evolution has a great influence on the evolution of surface plastic strain.
- A competition between stabilization of the cyclic plastic strain and its continuous perturbation by wear evolution is described.
- Zones located in the center of the contact surface have a stabilized plastic strain, which is progressively eroded due to material removal.
- The highest levels of plastic strain are found near the contact surface edges. These locations constantly move outwards due to contact surface enlargement.

Conclusion

When contacting bodies are subjected to fretting motion, wear may occur at the surface of the solids. Wear is a very intricate problem which originates from the microscopic interactions of surface asperities and macroscopically results in a progressive surface material removal. Beyond the multiscale nature of the phenomenon, its complexity also stems from the diversity of physical and chemical processes involved. Fretting wear of metals indeed depends on surface oxygenation and corrosion, on the possible presence of interfacial third body, and may occur through various surface material detachment mechanisms such as abrasion, adhesion, fatigue or delamination.

As a result, research on the subject is mainly conducted following experimental approaches. The most widespread wear models are empirical and are sometimes limited in predicting wear evolution because their parameters hide a dependence on diverse operating conditions. Moreover, simulation of wear is challenging, in particular due to the several non-linearities involved and to the need to compute very high amounts of time steps to capture the progressive evolution of wear.

In this respect, the work presented here proposes to tackle the problem of fretting wear through the perspective of modeling and numerical simulation. As a first step, a modeling approach based on the framework of continuum thermodynamics is presented. It results in the definition of a wear model using a damage variable to quantify the progressive accumulation of degradation eventually causing material detachment. This model relies on the use of the thick level set approach. It provides an original and consistent way to quantify material detachment based on sound thermodynamics principles, and has the advantage of being adaptable with different damage laws. The versatility it offers enables its use regardless of the loading type considered.

A simple simulation process is implemented in order to compute wear evolution with the thick level set wear model. The results show, as expected, that wear is preceded by an initial incubation phase. Once wear onsets, its evolution rate, driven by a fast progression on the edges, is much higher than expected. This is likely related to the delay between the moment the surface experiences loading and the moment wear onsets. Further investigation and additional results using this model, considering different parameters and on higher numbers of cycles, should enable a clearer understanding of its behavior. The comparison with experimental data is a key requirement to assess the capacity of the model to accurately represent experimentally observed wear evolution. The fact that the model features various parameterization means is an asset in this regard. In particular, it could be interesting to investigate the use of alternative functions for the evolution of damage over the partially damaged layer in the thick level set framework. By doing this, the number of cycles required for the initial wear-free level set propagation stage could be reduced, which might yield wear evolutions closer to the expectations.

In a second part, studies dealing more specifically with numerical aspects are presented. Here, wear is assumed to obey a more classical friction energy law. As the simulation of fretting wear requires the computation of numerous cycles, cycle jump methods are commonly used. It is however

well known that a too large cycle jump value may lead to spurious instabilities. Here, an implicit cycle jump method, as opposed to the usual explicit method, is developed. This effectively succeeds in eliminating the instabilities and participates, together with the use of an adaptive cycle jump, in mitigating the computational cost. In contrast with the usual choice, the adaptive cycle jump is based on the wear profile enlargement rate rather than the maximum wear depth rate. In order to improve the convergence of the implicit scheme, more efficient methods than the fixed-point algorithm could be considered. Alternative methods may require the computation of the Jacobian matrix of the wear rate with respect to the wear depth, which is not straightforward.

Finally, a simulation process is described to integrate elastoplastic material behavior models within high-cycle fretting wear simulation frameworks. It uses the direct cyclic method to determine, at fixed wear, a stabilized state for cyclic plasticity. This stabilized state is assumed to be representative of the actual plastic strain evolution over a certain amount of cycles during which wear progressively evolves. The cyclic plasticity state is updated on a regular basis using the direct cyclic method. Because it decouples wear evolution from plastic strain computation, this process has the advantage of offering a flexible choice in the cycle jump method used for the simulation of wear evolution. The simulation results show a competition between the stabilization of cyclic plastic strain, and wear evolution which continuously disturbs plastic strain stabilization by enlarging the contact surface. This results in a progressive displacement of the location of maximum plastic strain towards the surface edges, following the contact surface enlargement due to wear. Such simulation process coupling the evolution of wear with the development of plastic strains may help explore the role played by plastic strains in fretting wear mechanisms, and investigate possible correlations between their occurrence and wear kinetics.

Outlooks

Modeling and numerical simulation approaches remain uncommon in the study of wear problems, the lack of reliable and trusted wear models being the main reason for that. They could however offer, in the long term, better prediction capabilities. In the context of guide cards wear in pressurized water nuclear reactors, more accurate prediction capacities can lead to reduced monitoring and maintenance costs. Efficient numerical approaches are also cheaper than experimental studies, which may be more cumbersome, and could help design components with better wear resistance. For that, the understanding of wear phenomena has to be improved, and more appropriate models need to be developed.

The modeling framework developed here could provide a step towards the achievement of this objective. The relevance of the proposed model needs to be evaluated against experimental tests. Conducting interrupted wear tests may be helpful in order to access the evolution of wear profiles. It might also disclose the existence of an initial incubation stage before the onset of wear. The comparison between numerical simulations and experimental results should allow to adjust the model and determine the values for its parameters. In particular, it should enable the identification of one or several appropriate mechanical quantities to define a relevant driving force for wear. In the case of mild wear, it may rely on elastic strain and stress fields, whereas for severe wear it should probably include plastic variables. This necessitates an evolution of the model to be taken into account. Further improvements enhancing its completeness could integrate third body or account for corrosion effects. Accounting for such major features of fretting wear appears to be necessary in the objective of being able to accurately predict wear kinetics.

Besides, efficient numerical simulation strategies need to be developed for the computation

of wear. They should be designed to integrate appropriate wear models and provide a proper treatment of the different inherent non-linearities. With time, the consideration of additional effects that have an impact on wear, such as corrosion, might require multiphysical simulation frameworks. The issue of computational cost, which is prominent in wear simulations, needs to be tackled for the industrial implementation of numerical approaches.

Bibliography

Akel, S. and Nguyen, Q. S. (1989). Determination of the limit response in cyclic plasticity. *Proceedings of the 2nd International Conference on Computational Plasticity: Models, Software and Applications*, pages 639–650.

Akula, B. R. (2019). *Extended mortar method for contact and mesh-tying applications*. Ph. d. thesis, Université Paris sciences et lettres.

Archard, J. F. (1953). Contact and rubbing of flat surfaces. *Journal of Applied Physics*, 24(8):981–988.

Arnaud, P., Baydoun, S., and Fouvry, S. (2021). Modeling adhesive and abrasive wear phenomena in fretting interfaces: A multiphysics approach coupling friction energy, third body and contact oxygenation concepts. *Tribology International*, 161.

Arnaud, P. and Fouvry, S. (2018). A dynamical FEA fretting wear modeling taking into account the evolution of debris layer. *Wear*, 412-413:92–108.

Arnaud, P., Fouvry, S., and Garcin, S. (2017). A numerical simulation of fretting wear profile taking account of the evolution of third body layer. *Wear*, 376(B):1475–1488.

Banjac, M., Vencl, A., and Otović, S. (2014). Friction and wear processes-thermodynamic approach. *Tribology in Industry*, 36(4):341–347.

Basseville, S., Héripré, E., and Cailletaud, G. (2011). Numerical simulation of the third body in fretting problems. *Wear*, 270(11-12):876–887.

Basseville, S., Niass, M., Missoum-Benziane, D., Leroux, J., and Cailletaud, G. (2019). Effect of fretting wear on crack initiation for cylinder-plate and punch-plane tests. *Wear*, 420:133–148.

Basseville, S., Proudhon, H., Héripré, E., and Cailletaud, G. (2013). Étude numérique des paramètres affectant les profils d'usure en fretting. *Matériaux & Techniques*, 101(2):207.

Baydoun, S. (2020). *Etude du phénomène de fretting-usure d'un contact plan/plan 34NiCrMo16 : application et modélisation du concept d'oxygénation de l'interface*. Ph. d. thesis, Université de Lyon.

Baydoun, S., Arnaud, P., and Fouvry, S. (2020). Modelling adhesive wear extension in fretting interfaces: An advection-dispersion-reaction contact oxygenation approach. *Tribology International*, 151:106490.

Baydoun, S., Fouvry, S., and Descartes, S. (2022). Modeling contact size effect on fretting wear: a combined contact oxygenation - third body approach. *Wear*, 488-489.

Baydoun, S., Fouvry, S., Descartes, S., and Arnaud, P. (2019). Fretting wear rate evolution of a flat-on-flat low alloyed steel contact: A weighted friction energy formulation. *Wear*, 426-427:676–693.

Ben Dhia, H. and Torkhani, M. (2011). Modeling and computation of fretting wear of structures under sharp contact. *International Journal for Numerical Methods in Engineering*, 85(1):61 – 83.

Bernard, P., Moës, N., and Chevaugeon, N. (2012). Damage growth modeling using the Thick Level Set (TLS) approach: Efficient discretization for quasi-static loadings. *Computer Methods in Applied Mechanics and Engineering*, 233-236:11 – 27.

Berthier, Y. (2001). Background on Friction and Wear. In Lemaitre, J., editor, *Handbook of Materials Behavior Models*, pages 676–699. Academic Press, Burlington.

Berthier, Y., Vincent, L., and Godet, M. (1988). Velocity accommodation in fretting. *Wear*, 125(1-2):25–38.

Beyer, T., Chaise, T., Leroux, J., and Nélias, D. (2019). A damage model for fretting contact between a sphere and a half space using semi-analytical method. *International Journal of Solids and Structures*, 164:66–83.

Blanchard, P., Colombié, C., Pellerin, V., Fayeulle, S., and Vincent, L. (1991). Material effects in fretting wear: application to iron, titanium, and aluminum alloys. *Metallurgical Transactions A*, 22(7):1535–1544.

Boher, C., Barrau, O., Gras, R., and Rezai-Aria, F. (2009). A wear model based on cumulative cyclic plastic straining. *Wear*, 267(5-8):1087 – 1094.

Braunovic, M. (2009). Fretting in electrical/electronic connections: A review. *IEICE Transactions on Electronics*, E92-C(8):982–991.

Bryant, M., Khonsari, M., and Ling, F. (2008). On the thermodynamics of degradation. *Proceedings of the Royal Society A: Mathematical, Physical and Engineering Sciences*, 464(2096):2001–2014.

Burwell, J. and Strang, C. (1952). On the empirical law of adhesive wear. *Journal of Applied Physics*, 23(1):18–28.

Caradec, Q., Breuzé, M., Maitournam, H., Prabel, B., and Fayard, J.-L. (2023). Finite element simulation of high cycle fretting wear using an implicit adaptive cycle jump. *Wear*, 522. 24th International Conference on Wear of Materials (WOM), Banff, Canada, Apr 16-20, 2023.

Cast3M (2023). Cast3M. www-cast3m.cea.fr.

Cattaneo, C. (1938). Sul Contatto di Due Corpi Elastici: Distribuzione Locale Degli Sforzi. *Rendiconti dell'Accademia Nazionalle dei Lincei*, 27:342–348.

Chaboche, J. (1986). Time-independent constitutive theories for cyclic plasticity. *International Journal of Plasticity*, 2(2):149–188.

Cojocaru, D. and Karlsson, A. (2006). A simple numerical method of cycle jumps for cyclically loaded structures. *International Journal of Fatigue*, 28(12):1677 – 1689.

Colombié, C. (1986). *Usure induite sous petits débattements. Identification des phénomènes*. Ph. d. thesis, École Centrale de Lyon.

Colombié, C., Berthier, Y., Floquet, A., Vincent, L., and Godet, M. (1984). Fretting: load carrying capacity of wear debris. *Journal of Tribology, Transactions of the ASME*, 106(2):194–201.

D'Annibale, F. and Luongo, A. (2013). A damage constitutive model for sliding friction coupled to wear. *Continuum Mechanics and Thermodynamics*, 25(2-4):503–522.

Dhahri, H. (2019). *Endommagement en fatigue multiaxiale avec effet d'environnement REP*. Ph. d. thesis, Université Paris-Saclay (ComUE).

Ding, J., Leen, S., and McColl, I. (2004). The effect of slip regime on fretting wear-induced stress evolution. *International Journal of Fatigue*, 26(5):521–531.

Ding, J., McColl, I., Leen, S., and Shipway, P. (2007). A finite element based approach to simulating the effects of debris on fretting wear. *Wear*, 263(1-6 Spec. Iss.):481–491.

Doelling, K., Ling, F., Bryant, M., and Heilman, B. (2000). An experimental study of the correlation between wear and entropy flow in machinery components. *Journal of Applied Physics*, 88(5):2999 – 3003.

Done, V., Kesavan, D., Krishna R, M., Chaise, T., and Nélias, D. (2017). Semi analytical fretting wear simulation including wear debris. *Tribology International*, 109:1–9.

Dragon-Louiset, M. (2000). *Contribution à une approche théorique de la mécanique de l'usure*. Ph. d. thesis, École Polytechnique.

Dragon-Louiset, M. (2001). On a predictive macroscopic contact-sliding wear model based on micromechanical considerations. *International Journal of Solids and Structures*, 38(9):1625–1639.

Dragon-Louiset, M. and Stolz, C. (1999). Approche thermodynamique des phenomenes lies a l'usure de contact. *Comptes Rendus de l'Academie de Sciences - Serie IIb: Mecanique, Physique, Chimie, Astronomie*, 327(13):1275–1280.

Elleuch, K. and Fouvry, S. (2002). Wear analysis of A357 aluminium alloy under fretting. *Wear*, 253(5-6):662 – 672.

Elleuch, K. and Fouvry, S. (2005). Experimental and modelling aspects of abrasive wear of a A357 aluminium alloy under gross slip fretting conditions. *Wear*, 258(1-4):40–49. 2nd International Conference on Erosive and Abrasive Wear (ICEAW 2), Churchill Coll, Cambridge, England, Sep 22-25, 2003.

Feng, L. and Xu, J. (2006). The role of plastic anisotropy deformation in fretting wear predictions. *Wear*, 260(11-12):1274–1284.

Fillot, N., Iordanoff, I., and Berthier, Y. (2007). Wear modeling and the third body concept. *Wear*, 262(7-8):949–957.

Fouvry, S. (1997). *Etude quantitative des dégradations en fretting*. Ph. d. thesis, Université de Lyon.

Fouvry, S. (2001). Shakedown analysis and fretting wear response under gross slip condition. *Wear*, 250-251:1320–1331.

Fouvry, S., Arnaud, P., Mignot, A., and Neubauer, P. (2017). Contact size, frequency and cyclic normal force effects on Ti–6al–4v fretting wear processes: An approach combining friction power and contact oxygenation. *Tribology International*, 113:460–473. 43rd Leeds - Lyon Symposium on Tribology 2016.

Fouvry, S., Duó, P., and Perruchaut, P. (2004). A quantitative approach of Ti-6al-4v fretting damage: Friction, wear and crack nucleation. *Wear*, 257(9-10):916–929.

Fouvry, S., Kapsa, P., and Vincent, L. (1996). Quantification of fretting damage. *Wear*, 200(1-2):186–205.

Fouvry, S., Kapsa, P., and Vincent, L. (2001). Elastic-plastic shakedown analysis of fretting wear. *Wear*, 247(1):41–54.

Fouvry, S., Liskiewicz, T., Kapsa, P., Hannel, S., and Sauger, E. (2003). An energy description of wear mechanisms and its applications to oscillating sliding contacts. *Wear*, 255(1):287–298. 14th International Conference on Wear of Materials, Washington, D.C., Mar 30-Apr 03, 2003.

Gallego, L., Fulleringer, B., Deyber, S., and Nélias, D. (2010). Multiscale computation of fretting wear at the blade/disk interface. *Tribology International*, 43(4):708–718.

Gallego, L. and Nélias, D. (2007). Modeling of fretting wear under gross slip and partial slip conditions. *Journal of Tribology*, 129(3):528–535.

Garcin, S., Baydoun, S., Arnaud, P., and Fouvry, S. (2022). Fretting wear modeling of 3d and 2d Hertzian contacts with a third-body layer using a Winkler elastic foundation model. *Tribology International*, 170.

Garcin, S., Fouvry, S., and Heredia, S. (2015). A FEM fretting map modeling: Effect of surface wear on crack nucleation. *Wear*, 330(SI):145–159. 20th International Wear of Materials Conference (WOM), Toronto, Canada, Apr 12-16, 2015.

Gibert, G. (2019). *Propagation de fissures en fatigue par une approche X-FEM avec raffinement automatique de maillage*. Ph. d. thesis, Université de Lyon.

Godet, M. (1984). The third-body approach: A mechanical view of wear. *Wear*, 100(1-3):437–452.

Halphen, B. and Nguyen, Q. S. (1975). Sur les matériaux standard généralisés. *Journal de Mécanique*, 14:39–63.

Hertz, H. (1882). Über die Berührung fester elastischer Körper. *Journal für die Reine und Angewandte Mathematik*, (92):156–171.

Holm, R. (1946). *Electric contacts*. Gebers, Stockholm.

Huq, M. Z. and Celis, J.-P. (2002). Expressing wear rate in sliding contacts based on dissipated energy. *Wear*, 252(5-6):375–383.

Hurricks, P. (1972). The fretting wear of mild steel from room temperature to 200°C. *Wear*, 19(2):207–229.

Iordanoff, I., Berthier, Y., Descartes, S., and Heshmat, H. (2002). A Review of Recent Approaches for Modeling Solid Third Bodies. *Journal of Tribology*, 124(4):725–735.

Johansson, L. (1994). Numerical simulation of contact pressure evolution in fretting. *Journal of Tribology*, 116(2):247–254.

Johnson, K. L. (1985). *Contact Mechanics*. Cambridge University Press.

Kachanov, M. L. (1958). Time of the rupture process under creep conditions. *Izvestiia Akademii Nauk SSSR, Otdelenie Teckhnicheskikh Nauk*, 8:26–31.

Kaczorowski, D. and Vernot, J. P. (2006). Wear problems in nuclear industry. *Tribology International*, 39(10, SI):1286–1293. 4th International Symposium on Fretting Fatigue, Lyon, France, May 26-28, 2004.

Kapoor, A. (1997). Wear by plastic ratchetting. *Wear*, 212(1):119–130.

Kapoor, A. and Franklin, F. (2000). Tribological layers and the wear of ductile materials. *Wear*, 245(1-2):204 – 215.

Kapoor, A. and Johnson, K. (1994). Plastic ratchetting as a mechanism of metallic wear. *Proceedings of the Royal Society A: Mathematical, Physical and Engineering Sciences*, 445(1924):367–381.

Kapoor, A., Johnson, K., and Williams, J. (1996). A model for the mild ratchetting wear of metals. *Wear*, 200(1-2):38–44.

Khruschov, M. (1974). Principles of abrasive wear. *Wear*, 28(1):69–88.

Kiewel, H., Aktaa, J., and Munz, D. (2000). Application of an extrapolation method in thermocyclic failure analysis. *Computer Methods in Applied Mechanics and Engineering*, 182(1-2):55 – 71.

Kim, N. H., Won, D. K., Burris, D., Holtkamp, B., Gessel, G. R., Swanson, P., and Sawyer, W. G. (2005). Finite element analysis and experiments of metal/metal wear in oscillatory contacts. *Wear*, 258(11-12):1787–1793.

Kirk, A., Shipway, P., Sun, W., and Bennett, C. (2019). The effect of frequency on both the debris and the development of the tribologically transformed structure during fretting wear of a high strength steel. *Wear*, 426-427:694 – 703.

Klamecki, B. (1980). Wear - an entropy production model. *Wear*, 58(2):325–330.

Ko, P., Knowles, G., and Taponat, M.-C. (1997). Friction characteristics and the wear process of metal pairs in sliding contacts - With applications to modelling wear of power plant components. *Wear*, 213(1-2):148 – 158.

Ladevèze, P. (1985). Sur une famille d'algorithmes en mécanique des structures. *Comptes-rendus des séances de l'Académie des sciences. Série 2, Mécanique-physique, chimie, sciences de l'univers, sciences de la terre*.

Lemaitre, J., Chaboche, J., Benallal, A., and Desmorat, R. (2009). *Mécanique des matériaux solides - 3ème édition*. Physique. Dunod.

Lemoine, E., Nélias, D., Thouverez, F., and Vincent, C. (2020). Influence of fretting wear on bladed disks dynamic analysis. *Tribology International*, 145.

Lengiewicz, J. and Stupkiewicz, S. (2012). Continuum framework for finite element modelling of finite wear. *Computer Methods in Applied Mechanics and Engineering*, 205-208(1):178–188.

Lijesh, K., Khonsari, M., and Kailas, S. (2018). On the integrated degradation coefficient for adhesive wear: A thermodynamic approach. *Wear*, 408-409:138–150.

Lim, S. C. and Ashby, M. F. (1987). Wear-mechanism maps. *Acta Metallurgica*, 35(1):1–24.

Liu, Y., Liskiewicz, T., and Beake, B. (2019). Dynamic changes of mechanical properties induced by friction in the Archard wear model. *Wear*, 428-429:366–375.

Loew, P. J., Poh, L. H., Peters, B., and Beex, L. A. A. (2020). Accelerating fatigue simulations of a phase-field damage model for rubber. *Computer Methods in Applied Mechanics and Engineering*, 370.

Lê, M.-B. (2013). *Propagation de fissure par fatigue en présence d'une pré-déformation et de contraintes résiduelles*. Ph. d. thesis, École Polytechnique.

Madge, J., Leen, S., and Shipway, P. (2007). The critical role of fretting wear in the analysis of fretting fatigue. *Wear*, 263(1-6 Spec. Iss.):542 – 551.

Mai, S., Le-Corre, F., Foret, G., and Nedjar, B. (2012). A continuum damage modeling of quasi-static fatigue strength of plain concrete. *International Journal of Fatigue*, 37:79–85.

Maitournam, H. (2017). *Matériaux et structures anélastiques*. Éditions de l'École Polytechnique.

Maitournam, M. H., Pommier, B., and Thomas, J.-J. (2002). Determination of the asymptotic response of a structure under cyclic thermomechanical loading; [Détermination de la réponse asymptotique d'une structure anélastique sous chargement thermomécanique cyclique]. *Comptes Rendus - Mecanique*, 330(10):703 – 708.

Maouche, N. (1997). *Modélisation des phénomènes d'endommagements dus aux contacts à faible amplitude de débattement*. Ph. d. thesis, École Nationale des Ponts et Chaussées.

Maouche, N., Maitournam, M., and Dang Van, K. (1997). On a new method of evaluation of the inelastic state due to moving contacts. *Wear*, 203-204:139–147.

Marc, E. (2018). *Analyse de la réponse tribologique d'un contact cylindre/plan soumis à des sollicitations de fretting sous chargement complexe : influence d'une solution Lithium-Bore*. Ph. d. thesis, Université de Lyon.

Marc, E., Fouvry, S., Phalippou, C., and Maitournam, H. (2016). Fretting wear response of a nitrided 316l SS/304l SS interface: Effect of lithium/bore liquid environment. *Surface and Coatings Technology*, 308:226–235. 43rd International Conference on Metallurgical Coatings and Thin Films (ICMCTF), San Diego, CA, Apr 25-29, 2016.

Marigo, J. (1985). Modelling of brittle and fatigue damage for elastic material by growth of microvoids. *Engineering Fracture Mechanics*, 21(4):861–874.

Mary, C. and Fouvry, S. (2007). Numerical prediction of fretting contact durability using energy wear approach: Optimisation of finite-element model. *Wear*, 263(1-6 Spec. Iss.):444–450.

McColl, I. R., Ding, J., and Leen, S. B. (2004). Finite element simulation and experimental validation of fretting wear. *Wear*, 256(11-12):1114–1127.

Meng, H. C. and Ludema, K. C. (1995). Wear models and predictive equations - their form and content. *Wear*, 181(2):443–457. 10th International Conference on Wear of Materials, Boston, MA, Apr 09-13, 1995.

Mindlin, R. D. (1949). Compliance of elastic bodies in contact. *Journal of Applied Mechanics-Transactions of the ASME*, 16(3):259–268.

Mischler, S. and Munoz, A. I. (2018). Tribocorrosion. In Wandelt, K., editor, *Encyclopedia of Interfacial Chemistry*, pages 504–514. Elsevier, Oxford.

Mohd Tobi, A., Sun, W., and Shipway, P. (2017). Investigation on the plasticity accumulation of Ti-6al-4v fretting wear by decoupling the effects of wear and surface profile in finite element modelling. *Tribology International*, 113:448–459.

Mohd Tobi, A. L., Ding, J., Bandak, G., Leen, S. B., and Shipway, P. H. (2009). A study on the interaction between fretting wear and cyclic plasticity for Ti-6al-4v. *Wear*, 267(1-4):270–282.

Mohrbacher, H., Blanpain, B., Celis, J., Roos, J., Stals, L., and Van Stappen, M. (1995). Oxidational wear of TiN coatings on tool steel and nitrided tool steel in unlubricated fretting. *Wear*, 188(1-2):130 – 137.

Moës, N., Stolz, C., Bernard, P.-E., and Chevaugeon, N. (2011). A level set based model for damage growth: The thick level set approach. *International Journal for Numerical Methods in Engineering*, 86(3):358–380.

Nedjar, B. (1995). *Mécanique de l'endommagement. Théorie du premier gradient et application au béton*. Ph. d. thesis, ENPC.

Nélias, D., Boucly, V., and Brunet, M. (2006). Elastic-plastic contact between rough surfaces: Proposal for a wear or running-in model. *Journal of Tribology*, 128(2):236–244.

Oqvist, M. (2001). Numerical simulations of mild wear using updated geometry with different step size approaches. *Wear*, 249(1-2):6–11.

Paulin, C., Fouvry, S., and Deyber, S. (2005). Wear kinetics of Ti-6al-4v under constant and variable fretting sliding conditions. *Wear*, 259(1-6):292–299.

Paulin, C., Fouvry, S., and Meunier, C. (2008). Finite element modelling of fretting wear surface evolution: Application to a Ti-6al-4v contact. *Wear*, 264(1-2):26–36.

Peigney, M. (2004). Simulating wear under cyclic loading by a minimization approach. *International Journal of Solids and Sructures*, 41(24-25):6783–6799.

Popp, A. and Wall, W. (2014). Dual mortar methods for computational contact mechanics - Overview and recent developments. *GAMM Mitteilungen*, 37(1):66–84.

Pradeilles-Duval, R.-M. and Stolz, C. (1995). Mechanical transformations and discontinuities along a moving surface. *Journal of the Mechanics and Physics of Solids*, 43(1):91 – 121.

Proudhon, H., Savkova, J., Basseville, S., Guipont, V., Jeandin, M., and Cailletaud, G. (2014). Experimental and numerical wear studies of porous Reactive Plasma Sprayed Ti–6al–4v/TiN composite coating. *Wear*, 311(1):159–166.

Põdra, P. and Andersson, S. (1999). Simulating sliding wear with finite element method. *Tribology International*, 32(2):71–81.

Rabinowicz, E., Dunn, L., and Russell, P. (1961). A study of abrasive wear under three-body conditions. *Wear*, 4(5):345–355.

Rigney, D., Chen, L., Naylor, M., and Rosenfield, A. (1984). Wear processes in sliding systems. *Wear*, 100(1-3):195 – 219.

Sauger, E. (1997). *Contribution à l'étude de la transformation tribologique superficielle en fretting*. Ph. d. thesis, École Centrale de Lyon.

Sauger, E., Fouvry, S., Ponsonnet, L., Kapsa, P., Martin, J., and Vincent, L. (2000). Tribologically transformed structure in fretting. *Wear*, 245(1-2):39–52.

Shipway, P., Kirk, A., Bennett, C., and Zhu, T. (2021). Understanding and modelling wear rates and mechanisms in fretting via the concept of rate-determining processes - Contact oxygenation, debris formation and debris ejection. *Wear*, 486-487.

Simo, J. and Taylor, R. (1985). Consistent tangent operators for rate-independent elastoplasticity. *Computer Methods in Applied Mechanics and Engineering*, 48(1):101–118.

Stalin Muller, N. and Dang Van, K. (1997). Numerical simulation of the sliding wear test in relation to material properties. *Wear*, 203:180–186. 11th International Conference on Wear of Materials (WoM 97), San Diego, CA, Apr 20-23, 1997.

Stolz, C. (2010). Thermodynamical description of running discontinuities: Application to friction and wear. *Entropy*, 12(6):1418–1439.

Stowers, I. and Rabinowicz, E. (1973). The mechanism of fretting wear. *Journal of Tribology*, 95(1):65 – 70.

Strömberg, N., Johansson, L., and Klarbring, A. (1996). Derivation and analysis of a generalized standard model for contact, friction and wear. *International Journal of Solids and Structures*, 33(13):1817–1836.

Stupkiewicz, S. (2013). An ALE formulation for implicit time integration of quasi-steady-state wear problems. *Computer Methods in Applied Mechanics and Engineering*, 260:130–142.

Suh, N. (1973). The delamination theory of wear. *Wear*, 25(1):111 – 124.

Suh, N. (1977). An overview of the delamination theory of wear. *Wear*, 44(1):1–16.

Tang, Y., Kumar, A., Chen, D., Li, D., Li, Q., and Li, W. (2023). Bauschinger effect on wear of cold-worked Cu and Mg – A study combining molecular dynamics modeling and experimental investigation. *Wear*, 522.

Vakis, A. I., Yastrebov, V. A., Scheibert, J., Nicola, L., Dini, D., Minfray, C., Almqvist, A., Paggi, M., Lee, S., Limbert, G., Molinari, J. F., Anciaux, G., Aghababaei, R., Restrepo, S. E., Papangelo, A., Cammarata, A., Nicolini, P., Putignano, C., Carbone, G., Stupkiewicz, S., Lengiewicz, J., Costagliola, G., Bosia, F., Guarino, R., Pugno, N. M., Müser, M. H., and Ciavarella, M. (2018). Modeling and simulation in tribology across scales: An overview. *Tribology International*, 125:169–199.

Valoroso, N. and Stolz, C. (2022). Graded damage in quasi-brittle solids. *International Journal for Numerical Methods in Engineering*, 123(11):2467–2498.

van Herpen, A., Reynier, B., and Phalippou, C. (2001). Effect of test duration on impact/sliding wear damage of 304l stainless steel at room temperature: Metallurgical and micromechanical investigations. *Wear*, 249(1-2):37 – 49.

van Peteghem, B., Fouvry, S., and Petit, J. (2011). Effect of variable normal force and frequency on fretting wear response of Ti–6al–4v contact. *Wear*, 271(9):1535–1542. 18th International Conference on Wear of Materials.

Vincent, L., Berthier, Y., Dubourg, M. C., and Godet, M. (1992). Mechanics and materials in fretting. *Wear*, 153(1):135–148.

Vingsbo, O. and Söderberg, S. (1988). On fretting maps. *Wear*, 126(2):131–147.

Vor, K. (2009). *Etude expérimentale et modélisation numérique de la fermeture de fissures longues et courtes dans un acier inoxydable 304L*. Ph. d. thesis, École Nationale Supérieure de Mécanique et d'Aéronautique.

Warmuth, A., Shipway, P., and Sun, W. (2015). Fretting wear mapping: The influence of contact geometry and frequency on debris formation and ejection for a steel-on-steel pair. *Proceedings of the Royal Society A: Mathematical, Physical and Engineering Sciences*, 471(2178).

Waterhouse, R. (1977). The role of adhesion and delamination in the fretting wear of metallic materials. *Wear*, 45(3):355–364.

Waterhouse, R. (2000). Plastic deformation in fretting processes - a review. In *ASTM Special Technical Publication*, pages 3–18.

Waterhouse, R. and Taylor, D. (1974). Fretting debris and the delamination theory of wear. *Wear*, 29(3):337–344.

Waterhouse, R. B. (1984). Fretting wear. *Wear*, 100(1):107–118.

Wohlmuth, B. (2001). A mortar finite element method using dual spaces for the Lagrange multiplier. *SIAM Journal on Numerical Analysis*, 38(3):989–1012.

Wriggers, P. (2006). *Computational Contact Mechanics*. Springer-Verlag Berlin Heidelberg, 2 edition.

Yastrebov, V. (2011). *Computational contact mechanics: geometry, detection and numerical techniques*. Ph. d. thesis, École Nationale Supérieure des Mines de Paris.

Zhang, L., Ma, S., Liu, D., Zhou, B., and Markert, B. (2019). Fretting wear modelling incorporating cyclic ratcheting deformations and the debris evolution for Ti-6al-4v. *Tribology International*, 136:317–331.

Zhou, Z., Sauger, E., Liu, J., and Vincent, L. (1997). Nucleation and early growth of tribologically transformed structure (TTS) induced by fretting. *Wear*, 212(1):50–58.

Zhou, Z. and Vincent, L. (1995). Mixed fretting regime. *Wear*, 181-183(PART 2):531–536.

Zhu, T., Bennett, C., and Shipway, P. (2023). Debris expulsion as a rate determining process in fretting – The effect of slip amplitude on debris expulsion behaviour and rates. *Wear*, 523.

Zhu, T. and Shipway, P. (2021). Contact size and debris ejection in fretting: The inappropriate use of Archard-type analysis of wear data and the development of alternative wear equations for commonly employed non-conforming specimen pair geometries. *Wear*, 474-475.

Zhu, T., Shipway, P., and Sun, W. (2019). The dependence of wear rate on wear scar size in fretting; the role of debris (third body) expulsion from the contact. *Wear*, 440-441.

Zmitrowicz, A. (1987a). A thermodynamical model of contact, friction and wear: I governing equations. *Wear*, 114(2):135–168.

Zmitrowicz, A. (1987b). A thermodynamical model of contact, friction and wear: II constitutive equations for materials and linearized theories. *Wear*, 114(2):169–197.

Zmitrowicz, A. (1987c). A thermodynamical model of contact, friction and wear: III Constitutive equations for friction, wear and frictional heat. *Wear*, 114(2):199–221.

Appendix A

Contact formulations

As presented in Chapter 3, different formulations exist to integrate contact and friction conditions within a finite element formulation. Here, the two formulations which are used in the simulations presented in this document are briefly described. The contact formulations are written considering the Lagrange multipliers method for constraints enforcement, and for the sake of simplicity they are presented in the case of a frictionless contact. We recall the weak form for a frictionless contact problem written using the Lagrange multiplier method:

$$\forall \underline{u^*} \in \mathcal{U},\ \int_\Omega \underline{\underline{\sigma}}(\underline{u}) : \underline{\underline{\varepsilon}}(\underline{u^*})\, d\Omega = \int_{\partial\Omega_t} \underline{T_0} \cdot \underline{u^*}\, dS + \int_\Omega \underline{f} \cdot \underline{u^*}\, d\Omega + \int_{\partial\Omega_c} \lambda_n u_n^*\, dS \tag{A.1}$$

$$\forall \lambda_n^* \leq 0,\ \int_{\partial\Omega_c} g_n \lambda_n^*\, dS = 0 \tag{A.2}$$

where $g_n = [\![u_n]\!]_c + g_0$. Contact formulations seek to express the terms related to contact in these expressions, namely the integrals containing a contact Lagrange multiplier λ_n. The considered contact formulations are presented in a two-dimensional case with linear elements. More complete descriptions are given for example by Wriggers (2006).

Node-to-segment formulation

In a node-to-segment formulation, contact conditions are written between the nodes of one of the surfaces, referred to as the *impactor* surface, and the elements of the other – referred to as the *target* surface. Let us denote $\partial\Omega_c^1$ the impactor surface and $\partial\Omega_c^2$ the target surface. We consider a contact element $\partial\Omega_c^h$ composed of a node $\underline{x_1^1}$ from $\partial\Omega_c^1$ and two neighboring nodes $\underline{x_1^2}$ and $\underline{x_2^2}$ from $\partial\Omega_c^2$ (Figure A.1).

A Lagrange multiplier λ_n is associated with this contact element to enforce the normal contact condition. Let us define $\underline{n^2}$ and $\underline{t^2}$ respectively the unit normal and tangential vectors to the target element. We introduce the parameter $\xi \in [0,1]$ which measures the relative position in the target element of the projection of the impactor node $\underline{x_1^1}$ onto the target segment:

$$\xi = \frac{(\underline{x_1^1} - \underline{x_1^2}) \cdot \underline{t^2}}{\|\underline{x_2^2} - \underline{x_1^2}\|} \in [0,1]. \tag{A.3}$$

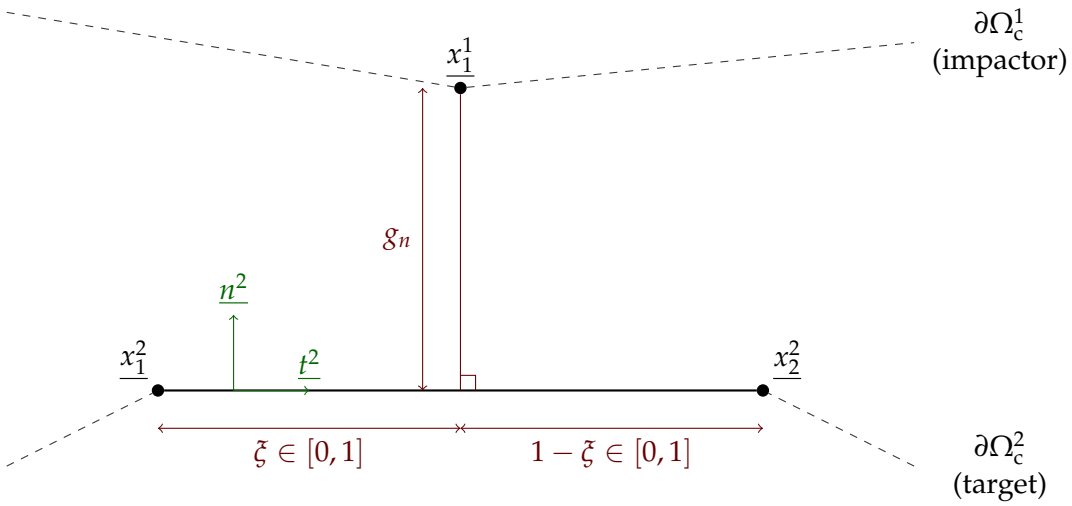

Figure A.1: Contact element for a node-to-segment contact formulation.

This parameter is used to define the normal gap between the impactor node $\underline{x_1^1}$ and the target element:

$$g_n = \left(\underline{x_1^1} - (1-\xi)\underline{x_1^2} - \xi\underline{x_2^2}\right) \cdot \underline{n^2} \tag{A.4}$$

and the normal displacement:

$$u_n = \left(\underline{u_1^1} - (1-\xi)\underline{u_1^2} - \xi\underline{u_2^2}\right) \cdot \underline{n^2}. \tag{A.5}$$

The term related to contact in Equation A.1 is approximated as the sum over all the contact elements of their respective contributions, which is for the considered contact element:

$$\int_{\partial\Omega_c^h} \lambda_n u_n^* \, dS = \|\underline{x_2^2} - \underline{x_1^2}\| \lambda_n \left(\underline{u_1^{1^*}} - (1-\xi)\underline{u_1^{2^*}} - \xi\underline{u_2^{2^*}}\right) \cdot \underline{n^2}. \tag{A.6}$$

The non-penetration constraint (A.2) is approximated in a similar fashion. These expressions are then written under a matrix form to be fitted in the finite element formulation, the unknowns being the nodal displacements and the Lagrange multipliers.

Mortar formulation

As the mortar formulation is a surface-to-surface formulation, contact elements are composed of an element from each of the opposing surfaces. Let us define one of the surfaces as the *mortar* surface, say $\partial\Omega_c^1$, the other surface $\partial\Omega_c^2$ being the *non-mortar* surface. We consider a contact element $\partial\Omega_c^h$ composed of a mortar element delimited by two nodes $\underline{x_1^1}$ and $\underline{x_2^1}$ from $\partial\Omega_c^1$ and a non-mortar element delimited by two nodes $\underline{x_1^2}$ and $\underline{x_2^2}$ from $\partial\Omega_c^2$ (Figure A.2). In the mortar framework, the Lagrange multipliers are defined on the nodes of the non-mortar surface and interpolated using a specific set of basis functions. Thus, we denote $\lambda_{n,1}$ and $\lambda_{n,2}$ the Lagrange multipliers for the normal contact condition, respectively associated with the nodes $\underline{x_1^2}$ and $\underline{x_2^2}$.

Mortar and non-mortar elements are respectively parameterized by variables $\zeta \in [0,1]$ and $\xi \in [0,1]$. We also define $\underline{n^1}$ and $\underline{t^1}$ the unit normal and tangential vectors to the mortar element.

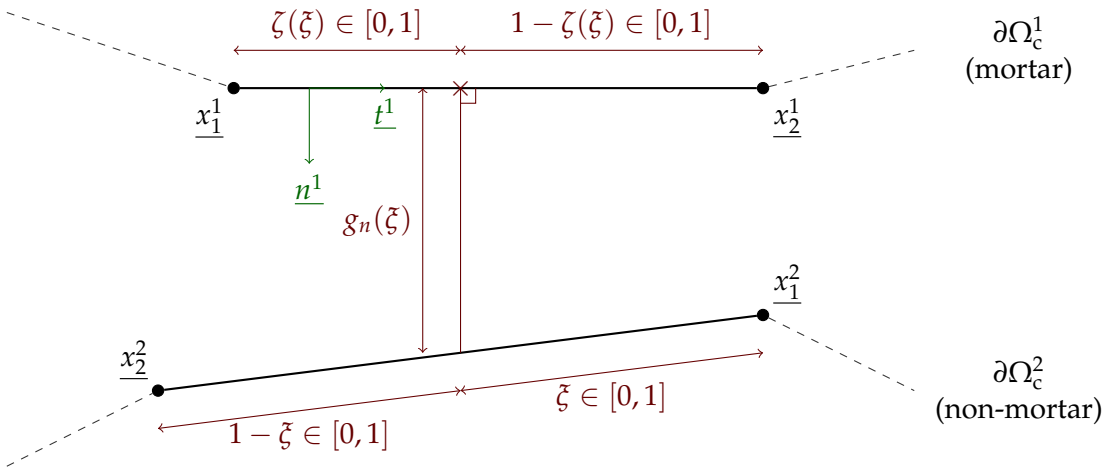

Figure A.2: Contact element for a mortar contact formulation.

Let us consider the orthogonal projection of any point from the non-mortar element onto the mortar element by giving the relation $\zeta(\xi)$:

$$\forall \xi \in [0,1],\ \zeta(\xi) = \frac{\left(\underline{x_1^2} + \xi(\underline{x_2^2} - \underline{x_1^2}) - \underline{x_1^1}\right) \cdot \underline{t^1}}{\|\underline{x_2^1} - \underline{x_1^1}\|}. \tag{A.7}$$

For each $\xi \in [0,1]$, the mortar element is indeed facing the considered point if $\zeta(\xi) \in [0,1]$. In this case, the normal gap is defined as

$$g_n(\xi) = \left((1-\xi)\underline{x_1^2} + \xi\underline{x_2^2} - (1-\zeta(\xi))\underline{x_1^1} - \zeta(\xi)\underline{x_2^1}\right) \cdot \underline{n^1} \tag{A.8}$$

and the normal displacement

$$u_n(\xi) = \left((1-\xi)\underline{u_1^2} + \xi\underline{u_2^2} - (1-\zeta(\xi))\underline{u_1^1} - \zeta(\xi)\underline{u_2^1}\right) \cdot \underline{n^1}. \tag{A.9}$$

The Lagrange multiplier is defined over the non-mortar element through an interpolation of the nodal values $\lambda_{n,1}$ and $\lambda_{n,2}$:

$$\lambda_n(\xi) = M_1(\xi)\lambda_{n,1} + M_2(\xi)\lambda_{n,2} \tag{A.10}$$

where M_1 and M_2 are the basis functions for the Lagrange multipliers. They can be chosen equal to the displacement's:

$$M_1(\xi) = 1 - \xi \text{ and } M_2(\xi) = \xi \tag{A.11}$$

or in the case of the dual mortar method [Wohlmuth 2001]:

$$M_1(\xi) = 2 - 3\xi \text{ and } M_2(\xi) = -1 + 3\xi. \tag{A.12}$$

The contribution of this contact element to the contact-related integral in Equation A.1 is calculated with a Gaussian quadrature. We consider $(\xi_G)_{1 \leq G \leq n_G}$ the set of parameters ξ of the Gauss points of the non-mortar element which project onto the considered mortar element, namely for which $\zeta(\xi_G) \in [0,1]$. This set may be empty if no Gauss point of the non-mortar element can be projected

onto the considered mortar element. We write:

$$\int_{\partial\Omega_c^h} \lambda_n u_n^* \, dS = \|\underline{x_2^2} - \underline{x_1^2}\| \sum_{G=1}^{n_G} w_G \lambda_n(\xi_G) u_n^*(\xi_G) \tag{A.13}$$

$$= \|\underline{x_2^2} - \underline{x_1^2}\| \sum_{G=1}^{n_G} w_G \left(M_1(\xi_G)\lambda_{n,1} + M_2(\xi_G)\lambda_{n,2}\right) \dots$$

$$\dots \left((1-\xi_G)\underline{u_1^{2^*}} + \xi_G \underline{u_2^{2^*}} - (1-\zeta(\xi_G))\underline{u_1^{1^*}} - \zeta(\xi_G)\underline{u_2^{1^*}}\right) \cdot \underline{n^1} \tag{A.14}$$

where w_G is the weight associated with the Gauss point parameterized by ξ_G in the Gaussian quadrature. The contact-related term of Equation A.1 is obtained as the sum of this expression over all the contact elements. This expression is then written under a matrix form to be integrated in the finite element formulation, the unknowns being the nodal displacements and the nodal Lagrange multipliers. The non-penetration constraint (A.2) is expressed in a similar fashion.

These contact formulations are briefly presented here in the simple case of frictionless contact, with two-dimensional linear elements. The extension to friction, three dimensions or higher-order elements is detailed by Wriggers (2006) or Popp and Wall (2014).

Appendix B

Resolution of a level set propagation step in the TLS framework

Let us consider an elastic problem with damage accounted for through the thick level set framework, as presented in Chapter 2 and Chapter 3. In an incremental step-by-step resolution process, the elastic problem is solved as a first step assuming a fixed damage field, then the propagation step of the level set front over the time step is computed. The resolution process to determine the incremental propagation of the level set is detailed here using the finite element code Cast3M.

Let us assume we calculate a certain time step t_{j+1}, knowing the solution at time step t_j. As a first step, the elastic problem is solved at fixed damage $d(t_j)$. Then we want to calculate the level set propagation increment $\boldsymbol{\Delta a}$ over the time step, yielding the new damage field $d(t_{j+1})$. The level set propagation increment is calculated through the resolution of the system:

$$\boldsymbol{K}\,\boldsymbol{\Delta a} = \boldsymbol{\Delta F} \tag{B.1}$$

where $\boldsymbol{K}$, $\boldsymbol{\Delta a}$ and $\boldsymbol{\Delta F}$ are respectively $n_s \times n_s$, $n_s \times 1$ and $n_s \times 1$ matrices – n_s being the number of level set nodes – whose coefficients are[1]:

$$K_{ij} = \int_{\Gamma_0} \int_0^l Y(\phi, s) d'(\phi) \left(1 - \frac{\phi}{r(s)}\right) d\phi\, N_i(s) N_j(s)\, ds \tag{B.2}$$

$$\Delta F_i = \int_{\Gamma_0} \int_0^l \frac{Y^2(\phi, s)}{Y_1(Y_0 + d(\phi) Y_1)} \langle \Delta Y(\phi, s) \rangle_+ \left(1 - \frac{\phi}{r(s)}\right) d\phi\, N_i(s)\, ds. \tag{B.3}$$

At first, we know the position of the level set at the previous time step t_j. The level set takes the form of a line mesh embedded within the main mesh representing the solid body (Figure B.1). This enables the determination of the scalar field $\phi(t_j)$ which is the field of distance to the level set (Figure B.2a). In Cast3M, this is done using the operator `PSIP`. This yields the scalar damage field

[1] The expressions provided for $\boldsymbol{K}$ and $\boldsymbol{\Delta F}$ depend on the damage law considered. Other forms may be envisioned using different damage laws.

$d(t_j)$ (Figure B.2b), for example:

$$\forall \phi \leq 0,\ d(\phi) = 0 \tag{B.4}$$

$$\forall \phi \in [0, l_c],\ d(\phi) = \frac{\phi}{l_c} \tag{B.5}$$

$$\forall \phi \geq l_c,\ d(\phi) = 1. \tag{B.6}$$

This field is originally defined on the mesh nodes, then transferred to the Gauss integration points – the transfer employs the basis functions of the finite element model.

Figure B.1: Level set (red line) embedded within the elastic body, at time step t_j.

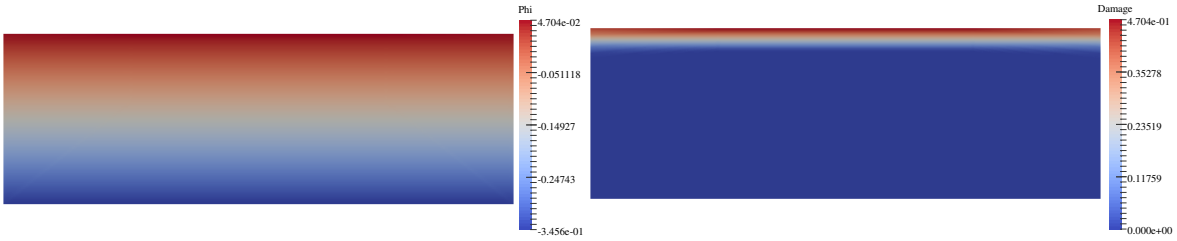

(a) $\phi(t_j)$ **(b)** $d(t_j)$

Figure B.2: Fields ϕ and d at time step t_j.

The solution to the elastic problem at fixed d gives the scalar field Y, for example (Figure B.3a):

$$Y(t_{j+1}) = \frac{\underline{\underline{\sigma}}(t_{j+1}) : \underline{\underline{\varepsilon}}(t_{j+1})}{2(1 - d(t_j))}. \tag{B.7}$$

This enables the calculation of (Figure B.3b)

$$\langle \Delta Y(t_{j+1}) \rangle_+ = \frac{1}{2} \left(Y(t_{j+1}) - Y(t_j) + |Y(t_{j+1}) - Y(t_j)| \right). \tag{B.8}$$

From this, we can build two scalar fields serving as the integrands to calculate the components of $\boldsymbol{K}$ and $\boldsymbol{\Delta F}$:

$$f_K = Y d'(\phi) \left(1 - \frac{\phi}{r} \right) \tag{B.9}$$

$$f_{\Delta F} = \frac{Y^2}{Y_1(Y_0 + Y_1 d)} \langle \Delta Y \rangle_+ \left(1 - \frac{\phi}{r} \right) \tag{B.10}$$

where r is the radius of curvature of the level set. These two fields, defined on the Gauss points,

are depicted in Figure B.4.

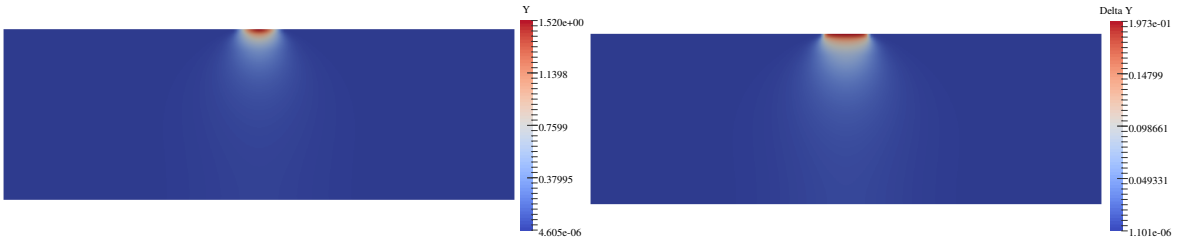

(a) $Y(t_{j+1})$ **(b)** $\langle \Delta Y(t_{j+1}) \rangle_+$

Figure B.3: Fields Y and $\langle \Delta Y(t_{j+1}) \rangle_+$ at time step t_{j+1}.

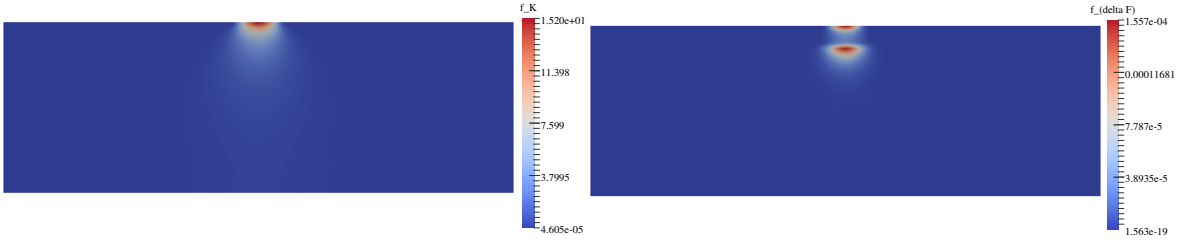

(a) f_K **(b)** $f_{\Delta F}$

Figure B.4: Fields f_K and $f_{\Delta F}$ at time step t_{j+1}.

Because we need to integrate these fields only on the partially damaged zone, their value is set to zero anywhere $\phi \leq 0$ or $\phi \geq l_c$ (Figure B.5):

$$\widetilde{f_K} = \begin{cases} f_k \text{ if } \phi \in [0, l_c] \\ 0 \text{ otherwise} \end{cases} \tag{B.11}$$

$$\widetilde{f_{\Delta F}} = \begin{cases} f_{\Delta F} \text{ if } \phi \in [0, l_c] \\ 0 \text{ otherwise.} \end{cases} \tag{B.12}$$

This is done using Cast3M operator `MASQ`.

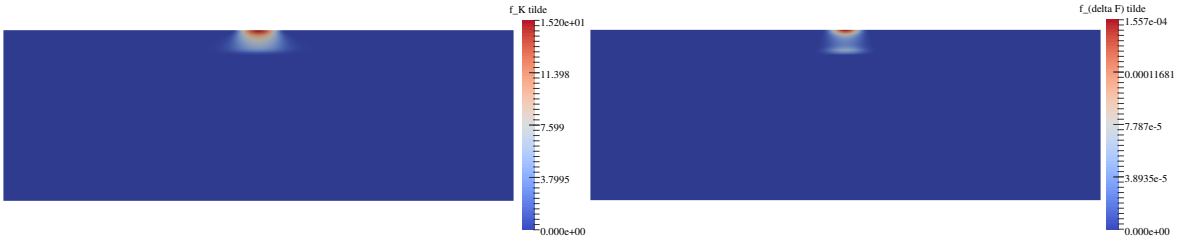

(a) $\widetilde{f_K}$ **(b)** $\widetilde{f_{\Delta F}}$

Figure B.5: Fields $\widetilde{f_K}$ and $\widetilde{f_{\Delta F}}$ at time step t_{j+1}.

After that, a loop is performed on the level set nodes. For each node s_i (for example Figure B.6),

we define the associated basis function N_i as a scalar field defined on the Gauss points:

$$N_i = \begin{cases} 1 - \frac{\psi}{ds\left(1-\frac{\phi}{r}\right)} \text{ if } |\psi| \leq ds\left(1-\frac{\phi}{r}\right) \\ 0 \text{ otherwise} \end{cases} \tag{B.13}$$

where ψ is the field of distance to the line orthogonal to the level set passing through s_i. This field is obtained using Cast3M operator `PSIP`.

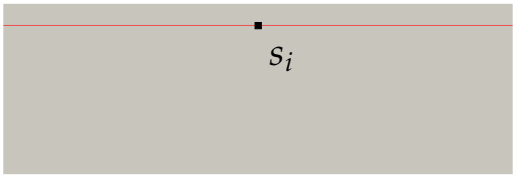

Figure B.6: Node s_i of the level set.

Then, we integrate the field $\widetilde{f_{\Delta F}}N_i$ (Figure B.7b) over the domain Ω using the operator `INTG`, yielding

$$\Delta F_i = \int_\Omega \widetilde{f_{\Delta F}}N_i \, d\Omega. \tag{B.14}$$

Within this first loop, a second nested loop is performed on the level set nodes. For each level set node s_j, the basis function N_j is built the same way as N_i. Then the field $\widetilde{f_K}N_iN_j$ is built (Figure B.7a) and integrated over the domain Ω:

$$K_{ij} = \int_\Omega \widetilde{f_K}N_iN_j \, d\Omega. \tag{B.15}$$

Note that the matrix $\boldsymbol{K}$ should be tridiagonal and symmetric: if $|i-j| \geq 2$, $N_iN_j = 0$.

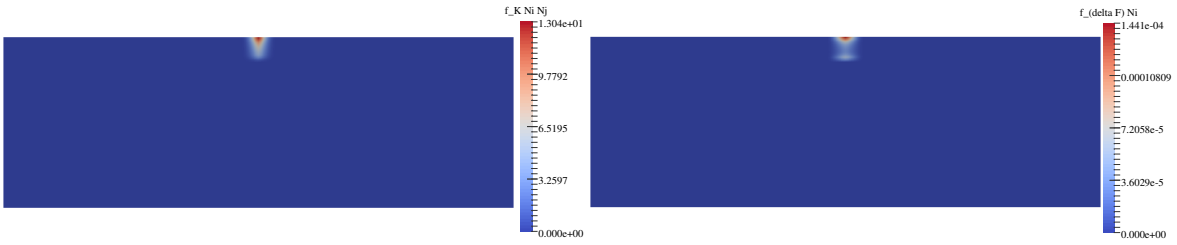

(a) $\widetilde{f_K}N_iN_j$ **(b)** $\widetilde{f_{\Delta F}}N_i$

Figure B.7: Fields $\widetilde{f_K}N_iN_j$ and $\widetilde{f_{\Delta F}}N_i$ at time step t_{j+1}.

When the matrices $\boldsymbol{K}$ and $\boldsymbol{\Delta F}$ are fully built, $\boldsymbol{\Delta a}$ is calculated through the resolution of the system (B.1) using the operator `RESO`. The level set is displaced accordingly, yielding updated distance ϕ and damage d fields.

Résumé en français

Introduction

L'usure désigne un processus de dégradation des matériaux qui se traduit par la perte progressive de matière en surface d'un corps solide, conséquence de contacts répétés avec frottement. Elle peut se produire dans de nombreux contextes industriels. Dans les réacteurs nucléaires à eau pressurisée (REP) en particulier, de l'usure peut être observée au niveau des guides de grappes. Les cartes de guidages qui les composent, qui guident le déploiement des barres de contrôle au sein du cœur du réacteur, peuvent être sujettes à de l'usure du fait des contacts répétés avec les barres de contrôle, mises en mouvement par l'écoulement du fluide primaire dans le réacteur. Dans ce contexte, la cinétique du contact correspond probablement à une combinaison entre de l'impact avec glissement et du *fretting*.

Le fretting fait référence à un mouvement de déplacement relatif tangentiel cyclique entre deux corps en contact, avec une très faible amplitude de déplacement. Ce type de sollicitation peut conduire à différents modes de dégradation des surfaces en contact, notamment l'initiation et la propagation de fissures de fatigue en régime de glissement partiel ou l'usure en régime de glissement total [Vingsbo and Söderberg 1988, Vincent et al. 1992]. Dans cette thèse, l'accent est mis sur les phénomènes d'usure se produisant sous sollicitations de fretting.

L'usure peut se produire par différents modes de détachement de la matière en surface à l'échelle des aspérités. On retient généralement l'abrasion, l'adhésion, la fatigue et le délaminage. Par ailleurs, les mécanismes d'endommagement qui sous-tendent l'usure peuvent être affectés par la possible présence de troisième corps piégé dans l'interface de contact, ou l'existence de phénomènes de corrosion. De façon générale, la littérature décrit une grande diversité de mécanismes en interaction à l'échelle microscopique susceptibles d'engendrer un détachement de matière et de l'usure à l'échelle macroscopique. Le phénomène a donc une nature multi-physique, et multi-échelles en espace et en temps, puisque l'usure est le résultat sur le temps long d'une multitude d'interactions sur des temps courts.

Pour ces raisons, la modélisation des phénomènes d'usure est très complexe. Il n'existe à ce jour aucun modèle largement adopté qui permettrait d'estimer l'évolution de l'usure de façon prédictive. Les modèles les plus répandus sont empiriques, à l'instar de la loi d'Archard qui relie le volume d'usure V à l'effort normal F_n et à la distance de déplacement δ, à travers un coefficient d'usure K [Archard 1953] :

$$V = K\, F_n\, \delta.$$

De façon analogue, une loi d'usure énergétique qui établit une relation de proportionnalité entre volume usé et énergie dissipée par les frottements E_d permet de mieux prendre en compte l'effet

du frottement sur l'évolution de l'usure [Fouvry et al. 1996] :

$$V = \alpha E_{\mathrm{d}}$$

où α est un coefficient énergétique d'usure. Ces modèles, s'ils permettent dans un grand nombre de cas de rendre compte de la cinétique d'usure observée expérimentalement, comportent néanmoins un certain nombre de limites. Certaines études décrivent en effet une dépendance supplémentaire du coefficient d'usure à différents paramètres, par exemple à l'effort normal [Fouvry 2001], l'amplitude de glissement [Fouvry et al. 2004, Paulin et al. 2005, Elleuch and Fouvry 2005], la fréquence du cycle de déplacement tangentiel [van Peteghem et al. 2011, Warmuth et al. 2015, Marc 2018], ou encore la largeur de la surface de contact [Baydoun et al. 2019].

Modélisation de l'usure dans un cadre thermodynamique

Dans cette thèse, une approche de modélisation des phénomènes d'usure dans le cadre de la thermodynamique des milieux continus est proposée. Ce travail s'inscrit dans la continuité des travaux de modélisation de Dragon-Louiset et Stolz, qui proposent de traiter le problème de l'évolution de l'usure comme la propagation d'une surface de discontinuité entre un milieu sain et un milieu usé, représentant le troisième corps [Pradeilles-Duval and Stolz 1995, Dragon-Louiset and Stolz 1999, Dragon-Louiset 2000, Stolz 2010]. Ici, cette approche est reprise en faisant l'hypothèse supplémentaire que le troisième corps est rapidement éjecté hors de l'interface de contact. L'analyse du problème dans le cadre de la thermodynamique des processus irréversibles permet d'exprimer une dissipation liée à l'évolution de l'usure, comme le produit d'une force thermodynamique généralisée $\mathcal{G}$ et du taux d'usure $\dot{h}$:

$$D = \mathcal{G}\dot{h}$$

où D est la puissance dissipée par unité de surface et $\dot{h}$ la vitesse de propagation de la surface d'usure, représentée comme une surface de discontinuité entre le corps sain et le troisième corps. Ici, la force thermodynamique $\mathcal{G}$ correspond à un taux de restitution d'énergie lié à l'avancée de la surface d'usure, et s'exprime:

$$\mathcal{G} = \rho[\![\psi]\!]$$

où ρ est la masse volumique, ψ l'énergie libre spécifique et où la notation $[\![\cdot]\!]$ indique la discontinuité de la grandeur à travers la surface d'usure.

Par la suite, un modèle d'usure basé sur la mécanique de l'endommagement est développé. Dans ce modèle, on considère que l'usure résulte d'une accumulation de dommages dans une couche en surface. On introduit alors une variable d'endommagement, notée d et associée à une force thermodynamique généralisée Y, et on suppose que l'usure se produit lorsque l'endommagement atteint un seuil d_{c} en surface. L'évolution de l'endommagement est traitée par une approche *thick level set* [Moës et al. 2011]. Dans cette approche, l'endommagement évolue au sein d'une couche partiellement endommagée dont l'épaisseur est limitée par un seuil. La surface qui délimite la zone non-endommagée de la zone partiellement endommagée est la level set. La loi locale d'endommagement est homogénéisée sur l'épaisseur de la couche partiellement endommagée pour exprimer l'évolution de l'endommagement à travers une loi non-locale de propagation de la level set. Le modèle suppose que l'évolution spatiale de l'endommagement à travers la zone partielle-

ment endommagée est donnée explicitement par une fonction de la distance à la level set, qui est un paramètre du modèle. Ainsi, l'évolution de l'endommagement découle directement de la propagation de la level set.

Cette méthode peut être adaptée en utilisant différentes formes pour la loi locale d'endommagement. Dans ce travail, un exemple est donné avec une loi d'endommagement propice à représenter une accumulation cyclique de dommages, ce qui permet de formuler le problème de propagation de la level set par la résolution d'un système linéaire. Le modèle proposé présente ainsi comme avantage d'être adaptable notamment par le choix de la loi d'endommagement, et de la forme choisie pour la force thermodynamique associée à l'endommagement. On peut par exemple envisager de ne considérer que la partie déviatorique des contraintes ou des déformations comme grandeurs mécaniques motrices de l'endommagement.

Simulation numérique des problèmes d'usure

La suite de la thèse traite des méthodes de simulation numérique pour la résolution des problèmes d'usure. La simulation numérique de l'usure présente un certain nombre de difficultés, en raison notamment des non-linéarités inhérentes au problème (contact, frottement, comportement des matériaux, évolution de la géométrie des surfaces) et de la nécessité de simuler de grands nombres de pas de temps.

La problématique du coût de calcul est abordée en suivant une hypothèse formulée par Lengiewicz and Stupkiewicz (2012) et fréquemment utilisée dans les travaux sur la simulation numérique de l'usure [Oqvist 2001, McColl et al. 2004] qui consiste à découpler le problème de contact-frottement du problème de l'évolution de l'usure. Ainsi, chaque cycle de chargement est calculé à usure fixée, comme un problème de contact-frottement classique et résolu incrémentalement comme une suite d'équilibres statiques sur un ensemble de pas de temps. Ensuite, l'évolution de l'usure engendrée sur le cycle est calculée en post-traitement à l'issue du cycle. Cela permet d'exprimer un taux d'usure cyclique, qui correspond à l'incrément de profondeur d'usure par cycle. Cette hypothèse autorise l'utilisation d'une méthode de saut de cycle. Un facteur d'accélération Δn est introduit, et le taux d'usure cyclique calculé sur un cycle de chargement est extrapolé sur Δn cycles, permettant un gain important en terme de temps de calcul.

Sur la base de cette hypothèse, une méthode de calcul d'usure utilisant le modèle d'usure basé sur l'endommagement avec l'approche thick level set présenté précédemment est décrite. Elle repose sur la méthode des éléments finis pour la résolution du problème incrémental de contact-frottement. Un modèle par éléments finis en deux dimensions est construit, représentant un problème simple de contact entre un cylindre et un plan. Le modèle est construit avec pour référence des essais expérimentaux de fretting réalisés par Marc (2018). Quelques résultats de calcul sont présentés, et les résultats obtenus avec le modèle d'usure par endommagement sont comparés avec des résultats obtenus en utilisant une loi d'usure énergétique.

Méthodes de saut de cycle pour la simulation de l'usure par fretting à grand nombre de cycles

Afin de pouvoir simuler l'évolution de l'usure sur de grands nombres de cycles de fretting, par exemple en lien avec les essais expérimentaux de Marc (2018), l'efficacité de la méthode de saut de cycle employée est primordiale. La méthode la plus fréquemment employée dans le cadre de la simulation de l'usure utilise un schéma d'Euler explicite, que l'on peut exprimer de la façon suivante :

$$h_{k+1} = h_k + \Delta n \, \partial_n h_k$$

où h_k et h_{k+1} désignent les profils d'usure respectivement aux cycles n_k et n_{k+1}, le facteur d'accélération correspondant à l'écart entre les deux cycles :

$$\Delta n = n_{k+1} - n_k$$

et où $\partial_n h_k$ correspond au taux d'usure par cycle, c'est à dire à l'incrément de profondeur d'usure généré par un cycle de chargement, calculé au cycle n_k. Ce schéma explicite permet de formuler une procédure de calcul simple : l'état d'usure au cycle n_k est connu, et la résolution du problème de contact-frottement sur ce cycle permet de connaître le taux d'usure $\partial_n h_k$ en utilisant la loi d'usure. En utilisant le schéma de saut de cycle explicite, on a directement accès à l'état d'usure au cycle n_{k+1}.

Il est néanmoins bien connu que l'utilisation d'un schéma de ce type conduit à des instabilités lorsque le facteur d'accélération est choisi trop grand [McColl et al. 2004, Mary and Fouvry 2007]. Par ailleurs, plus le maillage est fin, plus le facteur d'accélération critique de stabilité est faible ce qui rend le raffinement du maillage encore plus préjudiciable du point de vue du coût de calcul. Dans ce travail, une étude est menée sur l'utilisation de schémas de saut de cycle alternatifs. Dans un premier temps, des schémas explicites de Runge-Kutta du second et du quatrième ordre sont implémentés pour la simulation de l'usure. Les résultats obtenus montrent que ces schémas, s'ils permettent d'accroître légèrement la stabilité du calcul en terme de facteur d'accélération critique, n'offrent pas de gain en terme de coût de calcul en raison de la nécessité de calculer respectivement deux ou quatre cycles de chargement pour passer du cycle n_k au cycle n_{k+1}.

Une méthode de saut de cycle implicite est ensuite proposée. Le schéma utilisé peut s'écrire :

$$h_{k+1} = h_k + \Delta n \, \partial_n h_{k+1}$$

où cette fois le taux cyclique d'usure est calculé sur l'état au cycle n_{k+1}. Le schéma implicite est résolu par une méthode itérative de type point fixe avec relaxation, qui nécessite le calcul d'un cycle de chargement à chaque itération avant convergence. Les résultats obtenus avec un schéma de ce type montrent que le temps de calcul peut être significativement réduit, car l'utilisation d'une méthode implicite offre la possibilité de choisir un facteur d'accélération plus grand que la limite de stabilité en explicite tout en conservant un calcul stable. Le nombre d'itérations pour la convergence du schéma implicite reste limité.

Simulation de l'usure avec un comportement élastoplastique des matériaux

L'ensemble des développements présentés jusqu'ici sont réalisés en considérant que le comportement des matériaux est élastique – ou élastique-endommageable. Il apparaît cependant que la cinétique d'usure peut être corrélée à une accumulation de déformations plastiques dans une couche de matière en surface [Fouvry 2001]. Ainsi, la capacité à simuler l'évolution de l'usure en présence d'un matériau au comportement élastoplastique permettrait d'étudier plus en profondeur cet aspect des mécanismes d'usure. L'intégration de lois de comportement de ce type dans des calculs utilisant un saut de cycle n'est cependant pas directe. Les lois de comportement élastoplastique dépendent en effet du trajet de chargement, ce qui nécessite de décrire l'évolution des déformations plastiques et des variables internes d'écrouissage lors du saut de cycle.

Dans un premier temps, l'interaction entre l'évolution de l'usure et le développement de déformations plastiques proches de la surface est mise en avant. Des simulations par éléments finis sont réalisées sur une configuration cylindre-plan en utilisant une loi de Chaboche pour modéliser le comportement élastoplastique cyclique des matériaux. Cette loi intègre un écrouissage isotrope non-linéaire et un écrouissage cinématique non-linéaire. D'une part, un calcul de fretting sans usure ni saut de cycle est réalisé sur 100 cycles. Le résultat montre le développement de déformations plastiques cycliques en surface du cylindre et du plan, qui se stabilisent après plusieurs dizaines de cycles vers un état adapté ou accommodé. D'autre part, un calcul similaire en considérant cette fois une évolution de la géométrie de la surface due à l'usure est réalisé. En comparaison, la présence d'usure conduit à une adaptation beaucoup plus rapide, qui est liée à la diminution locale de la pression de contact du fait de l'élargissement de la surface de contact. Par ailleurs, l'élargissement continu de la surface de contact engendre, après un certain nombre de cycles, le développement de déformations plastiques en des points de la surface qui se trouvaient initialement en dehors de la zone de chargement. Ainsi, l'état cyclique n'est jamais complètement stabilisé : l'évolution donne lieu à une compétition entre, d'un côté, la stabilisation de l'état plastique cyclique, et de l'autre la perturbation de cet état stabilisé à cause de l'évolution de l'usure.

Les calculs réalisés jusqu'ici le sont sans saut de cycle et concernent donc des nombres de cycles relativement faibles, en raison du coût de calcul important. Afin de pouvoir traiter des nombres de cycles plus importants, une stratégie utilisant la méthode cyclique directe est mise en œuvre. La méthode cyclique directe permet de chercher directement, sans suivre de façon incrémentale l'histoire de la réponse du matériau au chargement, l'état cyclique asymptotique stabilisé en plasticité – s'il existe [Maouche et al. 1997, Maitournam et al. 2002]. La méthode de calcul proposée repose sur l'hypothèse que la durée caractéristique nécessaire à l'usure pour altérer significativement l'état de déformations plastiques cycliques est bien plus grande que la durée nécessaire pour atteindre un état stabilisé. Ainsi, on suppose que l'état cyclique stabilisé, calculé à l'aide de la méthode cyclique directe, fournit une bonne approximation de l'état cyclique réel si l'on calculait effectivement tous les cycles incrémentalement. Cela permet de calculer un certain nombre de cycles d'usure en utilisant les procédures habituellement utilisées en élasticité, sans recalculer les déformations plastiques. Après un certain nombre de cycles, lorsque l'usure a suffisamment évolué pour affecter l'état stabilisé de manière non-négligeable, la méthode cyclique directe est employée de nouveau pour mettre à jour l'état cyclique de déformations plastiques. Cette méthode, qui consiste donc en une résolution découplée et alternée de l'état cyclique plastique et de l'évolution de

l'usure, présente l'avantage de pouvoir intégrer sans difficultés les méthodes habituelles de saut de cycle pour l'usure, y compris l'utilisation d'un schéma implicite.

Un résultat de calcul utilisant cette méthode sur 30 000 cycles de fretting est présenté. Les déformations plastiques les plus importantes se situent, tout au long du calcul, sur les bords de la zone de contact, qui se déplacent en permanence vers l'extérieur à cause de l'élargissement de la zone usée. Lorsque la zone usée s'élargit, les points qui se situaient précédemment sur les bords de la surface de contact se retrouvent par la suite intégrés en son sein, et atteignent rapidement un état stabilisé. L'évolution de l'usure engendre également l'érosion progressive de la matière en surface, et donc une lente diminution de la déformation plastique en surface : les points qui étaient initialement en sous-surface, où la déformation plastique est moins importante, se retrouvent par la suite sur la surface libre à cause de l'enlèvement de matière.

Conclusion

L'étude de l'usure se fait encore principalement par des approches expérimentales, en raison notamment de l'absence de modèle fiable et largement accepté. Des approches couplant de la modélisation et de la simulation numérique pourraient néanmoins, sur le long terme, fournir de meilleures capacités prédictives de ce type de phénomène. À ce titre, le travail présenté ici propose un cadre formel de modélisation dans le cadre de la thermodynamique des milieux continus. Le modèle présenté suppose que l'usure résulte d'une accumulation de dommages dans une couche de matière proche de la surface, et peut être adapté par l'utilisation de différentes formes pour la force motrice du phénomène et de différentes loi d'évolution de l'endommagement. Afin d'établir la combinaison de quantités mécaniques qui serait la plus appropriée pour gouverner l'évolution de l'usure et d'identifier la cinétique du phénomène en lien avec ces quantités, une étude couplant modélisation, simulation numérique et essais expérimentaux est nécessaire.

La problématique du coût de calcul est prépondérante dans la simulation de l'usure, en raison des non-linéarités inhérentes au problème et de la nécessité de simuler de très grands nombres de pas de temps. Une étude est ainsi proposée sur les méthodes de saut de cycles les plus efficaces pour la simulation de l'usure par éléments finis. Par ailleurs, une stratégie de calcul intégrant l'utilisation de lois de comportement élastoplastique des matériaux est développée. Si ces travaux permettent effectivement d'accélérer les calculs d'usure en y intégrant la prise en compte d'une physique plus complexe, la question du temps de calcul reste une problématique importante pour le développement d'approches numériques sur des cas d'usure plus sophistiqués.

ECOLE DOCTORALE

Titre: Contribution à la modélisation et à la simulation numérique de l'usure par fretting

Mots clés: Usure, fretting, modélisation, simulation numérique, méthode des éléments finis

Résumé:
Lorsque deux corps en contact sont soumis à une sollicitation de fretting, c'est à dire un mouvement cyclique de déplacement relatif de faible amplitude, de l'usure peut se produire. Il s'agit d'un phénomène complexe qui trouve son origine à l'échelle microscopique dans les interactions entre aspérités de surface et se traduit sur le long terme, à l'échelle macroscopique, par une perte progressive de matière en surface. La diversité des mécanismes microscopiques qui sous-tendent l'usure, en plus de sa nature multi-physique et multi-échelles, en temps et en espace, rend le phénomène très complexe à modéliser. Les modèles les plus répandus sont empiriques et, s'ils parviennent dans un certain nombre de cas à corréler les résultats expérimentaux, ils ne permettent pas de prédire efficacement l'évolution de l'usure de façon générale. Pour ces raisons, l'étude des phénomènes d'usure se fait généralement par des approches expérimentales.
Le travail présenté s'attache à traiter le problème de la modélisation et de la simulation numérique de l'usure sous sollicitations de fretting. Le premier volet de ce travail consiste en une approche de modélisation originale, dans le cadre de la thermodynamique. L'accumulation progressive de dégradations conduisant à l'usure y est quantifiée au moyen d'une variable d'endommagement, et le modèle repose sur l'utilisation de l'approche *thick level set*. Une procédure de calcul utilisant la méthode des éléments finis est définie pour simuler l'usure en utilisant ce modèle.
Dans une seconde partie, l'accent est mis sur la simulation numérique. La simulation de l'usure présente un certain nombre de difficultés, d'une part du fait des non-linéarités inhérentes au problème (contact, frottement, évolution de la géométrie des surfaces, non-linéarité du comportement des matériaux), et d'autre part en raison de la nécessité de simuler de très grands nombres de pas de temps. Afin de conserver un temps de calcul raisonnable, une méthode de saut de cycle implicite est proposée. À l'inverse de la méthode explicite classiquement employée, elle permet d'éliminer les instabilités qui peuvent apparaître lorsque le saut de cycle est trop grand. Par ailleurs, une procédure de simulation permettant d'intégrer des lois de comportement élastoplastique dans les calculs d'usure est définie.

Title: On the modeling and numerical simulation of fretting wear

Keywords: Wear, fretting, modeling, numerical simulation, finite element method

Abstract:
When two contacting bodies are subjected to fretting motion, namely a cyclic tangential displacement with a very small displacement amplitude, they may experience different forms of degradation. Wear, which is defined as a progressive surface material removal, generally prevails under gross slip conditions. Wear of materials is a very complex phenomenon: it is the long-term, macroscopic result of various microscopic physical and chemical processes. This multi-physical and multi-scale nature makes its modeling difficult, such that there exists no widely adopted unified wear model. The most widespread wear models are empirical, and they sometimes fail to accurately predict wear evolution. As a result, studies on the subject are generally conducted through experimental approaches.
The work presented here proposes to tackle the problem through the angle of modeling and numerical simulation. In a first part, an original modeling approach is proposed based on a thermodynamic framework. In this model, wear is accounted for by means of a damage-like variable whose role is to quantify the progressive accumulation of degradation ultimately leading to material detachment. This model uses the thick level set approach to govern the evolution of the surface geometry following wear. A numerical simulation strategy using the finite element method is defined to compute wear evolution using this model.
In a second part, focus is on numerical aspects. The numerical simulation of wear problems is especially challenging, on the one hand because it involves several non-linearities (frictional contact, surface geometry evolution, material behavior), and on the other hand because it requires to simulate high amounts of time steps. In order to keep reasonable computational costs, an implicit cycle jump method is implemented. It proves to be more stable and efficient than the usually used explicit method. In addition, a simulation strategy is proposed to integrate the use of elastoplastic material behavior models within the wear simulation frameworks defined.

Institut Polytechnique de Paris
91120 Palaiseau, France